



Dipl.-Ing. Paul Meissner, BSc.

MULTIPATH-ASSISTED INDOOR POSITIONING

Dissertation

for the degree of:

Doctor of Technical Sciences

submitted at

Graz University of Technology

Supervisor and First Examiner:

Assoc.Prof. Dipl.-Ing. Dr. Klaus Witrisal

Signal Processing and Speech Communications Laboratory
Graz University of Technology, Austria

Second Examiner:

Prof. Moe Z. Win, PhD.

Laboratory for Information and Decision Systems
Massachusetts Institute of Technology, Cambridge, USA

Graz, October 2014

This work was partly supported by the Austrian Science Fund (FWF) within the National Research Network "SISE" project S10610, and by the Austria Research Promotion Agency (FFG) within KIRAS PL3, grant 832335 "LOBSTER".

Abstract

Location awareness is a key enabler for a multitude of indoor applications, such as logistics, intelligent warehouses, or flexible production. The robust provision of accurate position information requires a careful fusion of location-dependent parameters acquired by various sensors, including range measurements from radio signals. The latter are the basis for successful outdoor localization systems like the Global Positioning System (GPS). However, indoor environments are often characterized by dense multipath channels. These originate from the superposition of many physical propagation mechanisms, which are caused by many spatially close interacting objects. Especially for indoor localization systems, this is still the main source of errors. However, deterministic reflections of the radio signal on surfaces such as walls can be modeled geometrically, leading to defined relationships of their path parameters with the position of an agent that is receiving such a signal and thus additional position-related information.

The position-related information inherent in these signal paths is the main focus of this thesis. A geometric-stochastic channel model allows for the proper decomposition of signals into useful information and non-resolvable, interfering components. The concept of virtual anchors (VAs) is employed for the geometric modeling of deterministic multipath components (MPCs) using a known floor plan as prior knowledge. It is shown by experiments that these MPCs carry a significant part of the energy of a received radio signal. Statistical performance bounds are derived for multipath-assisted positioning, defining the position-related information of each MPC as a function of signal and channel parameters. Most importantly, a Signal-to-Interference-and-Noise Ratio (SINR) is introduced that quantifies the amount of this information for each MPC. Estimation methods are presented for the SINR, which allow to characterize the position-related information of an environment.

Based on the position-related information, the results presented in this thesis allow (i) to gain an understanding of the physically relevant propagation phenomena using measured data, (ii) to find statistical models to characterize their influence on the position-related parameters in the signals, and (iii) to show the excellent accuracy and robustness that can be achieved by exploiting multipath. Tracking algorithms are proposed that can be made aware of the position-relevant propagation phenomena and their respective uncertainty. Using experimental data from various scenarios, this is shown to be the key factor enabling the constructive use of MPCs for positioning, consistently leading to position errors below 5 cm for 90 % of the estimates.

The work in this thesis is in contrast to most existing literature on radio-based indoor positioning, in which methods are presented to counteract the performance impairments of multipath. One outcome is a real-time demonstration system that allows for fast and flexible testing of existing and new algorithms and serves as a proof-of-concept for multipath-assisted tracking. The experimental results in this thesis are valuable for the design and evaluation of future indoor wireless applications. This is especially true for the presented results on channel analysis, which give guidelines for the design and parametrization of spatially consistent geometric-stochastic channel models.

Kurzfassung

Die Möglichkeit zur Positionsbestimmung erlaubt eine Vielzahl von Innenraum-Anwendungen, wie etwa in der Logistik, in intelligenten Kaufhäusern sowie in der flexiblen Produktion. Robuste und akkurate Positionierung erfordert eine sorgfältige Kombination von positionsabhängigen Parametern, welche aus den Messwerten verschiedener Sensoren geschätzt werden. Distanzmessungen mittels Funksignalen sind hierbei populär und bilden die Basis für beispielsweise das Global Positioning System (GPS). Dieses und ähnliche Systeme sind hauptsächlich für Außenbereiche konzipiert. Ausbreitungskanäle in Innenräumen weisen oft eine große Anzahl und Dichte von Mehrwegekomponenten auf, was der Hauptgrund für die mangelnde Robustheit und die typischerweise größeren Fehler von Innenraum-Lokalisierungssystemen ist. Ein Teil der Mehrwegekomponenten trägt jedoch positionsrelevante geometrische Information in sich, welche durch geeignete Modellierung zur Positionierung genutzt werden kann.

Diese in den Funksignalen eingebettete positionsrelevante Information bildet den Schwerpunkt dieser Arbeit. Ein geometrisch-stochastisches Kanalmodell erlaubt die Zerlegung der Signale in nützliche Information und nicht auflösbare, interferierende Komponenten. Das Konzept der Spiegelquellen wird mit Hilfe eines Bauplans für die geometrische Modellierung der deterministischen Mehrwegekomponenten genutzt. Experimente mit gemessenen Signalen zeigen, dass ein signifikanter Teil der Energie eines empfangenen Funksignals auf diese Komponenten zurückzuführen ist. Statistische Schranken für den Positionierungsfehler von Mehrwege-unterstützter Positionierung führen zur formalen Definition der positionsrelevanten Information dieser Komponenten. Diese kann als Funktion von Signal- und Kanalparametern dargestellt werden und wird durch den Signal-zu-Interferenz-und-Rausch-Abstand der jeweiligen Mehrwegekomponente quantifiziert. In dieser Dissertation werden Schätzmethoden vorgeschlagen, die eine Charakterisierung dieser Information in einer Umgebung erlauben.

Die in dieser Arbeit präsentierten Resultate erlauben es, (i) ein Verständnis der physikalisch relevanten Ausbreitungsphänomene mit Hilfe gemessener Daten zu gewinnen, (ii) statistische Modelle zu finden, welche den Einfluss dieser Phänomene auf die positionsabhängigen Parameter in den Signalen charakterisieren und (iii) die exzellente Genauigkeit und Robustheit, welche durch die Ausnutzung von Mehrwegeausbreitung ermöglicht werden, zu zeigen. Es werden Tracking Algorithmen vorgeschlagen, die auf die positionsrelevanten Ausbreitungseigenschaften sowie deren Unsicherheiten eingestellt sind. Damit ist eine optimale Gewichtung der Information von Mehrwegekomponenten möglich. In verschiedenen Umgebungen können unter Verwendung gemessener Signale in 90% der Fälle Schätzfehler unter 5 cm erreicht werden. Dies zeigt die Robustheit und Genauigkeit des vorgeschlagenen Ansatzes.

Die vorliegende Arbeit steht im Gegensatz zur existierenden Literatur zu funkbasierter Lokalisierung, in welcher Mehrwegeausbreitung nur als Fehler- und nicht wie hier als Informationsquelle angesehen wird. Ein wichtiges Ergebnis ist ein Echtzeit-Demonstrationssystem, welches schnelle und flexible Tests von existierenden und neuen Algorithmen erlaubt, und gleichzeitig als Machbarkeitsnachweis von Mehrwege-unterstützter Positionierung dient. Die experimentellen Resultate sind wertvoll für zukünftige drahtlose Anwendungen. Dies gilt vor allem für die Resultate zur Kanalanalyse, welche als Basis für die Entwicklung und Parametrisierung von örtlich konsistenten, geometrisch-stochastischen Kanalmodellen dienen.

Acknowledgment – Danke!

After working for five years on this thesis, there are some people I would like to thank for their support, collegiality, inspiration and friendship.

First of all, I want to thank Klaus for being an awesome PhD advisor. I always had the freedom to pursue my research ideas and every time I got stuck you came up with an advice pointing me in the right direction. Thanks also for supervising my master thesis and bringing me to the SPSC lab as a study assistant. This enabled my first steps in research and teaching and showed me that I enjoy both a lot. I really hope that we can continue working together in the future. Another thanks to Gernot for granting me my assistant position at SPSC.

I want to thank Prof. Win for hosting me at MIT in 2012, this was a great experience for me. Furthermore, it is a major honor for me to have you as my second examiner. Thanks a lot for taking the journey to Graz! Another thank goes out in the same direction to the colleagues at MIT, especially Yuan, for the inspiring discussions.

A large number of thanks goes out to all my colleagues and friends at SPSC (in no particular order): Bernhard, Daniel, Thomas, Erik, Andreas P.-E., Andreas L., Kathi, Shuli, Markus, Michael, Stefan, and all the others. I will miss the endless discussions and most of all the coffee breaks!

I am also grateful for the collaborations with colleagues at other universities: Mingming, Gerhard, Samuel, Christoph, Thomas, Georg, Rudolf; Thanks a lot! I hope we can keep in touch in the future.

Another round of thanks is dedicated to my master students. I have been really lucky to supervise a lot of clever guys that provided invaluable input for my own research: Markus, Rudi, Christoph, Gregor, Manuel, Franz, Christian, Erwin; I wish you the best for the future.

A very large thanks belongs to my parents Margrit and Erich. You have always stood behind me and given me support. Thanks for enabling my education without any worries.

Most importantly, thanks to Silvia for your support, love and for bearing with me during the time needed for this thesis. Thanks for listening to my self doubts, my stories about reflection properties of different walls, and for sharing my happiness about achieving good results. I could not ask for a better family at my side. Finally, thanks to Simon, for your endless provision of inspiration. I hope I can teach you as much as you teach me.

Statutory Declaration

I declare that I have authored this thesis independently, that I have not used other than the declared sources/resources, and that I have explicitly indicated all material which has been quoted either literally or by content from the sources used. The text document uploaded to TUGRAZonline is identical to the present doctoral dissertation.

date

(signature)

*Round here,
something radiates*

– Counting Crows, “*Round Here*” [1]

*She knows there’s no success like failure,
and that failure’s no success at all*

– Bob Dylan, “*Love Minus Zero/No Limit*” [2]

*The echo of a distant time
Comes willowing across the sand
And everything is green and submarine*

– Pink Floyd, “*Echoes*” [3]

Contents

I	Thesis Overview	15
1	Introduction	17
1.1	Indoor Positioning Systems	17
1.1.1	Technologies used for Positioning	17
1.1.2	Algorithmic Approaches	19
1.1.3	Performance Considerations for Positioning Systems	20
1.1.4	Requirements for Positioning Systems	20
1.2	Motivation and Related Work	21
1.2.1	Research Challenges for UWB Systems for Indoor Positioning	21
1.2.2	Research Question of this Thesis	22
1.2.3	Overview of Related Work	22
1.3	Outline and Contributions of this Thesis	24
1.3.1	Outline of this Thesis	24
1.3.2	Contributions per Topic	24
1.3.3	Contributions in the Included Papers	25
1.3.4	List of Included Papers	26
2	Geometric/Stochastic Environment and Signal Modeling	29
2.1	Hybrid Geometric/Stochastic Signal Model	29
2.1.1	Geometric/Stochastic Channel Model	29
2.1.2	Channel Characterization by Channel Parameters	31
2.2	Representation of Floor Plan Information	32
2.2.1	Representation of Reflectors using Virtual Anchors	32
2.2.2	Visibility Regions of Reflections	34
3	Performance Bounds for Multipath-Assisted Localization – Position-Related Information	39
3.1	Performance Metrics for Positioning	39
3.1.1	Cramér-Rao Lower Bound	39
3.1.2	Geometric Dilution of Precision (GDOP)	40
3.1.3	Distribution of the Position Error	41
3.1.4	Comments on the CRLB and other performance metrics	41
3.2	Cramér-Rao Lower Bound for Multipath-assisted Positioning	42
3.2.1	Without Path Overlap – Orthogonal Multipath Components	42
3.2.2	Influence of Path Overlap on Localization	43
3.3	Example Results	43
3.4	Chapter Conclusions and Results in Included Papers	44
4	Channel Analysis – Estimation of Position-Related Information	47
4.1	Estimation of Deterministic Multipath Components	47
4.1.1	Approximate Maximum-Likelihood Estimation	47

4.1.2	Energy Capture Analysis of VA-modeled MPCs	48
4.2	SINR Estimation for Deterministic Multipath Components	49
4.2.1	SINR Estimation along a Motion Trajectory	49
4.2.2	SINR Estimation using Local Grid Measurements	50
4.3	Example Results	50
4.4	Chapter Conclusions and Results in Included Papers	52
5	Algorithms for Multipath-Assisted Tracking	53
5.1	General Problem Formulation	53
5.1.1	Motion Model	54
5.1.2	Measurement Models	54
5.2	Tracking Algorithms	55
5.2.1	Tracking Algorithms without Data Association	55
5.2.2	Tracking Algorithms with Data Association	56
5.3	Example Results	59
5.4	Chapter Conclusions and Results in Included Papers	60
6	Conclusions and Outlook	63
6.1	Conclusions	63
6.2	Ongoing and Future Work	64
II	Additional Results and Discussions	65
7	Additional Discussions	67
7.1	Overview over Propagation Mechanisms	67
7.2	Discussion of Power Delay Profiles	69
7.3	Overview of Related Channel Models	71
7.4	Chapter Conclusions	72
8	Additional Results	73
8.1	Energy Capture Analysis for Different Scenarios	73
8.2	Channel Parameter Estimation	77
8.3	SINR and CRLB Estimation and Performance Results	79
8.3.1	PEB and Performance in Demonstration Room	79
8.3.2	PEB, Performance and SINR Analysis in Seminar Room	80
8.3.3	PEB and SINR Analysis in the Laboratory Room	87
8.4	Chapter Conclusions	91
III	Included Papers	93
9.1	Meissner, P, Gigl, T., Witrisal, K.: <i>UWB Sequential Monte Carlo Positioning using Virtual Anchors</i> , International Conference on Indoor Positioning and Indoor Navigation, IPIN, 2010	94
9.2	Meissner, P, Arnitz, D., Gigl, T., Witrisal, K.: <i>Analysis of an Indoor UWB Channel for Multipath-Aided Localization</i> , IEEE International Conference on Ultra-Wideband (ICUWB), 2011	104
9.3	Witrisal, K, Meissner, P.: <i>Performance bounds for multipath-assisted indoor navigation and tracking (MINT)</i> , International Conference on Communications (ICC), 2012	109
9.4	Meissner, P., Witrisal, K.: <i>Analysis of Position-Related Information in Measured UWB Indoor Channels</i> , European Conference on Antennas and Propagation (EuCAP), 2012	114

9.5	Meissner, P., Witrisal, K.: <i>Multipath-Assisted Single-Anchor Indoor Localization in an Office Environment</i> , International Conference on Systems, Signals and Image Processing (IWSSIP), 2012	119
9.6	Meissner, P., Leitinger, E., Froehle, M., Witrisal, K.: <i>Accurate and Robust Indoor Localization Systems Using Ultra-wideband Signals</i> , European Navigation Conference (ENC), 2013	123
9.7	Meissner, P., Gan, M., Mani, F., Leitinger, E., Froehle, M., Oestges, C., Zemen, T., Witrisal, K.: <i>On the Use of Ray Tracing for Performance Prediction of UWB Indoor Localization Systems</i> , IEEE ICC Workshop on Advances in Network Localization and Navigation (ANLN), 2013	133
9.8	Meissner, P., Leitinger, E., Lafer, M., Witrisal, K.: <i>Real-Time Demonstration System for Multipath-Assisted Indoor Navigation and Tracking (MINT)</i> , IEEE ICC Workshop on Advances in Network Localization and Navigation (ANLN), 2014	139
9.9	Meissner, P., Leitinger, E., Witrisal, K.: <i>UWB for Robust Indoor Tracking: Weighting of Multipath Components for Efficient Estimation</i> , IEEE Wireless Communications Letters, 2014	145

IV Appendices **149**

A Descriptions of Channel Measurement Campaigns **151**

A.1	Overview	151
A.2	General Measurement Setup	152
	A.2.1 Frequency Domain Measurements – Vector Network Analyzer	153
	A.2.2 Time Domain Measurements – M-Sequence Radar	153
A.3	Measurement Post-Processing	153
	A.3.1 Frequency Domain Measurements – Vector Network Analyzer	153
	A.3.2 Time Domain Measurements – M-Sequence Radar	154
	A.3.3 Pulse Shaping Example	155
A.4	Large-Scale Environment – Corridor	156
	A.4.1 Trajectory Measurements	156
	A.4.2 Grid Measurements	156
A.5	Medium-Scale Environments	157
	A.5.1 Seminarroom at Graz University of Technology	157
	A.5.2 Demonstration Room at Graz University of Technology	160
	A.5.3 Demonstration Room at Montbeliard, France	161
A.6	Small-Scale Environment – Laboratory Room	162

B Modeling of Floor Plan Uncertainties **165**

Bibliography **169**

Part I

Thesis Overview

1

Introduction

Remark on the bibliography: This thesis is a collection of publications with an extended introduction an overview over the main results, and additional discussions and results. The included papers are referenced in the text using labels in the form [T#], to distinguish them from conventional references to work of others.

This chapter provides an introduction to the work in this thesis. Section 1.1 summarizes technologies, algorithms and performance considerations for indoor positioning systems¹. The research question and the relation to other work is discussed in Section 1.2. The contributions that have been made are lined out and are put in relation to related work in Section 1.3. Also, this chapter contains a list and a discussion of the papers that are included in Part III.

1.1 Indoor Positioning Systems

Outdoors, whether we are driving by car, hiking, or walking in a city, we are used to be able to determine our position all the time. This is enabled by systems like the global positioning system (GPS), whose use have become ubiquitous. While current research still tries to improve e.g. the sensitivity of the receivers or to reduce the impact of multipath propagation, the system already provides an acceptable level of positioning performance.

Inside buildings, the situation changes dramatically. GPS receivers are no longer able to demodulate satellite signals due to insufficient signal strength. Hence, dedicated indoor systems are needed, but as of today, no single such system is in widespread use. Instead, numerous competing enabling technologies exist and lead to a variety of different solutions [5–9]. This section summarizes technologies, algorithmic approaches and performance considerations.

1.1.1 Technologies used for Positioning

Throughout this thesis, we restrict the attention to systems that use so-called *anchors*, which are signal transmitters or receivers² at known locations. The position of an *agent* is estimated

¹ The term “positioning” describes the determination of the coordinates of an object in a defined coordinate system, while “localization” refers to the position of an object relative to topological relations [4]. These terms are often used interchangeably in the literature, despite the fact that in most cases positioning is the more correct term. In this thesis, coordinates w.r.t. a floor plan are estimated, in principle allowing for both terms.

² The first case corresponds to a navigation scenario, while the second case resembles tracking of an actively transmitting object.

based on observations of signals transmitted between the anchors and the agent, and position-dependent parameters embedded in these signals. Outdoors, the choice of satellites³ is natural as anchors for providing position-dependent signals for a sufficiently large area. Indoors, anchors can be employed using different signaling technologies.

In most systems, either the angle or the distance between anchor and agent is estimated. Since estimation of the angle requires multi-antenna systems and we focus on low-complexity devices, we restrict the attention to estimating the distance, or the time-of-arrival (ToA)⁴. Fig. 1.1 illustrates the basic principle using three anchors. With perfect distances as in Fig. 1.1a, all corresponding circles around the anchors intersect in a common point. Since in practice only noisy observations of these distances will be available, this uniqueness will be lost as in Fig. 1.1b, requiring to pose a criterion on the most suitable position, i.e. an estimation algorithm. In this thesis, multiple range estimates are obtained from one signal, each of which can be associated to the surrounding geometry. However, this association is not given a-priori, resulting in a situation as indicated in Fig. 1.1c. I.e. another level of ambiguity is introduced which needs to be resolved.

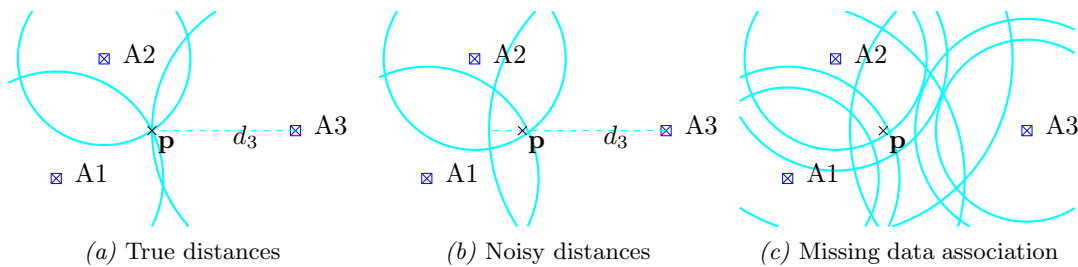


Figure 1.1: Error sources in range-based positioning: All three distance circles around the anchors intersect in one point (a). Erroneous range estimates result in ambiguities as shown in (b). This problem is much more severe if the association of ranges to the anchors is not given (c).

Positioning systems differ in the physical mechanisms that are used to estimate the distance to the anchors. The resulting uncertainty of the distance estimate must then be coped with by the data fusion, i.e. the estimation algorithm. In the following, we provide a brief overview over the principles used. An excellent and detailed survey of available systems can be found in [6].

Optical Techniques

Optical signals such as *infrared signals*, have the benefit that relatively cheap hardware implementations are available. Due to the employed wavelength, in principle a range accuracy in the millimeter range is possible. However, the most important drawback is that a strict optical line-of-sight connection between anchor and agent is needed.

Time-of-flight cameras are a relatively new development. They measure not only the light intensity on each sensor pixel, but also the corresponding time-of-flight of a light signal from the camera to the agent and back. Despite the fact that also here a line-of-sight (LOS) connection is needed, this is an interesting concept for future applications, since, given ever increasing computational power, a whole scene can be analyzed with a large update rate.

Acoustic Methods

The strict LOS requirement can be relaxed using acoustic signals including audible as well as ultrasonic sound. With wavelengths comparable to the microwave case, basically the same spatial

³ Or stars in classical celestial techniques. In local positioning systems, anchors are also called pseudolites [5,6].

⁴ Another possibility is to estimate the time-difference-of-arrival (TDoA) w.r.t. some anchor, if agent and anchors are not synchronized [10,11].

resolutions on centimeter level are possible. Acoustic devices may often be cheaper as high-frequency radio equipment, which also motivates their use in research. However, the acoustic propagation channel shows a strongly reverberant nature, with a large level of diffuse multipath (DM) [12]. The approach followed in this thesis has also been implemented in the audible acoustic domain in [13]. The results using electromagnetic signals could not be reproduced due to the difficulty of detecting reflected components in audio signals. Another difficulty is the long reverberation time of acoustic channels, that does not allow for assuming quasi-stationarity of the channel during tracking using realistic update rates.

Radio-based Methods

Some of these drawbacks are remedied using radio signals. They do not require an unblocked optical path between anchor and agent, which makes them usable in e.g. smoke. Also, current radio transceiver technology allows for small form factors and low power consumption, enabling their integration in other devices, such as smartphones. However, it is well known that a narrowband and also conventional wideband systems do not provide sufficient time resolution to separate the LOS path from the indirectly transmitted paths [14, 15]. One of the most popular radio-based techniques is wireless local area networks (WLAN) based positioning, since it makes use of hardware that is available nearly everywhere. The distance is estimated most often based on the received signal strength [16], which has a much larger variance than a direct estimation of the ToA using a wideband signal. Section 7.1 in Part II of this thesis gives an overview over the position-relevance of different propagation mechanisms.

In this thesis, we restrict our attention to *ultra-wideband* (UWB) systems [17, 18] that possess the advantage of the resolvability of the LOS path from the rest of the channel. UWB systems can be divided into two subclasses depending on their actual bandwidth [19]: UWB-ABS systems have an absolute bandwidth larger than 500 MHz, regardless of the center frequency of the band. UWB-REL systems have a relative bandwidth (bandwidth divided by the center frequency) larger than 20%. This distinction is important when channel parameters are estimated from measurements (see Section 7.2).

Inertial Measurement Units

Measurements of the acceleration of the agent w.r.t. the coordinates are different to the systems discussed above, since no range estimation to anchors is performed. Current research takes into account the high level of maturity of these sensors and the availability in e.g. smartphones. Here, the unknown orientation of the device w.r.t. the user provides additional difficulties [20]. Acceleration sensors can also be foot mounted, enabling relative positioning based on step length estimation [21, 22].

A basic principle followed is *dead reckoning*, i.e. based on a previous position estimate and current observations of acceleration and heading, the new position is calculated by integration. This explains why this technique is susceptible to accumulated errors and therefore drifts in the position estimation. We include this method here, since it is a useful complementary technique for anchor-based systems. The estimated acceleration can drive the state-space model (see Section 5.1.1) and therefore substantially help in the prediction step that is needed for a proper fusion of the range measurements.

1.1.2 Algorithmic Approaches

Once distance estimates to anchors have been obtained, they have to be transformed to a position estimate. As shown in Fig. 1.1, this is most often not possible unambiguously, hence an estimation algorithm is necessary [23]. A fundamental distinction of position estimation

algorithms is whether they work on isolated range measurements or if they also exploit previously estimated positions (together with a model of the agent’s motion) to infer the new position. Algorithms belonging to the latter class are usually called tracking algorithms.

In the example in Fig. 1.1a, subsets of circles will intersect in points other than the true position, also with perfect measurements. In a statistical model of the position as a function of these range estimates, this can lead to multimodality, i.e. local minima of a cost function. Hence, a suitable global optimization algorithm is needed, which often has large computational complexity, or a good guess of the initial position must be available for an iterative optimization procedure.

The latter case naturally leads to tracking algorithms. In a sequential positioning problem, the position estimate from the last time step may be used as prior knowledge for the estimation. A dynamic motion model allows to find the most likely new position of the agent *before* taking into account the current distance estimates. This predicted position can also be used in the fusion of the current measurements.

1.1.3 Performance Considerations for Positioning Systems

Accuracy will often be the first figure of merit that is reported for a positioning system. It is defined as an average quantity describing the *position error* (the Euclidean distance between true and estimated position), e.g. its root-mean-square value $[4, 10]^5$. This includes effects from systematic deviations, i.e. a bias, as well as the variance of the error. Due to harsh propagation conditions for signals used in different sensing technologies, reported accuracy levels often represent lower bounds on the position error. As such they may represent the general sensitivity of the measurements with respect to the position. To actually achieve them, defined environmental conditions have to be satisfied, such as line-of-sight situations for wireless systems.

For a realistic evaluation of the performance of a positioning systems, both accuracy and *robustness* are needed. Robustness can be defined as the percentage of cases in which a given system can actually reach the potential accuracy. In statistical signal processing, robustness is often understood as the ability of an estimator to deal with *unusual circumstances*, such as large measurement outliers or missing data, e.g. a ranging outage w.r.t. an anchor [8]. Here, these effects are encompassed by the definition of robustness on the position error level, and not on the measurement error level. This raises the question of how robustness can be evaluated for a given system. In this thesis, an experimental approach is followed, where measurements in a number of environments are used, which of course can only give an indication of the expected robustness in these or comparable environments.

1.1.4 Requirements for Positioning Systems

One of the big challenges concerning indoor positioning is the problem of heterogeneous requirements. Based on the application scenario, different scales of accuracy may be desired. Whereas for guidance of a customer in a mall, room-level accuracy may be enough, for tracking tools or parts in a production environment, sub-meter accuracy is needed for the system to be considered helpful. Also, the required level of robustness will be different in these cases.

Scalability and required infrastructure are other issues. While private users may be willing to pay a significant price for their individual device such as a smartphone [24], low costs are imperative in industrial or logistics environments, where many goods must be tracked continuously. This of course contradicts the above mentioned requirements on accuracy for these cases, highlighting the difficulties.

⁵ The positioning literature also contains the term *precision*, which denotes the deviation from the mean position, i.e. the variance of the position error. For unbiased estimates, precision and accuracy are equivalent [10].

The user experience w.r.t. position errors or even outage will be different compared to outdoor systems. For GPS, users may accept a performance deterioration in e.g. dense woods or urban canyons. Indoors, the cause for a sudden decrease of position accuracy is often not intuitive for the user, due to the complicated physical propagation phenomena. The requirement on a positioning system in this regard is the proper presentation of the current uncertainty to the user, who in general is only interested in the position estimate itself. All in all, this again boils down to robustness and its presentation to the user.

While not popular in the technical literature, *ethical issues* must be considered. Especially a technology enabling the knowledge of the position of an individual at a given time carries large risks of abuse. While [25] states that “...*the employer’s business interests may outweigh an employee’s privacy interest.*”, the author of this thesis fears that the latter is often not especially pronounced in the general public nowadays. Therefore, the implications and intricacies of ubiquitous location awareness need to be addressed in the context of today’s vast amount of personal data.

1.2 Motivation and Related Work

Based on the above discussion, the motivation behind the research done within this thesis is to use the most suitable radio technology together with an optimal estimation procedure to obtain an accurate and robust indoor positioning system. Therefore, ultra-wideband radio signals are selected as a basis to obtain measurements. Tracking algorithms are chosen for the position estimation, since they allow for an efficient mapping of propagation effects to the local geometry as explained in Chapters 2 and 5.

1.2.1 Research Challenges for UWB Systems for Indoor Positioning

Even given the favorable properties of UWB signals, the following key research challenges are identified:

Multipath Propagation – Robustness Issues: In indoor environments, especially in industrial scenarios [26], dense multipath propagation occurs, which means that the signal energy between anchors and the agent is divided in many different multipath components (MPCs) that can bias the range estimation. This is still the main source of estimation errors for range-based indoor localization approaches. It has been shown that available prior knowledge on deterministic multipath components can be beneficial for localization [27], which is a main motivation for the work in this thesis. Also, [28] shows that localization performance can be improved, integrating more information based on received signals than just the estimated direct path.

Non-Line-of-Sight (NLOS) Situations between Anchor and Agent: The problems caused by multipath propagation get even more severe in NLOS situations, i.e. when the direct path between an anchor and the agent is blocked. Indoors, this situation easily arises, as already a human body absorbs a large part of a radio signal’s energy. The estimation of the direct path is then even more difficult and ranging errors on meter level can be the result.

Need for Additional Infrastructure for Robustness: In conventional indoor localization methods, often the amount of infrastructure is increased to enhance the robustness of the system. For example, having more physical anchors in an environment leads to a higher probability of having sufficiently many reliable range estimates. Also, floor plans of the environment may be used to constrain the possible location of the agent to positions within the floor plan [29]. This requirement can be understood as additional infrastructure.

Complexity Considerations: Advanced algorithms for indoor localization make use of e.g. cooperation of multiple agents [30] to overcome NLOS situations. Also, location fingerprinting [31] can be used in harsh environments. It makes use of a-priori training signals in multiple regions of the environment to train a classification algorithm. In the localization phase, signals are compared with the training signals using suitable metrics. These methods have been demonstrated to be beneficial in dense multipath environments. The downside is the large effort that is required. In cooperative algorithms, computationally expensive statistical algorithms have to be used, which may not allow real-time implementation. In fingerprinting, a tedious training phase is needed, even if advanced methods [32] are employed.

These considerations lead to the formulation of the research question and the main approach followed in this thesis.

1.2.2 Research Question of this Thesis

UWB signals provide the possibility of separating the LOS path from reflected signal paths. This allows for more robust ranging than using conventional wideband signals [14]. Furthermore, also signal paths arriving later can in principle be isolated. Some of these paths are strongly related to the surrounding geometry, such as specular reflections of the radio signal on e.g. room walls. Based on the assumption of a known floor plan⁶ of the environment, these paths can be extracted from the radio signal and matched to the geometry. As Chapter 2 shows, this can be done by assigning *virtual anchors* (VAs) to each known potential reflector in the environment. In this way, one physically existing anchor can be turned into a set of VAs providing position information.

This potentially solves three of the four above mentioned key problems: (i) multipath propagation can be turned into an advantage instead of treating it as a problem; (ii) in NLOS situations, only one signal path out of several is lost, leading to a less severe impairment, and (iii) infrastructure can be used efficiently, i.e. a lower number of physical anchors can be deployed. Of course in this approach also the floor plan must be considered required infrastructure. As the results of Chapter 5 will show, also the fourth research challenge is addressed since the presented solution of the problem can be implemented using low-complexity algorithms that even allow for real-time operation.

However, for this idea to succeed, the *relevance* and the *accessibility* of potential geometric information of multipath components must be clarified. This leads to the statement of the principal research questions addressed in this thesis:

Assuming prior knowledge of a floor plan, can the *geometric information* embedded in multipath components be exploited for positioning? If so, how can this information be *modeled, quantified, and used* for *robust* position estimation?

1.2.3 Overview of Related Work

Conventional systems, i.e. systems like [33] that estimate the direct path from signals show the potential of UWB for indoor localization with accuracies on centimeter level. However, NLOS situations and impairments caused by multipath are not directly addressed [34]. In [35],

⁶ Since for most applications, a floor plan is anyways needed for a visualization of the estimated position to the user, this requirement may be met in many cases. Depending on the positioning approach, the required level of detail for this information may of course be larger for positioning than for visualization.

the achievable operating distance for standard-compliant UWB ranging is evaluated, showing surprisingly large values up to several hundred meters also for non-coherent detection.

If multipath is taken into account, it is most often in the form of an error source. In [14], error bounds for UWB ranging are derived, highlighting the importance of a large bandwidth. State of the art approaches in dealing with multipath either try to detect these situations statistically based on the received signals [36, 37], or to directly mitigate the corresponding errors with statistical techniques [38, 39]. These methods partly show impressive results, but nevertheless, they discard the geometric information of MPCs. This information was discussed in [27], but used in a cooperative scenario, only allowing for relative accuracy gains.

Statistical performance bounds for the position estimation give valuable insight in the role of different system and signal parameters. In [40, 41], the Cramér-Rao lower bound (CRLB) for LOS and NLOS ranges is derived, also considering the case of known statistics of the latter. However, the NLOS errors are modeled on the range level, giving no insight on the propagation channel influence. A framework for systematic evaluation of CRLBs has been formulated in [42, 43]. This framework is also used in this thesis, but extended with a geometric model for the deterministic MPCs as well as a stochastic model for the diffuse multipath. Similar methodology has been used in e.g. [44] to evaluate performance gains of MIMO radar systems. Ref. [29] presents analytical performance bounds for positioning using floor plan information. However, the latter is only used to generate prior distributions for the agent's position, and not in the processing of measurements. In [45], performance bounds are derived for joint RFID and radar sensor networks. The flow of position information through a network of navigating agents is presented in [46].

In [47], reflections of an audio signal are used to help in the estimation of position-dependent parameters, employing microphone arrays. Single-antenna anchor-free positioning is presented in [48], but with the requirement for many closely-spaced received signals to solve an optimization problem in localizing the virtual signal sources and the agent. Recently, a concept very similar to the one developed in this thesis using virtual sources and data association has been applied in the acoustic domain [49]. Using arrays, information from reflected components is also used in [50, 51]. A set of known antenna locations can be used to enable beamforming e.g. in imaging [52]. In an inverse problem, the room geometry can be inferred from the multipath and known measurement locations [53].

References [54, 55] present techniques to benefit from signal reflections from known indoor features such as walls. However, the important assumption of LOS conditions is made, which implies that no NLOS robustness can be obtained. Also, the reflections used must be detected, which means that they can not be used opportunistically as in this thesis. In [56], a method for the use of single-bounce components is derived. The method requires movement of the agent since the Doppler shift is included in the estimation procedure. Only simulation results are presented. In [57], multiple sub-groups of range measurements are used to obtain position estimates. A multi-hypothesis framework is employed for NLOS detection on the position level. The obtained probabilities are then used in a Kalman filter as weights. The work in [58–60] uses multipath for joint localization and room dimension estimation. However, the room geometry is fixed to be simple rectangular and a certain reflection order is assumed, sacrificing scalability of the method. In [61], TDoAs between MPCs are used without the need of a floor plan. Nevertheless, rather restrictive assumptions such as an antenna array with known orientation at the agent are made and the results are not conclusive.

In [31, 32, 62], a UWB fingerprinting approach is presented and evaluated. This can be accurate and robust in especially challenging environments. However, the required training phase as well as the missing flexibility w.r.t. changes in the environment may limit its application. Ref. [32] makes use of virtual sources to aid in the training phase. [63] uses a bat-type UWB radar with one TX and two RXs, which employs reflections as features for localization. A particle filter with data association is used, but only coarse results for the reconstruction of the room dimensions are given, and not for localization. Cooperative approaches to localization are discussed in e.g. [30],

demonstrating large benefits of using relative measurements between nodes. Our approaches using multipath have recently been extended to include cooperation [64–67].

This thesis follows an experimental approach to the topic since the constructive use of multipath heavily depends on properties of the propagation channel that need to be understood. Experimentation is a vital tool for designing positioning systems that need to fuse information from uncertain sources [68–70]. Competitions and evaluation projects such as [71, 72] show that indoor localization systems need to be evaluated in realistic environments as their performance is difficult to compare using e.g. simulation results.

The method presented in this thesis makes efficient use of multipath propagation based on the prior knowledge of the floor plan of the environment. It does so by weighting the location dependent information contained in deterministic multipath components optimally. The weights correspond to the actual path length uncertainties. This kind of weighting is often proposed in the literature, but previously implemented using heuristic measures as weights only, e.g. in [37]. The physical relevance of the MPC weights used in this thesis stems from the fact the DM is explicitly considered. Especially in indoor environments, this effect can be pronounced, leading to the necessity of its proper modeling [26, 73–77].

1.3 Outline and Contributions of this Thesis

In the light of the related work discussed above, the main contribution of the work presented in this thesis is the constructive use of multipath propagation. This is enabled by a proper geometric-stochastic channel model which is the basis for the quantification of the position information of deterministic MPCs.

1.3.1 Outline of this Thesis

This thesis is structured in four main parts: The first part contains this introduction as well as a summary of the main topics and results. In the second part, additional results and discussions relevant to the presented topics are found. The third part is a collection of the most relevant papers published in the time period of the research, and the fourth part contains appendices.

In Part I, Chapter 2 contains an extended discussion of the geometric model of the deterministic MPCs. It also discusses the used geometric-stochastic channel model. Hence, it is the basis for all following chapters and included papers. Chapter 3 deals with the derivation of performance bounds for multipath-assisted positioning, while Chapter 4 discusses the actual estimation of parameters of deterministic MPCs as well as their respective position-related information from measurement data. Tracking algorithms and the statistical models that are used are presented in Chapter 5. Chapter 6 provides conclusions and an outlook to ongoing and future research.

In Part II, Chapter 7 contains additional discussions about the propagation effects relevant for positioning, the estimation of power delay profiles and related channel models in the literature. Chapter 8 is a collection of additional results for the proposed channel analysis methods as well as for the estimation of the performance bounds using measured signals, highlighting the usefulness of these methods for understanding relevant propagation effects in an environment.

After Part III containing the included papers, Appendix A in Part IV presents the measurement campaigns [78] conducted. Appendix B presents a first treatment of the geometric uncertainty of the positions of the VAs, which has not been used in publications so far.

1.3.2 Contributions per Topic

The main overall contributions of this thesis are:

- The **relevance of deterministic MPCs** is shown in terms of energetic [T2] as well as information-theoretic measures [T3, T4, T7]. Numerous experiments are used to highlight the **importance of a proper geometric-stochastic model** of these MPCs in a channel model that also has to reflect the impairing effects of diffuse multipath.
- Based on statistical performance bounds for the position error, **position-related information** of MPCs can be quantified [T3]. This information can be estimated from measurements and can be used to evaluate the localization capabilities in a given environment [T4, T7].
- The estimated position-related information can be used as **model for the uncertainties** of the ranges of the reflected MPCs. In this way, an optimal weighting of the available information can be performed, demonstrated by results approaching the corresponding CRLB for measured signals [T8, T9].
- We demonstrate the feasibility of **single-anchor-tracking** with the presented methods, allowing for a minimum of required infrastructure besides the known floor plan [T1, T5]. Using multiple anchors, these methods are shown to outperform conventional methods in terms of accuracy and robustness to NLOS situations [T6].
- A **proof-of-concept** has been implemented in form of a real-time demonstration system. This allows for rapid and flexible performance assessment of the approach in different environments [T8].
- The numerous **measurements campaigns** obtained during the work on this thesis have been made publicly available to the research community to allow for performance evaluation of positioning and tracking algorithms [78].

In [T3], the term *multipath-assisted indoor navigation and tracking (MINT)* has been coined for the presented general approach. As we will not explicitly deal with navigation aspects, we do not directly use this term throughout this thesis. However, the presented algorithms allowing for the exploitation of multipath can be considered implementations of the general MINT approach.

1.3.3 Contributions in the Included Papers

The contributions in the individual papers comprising Part III are:

- [T1]** contains the application of several Bayesian state-space estimation algorithms to the statistical model of estimated and unassociated multipath delays first proposed in [79]. The missing data association and geometric symmetries cause multimodality. Tracking is introduced as a possible remedy.
- [T2]** discusses channel analysis results in an exemplary scenario. An analysis of the energy capture of the VA-modeled deterministic MPCs shows their relevance as channel features. These MPCs carry a significant fraction of the energy of the received signal, which has been confirmed in other environments later.
- [T3]** contains the derivation of the CRLB for multipath-assisted positioning as it is used in this thesis. It is authored by the supervisor of this thesis, the author contributed the computational framework for the numerical evaluation. This paper also introduces the channel model that is used in the following papers.
- [T4]** contains the derivation of an estimator for the signal-to-interference-and-noise ratio (SINR) of VA-modeled deterministic MPCs from signals. As this allows for an estimation of CRLBs using measurements, it shows how the localization capabilities of an environment can be characterized using a few signals at known positions.

- [T5]** introduces the tracking and data association algorithm that were the first implementation of the multipath-assisted indoor tracking approach using only a single anchor. It also contains results for the particle filter in [T1] for measurements.
- [T6]** extends [T5] with a detailed comparison of the MINT implementation to conventional tracking algorithms, highlighting the improved robustness in NLOS conditions also at comparably low bandwidths.
- [T7]** discusses the use of a ray-tracing tool [80] for performance prediction of multipath-assisted positioning by estimating CRLBs using ray-tracing signals and measurements from the same environment.
- [T8]** introduces the live-demonstration system for MINT using an M-sequence radar channel sounder. The MPC-SINR estimation techniques from [T4] are used to characterize two example environments in terms of the position error bounds. The presented tracking results match these bounds closely.
- [T9]** shows how to use the position-related information estimated using an extension of the technique in [T4] as measurement noise model in a tracking algorithm. The uncertainties of the range estimates w.r.t. a set of relevant MPCs are determined, providing awareness to the uncertainty of the information. Results show that this is the key enabler for robust indoor tracking.

In addition to these papers, [79] was the first paper of the author on the topic. It describes the use of a statistical model of unassociated delay estimates to VAs and its use for maximum likelihood positioning. It was not included in this thesis since during the work it quickly became clear that the multipath-assisted localization approach needs to be evaluated on the signal level, as it is strongly tied to propagation effects. The numerous channel measurement campaigns for performance evaluation are collected in [78] and have been made publicly available. The first public demonstration of MINT was performed at IPIN 2013 in Montbéliard, France [81].

The author has co-authored a number of papers that are related to the topic of this thesis. In terms of channel estimation, [82] describes the extension of [83,84] to the geometric VA model, while probability hypothesis density (PHD) filters are applied to UWB channels in [85]. An application of the SAGE algorithm [86] to UWB signals has been discussed in [87].

Channel modeling has been addressed in [80], which introduces a ray tracing method for ultra-wide bandwidths and is capable of modeling diffuse scattering, as analyzed in [T7]. To enhance the degree of realism of the signals, material parameter optimization has been done in [88]. A preliminary investigation on a combined modeling technique consisting of ray tracing and propagation graphs is presented in [89] and subject of current research.

Localization and tracking algorithms for cooperating agents have been investigated in [66] and [67]. The performance bounds in [T3] have been extended to a discrete time formulation and more setups in [64], backscatter channels have been considered in [90]. A first concept of a cognitive radar system using incorporating multipath has been introduced in [91]. Maximum-likelihood positioning using the statistical model of [T3] is presented in [92]. A system-level simulation tool for UWB positioning and tracking considering NLOS measurements has been introduced in [93].

Furthermore, the author has supervised a number of master theses which deal with topics related to this thesis. In [94], tracking of deterministic MPCs using PHD filters was addressed, leading to [85]. Some of the tracking algorithms presented in this thesis have been used with audio signals in the audible frequency range in [13]. The work in [65] presents extensions of the performance bounds for multipath-assisted localization to a cooperative scenario also using monostatic measurements. The impact of a clock offset on the localization performance was analyzed in [11], while first results on the detection of new features in the floor plan based on measurements can be found in [95].

List of Included Papers

- [T1] P. Meissner, T. Gigl, and K. Witrissal, “UWB Sequential Monte Carlo Positioning using Virtual Anchors,” in *International Conference on Indoor Positioning and Indoor Navigation (IPIN)*, Zurich, Switzerland, 2010.
- [T2] P. Meissner, D. Arnitz, T. Gigl, and K. Witrissal, “Analysis of an Indoor UWB Channel for Multipath-Aided Localization,” in *IEEE International Conference on Ultra-Wideband (ICUWB)*, Bologna, Italy, 2011.
- [T3] K. Witrissal and P. Meissner, “Performance bounds for multipath-assisted indoor navigation and tracking (MINT),” in *International Conference on Communications (ICC)*, Ottawa, Canada, 2012.
- [T4] P. Meissner and K. Witrissal, “Analysis of Position-Related Information in Measured UWB Indoor Channels,” in *6th European Conference on Antennas and Propagation (EuCAP)*, Prague, Czech Republic, 2012, convened session.
- [T5] —, “Multipath-Assisted Single-Anchor Indoor Localization in an Office Environment,” in *19th International Conference on Systems, Signals and Image Processing (IWSSIP)*, Vienna, Austria, 2012, invited paper.
- [T6] P. Meissner, E. Leitinger, M. Froehle, and K. Witrissal, “Accurate and Robust Indoor Localization Systems Using Ultra-wideband Signals,” in *European Navigation Conference (ENC)*, Vienna, Austria, 2013. [Online]. Available: <http://arxiv.org/abs/1304.7928>
- [T7] P. Meissner, M. Gan, F. Mani, E. Leitinger, M. Froehle, C. Oestges, T. Zemen, and K. Witrissal, “On the Use of Ray Tracing for Performance Prediction of UWB Indoor Localization Systems,” in *IEEE ICC Workshop on Advances in Network Localization and Navigation (ANLN)*, Budapest, Hungary, 2013, invited paper.
- [T8] P. Meissner, E. Leitinger, M. Lafer, and K. Witrissal, “Real-Time Demonstration System for Multipath-Assisted Indoor Navigation and Tracking (MINT),” in *IEEE ICC Workshop on Advances in Network Localization and Navigation (ANLN)*, Sydney, Australia, 2014.
- [T9] P. Meissner, E. Leitinger, and K. Witrissal, “UWB for Robust Indoor Tracking: Weighting of Multipath Components for Efficient Estimation,” *IEEE Wireless Communications Letters*, vol. 3, no. 5, pp. 501–504, Oct. 2014.

2

Geometric/Stochastic Environment and Signal Modeling

This chapter gives an overview of the geometric and stochastic signal and environment models that are used throughout this thesis and all the included papers. Because of space limitations in the papers, the related discussions there were kept rather brief and an extended version of the corresponding concepts is presented here. Virtual anchors⁷ (VAs) are the key concept that is used. VAs are well established in the literature to model specular reflections in wireless transmissions, be it acoustic [13, 53, 97–99] or electromagnetic [15, 32, 96]. In this thesis, their use is extended to model position-related information [T3, T4],[27, 42] from radio signals.

This chapter is organized as follows: First, Section 2.1 introduces the geometric-stochastic channel model and its characterization, which is the basis for all following chapters. Then, Section 2.2 contains a detailed treatment of the representation of floor plan information using VAs, including their construction and visibility regions. Chapter 7 in Part II contains additional discussions of related topics. Appendix B contains the discussion of the modeling of uncertainties in the floor plan.

2.1 Hybrid Geometric/Stochastic Signal Model

2.1.1 Geometric/Stochastic Channel Model

The most fundamental quantity describing the influence of a linear propagation channel on a radio system operating in it is the channel impulse response (CIR). As the application in this work is positioning and the propagation effects are functions of the surrounding geometry⁸, we use a position-dependent model for the channel between a fixed anchor at a position $\mathbf{a}_1^{(j)}$ and an agent at a position \mathbf{p}_ℓ [15]. Throughout the thesis, the anchors are indexed with j , while the index ℓ is used in the spatial domain for positions. The index k will be used as for deterministic multipath components (MPCs), where $k = 1$ for the respective anchor itself, i.e.

⁷ In the literature, the terms virtual source [96], virtual transmitter [15], virtual node [27] or image point (source) [32, 53, 97] can be found, which all basically denote the same concept. As the intended application here is localization with *anchors* as infrastructure, we stick to the notion of virtual anchors.

⁸ For simplicity, we assume a static environment and hence a time-invariant impulse response. Motion is mapped to position by the velocity vector of the moving agent.

its LOS component. The CIR is written as [T3]

$$h_\ell^{(j)}(t) = \sum_{k=1}^{K_\ell^{(j)}} \alpha_{k,\ell}^{(j)} \delta(t - \tau_{k,\ell}^{(j)}) + \nu_\ell^{(j)}(t). \quad (2.1)$$

The $\alpha_{k,\ell}^{(j)}$ and $\tau_{k,\ell}^{(j)}$ are the complex amplitudes and delays of the k -th deterministic MPC, respectively. Depending on the position, their number is denoted as $K_\ell^{(j)}$. These are the MPCs for which a convenient mathematical model exists for the relation of the parameters to the positions of anchor and agent. In this thesis, the $\{\tau_{k,\ell}^{(j)}\}$ are the delays of the specular reflections of the signal occurring on surfaces within the indoor environment (see Section 2.2).

The noise term $\nu_\ell^{(j)}(t)$ basically models “everything else” in the channel, i.e. all propagation effects not modeled by the deterministic MPCs. Most importantly, this is a model for the diffuse multipath (DM), but the general role of $\nu_\ell^{(j)}(t)$ as model mismatch term throughout the thesis should be noted. To be specific, the DM term models all multipath phenomena that are not or can not be modeled deterministically, in our case by the use of floor plan knowledge. This is in line with other work like [100], which in the context of ray-tracing channel predictions states that “... roughness thus describes all (physically present) objects that are not included in the used maps and building plans.” We model DM as a zero-mean Gaussian process, which can be completely described by its auto-covariance function

$$\mathbb{E} \left\{ \nu_\ell^{(j)}(\tau) [\nu_\ell^{(j)}(u)]^* \right\} = S_{\nu_\ell}^{(j)}(\tau) \delta(\tau - u) \quad (2.2)$$

that makes use of the uncorrelated scatterer (US) assumption [100, 101], i.e. contributions to the DM at different delays are uncorrelated. $S_{\nu_\ell}^{(j)}(\tau)$ is called the power delay profile (see also Section 7.2 for a detailed discussion of PDPs) of the DM. It reflects the non-stationarity of the DM process, as it represents the delay-variant variance of the DM.

The channel in (2.1) is observed by an anchor or agent receiving a signal with a certain bandwidth. We model this as the convolution of the CIR with a transmit pulse $s(t)$ with effective pulse duration T_p as [T2, T3]

$$r_\ell^{(j)}(t) = \sum_{k=1}^{K_\ell^{(j)}} \alpha_{k,\ell}^{(j)} s(t - \tau_{k,\ell}^{(j)}) + s(t) * \nu_\ell^{(j)}(t) + w(t), \quad (2.3)$$

where the signal $w(t)$ denotes white Gaussian measurement noise with double-sided power spectral density (PSD) of $N_0/2$. In this thesis, we generally assume a unit-energy pulse $s(t)$, such that the energy of the k -th MPC is given as $|\alpha_{k,\ell}^{(j)}|^2$. It is obvious that the process $\nu_\ell^{(j)}(t)$ represents *interference* to the deterministic MPCs in addition to the AWGN. The energy that the deterministic MPCs carry can be large in indoor environments. This is shown in [T2] and also pointed out in [73] as: “... the amount of specular ... propagation paths in a scenario is relatively small but their contribution to the total power transferred from the transmit antenna to the receive antenna is usually dominating the transmission.” This provides a motivation for using these MPCs for localization.

Nevertheless, energy-based considerations give no insight about the proper characterization of interference of the DM and the corresponding uncertainties in estimating position-related parameters from the signal in (2.3), which is paramount for multipath-assisted localization. These issues will be discussed in Chapters 3 and 4.

2.1.2 Channel Characterization by Channel Parameters

The channel can be characterized by defining deterministic or statistic models for any of its parameters. A fundamental model goes back to the work in [102, 103], where the multipath channel results in a number of scaled and shifted, but undistorted copies of the transmit signal at the receiver. Since we will in practice always observe a band-limited version of the CIR with a bandwidth of B (c.f. (2.3)), MPCs within one *delay bin* of size $1/B$ can not be resolved and thus add up to an effective MPC. This causes *small scale fading*, i.e. fluctuations of the path gains $\alpha_{k,\ell}$ ⁹ when moving within a small distance in the order of the wavelength, because the different unresolvable MPCs change their phases rapidly. The $\alpha_{k,\ell}$ are usually modeled statistically using e.g. Rayleigh (for their amplitude) or other distributions [100].

Channel Parameters

The complex behavior of multipath channels is often broken down in single number parameters to allow for general discussions and comparisons. Two of the most widely used parameters are the root mean square (RMS) delay spread τ_{RMS} and the K-factor w.r.t. the LOS component¹⁰ K_{LOS} . The root mean square (RMS) delay spread is the second central moment of the normalized PDP [15, 105]

$$\tau_{\text{RMS}} = \sqrt{\frac{\int_{-\infty}^{\infty} (\tau - \tau_{\text{avg}})^2 S_h(\tau) d\tau}{\int_{-\infty}^{\infty} S_h(\tau) d\tau}} \quad \text{using} \quad \tau_{\text{avg}} = \frac{\int_{-\infty}^{\infty} \tau S_h(\tau) d\tau}{\int_{-\infty}^{\infty} S_h(\tau) d\tau} \quad (2.4)$$

where the latter expression is the average delay of the channel. Note that (2.4) is derived from the PDP (see also (7.2)) and as such is an average quantity. If necessary, also *instantaneous* delay spreads $\tau_{\text{RMS},\ell}$ can be computed using instantaneous PDPs $|h_\ell(\tau)|^2$.

The K-factor w.r.t. the LOS component is the ratio between the energy of the LOS component and the energy in the rest of the channel. Using (2.3), this can be written as

$$K_{\text{LOS},\ell} = \frac{|\alpha_{\text{LOS},\ell}|^2}{\int_{-\infty}^{\infty} |r_\ell(t) - \alpha_{\text{LOS},\ell} s(t - \tau_{\text{LOS},\ell})|^2 dt}. \quad (2.5)$$

The significance of these channel parameters stems from the fact that MPCs arriving after the LOS but with a large energy result in an increased τ_{RMS} and a decreased K_{LOS} . For range-based positioning, such MPCs can easily result in large range and position errors: In the narrowband case, only the (average) group delay of the channel is observed, which is heavily influenced by strong MPCs that cannot be resolved [106]. In the (ultra-)wideband case, where the LOS component can be resolved, MPCs arriving later may be stronger than a possibly obstructed LOS component and thus bias the range estimate [14], [T6].

Nevertheless, τ_{RMS} and K_{LOS} are *global* average parameters w.r.t. the delay domain and do not allow for conclusive statements about individual MPCs. In Chapters 3 and 4, measures that quantify the *position-related information* of certain MPCs and that can be estimated from signals will be introduced.

⁹ The anchor index j is dropped for brevity when not explicitly needed. Signals involving different anchors are always assumed to be separable by a suitable multiple access scheme.

¹⁰ The original Ricean K-factor [104] is defined w.r.t the *dominant* component, which does not need to correspond to the LOS. However, when ranging and localization are considered, the LOS component is important, hence we specifically discuss K_{LOS} .

2.2 Representation of Floor Plan Information

To answer the research question whether floor plan information can be used beneficially for localization, this information needs to be represented in a suitable way. In this thesis, a floor plan is understood as a list of wall segments¹¹ of an indoor scenario. The positions of the anchors within this floor plan can be mirrored with respect to the wall segments to obtain *virtual anchors* (VAs). This section describes how these VAs are used as models for the propagation delays of the corresponding MPCs.

2.2.1 Representation of Reflectors using Virtual Anchors

Fig. 2.1 shows a part of an example indoor scenario. The floor plan is given as a list of N_{seg} line segments¹². In general, a number of J physically existing anchors are present within the scenario. The area shown is for the scenario presented in Section A.4, around Anchor 3.

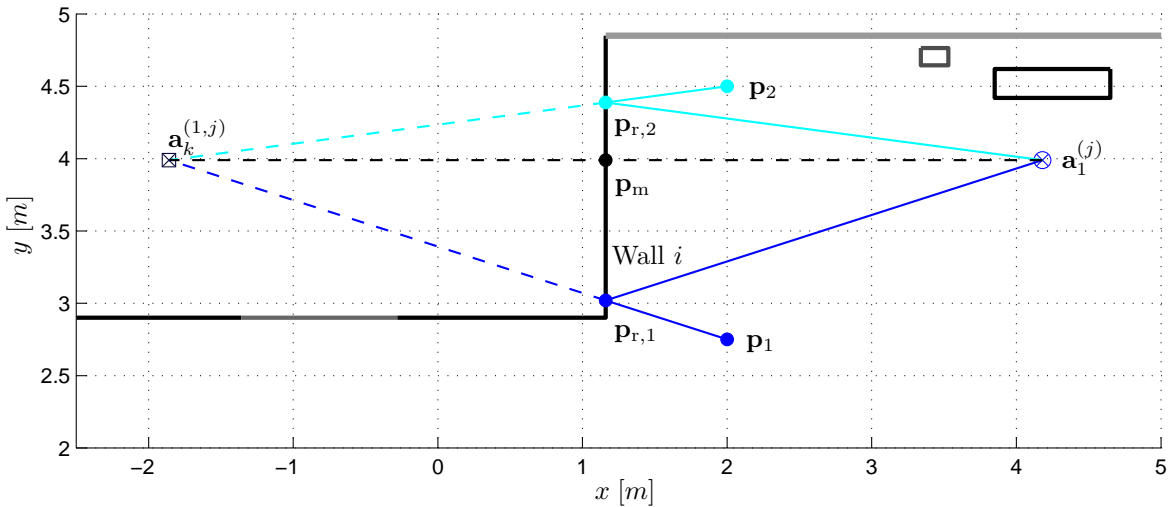


Figure 2.1: Example for computation of a VA in an indoor scenario. The position of the j -th physically existing anchor $\mathbf{a}_1^{(j)}$ is mirrored w.r.t. the i -th wall segment to obtain a first-order VA $\mathbf{a}_k^{(1,j)}$. It models the delay and AoA for any point within its visibility region.

Using the position of the j -th anchor $\mathbf{a}_1^{(j)} = [x_1^{(j)}, y_1^{(j)}]^T$, the position of the first-order VA $\mathbf{a}_k^{(1,j)} = [x_k^{(j)}, y_k^{(j)}]^T$ corresponding to the i -th wall¹³ can be computed¹⁴ using [32, 53, 99]

$$\mathbf{a}_k^{(1,j)} = \mathbf{a}_1^{(j)} + 2\mathbf{n}_i^T (\mathbf{p}_i - \mathbf{a}_1^{(j)}) \mathbf{n}_i \quad (2.6)$$

$$= 2\mathbf{p}_m - \mathbf{a}_1^{(j)} \quad (2.7)$$

where \mathbf{p}_i is an arbitrary point on the i -th wall segment, e.g. one of its end points given in the floor plan. The vector \mathbf{n}_i is the segment's unit normal vector, defined as pointing away from the anchor, i.e. to the outside of the corresponding wall. Using the orthogonal projection of the

¹¹ The term *wall segment* is used here as a generalization of all types of floor plan elements representable with lines (in 2D), such as windows, flat pillars, etc. Hence, all wall segments act as potential specular reflectors.

¹² Throughout this thesis, the restriction to a 2D geometry is applied to simplify computations and visualizations. Note that an extension of the techniques to 3D is straightforward. W.r.t. the geometric model, line segments just have to be replaced by plane segments.

¹³ The different indices k for the VA and i for the wall are chosen deliberately. As shown in this section, one VA can model more than one wall which will be accounted for using (2.9). Also, the index k is used for the MPCs comprising a CIR and as such, the choice of the index is arbitrary.

¹⁴ See [65] for a different mathematical formalization of the VA computation and [99] for a treatment of similar computational techniques to obtain VAs.

anchor onto the wall segment, the mirror point \mathbf{p}_m , gives the simpler relation (2.7). Fig. 2.1 shows an example for a first-order VA of the j -th anchor.

To obtain higher-order VAs, lower-order VAs are mirrored again using (2.6), such that a set

$$\mathcal{A}^{(j)} = \left\{ \mathbf{a}_i^{(q,j)}, i = 1, \dots, N_{\text{VA}}^{(j)}, q = 1, \dots, Q \right\} \quad (2.8)$$

of VAs is obtained for the j -th anchor, where Q is the maximum interaction order taken into account. Fig. 2.2 shows an example for a second-order VA modeling the reflections w.r.t. wall segments i and i' . It should be noted that for this special case of a so-called corner VA, where the angle between the two walls is 90° , the order of these wall segments does not matter for the position of the VA.

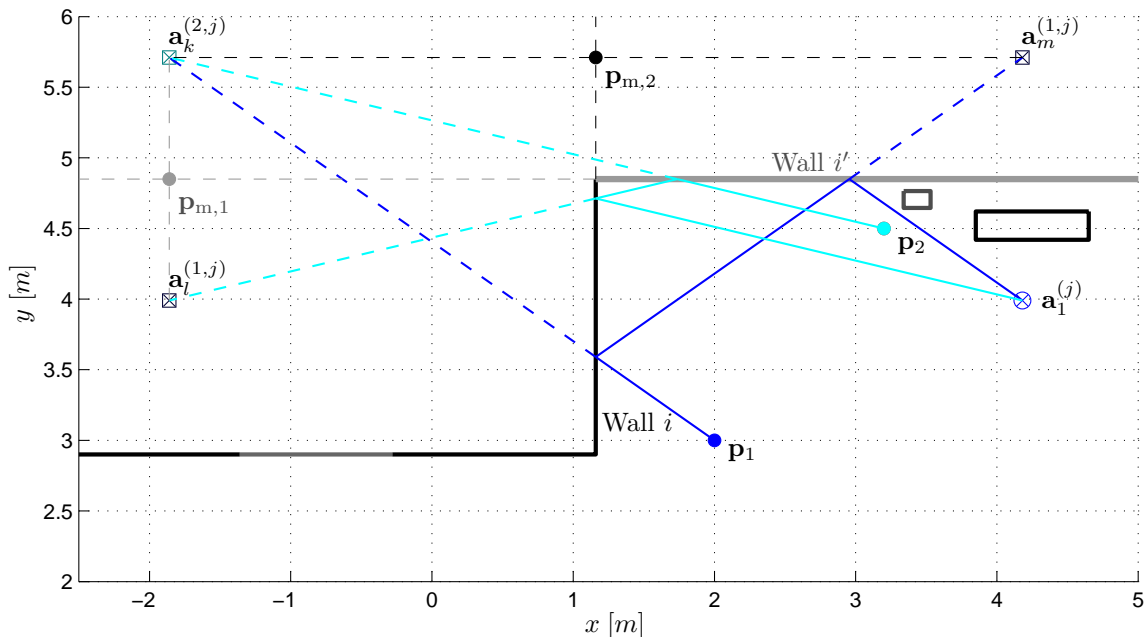


Figure 2.2: Example for the computation of a second-order VA. Its position $\mathbf{a}_k^{(2,j)}$ is obtained by mirroring $\mathbf{a}_i^{(1,j)}$ w.r.t. the i' -th wall. Alternatively, $\mathbf{a}_m^{(1,j)}$ can be mirrored w.r.t. the i -th wall to obtain a VA at the identical location.

This is an example for the case that one VA models multiple signal paths. Another example for this rather common case is the lower-left horizontal wall segment in Fig. 2.1. It is divided into one gray segment and two black segments, indicating different materials (c.f. Sec. A.4). First-order VAs of these segments would be at exactly the same position, but model different interactions.

This is represented by assigning a set of *paths* \mathcal{G}_k to each VA:

$$\mathbf{a}_k^{(q,j)} \rightarrow \mathcal{G}_k = \{ \dots, \mathbf{w}_{k,i}, \dots \}, \text{ with } |\mathcal{G}_k| = N_{\text{paths}} \text{ and } \mathbf{w}_{k,i} \in \mathbb{N}^q \quad (2.9)$$

The individual paths $\mathbf{w}_{k,i}$ are vectors containing the corresponding wall segment indices. Hence, a path¹⁵ identifies the sequence of interactions. For the example of the second-order VA $\mathbf{a}_k^{(2,j)}$ in Fig. 2.2, the set of paths would be

$$\mathcal{G}_k = \left\{ \begin{bmatrix} i \\ i' \end{bmatrix}, \begin{bmatrix} i' \\ i \end{bmatrix} \right\}. \quad (2.10)$$

A total number of $N_{\text{VA}} = \sum_{q=1}^Q N_{\text{VA}}^{(q)}$ potential VAs are generated using (2.6) for all J anchors

¹⁵ This concept is also known as ray signature in [107].

and N_{seg} wall segments. The number of q -th order VAs is given as $N_{\text{VA}}^{(q)} = JN_{\text{seg}}(N_{\text{seg}} - 1)^{q-1}$. Strictly speaking, $N_{\text{VA}}^{(q)}$ is the number of q -th order reflection *paths*, which is usually larger than the number of VAs. This is due to the above mentioned fact that one VA may model multiple signal paths. Also, N_{VA} is a loose upper bound for the number of paths, since there exist conditions under which two wall segments cannot have a specular reflection occurring between them:

- *Visibility*: If all lines connecting arbitrary points on two wall segments intersect another feature in the floor plan, this part of the reflection is blocked. For a first-order VA, this means that the anchor has to “see” at least a part of the wall segment to make the reflection path possible.
- *Segment properties*: Some segments may not qualify for specular interactions, e.g. the spatial extent of a wall segment might be too small or the material may be unsuitable for the segment to be taken into account as a specular reflector.
- *Colinearity*: Some wall segments are simply continuations of each other, such as a door in a wall. A direct specular interaction between two such segments l and m is not possible, i.e. there can be no $\mathbf{w}_{k,i}$ where l and m directly follow each other.

The key property of VAs is that the delay of any specular reflection w.r.t. the i -th wall segment can be modeled by the respective VA. At a position $\mathbf{p}_\ell = [x_\ell, y_\ell]^T$, this delay is given as

$$\tau_{k,\ell}^{(j)} = \frac{1}{c}d(\mathbf{a}_k^{(q,j)}, \mathbf{p}_\ell) = \frac{1}{c}\|\mathbf{a}_k^{(q,j)} - \mathbf{p}_\ell\| \quad (2.11)$$

where c denotes the speed of light. The AoA $\phi_{k,\ell}^{(j)}$, i.e. the angle between the k -th VA and \mathbf{p}_ℓ , is defined by

$$\tan(\phi_{k,\ell}^{(j)}) = \frac{y_\ell - y_k^{(j)}}{x_\ell - x_k^{(j)}}, \quad \cos(\phi_{k,\ell}^{(j)}) = \frac{x_\ell - x_k^{(j)}}{\|\mathbf{p}_\ell - \mathbf{a}_k^{(q,j)}\|}, \quad \sin(\phi_{k,\ell}^{(j)}) = \frac{y_\ell - y_k^{(j)}}{\|\mathbf{p}_\ell - \mathbf{a}_k^{(q,j)}\|}. \quad (2.12)$$

These relations are true for any position \mathbf{p}_ℓ at which the corresponding reflection is possible. As Fig. 2.1 shows, although the specific reflection point on the wall, $\mathbf{p}_{r,i}$, changes for the reflections from \mathbf{p}_1 and \mathbf{p}_2 , the geometric properties of both interaction are modeled by the same VA.

In the remainder of this thesis, the notation used for a certain VA of the j -th anchor is $\mathbf{a}_k^{(j)}$, where the index k is understood as the index of the corresponding modeled MPC in the signal model. Hence, the order of the VA and the association of the VA to its wall segments will usually not be indicated, since they are not important in the signal models.

2.2.2 Visibility Regions of Reflections

Once a set of VAs is obtained for a given scenario, their visibility regions, i.e. the regions within the environment in which the corresponding reflections are geometrically possible, can be calculated [99]. Within this thesis, this is done merely for illustrative purposes, such as Fig. 2.3 which shows the visibility region for the second-order VA explained in Fig. 2.2. For the tracking algorithms discussed in Chapter 5, precomputed visibility regions can be used for a certain spatial resolution for a fast look-up of the VAs that are expected to be visible at a certain position.

The visibility of a VA $\mathbf{a}_k^{(j)}$ belonging to the j -th anchor can be formulated with the Boolean

function

$$f_{\text{vis}}(\mathbf{a}_k^{(j)}, \mathbf{p}) = \begin{cases} 1, & \text{if VA } \mathbf{a}_k^{(j)} \text{ is visible at } \mathbf{p} \\ 0, & \text{else.} \end{cases} \quad (2.13)$$

Algorithm 1 contains the recursive ray-tracing algorithm implementing (2.13) that determines the visibility of the q -th order VA $\mathbf{a}_k^{(j)}$ at the point \mathbf{p}_ℓ . The VA has to be visible through one, say the m -th, of its associated q -th-order wall segments, i.e. the segments that form the q -th entry of the paths $\mathbf{w}_{k,i}$ in (2.9). This means that no other element of the floor plan obstructs the line from \mathbf{p}_ℓ to the corresponding reflection point on the m -th segment $\mathbf{p}_{r,m}$. If this condition is met, the corresponding VA of order $q - 1$ is determined from the stored associations and the ray is recursively launched to it from the reflection point. This procedure is repeated until the anchor j is reached.

Algorithm 1 Recursive ray-tracing for visibility calculation

```

1: procedure  $f_{\text{vis}}(\mathbf{a}_k^{(j)}, \mathbf{p}_\ell)$ 
2:    $q \leftarrow$  Order of VA  $\mathbf{a}_k^{(j)}$ 
3:   if  $q == 0$  then ▷  $\mathbf{a}_k^{(j)}$  is an anchor
4:     for wall segments  $i_{\text{seg}} = 1 \rightarrow N_{\text{seg}}$  do
5:        $\mathbf{p} \leftarrow$  Intersect wall segment  $i_{\text{seg}}$  and line from  $\mathbf{p}_\ell$  to  $\mathbf{a}_k^{(j)}$ 
6:       if  $\mathbf{p} \neq \square$  then return 0 ▷ Break as soon as obstruction found
7:       end if
8:     end for
9:     if  $\mathbf{p} == \square$  then ▷ No obstructions found,  $\mathbf{a}_k^{(j)}$  is visible at  $\mathbf{p}_\ell$ 
10:      return 1
11:    end if
12:  else ▷  $\mathbf{a}_k^{(j)}$  is a VA of order  $q \geq 1$ 
13:    for  $i_{\text{path}} = 1 \rightarrow N_{\text{paths}}$  do ▷ All paths  $\mathbf{w}_{k,i}$ ,  $i = 1, \dots, N_{\text{paths}}$  modeled by  $\mathbf{a}_k^{(j)}$ 
14:       $\mathbf{p}_r \leftarrow$  Intersect assoc. segment  $w_{k,i_{\text{path}}}[q]$  and line from  $\mathbf{p}_\ell$  to  $\mathbf{a}_k^{(j)}$ 
15:    end for
16:    if  $\mathbf{p}_r == \square$  then ▷  $\mathbf{a}_k^{(j)}$  not visible through an associated segment
17:      return 0
18:    else ▷ Check if anything obstructs the line from  $\mathbf{p}_r$  to  $\mathbf{p}_\ell$ 
19:      for wall segments  $i_{\text{seg}} = 1 \rightarrow N_{\text{seg}}$  do
20:         $\mathbf{p} \leftarrow$  Intersect wall segment  $i_{\text{seg}}$  and line from  $\mathbf{p}_r$  to  $\mathbf{p}_\ell$ 
21:      end for
22:      if  $\mathbf{p} \neq \square$  then ▷ Path to reflection point  $\mathbf{p}_r$  obstructed
23:        return 0
24:      end if
25:    end if
26:    Look-up  $\mathbf{a}_{k'}^{(j)}$  using segment containing  $\mathbf{p}_r$  ▷ Find VA modeling interaction of order  $q - 1$ 
27:     $f_{\text{vis}}(\mathbf{a}_{k'}^{(j)}, \mathbf{p}_r)$  ▷ Launch ray to corresponding  $(q - 1)$ -th-order VA
28:  end if
29: end procedure

```

Fig. 2.3 illustrates this procedure for the second-order VA $\mathbf{a}_k^{(j)}$. A ray launched from \mathbf{p}_1 successfully reaches the anchor at $\mathbf{a}_1^{(j)}$, while the last path of the ray from \mathbf{p}_2 to the anchor is blocked by a pillar on the upper side of the scenario. Fig. 2.4 shows the number of visible VAs for Anchor 3 over the example scenario discussed in A.4 for VAs up to order three. It highlights that despite the simple looking geometry, the visibility regions can assume complicated patterns.

Using (2.13) for all VAs in the set $\mathcal{A}^{(j)}$ (c.f. (2.8)) at a position \mathbf{p}_ℓ yields the set of *expected*

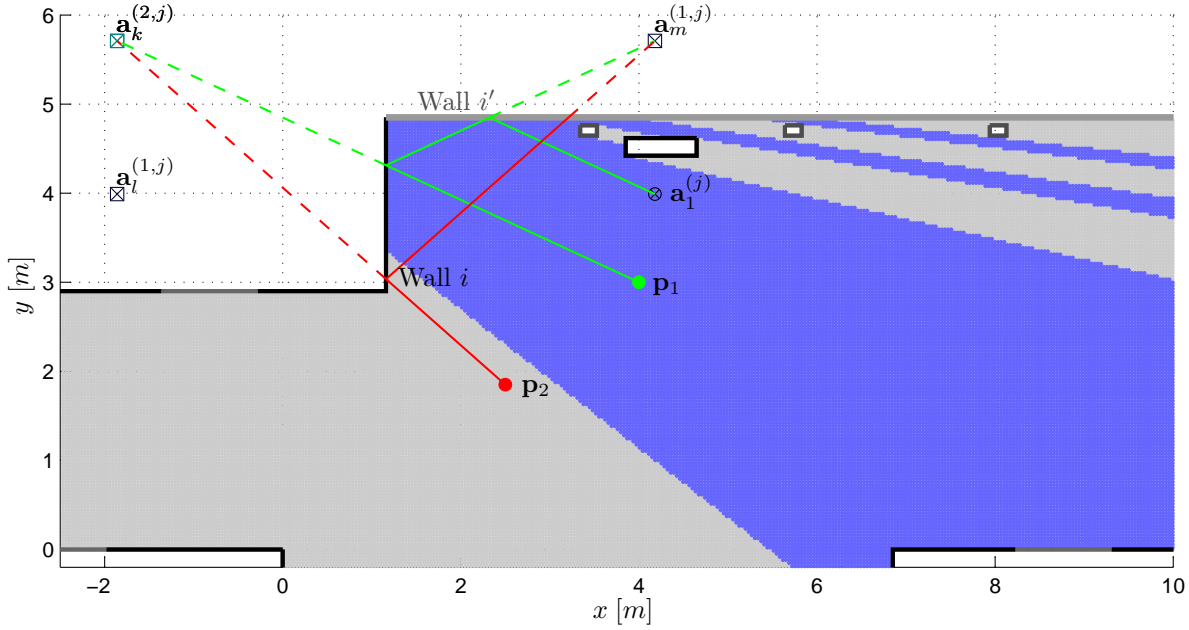


Figure 2.3: The expected visibility region of a second-order VA computed by ray-tracing described in Algorithm 1, indicated in blue. The reflection is possible at point \mathbf{p}_1 , but not at \mathbf{p}_2 .

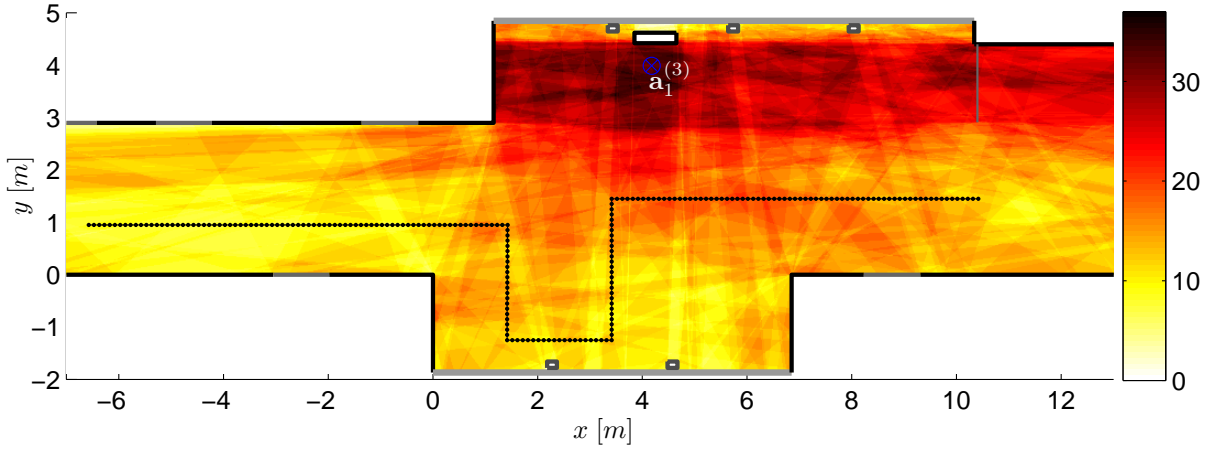


Figure 2.4: The expected number of visible VAs over the floor plan when considering VAs up to order three using Algorithm 1 for Anchor 3.

VAs at \mathbf{p}_ℓ

$$\mathcal{A}_\ell^{(j)} = \left\{ \mathbf{a}_{\ell,1}^{(j)}, \dots, \mathbf{a}_{\ell,K_\ell^{(j)}}^{(j)} \right\} = \left\{ \mathbf{a}_k^{(j)} : f_{\text{vis}}(\mathbf{a}_k^{(j)}, \mathbf{p}_\ell) = 1 \right\} \quad (2.14)$$

which can easily be transformed into the set of expected MPC delays $\mathcal{D}_\ell^{(j)}$ using (2.11)

$$\mathcal{D}_\ell^{(j)} = \left\{ d(\mathbf{a}_{\ell,k}^{(j)}, \mathbf{p}_\ell) : f_{\text{vis}}(\mathbf{a}_{\ell,k}^{(j)}, \mathbf{p}_\ell) = 1 \right\}. \quad (2.15)$$

Fig. 2.5 shows the expected delay tracks of VAs up to order three, i.e. the entries of the sets $\mathcal{D}_\ell^{(j)}$ for all positions \mathbf{p}_ℓ in the seminar room scenario (c.f. Section A.5.1) overlaid over measured signals at bandwidths of 2 GHz and 0.5 GHz, respectively. Especially for the larger bandwidth, many of the expected specular components are present in the signal. Also, the visibility regions seem reasonable, e.g. the NLOS region created by the pillar between positions 77 and 99, is

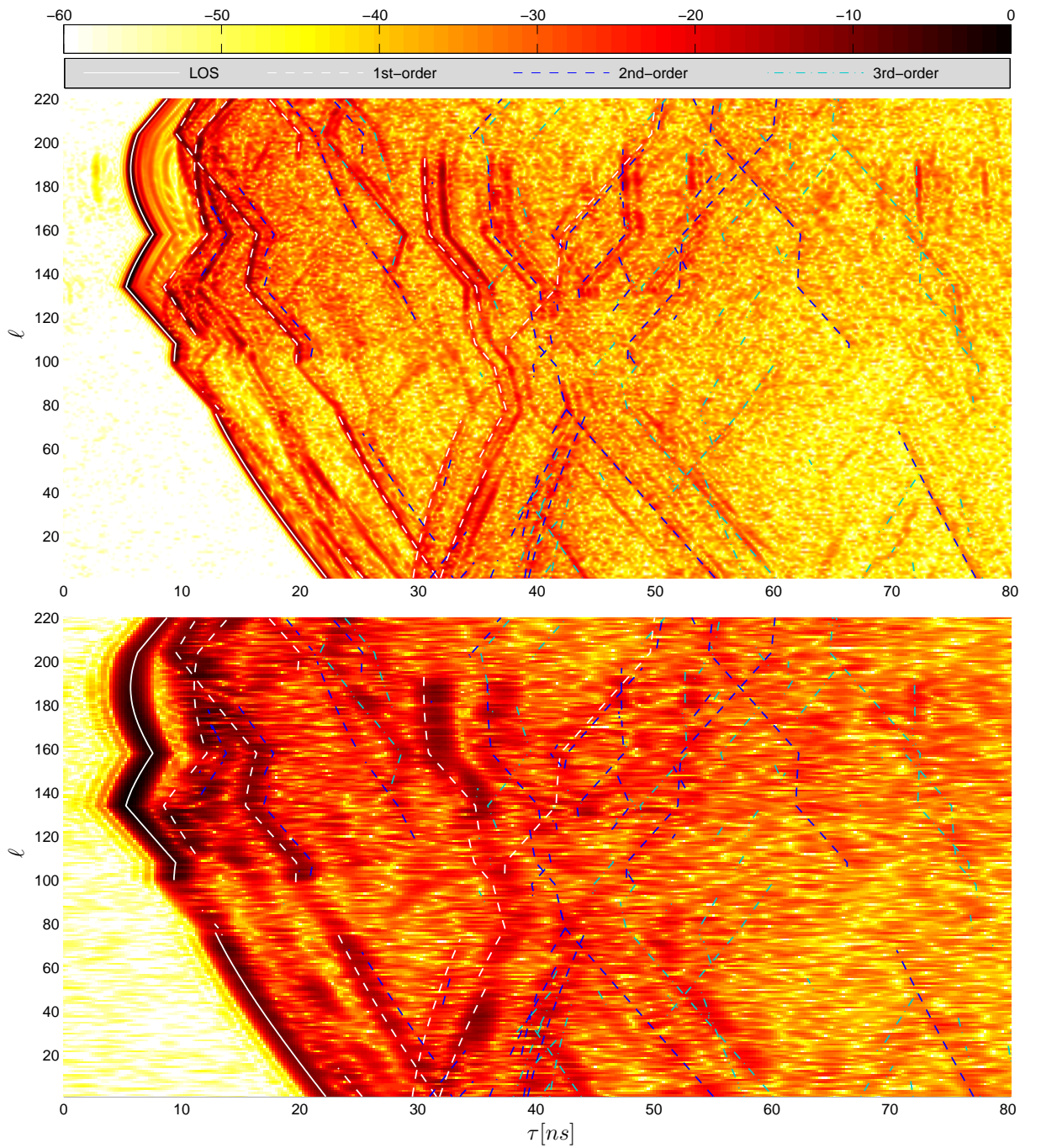


Figure 2.5: Expected delay tracks of VAs up to order three in the seminar room scenario (c.f. Section A.5.1) for measurement trajectory 2 and Anchor 1. Top and bottom plots show the measured signals in dB relative to the maximum LOS component, over all 220 positions using bandwidths of 2 GHz and 0.5 GHz, respectively.

represented well. However, there is still signal energy in this region, which most probably is explained by diffraction, which is not modeled in this framework. This effect is also visible for other MPCs outside their visibility regions.

Observing the lower bandwidth gives a foretaste of the importance of path overlap. As the deterministic MPCs now cover broader regions in the delay domain, the probability of overlap is much larger than for the larger bandwidth. Also, the increased influence of DM at the lower bandwidth is observable.

3

Performance Bounds for Multipath-Assisted Localization – Position-Related Information

This chapter summarizes the main results and findings concerning Cramér-Rao Lower Bounds (CRLBs) on multipath-assisted indoor positioning as derived in [T3], building on the work in [42, 44]. These results have been extended to a discrete-time formulation and multiple setups (e.g. cooperative positioning and monostatic measurements) in [64] using results of [11, 65].

This chapter is organized as follows: Section 3.1 introduces performance metrics for positioning used in this thesis and in the papers comprising it. Also the CRLB as a performance metric is discussed in general. Section 3.2 contains the main results of [T3], i.e. of the derivation of the CRLB for multipath-assisted positioning. Sections 3.3 and 3.4 contain example results and the chapter conclusions, respectively.

3.1 Performance Metrics for Positioning

To evaluate the performance of a positioning system, statistical measures and fundamental bounds of the position error $\epsilon = \|\hat{\mathbf{p}} - \mathbf{p}\|$, i.e. the Euclidean distance between the true position \mathbf{p} and its estimate $\hat{\mathbf{p}}$, are needed. The measures that are used in the papers comprising this thesis are discussed here.

3.1.1 Cramér-Rao Lower Bound

Based on the model (2.3) of the signals transmitted between J anchors at known positions $\mathbf{a}_1^{(j)}$, $j = 1, \dots, J$ and an agent at position \mathbf{p} , we aim at finding a lower bound on the position error. The CRLB is the lower bound on the variance of an unbiased estimator of a given parameter. For a parameter vector $\boldsymbol{\theta}$, the CRLB states that the covariance matrix of such an estimator $\hat{\boldsymbol{\theta}}$ is bounded by

$$\mathbb{E}_{\mathbf{r}|\boldsymbol{\theta}} \left\{ (\hat{\boldsymbol{\theta}} - \boldsymbol{\theta})(\hat{\boldsymbol{\theta}} - \boldsymbol{\theta})^H \right\} \succeq \mathbf{J}_{\boldsymbol{\theta}}^{-1} \quad (3.1)$$

where $\mathbf{J}_{\boldsymbol{\theta}}$ is called the Fisher Information Matrix (FIM) of the vector $\boldsymbol{\theta}$. For the moment, we consider a single anchor, as the FIMs for independent data are additive. The FIM is defined as the expectation of the second derivative w.r.t. the parameter vector $\boldsymbol{\theta}$ of the log-likelihood

function of the signal $r(t)$ conditioned on $\boldsymbol{\theta}$ [108]

$$\mathbf{J}_\theta = \mathbb{E}_{\mathbf{r}|\theta} \left\{ \left[\frac{\partial}{\partial \theta} \ln f(\mathbf{r}|\theta) \right] \left[\frac{\partial}{\partial \theta} \ln f(\mathbf{r}|\theta) \right]^T \right\}. \quad (3.2)$$

The received signal is denoted by the vector \mathbf{r} , which can be obtained using the Karhunen-Loève Expansion [42, 109, 110]. In the present case, the parameter vector of interest contains the position of the agent and the real and imaginary parts of the complex MPC amplitudes as nuisance parameters, i.e. $\boldsymbol{\theta} = [\mathbf{p}^T (\boldsymbol{\alpha}^R)^T (\boldsymbol{\alpha}^I)^T]^T \in \mathbb{R}^{2+2K}$. Since the signal model and therefore the likelihood function depend on the position \mathbf{p} through the vector of multipath delays $\boldsymbol{\tau} = [\tau_1, \dots, \tau_K]^T$, it is convenient to derive the CRLB for the channel parameter vector $\boldsymbol{\psi} = [\boldsymbol{\tau}^T (\boldsymbol{\alpha}^R)^T (\boldsymbol{\alpha}^I)^T]^T \in \mathbb{R}^{3K}$ and then use the chain rule [108] to find the FIM for $\boldsymbol{\theta}$ as

$$\mathbf{J}_\theta = \mathbf{T} \mathbf{J}_\psi \mathbf{T}^T. \quad (3.3)$$

The Jacobian matrix \mathbf{T} contains the transformation as

$$\mathbf{T} = \frac{\partial \boldsymbol{\psi}}{\partial \boldsymbol{\theta}} = \begin{bmatrix} \mathbf{H}_{2 \times K} & \mathbf{0}_{2 \times 2K} \\ \mathbf{0}_{2K \times K} & \mathbf{I}_{2K \times 2K} \end{bmatrix} \quad (3.4)$$

where the geometry is included in the subblock \mathbf{H} , which is defined as

$$\mathbf{H} = \frac{1}{c} \begin{bmatrix} \cos(\phi_1) & \dots & \cos(\phi_K) \\ \sin(\phi_1) & \dots & \sin(\phi_K) \end{bmatrix}. \quad (3.5)$$

The ϕ_k are the angles from the k -th VA to the point \mathbf{p} as in (2.12). Once the FIM \mathbf{J}_θ is obtained, the position error bound (PEB) [42] is defined as

$$\mathcal{P}(\mathbf{p}) = \sqrt{\text{tr} \{ [\mathbf{J}_\theta]_{2 \times 2} \}} \quad (3.6)$$

i.e. the square root of the trace of the upper left 2×2 submatrix of the FIM, which contains the entries for \mathbf{p} . As derived in [T3], \mathbf{J}_ψ obtained using (3.2) has a block structure as

$$\mathbf{J}_\psi = \begin{bmatrix} \boldsymbol{\Lambda}_A & \boldsymbol{\Lambda}_B \\ \boldsymbol{\Lambda}_B^T & \boldsymbol{\Lambda}_C \end{bmatrix}. \quad (3.7)$$

We can then use block-wise inversion [27, 40, 42, 44] to obtain the desired subblock of the FIM \mathbf{J}_θ incorporating the transformation (3.3) as

$$\mathbf{J}_\mathbf{p} = [\mathbf{J}_\theta]_{2 \times 2} = \mathbf{H} (\boldsymbol{\Lambda}_A - \boldsymbol{\Lambda}_B \boldsymbol{\Lambda}_C^{-1} \boldsymbol{\Lambda}_B^T) \mathbf{H}^T. \quad (3.8)$$

Since this only requires an explicit inversion of $\boldsymbol{\Lambda}_C$, this often allows for closed-form solutions for the FIM of the position $\mathbf{J}_\mathbf{p}$, e.g. if the MPCs are orthogonal. The FIM $\mathbf{J}_\mathbf{p}$ obtained using (3.8) is referred to as *equivalent FIM* (EFIM) [42].

3.1.2 Geometric Dilution of Precision (GDOP)

GDOP is a popular measure for the performance of positioning systems [111, 112]. Depending on the parameters included in the position vector, different versions of the GDOP are used. Since we deal with two-dimensional positioning, we use the horizontal DOP (HDOP). For an unbiased range-based estimator of the position, it is defined as [4, 17]

$$\text{HDOP} = \frac{\sqrt{\mathbb{E} \{ \|\hat{\mathbf{p}} - \mathbf{p}\|^2 \}}}{\sigma_d} = \frac{\sqrt{\sigma_x^2 + \sigma_y^2}}{\sigma_d} \quad (3.9)$$

where σ_x^2 and σ_y^2 are the variance of the position estimation in x - and y -direction, and σ_d is the (common) standard deviation of the range measurements. An HDOP $\gg 1$ indicates a bad geometric constellation of the anchors that are used.

3.1.3 Distribution of the Position Error

The distribution of the position error over a geometric area can give important insights on e.g. the measurement model. Throughout the papers included in this thesis, cumulative distribution functions (CDFs) of the position error have been used for performance evaluation, since they can present a complete quantification of the errors. Also the distribution of the error across the room is helpful in analyzing geometric considerations. In this light, CDFs of the position error (or also of the PEB) evaluated over a whole scenario are reasonable, especially when different setups need to be compared. A popular performance figure especially in the GNSS community is circular error probable (CEP) [111], which defined as the radius of a circle in which 50 % of the position errors lie. It is obvious that a CDF includes this measure and provides a much more complete picture of the performance, e.g. the amount of outliers can be inferred easily.

3.1.4 Comments on the CRLB and other performance metrics

One of the reasons for the popularity of the CRLB in the literature is the fact that it is often possible to obtain closed-form results. When used as performance benchmark for an estimator, there are important theoretical implications that one should keep in mind.

- The CRLB (3.1) is defined as the average curvature of the log-likelihood function at the true value of the parameter. Hence, it locally evaluates the sensitivity of the measurement model with respect to the parameters. Given a specific estimator, this is related to its potential accuracy (see Sec. 1.1.3), but not to its robustness.
- When measures derived from the CRLB, such as the PEB, are plotted in e.g. CDFs for a whole scenario, this evaluates the best possible *local* accuracy. This does not mean that this accuracy can actually be achieved by an estimator, since the CRLB can by definition not take into account global phenomena like multimodality of the likelihood function.
- The CRLB is a lower bound of the variance of any *unbiased* estimator. Mismatches in the channel models can lead to a bias in the position estimation, which renders the CRLB useless.
- It is generally known that the CRLB is tight only for medium to high SNRs [113]. In the present case, this means that the *detectability* of the MPCs is not addressed, which could lead to an overly optimistic PEB when the power of the DM is large. In such cases, other bounds like the Zik-Zakai bound [14] may produce more realistic results.

The CRLB can give good predictions of the expected performance of multipath-assisted positioning in an environment when its parameters are estimated from a few training signals, as shown in Chapter 4 and [T4, T8, T9].

The HDOP is used in [T6] mainly to show the advantage of multipath-assisted tracking to conventional range-based tracking. The improved constellations are due to the large set of VAs that can be used. However, evaluating the EFIM using channel estimation can provide similar information in terms of the covariance matrix of the position error as used in [T8, T9] with more insight on the channel parameters. Since DOP requires variances of position and range measurements, its usefulness is more in the design phase of a localization system, facilitating considerations such as anchor placement.

3.2 Cramér-Rao Lower Bound for Multipath-assisted Positioning

The EFIM for the signal parameters \mathbf{J}_ψ has been derived in [T3] using a likelihood function corresponding to the signal model in (2.3)

$$\begin{aligned} \ln f(\mathbf{r}|\psi) &\propto \frac{2}{N_0} \int_0^T \Re \left\{ r(t) \sum_{k=1}^K w_k^2 \alpha_k^* s(t - \tau_k) \right\} dt \\ &\quad - \frac{1}{N_0} \int_0^T \sum_{k'=1}^K w_{k'} \alpha_{k'} s(t - \tau_{k'}) \sum_{k=1}^K w_k \alpha_k s(t - \tau_k) dt. \end{aligned} \quad (3.10)$$

The factors w_k account for the non-stationary statistics of the DM (2.2), which make a whitening operation necessary to obtain a tractable likelihood function [109]. The derivation of this likelihood function builds on the assumptions that the signal $s(t)$ has a block spectrum and that the individual deterministic MPCs do not overlap, i.e. they are orthogonal.

3.2.1 Without Path Overlap – Orthogonal Multipath Components

For orthogonal deterministic MPCs, i.e. no *path overlap* (PO) [114], a canonical form can be found for the EFIM for the position estimation using J anchors [T3]

$$\mathbf{J}_\mathbf{p} = \frac{8\pi^2 \beta^2}{c^2} \sum_{j=1}^J \sum_{k=1}^{K^{(j)}} \text{SINR}_k^{(j)} \mathbf{J}_r(\phi_k^{(j)}). \quad (3.11)$$

where β is the effective bandwidth [14] of $s(t)$. The matrix

$$\mathbf{J}_r(\phi_k^{(j)}) = \begin{bmatrix} \cos^2(\phi_k^{(j)}) & \cos(\phi_k^{(j)}) \sin(\phi_k^{(j)}) \\ \cos(\phi_k^{(j)}) \sin(\phi_k^{(j)}) & \sin^2(\phi_k^{(j)}) \end{bmatrix} \quad (3.12)$$

is called the ranging direction matrix [42]. It is a rank-one matrix with one eigenvector pointing from the k -th VA to the agent at \mathbf{p} . The Signal-to-Noise-and-Interference ratio (SINR) of the k -th MPC is defined as

$$\text{SINR}_k^{(j)} = \frac{|\alpha_k^{(j)}|^2}{N_0 + T_p S_\nu^{(j)}(\tau_k^{(j)})} \quad (3.13)$$

where again T_p is an effective pulse duration of $s(t)$ [T3], [64]. The SINR indicates the ratio of the energy of the deterministic MPCs to the combined effect of AWGN and DM. The latter is quantified by its PDP $S_\nu^{(j)}(\tau_k^{(j)})$, evaluated for the ToA of the respective MPC and is scaled by the pulse duration. The EFIM (3.11) gives an intuitive decomposition of the *position-related information* of each MPC. The ranging direction matrix indicates the direction of the potential information, while the SINR quantifies how much of this information is actually available.

Using (3.3), the SINR can be directly related to the CRLB on the ranging to the k -th MPC [T9]

$$\mathbf{J}_r^{-1}(d_k^{(j)}) = \left(\frac{8\pi^2 \beta^2}{c^2} \text{SINR}_k^{(j)} \right)^{-1} \leq \text{var} \left\{ \hat{d}_k^{(j)} \right\} \quad (3.14)$$

where $\mathbf{J}_r(d_k^{(j)})$ denotes the Fisher information about the distance $d_k^{(j)}$ to the k -th VA.

3.2.2 Influence of Path Overlap on Localization

Despite the fact that the likelihood function (3.10) assumes orthogonal MPCs, evaluating (3.8) without this assumption still gives an EFIM that accounts for path overlap. A formulation of the problem using discrete-time signals as in [64] allows for exact results for the CRLB.

An approximation of the influence of PO that will already indicate the regions where performance impairments are to be expected can be obtained by restricting the sum in (3.11) to the orthogonal MPCs. For this, we re-introduce the position index ℓ , since PO is a local phenomenon, and define the set of MPC delays at \mathbf{p}_ℓ as $\{\tau_{k,\ell}\}_{k=1}^{K_\ell}$. The set of all VAs that are subject to PO at this position is defined as

$$\mathcal{C}_\ell = \{\mathbf{a}_{k,\ell} \in \mathcal{A}_\ell : |\tau_{k,\ell} - \tau_{k',\ell}| < T_p \text{ with } k' \neq k, \text{ and } \mathbf{a}_{k'} \in \mathcal{A}_\ell\}. \quad (3.15)$$

This set can be split in the contiguous clusters of MPCs [42], i.e. the different, disjoint sets of overlapping MPCs. As (3.11) may be too optimistic by summing over all MPCs (also those within a cluster), the EFIM can be modified to

$$\mathbf{J}_{\mathbf{p}_\ell} = \frac{8\pi^2\beta^2}{c^2} \sum_{j=1}^J \sum_{k:\mathbf{a}_{k,\ell} \in \mathcal{A}_\ell \setminus \mathcal{C}_\ell} \text{SINR}_{k,\ell}^{(j)} \mathbf{J}_r(\phi_{k,\ell}^{(j)}). \quad (3.16)$$

i.e. considering only those MPCs which are not subject to PO. According to (3.15), this imposes a hard limit as to whether an MPC is considered or not. In [42, 114] a path overlap coefficient is derived that allows for a more gradual evaluation of the information loss due to decreasing MPC spacing. The usefulness of (3.16) lies in the fact that the SINRs can be estimated from signals (see Chapter 4), with which an estimate of the CRLB can be obtained. Section 8.3 contains results for this definition of the CRLB.

3.3 Example Results

Fig. 3.1 shows computational results for the PEB $\mathcal{P}(\mathbf{p})$ evaluated over a room. These results are adapted from [T3]. We use a free-space pathloss model for the distance dependence of the path amplitudes of the deterministic MPCs for a center frequency of 7 GHz, adding 3 dB of attenuation per reflection order. A double exponential PDP is used for the DM as in [26]. For the transmit pulse $s(t)$, a raised-cosine pulse with roll-off factor $\beta_R = 0.6$ and a pulse duration of $T_p = 1$ ns is used. Subplot (a) shows the set of first- and second-order VAs that have been taken into account.

Subplots (b), (c) and (d) illustrate the PEB $\mathcal{P}(\mathbf{p})$ using the complete EFIM (3.8), the EFIM neglecting PO in (3.11), and the EFIM with the simplified consideration of PO MPCs as in (3.16), respectively. Range-based localization is possible throughout the whole room with just one physical anchor. Uncertainty ellipses are clearly oriented towards the anchors, reflecting the fact that usually the LOS component is the one with the largest SINR. This is the fact because it is least impaired by DM, an effect that could be verified using measurements [T4, T7, T8].

Subplot (b) shows the adverse effect of symmetries, i.e. regions affected by PO and the corresponding loss of information. This is neglected in (c), nevertheless the main regions of different expected localization accuracy are still visible. This reflects the different visibility regions of the VAs as well as the distance dependence of their amplitudes. For subplot (d), the influence of PO is approximated as in (3.16), i.e. excluding all MPCs whose arrival times are spaced by less than T_p as defined in (3.15). Completely black regions in (d) indicate regions where less than two VAs are usable. Here the EFIM $\mathbf{J}_{\mathbf{p}}$ is rank-deficient and no localization is possible. Compared to (b), this approximates the influenced regions reasonably well, but may be overly pessimistic, due to the fact that all potential information contained in a contiguous

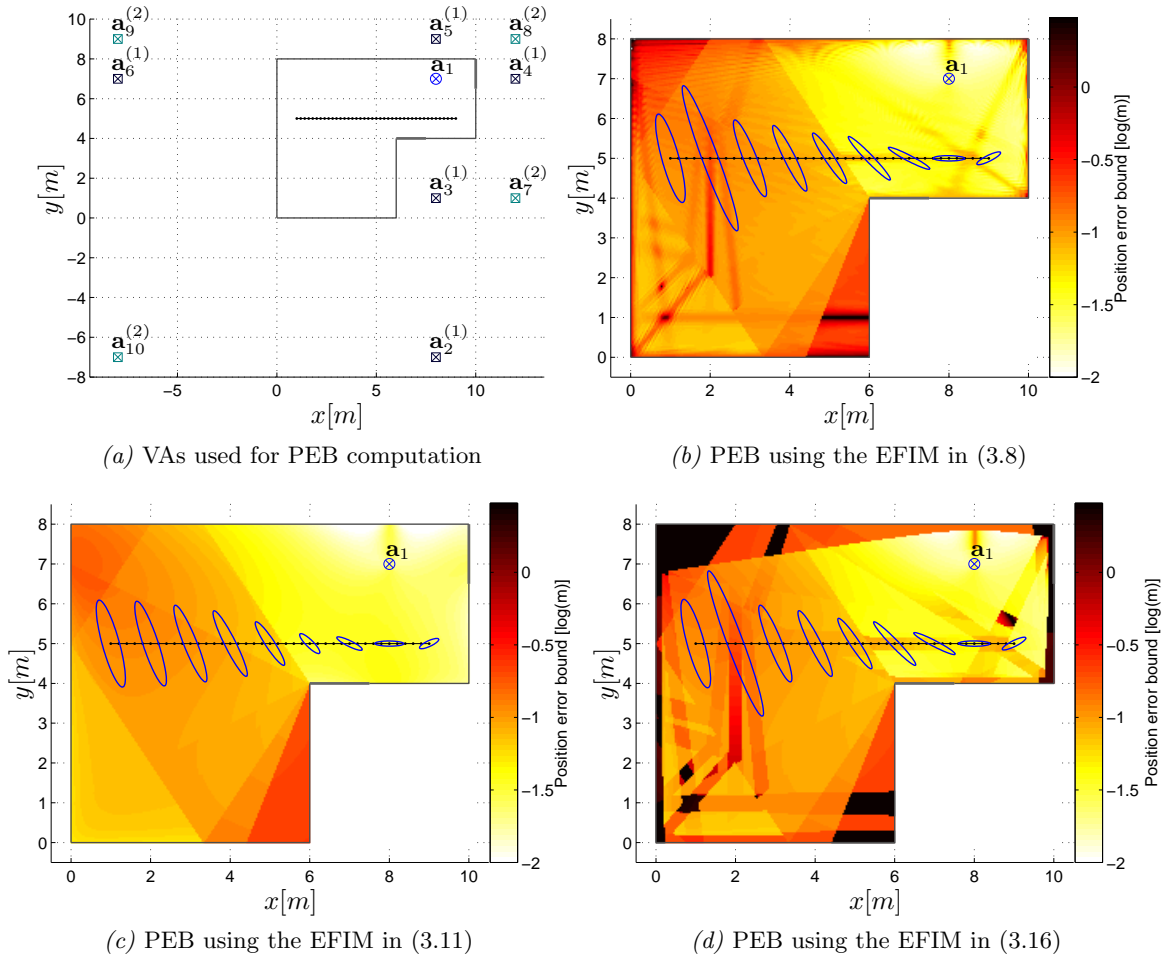


Figure 3.1: Computational results for the logarithmic PEB over a room, adapted from [T3]. (a) shows the used scenario with the floor plan, the anchor at \mathbf{a}_1 , and the first- and second-order VAs $\mathbf{a}_k^{(1)}$ and $\mathbf{a}_k^{(2)}$. (b) illustrates the PEB $\mathcal{P}(\mathbf{p})$ considering path overlap (PO) as in (3.8), while PO is neglected in (c). The PEB only considering MPCs which do not overlap as in (3.16) is shown in (d). Blue ellipses denote the 10-fold standard deviation at selected points.

cluster is completely discarded. The more complete formulation in (3.8) predicts a more gradual decrease of performance up to the point of complete PO, as indicated in subplot (b).

3.4 Chapter Conclusions and Results in Included Papers

The CRLB derivation in [T3] reveals important insights on multipath-assisted positioning that have been the basis for following work. The following conclusions concerning the use of multipath for positioning can be made.

- A large **bandwidth** influences the performance in multiple ways: (i) It of course influences the ranging accuracy beneficially due to the finer delay resolution. (ii) Due to the same reason, path overlap gets less probable. (iii) The adverse influence of DM diminishes with increasing bandwidth as seen in (3.13).
- The impact of **diffuse multipath** is accounted for through (3.13). This is also seen in the MPC ranging bound in (3.14) that extends existing bounds for the LOS component in e.g. [14] in terms of the influence of the DM in the SINR.

- The **geometric information** available in a multipath channel [27] is made explicit by the geometry of the VAs. This is in contrast to e.g. [42], where the signal as a whole is modeled to come from the direction of the corresponding anchor.
- The **position-related information** of an MPC can be quantified using the ranging direction matrix (3.12) and the SINR (3.13). The latter is an important measure of the reliability of the respective MPC.

Computational results in [T3] show the conclusions that can be drawn from the derived CRLB in an example environment. A single anchor can provide position information, even in NLOS regions. The EFIM in (3.8) gives insights in the adverse effects of room symmetries and the path overlap phenomenon.

The CRLB presented has been used in numerous papers following [T3]. In [T4], an estimator for the MPC SINR has been derived based on training signals obtained on short trajectory segments. Together with the given geometry, this is the basis for evaluating an estimated CRLB (as in (3.11) neglecting path overlap) over a scenario. This method is used in [T7, T8] for performance predictions. The MPC ranging bounds in (3.14) have been used in [T9] as a noise model for the range estimates in a tracking filter, resulting in excellent results in terms of robustness and accuracy. This confirms the validity and the usefulness of the derived CRLB also in practical scenarios.

4

Channel Analysis – Estimation of Position-Related Information

This chapter summarizes the main findings concerning channel analysis for multipath-assisted positioning as presented in [T2, T4, T7]. The main aim is to characterize the relevance of certain deterministic MPCs, especially w.r.t. positioning. Chapter 8 contains additional results for the presented concepts. The channel measurement campaigns that have been performed have been made publicly available [78]. Appendix A describes these measurements in detail.

This chapter is organized as follows: Section 4.1 introduces the maximum-likelihood estimation procedure for the deterministic MPCs and the analysis of their energy capture. The estimation of the signal-to-interference-and-noise-ratio of the deterministic MPCs is discussed in Section 4.2. Example results and conclusions are presented in Sections 4.3 and 4.4, respectively.

4.1 Estimation of Deterministic Multipath Components

For all further analysis methods that are presented in this chapter, an estimation procedure for the channel parameters from a signal $r_\ell^{(j)}(t)$ transmitted between an anchor at $\mathbf{a}_1^{(j)}$ and an agent at \mathbf{p}_ℓ is necessary. As we are restricted to single-antenna agents and anchors, the channel parameters of interest are the path delays $\{\tau_{k,\ell}^{(j)}\}$ and complex amplitudes $\{\alpha_{k,\ell}^{(j)}\}$.

4.1.1 Approximate Maximum-Likelihood Estimation

The arrival time estimation at position \mathbf{p}_ℓ is realized without prior knowledge on the channel parameters as an iterative least-squares approximation of the signal received from the j -th anchor (2.3) [T9]

$$\hat{\tau}_{k,\ell}^{(j)} = \arg \min_{\tau} \int_0^T \left| r_\ell^{(j)}(t) - \hat{r}_{\ell,k-1}^{(j)}(t) - \hat{\alpha}(\tau) s(t - \tau) \right|^2 dt, \quad k = 1, \dots, \hat{K}_\ell^{(j)} \quad (4.1)$$

using a template signal $\hat{r}_{\ell,k}^{(j)}(t) = \sum_{k'=1}^k \hat{\alpha}_{k',\ell}^{(j)} s(t - \hat{\tau}_{k',\ell}^{(j)})$ for all MPCs up to the k -th. The path amplitudes are nuisance parameters, estimated using a projection of $r_\ell^{(j)}(t)$ onto a unit energy

pulse $s(t)$ as

$$\hat{\alpha}(\tau) = \int_0^T [r_\ell^{(j)}(t)]^* s(t - \tau) dt; \quad \hat{\alpha}_{k,\ell}^{(j)} = \hat{\alpha}(\hat{\tau}_{k,\ell}^{(j)}). \quad (4.2)$$

The number of estimated MPCs $\hat{K}_\ell^{(j)}$ should be chosen according to the number of expected specular paths in an environment. With the assumptions of separable MPCs and white noise, (4.1) and (4.2) correspond to a maximum-likelihood (ML) estimation of the deterministic MPCs.

Prior knowledge on the channel parameters is introduced by the known agent position \mathbf{p}_ℓ , as in channel analysis scenarios. In this case, a hypothesis for the delay of the k -th deterministic MPC is available using the distance between the corresponding k -th VA at $\tilde{\mathbf{a}}_k^{(j)}$ and \mathbf{p}_ℓ (2.11)

$$\tilde{\tau}_{k,\ell}^{(j)} = \frac{1}{c} \|\tilde{\mathbf{a}}_k^{(j)} - \mathbf{p}_\ell\|. \quad (4.3)$$

The tilde denotes the fact that the hypothesis computed using the floorplan may be uncertain. The hypothesis can be used to restrict the search space for τ in (4.1), as in the energy capture analysis in [T2] and in Section 4.1.2. Another method is to find a suitable point estimate for $\tau_{k,\ell}^{(j)}$ based on (4.3) and directly evaluate the path amplitude in (4.2) with it, as for the SINR estimation technique used in [T4, T9] and in Section 4.2.

The choice of the number of estimated MPCs $\hat{K}_\ell^{(j)} = |\{\tau_{k,\ell}^{(j)}\}|$ also depends on the fact if \mathbf{p}_ℓ is known or not. If it is known, $\hat{K}_\ell^{(j)} = K_\ell^{(j)} = |\mathcal{A}_\ell|$, i.e. the cardinality of the expected set of visible VAs (2.14). If \mathbf{p}_ℓ is unknown, a maximum number of MPCs has to be selected, which we denote as $\hat{K}_\ell^{(j)} = K_{\max}$, i.e. independent of position and anchor. After $\hat{K}_\ell^{(j)}$ MPCs have been estimated from $r_\ell^{(j)}(t)$, also an estimate of the filtered DM is available as¹⁶

$$s(t) * \nu_\ell^{(j)}(t) \approx r_\ell^{(j)}(t) - \hat{r}_{\ell, \hat{K}_\ell^{(j)}}^{(j)}(t). \quad (4.4)$$

4.1.2 Energy Capture Analysis of VA-modeled MPCs

Inspired by [115], we have performed an analysis of the energy capture (EC) of the VA-modeled deterministic MPCs in [T2]. The energy capture of an MPC in the signal $r_\ell^{(j)}(t)$ transmitted between an anchor at $\mathbf{a}^{(j)}$ and an agent at \mathbf{p}_ℓ is estimated as

$$\text{EC}_\ell = 1 - \frac{\int_0^T |r_\ell^{(j)}(t) - \hat{r}_{\ell, \hat{K}_\ell^{(j)}}^{(j)}(t)|^2 dt}{\int_0^T |r_\ell^{(j)}(t)|^2 dt}. \quad (4.5)$$

In the estimation of the deterministic part of the received signal using (4.1) and (4.2), the search space for τ has been restricted for the k -th MPC using the constraint that $\tau \in [\tilde{\tau}_{k,\ell}^{(j)} - T_p/2, \tilde{\tau}_{k,\ell}^{(j)} + T_p/2]$.

Section 8.1 shows additional results for the EC analysis in different measurement scenarios discussed in Appendix A. Figure 8.1 contains the EC results for a part of the trajectory analyzed in [T2]. The comparison with [T2] is done because in the paper, no projection operation as in (4.2) was performed for the MPC amplitudes, only the amplitude at the estimated delay was chosen from the signal. The differences that are observed are mainly quantitative, the qualitative trends are similar.

¹⁶ As the received signal is used instead of the channel, this also includes observation noise as in (2.3). However, its effect is negligible in all our measurements. A more interesting consequence of using $r_\ell^{(j)}(t)$ is that it includes the effects of the bandwidth limitation due to $s(t)$.

4.2 SINR Estimation for Deterministic Multipath Components

The EC analysis showed that VA-modeled MPCs carry a large fraction of the signal energy. However, to estimate the position-related information as defined in Chapter 3, the estimation of the SINR of the MPCs (3.13) is necessary. With these, the MPC range uncertainties can be estimated using (3.14).

4.2.1 SINR Estimation along a Motion Trajectory

To avoid the explicit estimation of the PDP of the DM, we have derived an estimator for the average SINR of an MPC in [T4]. It requires only a short segment of training signals at known positions $\mathbf{p}_\ell, \ell = L_1, \dots, L_2$, such as along a trajectory. This makes it also suitable for online SINR estimation, i.e. during the tracking, for which first results are presented in [95].

The signals on the segment of the trajectory used for SINR estimation are stacked in the vector

$$\mathbf{r}^{(j)}(t) = [r_{L_1}^{(j)}(t), \dots, r_{L_2}^{(j)}(t)]^T. \quad (4.6)$$

For the estimation of the MPC amplitudes along the segment, (4.2) is used with the delay hypotheses from the floor plan (4.3). As these are subject to uncertainties, the VA positions are corrected using a prior distribution $p(\tilde{\mathbf{a}}_k^{(j)})$ for the position of the k -th VA. This leads to the MAP estimate

$$\hat{\mathbf{a}}_k^{(j)} = \arg \max_{\tilde{\mathbf{a}}_k^{(j)}} \ln p(\mathbf{r}^{(j)}(t) | \tilde{\mathbf{a}}_k^{(j)}) + \ln p(\tilde{\mathbf{a}}_k^{(j)}) \quad (4.7)$$

with a likelihood function that evaluates the contribution of the k -th VA to all estimation signals $\mathbf{r}^{(j)}(t)$ (c.f. [T3] but neglecting the whitening to account for the DM)

$$\ln p(\mathbf{r}^{(j)}(t) | \tilde{\mathbf{a}}_k^{(j)}) \propto \frac{2}{N_0} \sum_{\ell \in \mathcal{P}_k^{(j)}} \int_0^T \Re \{ [r_\ell^{(j)}(t)]^* \tilde{s}_{k,\ell}^{(j)}(t) \} dt - \frac{1}{N_0} \int_0^T |\tilde{s}_{k,\ell}^{(j)}(t)|^2 dt.$$

Here, $\tilde{s}_{k,\ell}^{(j)}(t) = \tilde{\alpha}_{k,\ell}^{(j)} s(t - \tilde{\tau}_{k,\ell}^{(j)})$ is a template signal where $\tilde{\tau}_{k,\ell}^{(j)} = \frac{1}{c} \|\tilde{\mathbf{a}}_k^{(j)} - \mathbf{p}_\ell\|$ and the MPC amplitudes are again nuisance parameters and estimated using (4.2). The sets $\mathcal{P}_k^{(j)}$ contain the indices of those points \mathbf{p}_ℓ , on which the k -th VA is *observable*, i.e. where it is visible (2.13) and there is no path overlap with any other deterministic VA [T9].

In the next step, estimates of the first and second moments of the energy samples $|\alpha_{k,\ell}|^2$ are computed, denoted as $\hat{m}_{1,k}^{(j)}$ and $\hat{m}_{2,k}^{(j)}$. For these, the optimized VA positions (4.2) with (4.7) are used. As detailed in [T4, T9], an estimate of the average SINR of the k -th MPC is found based on a Ricean model of $|\alpha_{k,\ell}|$ as

$$\widehat{\text{SINR}}_k^{(j)} = \left(\frac{\hat{m}_{1,k}^{(j)}}{\sqrt{\hat{m}_{1,k}^{(j)2} - \hat{m}_{2,k}^{(j)}}} - 1 \right)^{-1}. \quad (4.8)$$

This moment-based estimator is similar to a classical method for the estimation of the Ricean K-factor of narrowband channels [116, 117]. The method is extended here to *local* (in the delay domain) K-factors of deterministic MPCs. In [118, 119], asymptotic variance analysis of these types of estimators has shown satisfying performance in general. This is especially interesting as moment-based estimates of the K-factor are computationally much less demanding than other methods like expectation-maximization approximations of maximum likelihood estimation as in [120].

The SINR estimates can be related to ranging uncertainties w.r.t. the VAs using (3.14). This is used in Section 5.2.2 to tune the measurement noise model of a tracking filter.

Choice of segment location: On the respective trajectory segment, only a subset of all potential VAs are observable (see visibility regions in Fig. 2.4). Hence, we have extended the method to multiple disjoint segments of points. The detailed description is found in [T9]. Generally, estimation segments should be chosen based on the number of visible deterministic MPCs (see e.g. Fig. 2.4), taking path overlap into account. Within such a region, propagation conditions are assumed to be stationary¹⁷.

4.2.2 SINR Estimation using Local Grid Measurements

SINR estimation can be done by evaluating (3.13) [T7]. This requires the PDP of the DM to be known, which in most cases may not be the case due to a lack of suitably spaced measurements as discussed in Section 7.2. If the PDP of the DM is estimated using (4.4), possible artifacts resulting from the MPC subtraction cause difficulties in choosing a concrete value from the estimated PDP for a certain MPC. A “true” PDP may be available using ray-tracing, e.g. with the method in [80]. This allows for signals decomposed in deterministic reflections and diffuse scattering. With this, results in [T7] confirm the SINR estimation method in (4.8).

4.3 Example Results

Fig. 4.1 shows example signals as well as estimated SINRs and the EC of selected deterministic MPCs in the demonstration room in Graz (see Appendix A.5.2) using Anchor 1 and trajectory 1. A pulse duration of $T_p = 0.5$ ns is used for two different center frequencies of $f_c = 7$ GHz (a) and $f_c = 8$ GHz (b). The SINRs are estimated using 60 points, divided into 20 points at the beginning, in the middle and at the end of the trajectory. For this, the method explained in Section 4.2.1 is employed together with its extension to multiple segments proposed in [T9]. The mean and standard deviation of the EC are estimated using the same set of points.

The results show the relevance of different, VA-modeled MPCs. For the Anchor, i.e. the LOS component, the influence of DM is less than for all later-arriving MPCs. Therefore and due to the LOS situation, it shows the largest SINR as well as the the largest EC. The influence of the center frequency can be observed best for the left wall, which is made of plasterboard (see Appendix A.5.2). At $f_c = 7$ GHz, the amplitude of the corresponding MPC is rather low and shows large variations, leading to a moderate SINR of 6.7 dB. At $f_c = 8$ GHz, the amplitude track is more constant, which leads to a considerably larger SINR of 10.8 dB. Since the left wall is a large potential reflector, it is important for multipath-assisted localization. The SINRs of the window on the upper side of the room¹⁸ show an even larger influence of the center frequency. Despite the slightly larger EC of the corresponding MPC at $f_c = 7$ GHz, the SINR rises from 2.2 dB to 6.5 dB at $f_c = 8$ GHz.

Such results can be used for a detailed analysis of relevant propagation effects in an environment. In the present example, the advantage of using a larger center frequency can be observed. In [T8], this analysis has been applied for the setup of a demonstration system for multipath-assisted tracking.

¹⁷ As explained in [T4], deterministic variations of $\alpha_{k,\ell}$ should be corrected, such as the dependence on the distance.

¹⁸ To be specific, the two right-most windows, which are modeled by the same VA.

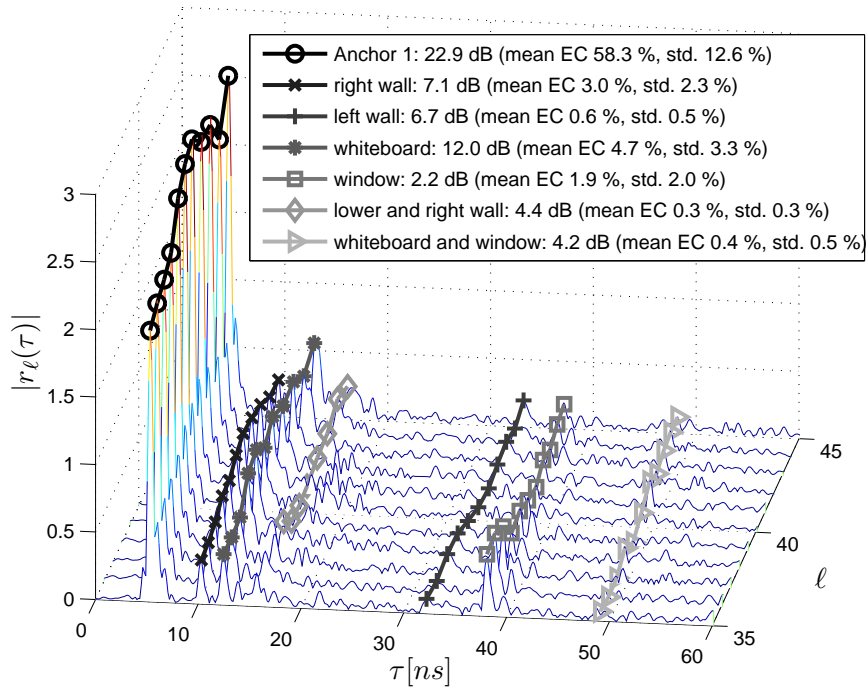
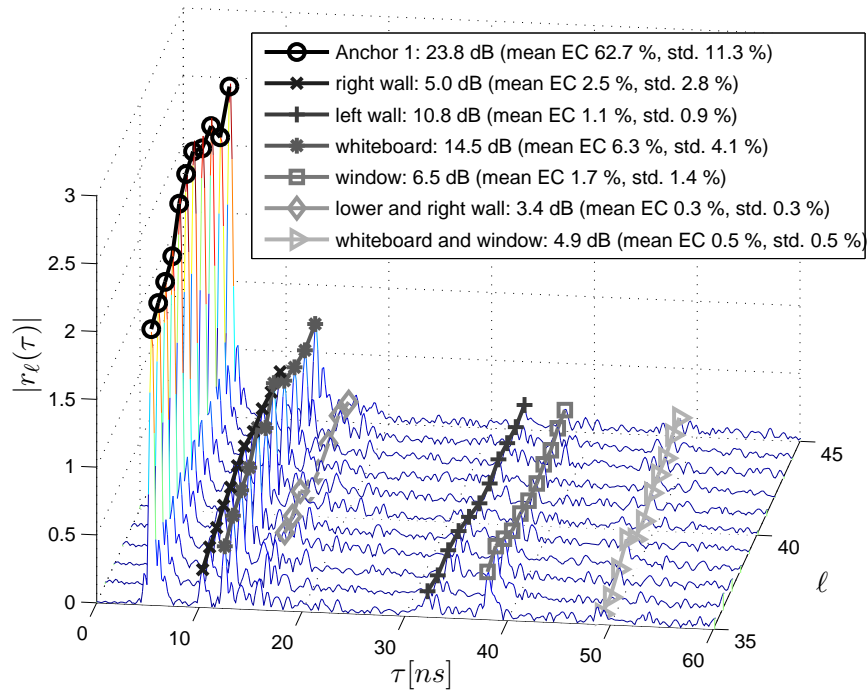
(a) $T_p = 0.5$ ns, $f_c = 7$ GHz(b) $T_p = 0.5$ ns, $f_c = 8$ GHz

Figure 4.1: Set of 11 signals (i.e. a subset of the 60 signals used for the SINR and EC estimation) measured in the Demonstration room in Graz (see Appendix A.5.2) using Anchor 1 and trajectory 1 and two different center frequencies. The legend shows the SINRs as well as the mean and standard deviation of the EC of selected deterministic MPCs estimated on 60 positions on the trajectory.

4.4 Chapter Conclusions and Results in Included Papers

This chapter and results in [T2] provide insights on the energy capture of VA-modeled, deterministic MPCs in UWB signals. Chapter 8 provides additional results for other scenarios. The following conclusion is made as the basis for following work.

- Deterministic MPCs resulting from specular reflections carry a **large part of the energy** of the received signal in all the scenarios where we have analyzed measurements. This motivates their use for positioning and justifies the use of local-maxima-based MPC estimation algorithms.

More importantly, this chapter and the according results in [T4, T7, T9] provide a link between the theoretical definition of position-related information in Chapter 3 and in [T3] and the multipath-assisted tracking algorithms in Chapter 5 and [T5, T8, T9]. Further exemplary values for SINRs can be found in [T4] for the scenario explained in Appendix A.4. For the scenarios in Appendix A.5.2 and A.5.3, SINR estimation results are included in [T8], showing that the estimation of the SINRs and the corresponding evaluation of the PEB (3.6) with (3.11) can be used to find e.g. the optimal frequency range for positioning in a given environment. Chapter 8 contains additional results.

- MPC SINRs as the signal-dependent part of **position-related information can be estimated** from a small set of training signals. Together with the known geometry, these values characterize the localization capabilities of an environment.
- The estimation method **avoids the need to estimate the PDP of the DM**, which would require closely-spaced measurements. At ultra-wide bandwidths, additional delay dispersion due to averaging over a larger region would possibly impair the estimation.
- The estimated SINRs can be used to **analyze and optimize the performance** of multipath-assisted positioning in a given environment. One possibility for optimization is the selection of a frequency band where the environment exhibits good reflection properties.

In other work related to the presented topics, the ray-tracing tool analyzed in [T7] has been presented in [80] and optimized in [88]. A geometric scatterer detection method from [83,84] has been applied using the VA model in [82]. Probability hypothesis density filters have been applied to the tracking of MPCs in [85]. Preliminary investigations on the combination of ray-tracing and stochastic propagation graphs have been presented in [89].

5

Algorithms for Multipath-Assisted Tracking

This chapter summarizes the multipath-assisted tracking algorithms that have been presented and analyzed in [T5, T6, T8, T9]. The focus is on the statistical models used for the motion dynamics and most importantly, the measurements, i.e. the MPC delays modeled by VAs.

This chapter is organized as follows: Section 5.1 introduces a general formulation of the problem in terms of motion- and measurement models. Tracking algorithms implementing these models as well as a possible data association approach are discussed in Section 5.2. Example results and conclusions are presented in Sections 5.3 and 5.4, respectively.

5.1 General Problem Formulation

As first work in [79],[T1] has shown, statistical measurement models, i.e. the likelihood function¹⁹, for multipath-assisted positioning are subject to multimodality. First of all this is due to the non-linear transformation of the range measurements to the position domain. Here, subsets of the circles according to the ranges w.r.t. multiple anchors may intersect in more than one point. Secondly, the DM considered in the signals acts as additional noise that allows the log-likelihood (3.10) to add up at wrong position hypotheses. Furthermore, for the approach followed in this thesis, the association of the range measurements to the VAs is not assumed to be known, causing an additional source of uncertainty.

Despite the fact that multiple modes may be present in the measurement model, for a sufficiently large observation time of a *moving* agent in the scenario, only the correct mode should stay persistent. This has been the main motivation to consider tracking algorithms in this thesis. Such algorithms operate on a sequence of measurements in alternating prediction and update phases [121–123]. In the former, the most likely prediction of the next *state* of the agent is calculated based on a physical model of the motion. In the latter, the current set of measurements is used to correct the prediction.

Probabilistic tracking (i.e. state-space-estimation) algorithms aim at computing the posterior probability density function (PDF) $p(\mathbf{x}_\ell | \mathbf{Z}_\ell)$ of the state using all previous measurement vectors $\mathbf{Z}_\ell = \{\mathbf{z}_i : i = 1, \dots, \ell\}$ [123]. We define the state of the agent at the ℓ -th position of its motion

¹⁹ See also [92] for a detailed discussion of the likelihood function.

trajectory²⁰ as

$$\mathbf{x}_\ell = [x_\ell, y_\ell, v_{x,\ell}, v_{y,\ell}]^T \quad (5.1)$$

i.e. containing the x - and y -coordinates and the velocity vector. Furthermore, we denote the predicted state space estimate as $\hat{\mathbf{x}}_\ell^-$ and the updated (posterior) estimate as $\hat{\mathbf{x}}_\ell^+$ ²¹.

Formally, the prediction step is expressed with the Chapman-Kolmogorov equation as

$$p(\mathbf{x}_\ell | \mathbf{Z}_{\ell-1}) = \int p(\mathbf{x}_\ell | \mathbf{x}_{\ell-1}) p(\mathbf{x}_{\ell-1} | \mathbf{Z}_{\ell-1}) d\mathbf{x}_{\ell-1} \quad (5.2)$$

With the current measurement \mathbf{z}_ℓ , the posterior PDF can be calculated using Bayes' theorem

$$p(\mathbf{x}_\ell | \mathbf{Z}_\ell) = \frac{p(\mathbf{z}_\ell | \mathbf{x}_\ell) p(\mathbf{x}_\ell | \mathbf{Z}_{\ell-1})}{\int p(\mathbf{z}_\ell | \mathbf{x}_\ell) p(\mathbf{x}_\ell | \mathbf{Z}_{\ell-1}) d\mathbf{x}_\ell}. \quad (5.3)$$

A Bayesian tracking algorithm is an implementation of (5.2) and (5.3). The components that are required are: (i) The *motion model* $p(\mathbf{x}_\ell | \mathbf{x}_{\ell-1})$ describing the statistical evolution of the agent's state. (ii) The *measurement model* (likelihood) $p(\mathbf{z}_\ell | \mathbf{x}_\ell)$ describing the probability of the current measurement given the state. (iii) Update rules that either solve or approximate the integrals.

5.1.1 Motion Model

The motion model describes the state dynamics and is needed in (5.2). Any knowledge of the agent's typical motion patterns can help to keep a state space estimation algorithm on track, even if unreliable measurements are available in the update step. There are numerous dynamic models that allow to integrate prior knowledge of the motion (or deviations from it, usually called maneuvers) into the tracking algorithm [124]. However, in this work we focus at the influence of the measurements, i.e. the range estimates to the VAs, on the tracking performance. Hence, we choose a simple linear Gaussian constant-velocity motion model

$$\begin{aligned} \mathbf{x}_{\ell+1} &= \mathbf{F}\mathbf{x}_\ell + \mathbf{G}\mathbf{n}_{a,\ell} \\ &= \begin{bmatrix} 1 & 0 & \Delta T & 0 \\ 0 & 1 & 0 & \Delta T \\ 0 & 0 & 1 & 0 \\ 0 & 0 & 0 & 1 \end{bmatrix} \mathbf{x}_\ell + \begin{bmatrix} \frac{\Delta T^2}{2} & 0 \\ 0 & \frac{\Delta T^2}{2} \\ \Delta T & 0 \\ 0 & \Delta T \end{bmatrix} \mathbf{n}_{a,\ell}, \end{aligned} \quad (5.4)$$

where ΔT denotes the update time. The driving acceleration noise term $\mathbf{n}_{a,\ell}$ is zero-mean and has a covariance matrix $\sigma_a^2 \mathbf{I}$. It models motion changes that deviate from the constant-velocity assumption. As in [T6], the process noise variance σ_a^2 is chosen based on selecting a maximum velocity in e.g. the x -direction $v_{x,\max}$. This defines the 3σ point of the noise in velocity domain. The corresponding variance in the acceleration domain is then $\sigma_a^2 = (v_{x,\max}/(3\Delta T))^2$.

5.1.2 Measurement Models

The measurement model describes the dependence of the current measurement on the state vector. In this thesis, measurements are estimates of the distances between the agent position

²⁰ As in [T6, T9] we use the general position index ℓ for tracking instead of a dedicated time index, as position can be mapped to time using the velocity.

²¹ To be specific, these are the point estimates computed from either the prior $p(\mathbf{x}_\ell | \mathbf{Z}_{\ell-1})$ or the posterior $p(\mathbf{x}_\ell | \mathbf{Z}_\ell)$.

\mathbf{p}_ℓ and the visible VAs. These distances can be estimated e.g. using (4.1) and are modeled as

$$\mathbf{z}_\ell = h(\mathbf{x}_\ell) + \mathbf{n}_{z,\ell} \quad (5.5)$$

$$= [\dots, \|\mathbf{a}_k - \mathbf{p}_\ell\|, \dots]^T + \mathbf{n}_{z,\ell}, \mathbf{a}_k \in \mathcal{A}_\ell. \quad (5.6)$$

The second line states the specific model for range estimates to the VAs in the current set of visible VAs \mathcal{A}_ℓ . The measurement noise $\mathbf{n}_{z,\ell}$ describes the *inaccuracy* [125] of the range estimates and is modeled as zero-mean Gaussian with a covariance matrix \mathbf{R}_ℓ .

However, since the entries of \mathbf{z}_ℓ are extracted from the signal $r_\ell(t)$ at the agent as in (4.1), there is no association of the range estimates to the VA positions as required in (5.5). This causes an additional *uncertainty*²² [125] in the mapping of the measurements to the features from the prior knowledge, requiring data association [126, 127].

In the first papers [79] and [T1] on this topic, we proposed a probabilistic model for the vector of range estimates that does *not* require data association. In this case, $\mathbf{z}_\ell = [z_{\ell,1}, \dots, z_{\ell,N_\ell}]^T$ with $N_\ell \geq |\mathcal{A}_\ell|$, i.e. it may have more entries than available VAs²³. The model reads

$$\begin{aligned} p(\mathbf{z}_\ell | \mathbf{x}_\ell) &= \prod_{i=1}^{N_\ell} p(z_{\ell,i} | \mathbf{x}_\ell) \\ &= \prod_{i=1}^{N_\ell} \frac{P_{\text{VA}}}{\sum_k^{|\mathcal{A}_\ell|} P_{V,k}} \sum_{k=1}^{|\mathcal{A}_\ell|} P_{V,k} \mathcal{N}(z_{\ell,i} | \|\mathbf{p}_\ell - \mathbf{a}_k\|, \sigma_k^2) + (1 - P_{\text{VA}}) p_{\overline{\text{VA}}}(z_{\ell,i} | \mathbf{x}_\ell). \end{aligned} \quad (5.7)$$

Hence, the range measurements are treated as independent, and each one follows a mixture distribution modeling its possible sources. P_{VA} denotes the probability that $z_{\ell,i}$ corresponds to a VA at all. If it does, its distribution is Gaussian with a certain range variance σ_k^2 . If it is a spurious measurement, i.e. not caused by a VA, its distribution is $p_{\overline{\text{VA}}}(z_{\ell,i} | \mathbf{x}_\ell)$. In [T1], this has been chosen as uniform between zero and a maximum range value. The visibility probability $P_{V,k}$ for the k -th VA accounts for the fact that a certain VA-modeled MPC might or might not be detected.

Plots of (5.7) are shown in [79] and [T1], illustrating the large degree of multimodality. A straightforward maximization w.r.t. \mathbf{p} thus results in a large percentage of outliers.

5.2 Tracking Algorithms

5.2.1 Tracking Algorithms without Data Association

The multimodality of (5.7) over \mathbf{p} as well as the fact that no deterministic measurement model $h(\mathbf{x}_\ell)$ exists, renders the application of standard tracking algorithms such as a Kalman filter (KF) impossible when directly using the range estimates as measurement inputs.

Position Estimate as Measurement Input

In [T1], two tracking filters have been proposed that work with a position estimate as the measurements input. This position estimate is the maximum-likelihood estimate according to (5.7) which has been shown to follow a heavy-tailed distribution, such as a Cauchy distribution, truncated at the room boundaries.

²² As we do not aim at quantifying this effect, we use the term uncertainty also for measurement inaccuracies.

²³ Note that only rectangular rooms have been used in [79] and [T1], making all VAs visible throughout the entire room, i.e. $\mathcal{A}_\ell = \mathcal{A}$.

- *KF with measurement refinement*: Assuming that the previous posterior state estimate was close to the true position, we modify the ML position estimate to a maximum a-posteriori (MAP) estimate. This is done by multiplying (5.7) with a Gaussian distribution centered at the predicted position of the KF before maximization. Then, the standard KF update equations are performed.
- *Gaussian Sum Filter – Initialization*: For initialization of the above mentioned filter, a Gaussian Sum Filter (GSF) [128] has been presented. It represents the posterior distribution of the position as a Gaussian mixture model (GMM) and contains update rules for the weights of the components. With this, multiple Gaussian position hypotheses can be placed inside the room (e.g. at the room doors). Gaussian components whose weights drop below a certain threshold are pruned from the model.
- *Particle filter (PF) with Cauchy error model*: To find out the performance limits that tracking using the ML position estimates from (5.7) can yield, we employed a sampling-importance-resampling (SIR) PF [122, 123] using a truncated isotropic bivariate Cauchy distribution [129–131] centered at the ML estimate as particle weights.

Range Estimates as Measurement Input

The range estimates can be used directly as measurement inputs in a SIR-PF by calculating the particle weights according to (5.7). As for the PF using the ML position estimate, the median of the particles in x - and y -dimension is chosen as the final estimate of \mathbf{p}_ℓ .

5.2.2 Tracking Algorithms with Data Association

In Chapter 2, a hybrid geometric-stochastic channel model (GSCM) has been discussed as the basis for multipath-assisted positioning. In [T1], this has not been considered. Performance evaluations have been performed based on simulated delays generated according to the model in (5.7). However, in order to take into account the effects responsible for these estimated delay tracks and to work with measured signals, a tracking algorithm has to include the channel estimation step and work directly with the signal $r_\ell(t)$ at the agent.

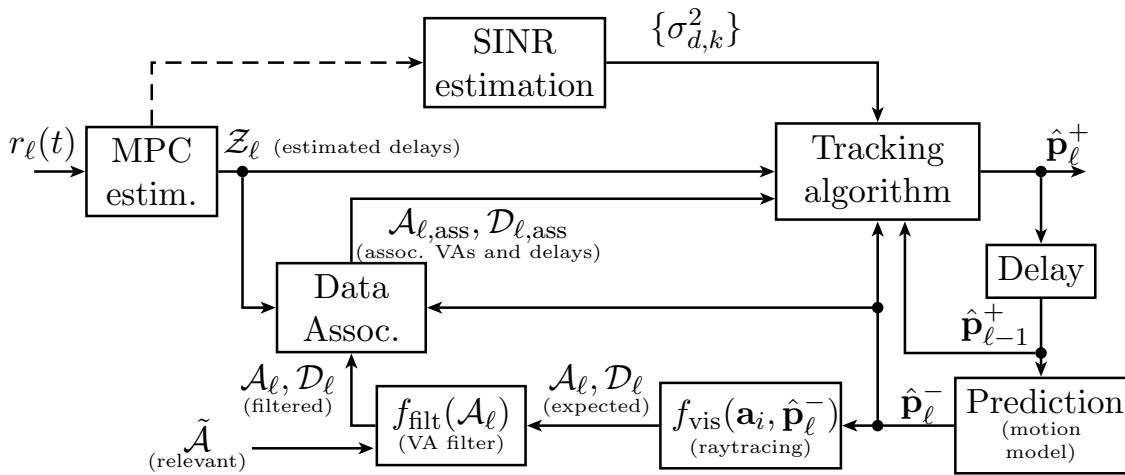


Figure 5.1: Block diagram of tracking and data association scheme using MPC range estimates.

Fig. 5.1 shows an overview of the multipath-assisted tracking concept, of which a first version was presented in [T5]. A performance analysis was performed in [T6] and the full concept

shown in Fig. 5.1 has been developed in [T9]. The tracking algorithm is an Extended Kalman Filter (EKF) that uses a linearization of (5.6) as measurement equation. At the ℓ -th position, the set²⁴ of MPC delays \mathcal{Z}_ℓ is estimated using (4.1). The expected sets of visible VAs \mathcal{A}_ℓ and the corresponding expected delays \mathcal{D}_ℓ are computed²⁵ using (2.14) and (2.15) at the predicted position $\hat{\mathbf{p}}_\ell^-$ that is obtained with (5.4). The expected VAs are matched to the estimated delays from the signal using data association, as discussed in the next subsection. If information about relevant VAs in a scenario is available, the VAs can be filtered accordingly. The tracking algorithm can further benefit from channel information, i.e. it can weight the measurements according to their uncertainties. These can be obtained using the SINR estimation described in Section 4.2 and (3.14).

Data Association

As \mathcal{D}_ℓ and \mathcal{Z}_ℓ are sets of usually different cardinalities, i.e. $|\mathcal{Z}_\ell| = \hat{K}_\ell \neq |\mathcal{D}_\ell| = K_\ell$, no conventional distance measure is defined and therefore there is no straightforward way of an association. Inspired by our work on multi-target tracking in [85, 94], we employ a well-known multi-target miss-distance, the *optimal sub-pattern assignment* (OSPA) metric [132]. For $\hat{K}_\ell \geq K_\ell$, which can be ensured by filling up \mathcal{Z}_ℓ with dummy clutter, it is defined as

$$d_{\text{OSPA}}(\mathcal{D}_\ell, \mathcal{Z}_\ell) = \left[\frac{1}{\hat{K}_\ell} \left(\min_{\pi \in \Pi_{\hat{K}_\ell}} \sum_{i=1}^{K_\ell} \left[d^{(d_c)}(d_{\ell,i}, z_{\ell,\pi_i}) \right]^p + d_c^p (\hat{K}_\ell - K_\ell) \right) \right]^{1/p} \quad (5.8)$$

where Π_N is defined as the set of permutations of positive integers up to N . The function $d^{(d_c)}(x, y) = \min(d_c, d(x, y))$, i.e. an arbitrary distance metric $d(\cdot)$ that is cut off at a $d_c > 0$, the so-called *cut-off distance*, which is a design parameter. The metric order is denoted as p . The first sum in the metric is the cumulative distance over the optimal sub-pattern assignment of \mathcal{Z}_ℓ to \mathcal{D}_ℓ , i.e. where K_ℓ entries of \mathcal{Z}_ℓ are assigned optimally to the entries of \mathcal{D}_ℓ . The Hungarian or Munkres algorithm can be used for this assignment [132, 133]. For the remaining $\hat{K}_\ell - K_\ell$ entries of \mathcal{Z}_ℓ , d_c is assigned as penalty distance.

With the OSPA distance, the quality of extracted MPC parameters can be evaluated [T5]. For performing the DA, we introduce a set \mathcal{C}_ℓ of correspondence variables [134], whose i -th entry $c_{\ell,i}$ is defined as

$$c_{\ell,i} = \begin{cases} k, & \text{if } z_{\ell,i} \text{ corresponds to VA } \mathbf{a}_k \\ 0, & \text{if } z_{\ell,i} \text{ corresponds to clutter.} \end{cases} \quad (5.9)$$

The optimal sub-pattern assignment between \mathcal{D}_ℓ and \mathcal{Z}_ℓ is reflected by the first part of (5.8)

$$\boldsymbol{\pi}_{\text{opt}} = \arg \min_{\pi \in \Pi_{\hat{K}_\ell}} \sum_{i=1}^{K_\ell} d^{(d_c)}(d_{\ell,i}, z_{\ell,\pi_i})^p. \quad (5.10)$$

The first K_ℓ entries of $\boldsymbol{\pi}_{\text{opt}}$ contain the indices of those entries of \mathcal{Z}_ℓ that have been optimally assigned to \mathcal{D}_ℓ . For some entries of \mathcal{D}_ℓ , we will probably have $d^{(d_c)}(d_{\ell,i}, z_{\ell,\pi_{\text{opt},i}}) = d_c$, i.e. this expected distance has an assigned measurement, but the difference between measurement and expected distance is larger or equal than the cutoff distance. We expect that by using UWB signals, the estimated path delays will be quite accurate, provided that they are detected. Hence, we select a certain d_c that may depend on the bandwidth and reject the corresponding

²⁴ Sets are used as the MPC estimation results in unordered and unassociated delays, of which the number can be different for each ℓ .

²⁵ Note that sets $\mathcal{Z}_\ell^{(j)}$, $\mathcal{A}_\ell^{(j)}$, $\mathcal{D}_\ell^{(j)}$ exist for each of the J anchors that are used. Nevertheless, we drop the anchor index here, since signals $r_\ell^{(j)}(t)$ from different anchors are independent and the DA can be done separately.

assignments as outliers²⁶. Formally, the DA is expressed by setting the correspondence variables as

$$c_{\ell,i} = \begin{cases} k, & \text{if } [\boldsymbol{\pi}_{\text{opt}}]_k = i \text{ and } d^{(d_c)}(d_{\ell,k}, z_{\ell,i}) < d_c \\ 0, & \text{else,} \end{cases} \quad (5.11)$$

where $[\boldsymbol{\pi}_{\text{opt}}]_k$ denotes the k -th entry of the optimal sub-pattern assignment. Due to its origin in the OPSA distance metric, we refer to this DA approach as *constrained optimal sub-pattern assignment*.

Tracking and Measurement Noise Model

Re-introducing the anchor index, the DA procedure results in sets of associated VAs and corresponding delays. These sets are passed to the EKF after joining information from each anchor as

$$\mathcal{A}_{\ell,\text{ass}} = \bigcup_{j=1}^J \mathcal{A}_{\ell,\text{ass}}^{(j)} \quad \text{and} \quad \mathcal{D}_{\ell,\text{ass}} = \bigcup_{j=1}^J \mathcal{D}_{\ell,\text{ass}}^{(j)}. \quad (5.12)$$

The tracking scheme using an EKF and the DA (abbreviated as EKF-DA) as described above has been evaluated in [T5]. For performance evaluation, a version with genie-aided DA (EKF-GADA) has also been proposed, where the DA makes use of the *true* instead of the predicted position. The EKF requires choosing a value for the cutoff distance d_c , which can be based on the bandwidth [T6]. As for every tracking filter, also the measurement noise has to be characterized, in this case the covariance matrix \mathbf{R}_{ℓ} for the noise vector $\mathbf{n}_{z,\ell}$ in (5.5). In [T5, T6], this has also been done based on the bandwidth and the expected ranging uncertainty, i.e. $\mathbf{R}_{\ell} = \sigma_d^2 \mathbf{I}_{|\mathcal{A}_{\ell,\text{ass}}|}$. While this works [T6], it is not optimal, as it does not perform a weighting of the MPC according to their individual uncertainties (3.14)²⁷ and it requires manual tuning of σ_d^2 . Weighting the ranges according to their variance is often proposed [34, 136], but in implementations, heuristic weights are used instead of the unknown, true variances.

Using the channel estimation methods discussed in [T4] and Chapter 4, we applied a weighting w.r.t the estimated ranging variances in [T9]. This is done by using the a-priori estimates of the range estimation uncertainties as the measurement covariance matrix

$$\mathbf{R}_{\ell} = \text{diag} \left\{ \text{var} \left\{ \hat{d}_{k,\ell}^{(j)} \right\} \right\} \quad \forall k, j : \mathbf{a}_k^{(j)} \in \mathcal{A}_{\ell,\text{ass}}. \quad (5.13)$$

These uncertainties can be obtained using the SINR estimates (4.8) and (3.14). In Fig. 5.1, this is indicated by the topmost block that links the channel estimation and the tracking algorithm. The dashed line can be understood in two ways: First, this step of acquiring channel information for the tracking is optional (it was not used in [T5, T6]). Second, in the current implementation of this tracking scheme, it is not implemented based on the received signal during the tracking, but on multiple pre-measured training signals²⁸.

It is important to note that by selecting the range uncertainties using equality in (3.14), we imply that the MPC delays are estimated efficiently, i.e. using an estimator that actually attains the CRLB. The ML estimator is known to be asymptotically efficient [108]. Due to the fact that DM is neglected, (4.1) is only an approximation of the ML estimator (see e.g. [73, 74]), thus we

²⁶ This can be compared to validation gating [135], in which measurements are subject to a statistical test.

²⁷ See also Fig. 5 in [T4] for a comparison of covariance ellipses of the EKF compared to the estimated CRLB that accounts for the weighting.

²⁸ In current work, we extend the EKF-DA tracking to include the VA positions as well as the range uncertainties. This allows to account for changes in the environment and does not require training measurements. First results were presented in [95].

expect a performance penalty.

Fig. 5.1 also shows a block $f_{\text{filt}}(\mathcal{A}_\ell)$. This accounts for the fact that additional prior knowledge in terms of the *relevant* VAs $\tilde{\mathcal{A}}$ may be available, resulting in $f_{\text{filt}}(\mathcal{A}_\ell) = \mathcal{A}_\ell \cap \tilde{\mathcal{A}}$. In [T9], $\tilde{\mathcal{A}}$ has been chosen as the set of VAs for which range estimation uncertainties are available. This provides two main advantages: First, while many *potential* VAs may be computed from a given building layout (see Section 2.2), only a small subset of them might provide reliable position-related information, which is accounted for by filtering the VAs. Second, it helps in the DA procedure, as less candidate VAs will be associated to clutter delay estimates. Of course it will also make the DA procedure considerably faster.

5.3 Example Results

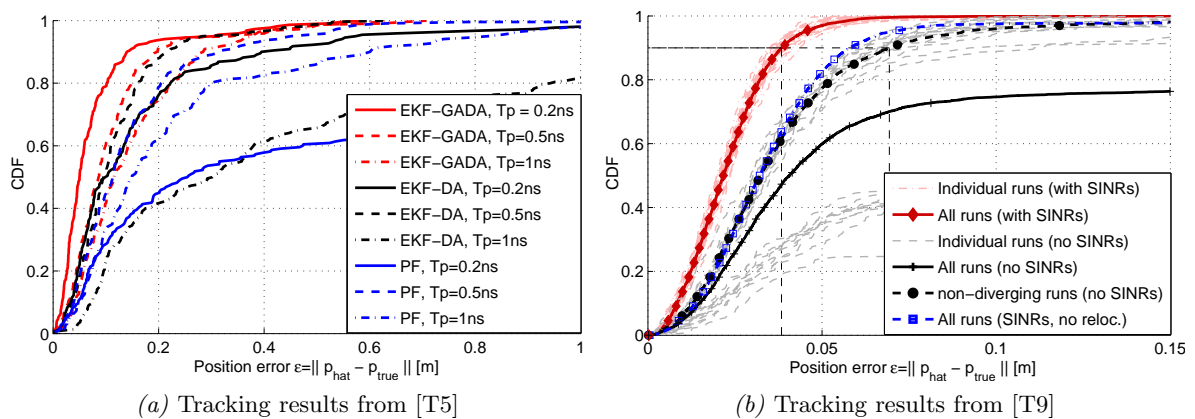


Figure 5.2: CDFs of the position error for different multipath-assisted tracking algorithms presented in this chapter. Results in (a) are from [T5] and use the corridor scenario explained in Appendix A.4. Only a single anchor is used, employing different bandwidths and the EKF-based and PF tracking methods. For (b), the results in [T9] are used, which were obtained in the seminarroom scenario explained in Appendix A.5.1 using two anchors and the EKF-DA method with and without estimated range uncertainties.

In Fig. 5.2a, tracking results from [T5] are presented. In the large-scale corridor scenario explained in Appendix A.4, the EKF-DA (black lines) and the EKF-GADA (red lines) discussed in Section 5.2.2 are applied for different pulse durations $T_p \in \{0.2 \text{ ns}, 0.5 \text{ ns}, 1 \text{ ns}\}$. Also, results for the PF with unassociated range estimates (blue lines) as discussed in Section 5.2.1 are included. Only the single anchor at $\mathbf{a}_1^{(3)}$ is used with VAs up to order 2, and the first 220 positions of the trajectory. This approximately corresponds to the right half of Fig. A.4. For the range uncertainties, a constant value is used for all VAs as in [T5, T6]. At $T_p = 0.5 \text{ ns}$, the EKF-DA approaches the performance of the EKF-GADA with 90% of the estimates within 22 cm. While the EKF-GADA shows the potential advantage of a large signal bandwidth, the EKF-DA cannot reach this performance. For the largest bandwidth ($T_p = 0.2 \text{ ns}$), the DA procedure is tricky, since often the diffuse tails of deterministic MPCs are resolved, leading to erroneous range estimates close to the true ones. This can easily lead to wrong associations. At the lowest bandwidth ($T_p = 1 \text{ ns}$), path overlap makes more and more MPCs unusable with this method. Results in [T6] in this scenario show that if more anchors are used, robust tracking using the EKF-DA is still possible even at $T_p = 4 \text{ ns}$. The PF shows the same general trend with the bandwidth. Here, MPCs corresponding to diffuse tails lead to erroneous modes in the multimodal likelihood function (5.7), which are in the vicinity of the true mode and thus can lead to tracking errors.

Fig. 5.2b shows tracking results from [T9]. Here, the seminarroom scenario explained in Appendix A.5.1 is used with two anchors, trajectory 2, VAs up to order two and the time-domain measurements with $T_p = 0.5$ ns. As Fig. A.6 shows, this allows for 25 parallel trajectories of 220 points each that are used for tracking. The gray dashed lines show the performance of the EKF-DA for the 25 individual runs if the range uncertainties are selected as constant for all VAs²⁹, i.e. such as for Fig. 5.2a. In this case, 10 of 25 runs diverge, mostly in the NLOS region w.r.t. $\mathbf{a}_1^{(1)}$ behind the concrete pillar. For the 15 non-diverging runs, on average 90% of the estimates have an error of less than 7 cm, indicated by the bold black dashed line with circle markers. The red dashed lines indicate the performance if the measurement covariance matrix of the EKF is chosen according to (5.13), i.e. with range uncertainties estimated according to Section 4.2.1 and (3.14). Here, all 25 runs achieve similar, excellent performance, i.e. 90% of the estimates have an error of less than 4 cm. The blue dashed line with square markers shows the overall performance with estimated range uncertainties, but without the optimized VA positions using (4.7). It can be observed that the awareness to the range uncertainties provides the robustness while the optimized VA positions further improve the accuracy.

5.4 Chapter Conclusions and Results in Included Papers

The algorithms and results in our first papers [79] and [T1] give rise to the following conclusions.

- Tracking exploiting range **information from MPCs** is possible, even using algorithms that do not require data association or work with intermediate position estimates that show a large percentage of outliers.
- However, the **validity of the models** that have been used for the MPC delays is unclear, as they are not related to realistic channel models.

In [T5], the tracking scheme with OSPA-based DA and an EKF are presented, showing results for single-anchor tracking and measured signals. Besides being a proof-of-concept for multipath-assisted tracking, it also includes results for the PF presented in [T1] that does not require DA. It is shown that especially the distribution of the DM in the delay domain is problematic for the PF, as it assumes a uniform distribution. Clutter delay estimates from diffuse tails of deterministic MPCs lead to estimation errors that are due to spurious modes of the likelihood function in the vicinity of the correct mode. The tracking algorithms presented in [T5, T6, T9] work with the signal at the agent and include the channel estimation.

In [T6], the presented tracking scheme using EKF and DA has been compared to conventional EKF tracking schemes that only make use of the LOS component. An NLOS situation has been generated using the same measurements as in [T5], by artificially placing an obstruction in the environment and modifying the signals in a spatially consistent way, i.e. decreasing the SINR of the LOS component by 10 dB, but also all SINRs of reflected MPCs influenced by the obstruction.

The above mentioned investigations allow for important conclusions based on propagation conditions in real environments, which is vital for the use of multipath in positioning.

- Using suitable data association, **single anchor tracking** is possible at centimeter level accuracy [T5]. The only tuning parameter introduced in addition to conventional tracking algorithms is the cut-off distance. It can be selected intuitively based on the expected maximum range uncertainty of the MPCs and allows to reject outliers.

²⁹ In this case, the constant range variance is selected as the mean of all the estimated ones. Although this value is not available when SINRs are not estimated, it facilitates the comparability. Also, it represents a best case, since this value has often shown the best performance in the case that SINRs are not available.

- Data association based on **constrained optimal sub-pattern assignment** [T5] works well using the geometric VA model introduced in Chapter 2 as long as the tracking filter is approximately on track. Suitable divergence detection and initialization schemes are subject of current research.
- The performance evaluation in [T6] has shown the **robustness benefit** compared to conventional tracking. In an artificial NLOS situation based on measurements, VA-modeled MPCs provide significant position information in NLOS regions.
- With **awareness to the uncertainty** of the range estimates to the VAs as described in Chapter 4 and [T4, T9], an accuracy of a few centimeters can be achieved with almost no outliers, i.e. at a high level of robustness. These results can be reproduced with the developed **live demonstration system** [T8] in different environments.
- The estimation of the range uncertainties for the tracking measurement noise model allows to **prune the large set of potential VAs to the relevant ones**. Also, a considerably smaller cutoff distance can be chosen. This leads to a reduced number of erroneous data associations.
- Interestingly, a **single value is enough for the uncertainty** of the range information of each MPC for the whole environment to reach performance results close to the according CRLB. This gives rise to the conclusion that the relative importance of deterministic MPCs may be modeled globally. As this conclusion is based on specific measurement results in example environments³⁰, its validity needs to be addressed using properly derived, general channel models.

³⁰ However, consistent results are obtained in all of the investigated environments.

6

Conclusions and Outlook

6.1 Conclusions

The chapter conclusions have stated the more specific research findings of the individual papers included in this thesis. This final section of the thesis overview provides general conclusions that help to put these findings in a more global context.

This thesis provides a *proof-of-concept of multipath-assisted positioning and tracking*. At the starting point of the performed research, it was not clear if the known geometric structure of the multipath channel can be exploited for positioning. By the use of floor plan knowledge and ultra-wideband signals, it has been shown that this is indeed possible and provides excellent robustness and accuracy, if an *awareness to propagation conditions* of the deterministic MPCs is available. Using a geometric-stochastic framework for a proper modeling of relevant propagation phenomena, the principal research question stated in Sec. 1.2.2 has been answered:

The geometric information embedded in reflected multipath components *can* be exploited for positioning. Statistical bounds on the position error allow for the quantification of the *relevance of the position-related information* of a multipath component. This relevance can be estimated from signals and used as a reliability metric for the range information of the respective component, allowing for an optimal weighting of its contribution.

The characterization of the position-relevance of MPCs in a wireless signal is at the heart of this thesis. For this, a signal-to-interference-and-noise-ratio (SINR) for deterministic MPCs has been defined as the ratio of its energy to the combined power of measurement noise and diffuse multipath. This SINR is not only important for the presented application of multipath-assisted positioning, but also for proper indoor channel models in general. A channel model can be made both *spatially consistent* using the simple geometric modeling and *realistic* in terms of a proper representation of non-resolvable, statistically modeled components.

The presented algorithms for multipath-assisted tracking allow for robust position estimation at low complexity if uncertainty information of the MPCs is taken into account. Our observations with the live-demonstration system in different environments consistently led to similar results. Based on this, we conclude that accurate measurement noise models are the key component of robust positioning and tracking systems. The results especially highlight the importance of a proper model for diffuse, not deterministically modeled multipath.

6.2 Ongoing and Future Work

The proof-of-concept implementation still operates under controlled conditions. While it shows the general applicability, still important research questions are open. Considering the practical use of the system, it is not clear how different antenna orientations or carrying the agent device on or near to the body will influence the performance. This needs to be approached in controlled conditions considering individual MPCs as well as considering the overall positioning performance.

The MPC SINRs, which are the key enabler for the accurate and robust performance, have been estimated using pre-recorded measurements. While performing this procedure is possible when installing such a system in an environment, it is of course more convenient to let the tracking system learn the MPC parameters during the tracking phase. For such an online scheme, first results are available, showing that the performance of the offline approach can be reproduced. The online estimation has the additional benefit of being able to adapt to changes in the environment, since also the VA positions themselves can be added to the state vector. Also, the detection of new features in the environment such as in simultaneous localization and mapping are important possible extensions of the concept. In this regard, it is important to answer the question of the required level of accuracy of the floor plan information.

After first results have been obtained using simulated MPC parameters, this thesis followed an experimental approach, since the question that the author was most often asked in the beginning was: “Do you think this works with real signals?” Since any positioning system needs to estimate location-dependent features from observations of physical processes, evaluating the performance with realistic signals is vital. Further research is needed on channel models that can reproduce the geometric structure of MPCs as well as the important role of DM. The vision is a channel model allowing for realistic signals for performance evaluation that can be calibrated to an environment using only a few, ideally only coarsely localized measurements. Due to our work on channel modeling tools such as ray-tracing or stochastic propagation graphs (not contained in this thesis), we believe that properly parametrized geometric-stochastic models are the most promising approach.

The positioning problem itself needs to be addressed, i.e. the global solution for multipath-assisted localization without prior information on the position, such as in tracking. Results are already published for Bayesian estimation algorithms based on the likelihood function used to derive the CRLB. But also in this regard, low complexity schemes are of interest that allow for a consideration of uncertainty models for the MPCs. Such methods can be used to rapidly initialize the tracking algorithms e.g. when divergence from the true trajectory occurs. The detection of such situations is also important. Standard tools for consistency or convergence checks for Kalman filters did not perform well in our experiments, which may be due to symmetries and ambiguities that allow for many positions to match to a given pattern of non associated multipath delays.

Finally, a relatively simple energy-based channel estimation algorithm has been used to estimate MPC delays and amplitudes in this thesis. The responsibility of taking into account the DM properly has been shifted to the data association and the noise model of the tracking filter. In this regard, we think that considerable gains are possible by Bayesian channel estimation strategies that also allow for a tracking of the channel model parameters themselves. Cognitive processing may be a key factor here, as it explicitly considers an information flow and an interplay of the measurement and the estimation procedures. Above this, global models can be updated to reflect the current state of knowledge of the environment.

Part II

Additional Results and Discussions

7

Additional Discussions

This chapter contains additional discussions about the radio channel that are important for this thesis. Section 7.1 deals with propagation effects that are relevant for positioning. Section 7.2 contains a discussion of power delay profiles for channel characterization. Section 7.3 gives an overview of related channel models from the literature, while Section 7.4 briefly concludes the chapter.

7.1 Overview over Propagation Mechanisms

As discussed in Section 1.1.1, localization methods infer the position of an agent by the use of position-related parameters in the respective signals [4, 17]. Hence, we briefly review the most prominent propagation effects in a radio channel and their position dependence.

Reflection, Transmission and Diffraction

A homogeneous plane wave incident on a sufficiently smooth and large (compared to the wavelength) surface results in a *specular reflection* [100]. This is the electromagnetic interaction whose resulting deterministic propagation path carries the most easily accessible position-related information, i.e. the AoA and, most importantly, the ToA of the corresponding MPC. Besides the reflection, a part of the signal energy is also transmitted through the medium via refraction, quantified by the respective reflection- and transmission coefficients. As the reflecting surfaces have a finite extent, also diffraction will occur at the surface boundaries, which can be described by a diffraction coefficient.

For *broadband* signals, specifically any signal that is used in this thesis, the complication arises that electrical properties like the dielectric constant and the conductivity change significantly over the bandwidth of interest [137, 138]. This frequency dependence of the interaction causes a dispersion of the signal in the delay domain, i.e. a deviation from the pure specular reflection, which has to be accounted for in the respective channel model (see Section 2.1).

Ray-tracing is a popular method for the simulation of wireless propagation channels. Geometric optical principles are used to find possible propagation paths in some environment, whose propagation-relevant features have to be known a-priori. Once those paths are determined, Maxwell's equations (or suitable approximations) can be solved to determine the electromagnetic field for specific positions. The frequency dependence makes the simulation difficult if

ultra-wideband signals are desired. This can be accounted for by sub-band divided ray tracing methods [80], in which the electrical properties of the interacting objects have to be known over the desired frequency band. Another option is to calibrate these properties using measurement data in some environment [88]. The latter method can lead to more realistic signals than conventional methods [T7], but no insight is given on the obtained signal parameters.

Due to these considerations, we chose to use only the geometric quantities describing specular reflections in this work, i.e. AoA and ToA. These can be conveniently computed using optical ray-tracing as explained in Section 2.2. Diffraction would in principle lead to larger areas of visibility for MPCs (e.g. diffraction of the LOS component around a corner), but since this is extremely site-specific and difficult to describe, we omit to model this effect. Transmission and other losses in terms of signal power due to interactions are accounted for indirectly. This means that path amplitudes are not computed directly, but their statistics are estimated to account for the *reliability* of different reflections (see Chapter 4 and [T4, T9]).

Diffuse Scattering

Most surfaces are not perfectly smooth w.r.t. their reflection characteristics. The resulting phenomenon is generally called *diffuse scattering*. Using geometric optics terms again, a ray incident on a surface causes multiple emerging rays. Only one of these rays represents the specular reflection, where incident and emergent angles are equal. The “newly generated” rays are *scattered* in different directions. Actually computing all scattered components is impossible, since, this would require accurate knowledge of the surface including possibly sub-surface structures at every point, not to mention complexity. A possible simulation method based on ray-tracing is dividing the surface in tiles, whose sizes depend on the wavelength. For each tile, a number of scattered paths are generated with random phases, weighted by a scattering pattern [80]. In a completely different method, propagation graphs are used to model interactions between scatterers [139]. Loops in these graphs lead to recursive structures that can nicely model diffuse contributions.

Both of these methods to generate diffuse components result in large numbers of often unresolvable MPCs³¹. Hence, diffuse scattering is also known as dense multipath [73] or diffuse multipath (DM) [T3] and modeled using a *power delay profile* (PDP), which describes the distribution of the DM power in the delay domain (see Section 2.1.2 and Fig. 2 in [T3]). In the ray-tracing literature, the specular paths are often called the *coherent*, and the diffuse scattered paths the *incoherent* part of the channel [140]. This terminology nicely suggests to consider the diffuse scattered components as unresolvable, *interfering*³² part of the channel.

Pathloss and Received Power

The received power at a distance d from the transmitter can be written as a function of the transmitted power P_{TX} [100]

$$P_{\text{RX}}(d) = P_{\text{TX}} G_{\text{RX}} G_{\text{TX}} \left(\frac{\lambda}{4\pi d} \right)^n \quad (7.1)$$

where G_{RX} and G_{TX} are the average antenna gains of receiver and transmitter in the corresponding directions and the last term is usually called the path loss. The form of (7.1) with $n = 2$ is generally known as the Friis’ equation, describing the received power in free space. In the presence of multipath, the path loss exponent n may be considerably greater but also less than two, strongly depending on the specific environment. For positioning, the relation (7.1) can

³¹ Resolvability of course depends on the measurement bandwidth. Nevertheless, we assume that diffuse components are not resolvable even at ultra-wide bandwidths.

³² “Interfering” in terms of representing additional noise to the deterministic MPCs caused by specular reflections.

be used in two ways. The first option is to use a suitable approximation of (7.1) for ranging, e.g. neglecting the antenna gains [16]. This approach suffers from the fact that the received power is a function of many propagation effects and as such it is highly dynamic, which in general leads to position errors on meter level with a large variance [141].

The second option is fingerprinting. The received signal strength (RSS) values w.r.t. to multiple transmitters are measured and compared with a prerecorded database using probabilistic methods. This requires a training phase and still suffers from low accuracy. Also, it shares the common drawback of fingerprinting methods, i.e. changes in the environment lead to a potential loss of the usefulness of the recorded fingerprints.

In this work, path loss is only used in [T4, T9] to correct relatively small deterministic distance dependencies of path amplitudes and in computational evaluations of performance bounds like in [T3, T8] for the generation of path amplitudes. In the latter case, the Friis equation is used for the LOS component. An additional loss factor of e.g. 3 dB per interaction order has been assigned to deterministic MPCs as a simple model that does not account for wall materials.

7.2 Discussion of Power Delay Profiles

To evaluate the *average* behavior of the channel in an area around a center position $\mathbf{p}_{\bar{\ell}}$, averaged over the small scale fading, the PDP is defined using the local CIRs $h_{\ell}(\tau)$ as [15, 100, 105, 142]

$$S_{h, \bar{\ell}}(\tau_{e, \ell}) = \mathbb{E}_{\mathbf{p}_{\ell}} \{h_{\ell}(\tau + \tau_{1, \ell})h_{\ell}^*(\tau + \tau_{1, \ell})\} \quad (7.2)$$

$$\approx \frac{1}{L} \sum_{\ell \in \mathcal{P}_{\bar{\ell}}} h_{\ell}(\tau + \tau_{1, \ell})h_{\ell}^*(\tau + \tau_{1, \ell}), \quad (7.3)$$

i.e. an ensemble average over the CIR. Note that the PDP is defined over the *excess delay* $\tau_{e, \ell} = \tau + \tau_{1, \ell}$, i.e. the delay w.r.t. the LOS component at \mathbf{p}_{ℓ} , whose delay is denoted as $\tau_{1, \ell}$. An important consideration is the region over which averaging is performed in practice. This region is defined as the set of position indices $\mathcal{P}_{\bar{\ell}}$ around a center point $\mathbf{p}_{\bar{\ell}}$ in (7.3). As discussed in [143], the spatial separation $\Delta d = \|\mathbf{p}_{\ell} - \mathbf{p}_{\ell'}\|$ with $\ell, \ell' \in \mathcal{P}_{\bar{\ell}}$ between points should be larger than the wavelength c/f_c to allow for uncorrelated samples, but smaller than c/B to prevent MPCs from changing delay bins. For UWB-REL signals (see Section 1.1.1), these two conditions get close to each other. A meaningful PDP can only be obtained in a very limited spatial region. If $\Delta d > c/B$, additional delay dispersion will result from the averaging, since energy of a certain MPC is spread over multiple delay bins.

Channel models and their characterizations differ in the deterministic or random definition of their parameters. This has consequences on the PDP estimation in terms of the averaging process in (7.2). In this thesis, floor plan knowledge is used to model the parameters of the specular reflections of the signal as deterministic. Therefore, the relevant part of the channel for averaging to obtain a PDP is the DM as in (2.2). The corresponding PDP $S_{h, \bar{\ell}}(\tau_{e, \ell})$ can be estimated by removing all deterministic MPCs from signals in a spatial region and average the obtained signals as in (7.3). This procedure is explained in Section 4.1.1.

Fig. 7.1 shows PDPs of signals at different bandwidths (2 GHz and 500 MHz³³ at a center frequency of $f_c = 7$ GHz) at three positions in an indoor scenario together with several PDP estimates (see Section 4.1.1). The blue lines show the PDP according to (7.3), i.e. using the filtered CIRs. For the black lines, the VA-modeled MPCs have been removed, while for the gray dashed lines, the 20 strongest MPCs are taken into account, i.e. black and gray lines correspond to different estimates of the PDP of the DM.

At the center frequency of $f_c = 7$ GHz, the larger bandwidth corresponds to the UWB-REL case while the lower bandwidth can only be classified as UWB-ABS. While the carrier wavelength

³³ Obtained using filtering with a raised-cosine pulse with $T_p = 0.5$ ns and $T_b = 2$ ns, see Appendix A.3.

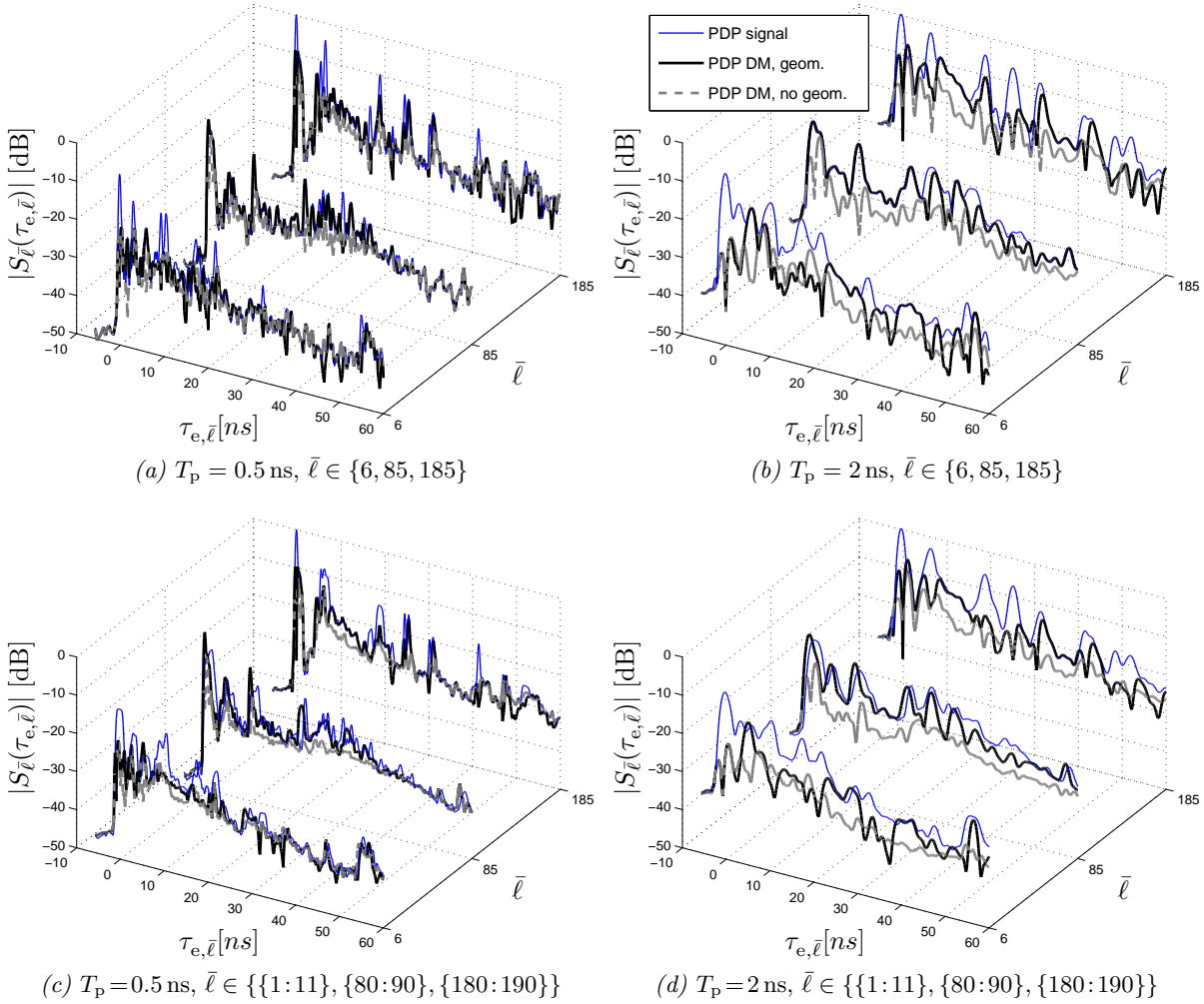


Figure 7.1: PDPs of the received signals (blue lines) and estimates of the diffuse multipath (for the black lines, the VA is used to model the deterministic MPCs, for the gray dashed lines, the 20 strongest MPCs are taken into account). Different bandwidths around $f_c = 7$ GHz are used in the seminar-room scenario (c.f. Section A.5.1 and Fig. A.6). Anchor 1 and three center positions $\bar{\ell} \in \{6, 85, 185\}$ of trajectory 2 are used. For (a) and (b), the 25 local grid points around $\bar{\ell}$ have been used for averaging, for (c) and (d), the region was extended to 5 center points before and after each $\bar{\ell}$ together with their local grids, giving 275 points for each PDP.

is roughly 4 cm, the spatial extent of a delay bin c/B is 14 cm and 60 cm, respectively. For the top plots, 25 1-cm-spaced local grid points³⁴ around the center points $\mathbf{p}_{\bar{\ell}}$ have been used for averaging, resulting in a maximum spatial separation of $\Delta d = 5.6$ cm. For the lower plots, ten additional trajectory center points and their 1-cm-spaced local grid points have been used for averaging, resulting in 275 points per PDP and a maximum spatial separation of $\Delta d = 54$ cm. In the light of the channel model (2.1), averaging considerations should also account for the expected visibility regions of deterministic MPCs³⁵ as these will also govern spatial regions of stationary channel behavior.

The PDPs using the large bandwidth show a large amount of local details as long as the averaging conditions are fulfilled. If this is not the case, like in Fig. 7.1c, local variations are clearly averaged out. However, the PDP of the estimated DM, obtained by removing the deterministic MPCs, still seems comparable to Fig. 7.1a. This indicates that the prominent differences stem from additional delay dispersion of the deterministic MPCs. If the bandwidth

³⁴ See Section A.5.1 for a description of the measurements.

³⁵ See Figs. 2.3 and 2.4 for an example in a different environment.

is reduced to UWB-ABS as for the two right figures, the spatial averaging conditions are fulfilled in both cases. This leads to comparable results also for the PDPs including the deterministic MPCs.

For bandwidths lower than UWB, [142] points out that the PDP shows exponentially decaying behavior with a similar slope within a room due to reverberation effects that can not be resolved. Here, the significantly larger bandwidths do not allow for such simple models, as the large time resolution enables to resolve many contributions to the signal. This is shown in Fig. 7.1 by the local variations in the PDPs. However, in numerical computations of performance bounds such as in [T3], a double exponential model such as in [26] is used. This model accounts for “soft onset” effects for components after the LOS components, which to some extent can be observed in our measurements, e.g. in Fig. 7.1.

7.3 Overview of Related Channel Models

One of the most widely cited models for UWB channels is given in [19] as (extended with the position index)

$$h_\ell(\tau) = \sum_{k=1}^{K_\ell} \alpha_{k,\ell} \chi_k(\tau) * \delta(\tau - \tau_{k,\ell}) \quad (7.4)$$

where the impulse response $h_\ell(\tau)$ is modeled as a sum of K_ℓ MPCs with amplitudes $\alpha_{k,\ell}$ and delays $\tau_{k,\ell}$. The function $\chi_k(\tau)$ represents pulse distortion, i.e. a frequency dependence in the interaction process that generated the respective MPC. Though this is an effect that will most certainly occur in UWB systems due to the fact that an MPC experiences different propagation properties in different frequency bands, $\chi_k(\tau)$ is not considered in most channel models. This is due to the fact that the proper characterization of $\chi_k(\tau)$ is site- and material-specific and would require large databases of measurement results as well as implementations of channel models capable of using those.

Taking into account the above discussion on propagation effects, the pulse distortion $\chi_k(\tau)$ in (7.4) can be understood as DM associated with the k -th MPC, i.e. the MPC’s respective non-specular part. UWB channel models such as in [96] propose so-called *diffuse tails* of deterministic MPCs. These are different from the classical *clusters* of MPCs in the Saleh-Valenzuela (SV) Model [143, 144] that may be understood as stemming from groups of spatially extended scatterers. The definition and parametrization of clusters will be different depending on the bandwidth and the application area of the channel model.

Models like [26, 75] allow for the reproduction of channel behavior that has been parametrized using measurements in some environment. While [26] uses the SV model (with the extension of also considering a power-law instead of an exponential per-cluster power decay), [75] also includes geometric effects such as visibility regions of clusters that can be estimated from measurements [82, 84]. Such visibility regions are also used in [145], allowing for spatially consistent channel simulations in a defined environment.

The arrival times of MPCs are accounted for implicitly by random or deterministic placement of the scatterers. In classical models such as [102, 103], the inter-arrival times of MPCs are treated as Poisson distributed, which can be related to uniformly distributed scatterers in the spatial domain. This notion has been extended to clusters in [144], where the arrival times of the clusters as well as those of the constituent MPCs are described by homogeneous Poisson processes. A novel modeling aspect in this regard is done in [146], where spatial point processes are used to model the birth and death dynamics of MPCs in time-varying channels.

Although some of the above models include the effect of DM, it is modeled once that deterministic MPCs have been taken into account, i.e. to model the remaining energy of the channel

that can not be explained. An explicit estimation of DM is done in [76] and [73], relying on models of the PDP shape. This allows for a structured decomposition and estimation of the parts of the channel. Another different approach to the modeling of dense channels is the use of propagation graphs [139]. Graph theory is used to model the interplay of scatterers in a recursive way, allowing for closed-form expressions of channel transfer functions.

The model (2.1) used in this thesis clearly separates the description of deterministic and diffuse multipath. By a suitable choice of the PDP of the DM in (2.2), different power distributions can be achieved in the delay domain. Clustering can either be modeled using groups of deterministic MPCs (which would be given by the geometry) or by a mixture model representation of $S_{\nu,\ell}(\tau)$ that could also depend on the deterministic MPCs to model diffuse tails. In this thesis, we restrict $S_{\nu,\ell}(\tau)$ to global models w.r.t. the delay domain when explicitly using it [T3]. However, when estimating position-related information [T4, T8, T9] from signals, the local interplay between deterministic MPCs and the DM can be accounted for without explicitly estimating $S_{\nu,\ell}(\tau)$.

7.4 Chapter Conclusions

This chapter discussed several issues concerning radio propagation effects and their characterization that are relevant for this thesis. In terms of position dependence, the *propagation delay* of the radio signal (and its specular reflected MPCs) provides the most useful physical phenomenon to exploit. PDPs are very useful for the average characterization of radio channel in the delay domain. In this thesis, the PDP of the diffuse multipath represents the main source of uncertainty in the estimated path delays of deterministic MPCs. The estimation of PDPs exhibits some intricacies, especially at ultra-wide bandwidths. Finally, the relation of the used channel model has been discussed with respect to the literature.

8

Additional Results

This chapter contains additional results using the measurements discussed in Appendix A. Section 8.1 presents results for the energy capture (EC) analysis discussed in Section 4.1.2 for different scenarios. For the same scenarios, Section 8.2 contains estimation results for the K-factor w.r.t. the LOS component and the RMS delay spread as discussed in Section 2.1.2. In Section 8.3, the SINR estimation technique from Section 4.2 is applied for different scenarios to predict the performance using the PEB. Comparisons are done with the tracking performance that can be achieved. Section 8.4 briefly concludes the chapter.

8.1 Energy Capture Analysis for Different Scenarios

This section provides additional results for Section 4.1.2. For all plots, the black lines denote the EC of all VA-modeled MPCs up to order three. For the EC denoted by the blue lines, the respective same number of *strongest* components are taken into account, i.e. (4.1) and (4.2) with $\hat{K}_\ell^{(j)} = |\mathcal{A}_\ell|$. The grey dashed lines correspond to the black lines, but with the LOS component removed from \mathcal{A}_ℓ to show the EC of only the reflected components. A general conclusion from Figs. 8.1-8.6 is that the EC of VA-modeled deterministic MPCs is also significant in scenarios other than the one used in [T2]. Much of the energy is contained in reflected MPCs.

Fig. 8.1 shows the EC for the first 220 trajectory positions (the rightmost part in Fig. A.4) of the corridor scenario, using Anchor 3 and two different pulse durations of $T_p = 0.2$ ns (using $f_c = 7$ GHz) and $T_p = 0.5$ ns (using $f_c = 6.85$ GHz). The trend in the EC over the trajectory is similar for both pulse durations. Nevertheless, a shorter pulse corresponds to a lower EC, since a narrower pulse contains less contributions of the DM. These results correspond to those in [T2] (e.g. Fig. 6), where a slightly different methodology was followed as explained in Section 4.1.2. In [T2], the maximum amplitude of the received signal was taken as the MPC amplitude within an uncertainty window corresponding to the pulse duration. In general, this leads a slightly larger EC than presented here. Also, a different pulse shape was used in [T2] to filter out the band of interest (a Parzen window in frequency domain). Despite these differences in methodology, the results match well qualitatively.

Fig. 8.2 shows the EC for the seminarroom scenario (see Section A.5) using Anchor 1 and agent 2 and a pulse duration of $T_p = 0.5$ ns at a center frequency of $f_c = 7$ GHz. The measurements obtained with the M-sequence channel sounder and the vector network analyzer are compared. In terms of EC, both agree quite well, especially for the NLOS MPCs. Differences come from the

different, unknown antenna orientations in both campaigns, which most prominently influence the LOS component. Between $\ell = 80$ and $\ell = 100$, the NLOS region caused by the pillar can be observed. Here, much of the energy in the strongest components (blue line) still comes from the diffracted LOS component.

Figs. 8.3 and 8.4 compare the two demonstration rooms in Graz (see Section A.5.2) and Montbéliard (see Section A.5.3), respectively. For the first, the two different anchors are shown, leading to comparable levels of EC. For the second, two center frequencies $f_c = 7$ GHz and $f_c = 8$ GHz are analyzed at a pulse duration of $T_p = 0.5$ ns. This was done as the larger f_c shows considerably better performance with the real-time demonstration system, as explained in [T8]. In the EC, this advantage is only seen slightly.

Figs. 8.5 and 8.6 compare measurements in the laboratory room (see Section A.6), at pulse durations $T_p = 0.5$ ns and $T_p = 0.2$ ns, respectively. For both figures, the empty and full rooms are compared. Interestingly, the difference in room configurations can not be distinguished clearly using the EC, even using the shorter pulse duration.

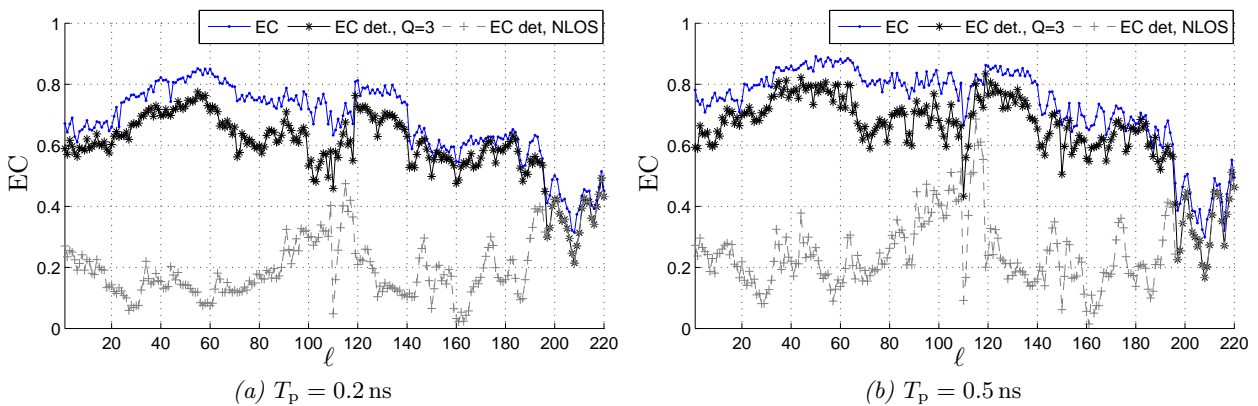


Figure 8.1: Energy capture as defined in (4.5) for positions $\ell = 1, \dots, 220$ of the corridor scenario (see Section A.4). Anchor 3 is used for two pulse durations $T_p = 0.2$ ns and $T_p = 0.5$ ns.

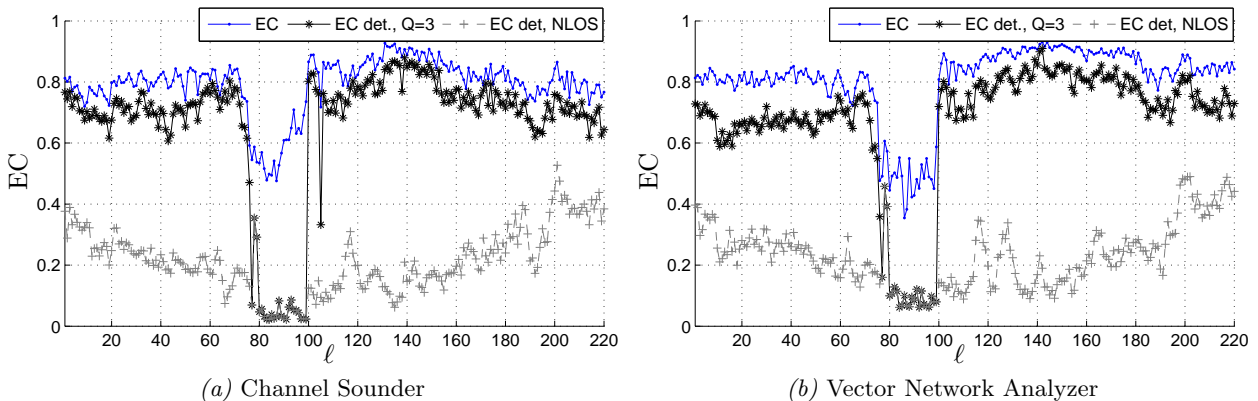


Figure 8.2: Energy capture as defined in (4.5) for the seminarroom scenario (see Section A.5). Anchor 1 and agent 2 have been used with a pulse duration of $T_p = 0.5$ ns at a center frequency of $f_c = 7$ GHz. Left plot shows measurements obtained with the M -sequence channel sounder (see Section A.2.2), right plot for the Vector Network Analyzer (see Section A.2.1).

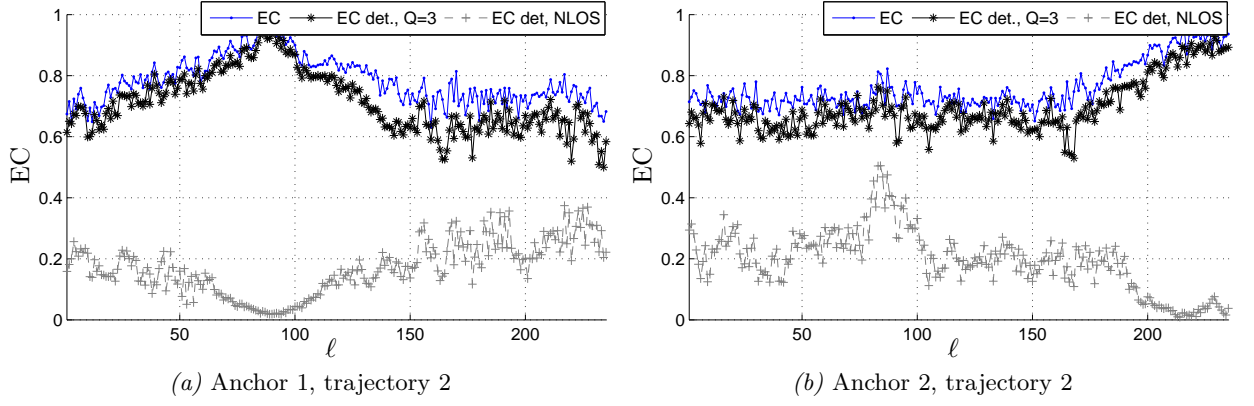


Figure 8.3: Energy capture as defined in (4.5) for the demonstration room scenario in Graz (see Section A.5.2). Anchor 1 and 2 are used on trajectory 2 with a pulse duration of $T_p = 0.5$ ns at a center frequency of $f_c = 7$ GHz.

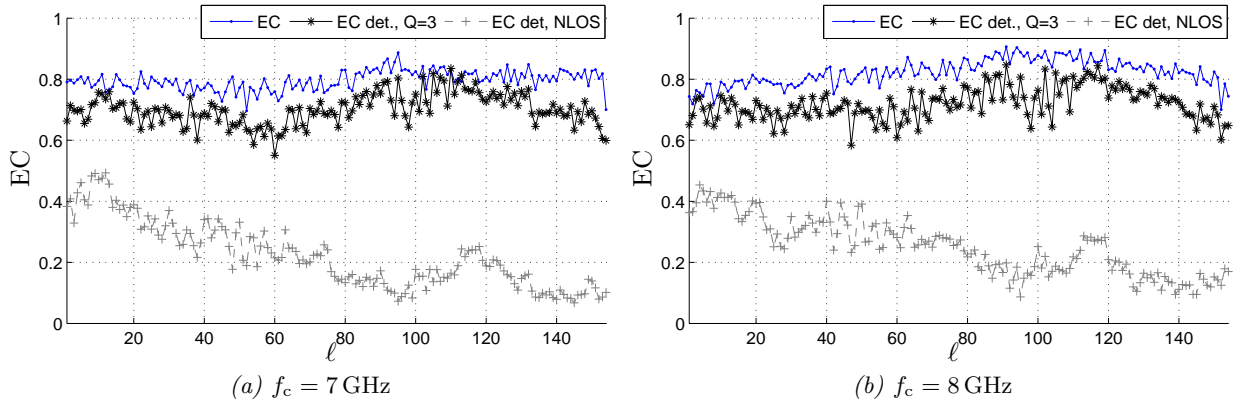


Figure 8.4: Energy capture as defined in (4.5) for the demonstration room scenario in Montbéliard (see Section A.5.3). Anchor 1 and agent 1 have been used with a pulse duration of $T_p = 0.2$ ns at a center frequencies of $f_c = 7$ GHz and $f_c = 8$ GHz.

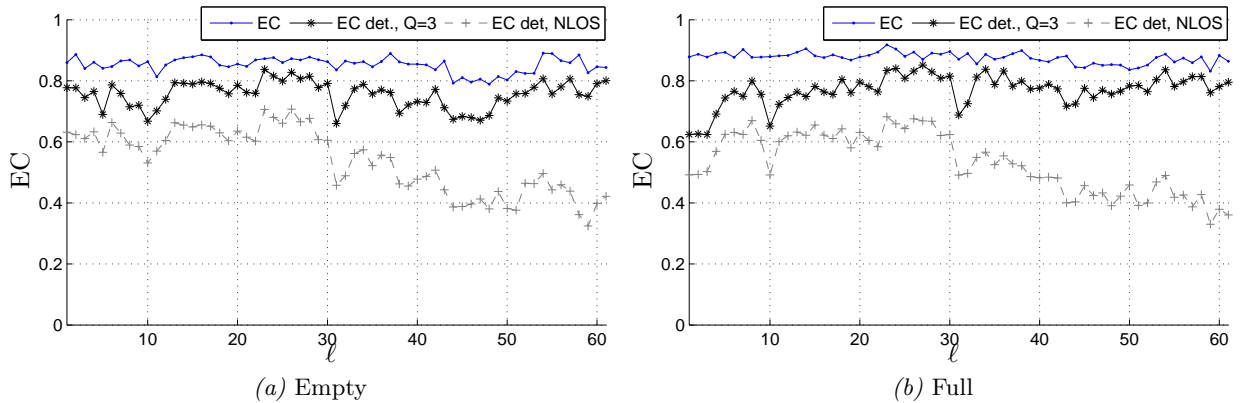


Figure 8.5: Energy capture as defined in (4.5) for the laboratory room scenario (see Section A.6). Anchor 1 has been used with a pulse duration of $T_p = 0.5$ ns at a center frequency of $f_c = 7$ GHz. The left plot uses the measurements in the empty room, for the right plot, a lot of measurement equipment was inside.

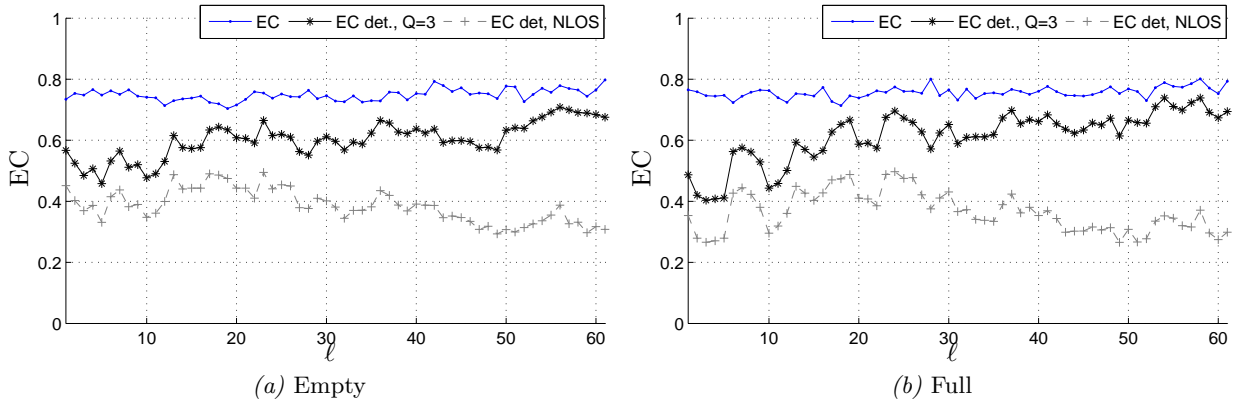


Figure 8.6: Energy capture as defined in (4.5) for the laboratory room scenario (see Section A.6). Anchor 1 has been used with a pulse duration of $T_p = 0.2$ ns at a center frequency of $f_c = 7$ GHz. The left plot uses the measurements in the empty room, for the right plot, a lot of measurement equipment was inside.

8.2 Channel Parameter Estimation

This section provides additional results for the estimation of the channel parameters rms delay spread τ_{RMS} (2.4) and K-factor w.r.t. the LOS component K_{LOS} (2.5), as explained in Section 2.1.2. As in [T2], the instantaneous values $\tau_{\text{RMS},\ell}$ and $K_{\text{LOS},\ell}$ are shown over the trajectories. The same scenarios as in the previous Section 8.1 are used. Fig. 8.7 shows the scenario used in [T2]. The results agree well with the paper, despite the slightly different methodology as explained in Section 8.1. There are almost no differences between the two bandwidths. Fig. 8.8 shows the comparison of the estimated channel parameters for the M-sequence channel sounder and the VNA data. Quantitatively, there are considerable local differences, although the overall trend is similar. This goes in line with the EC analysis in Fig. 8.2.

The comparisons of the two demonstration rooms in Graz and Montbéliard is shown in Figs. 8.9 and 8.10. The general trend of the channel parameters w.r.t. the distance to the anchors can be observed. No significant differences can be seen for the two different center frequencies.

For the laboratory room, only the results for the pulse duration $T_p = 0.5$ ns are shown in Fig. 8.11, as there are no significant differences to the shorter pulse duration. The K-factor shows a small dependence on the distance to the anchor. Other than this, the channel parameters do not vary much over this short trajectory which is due to the small room dimensions.

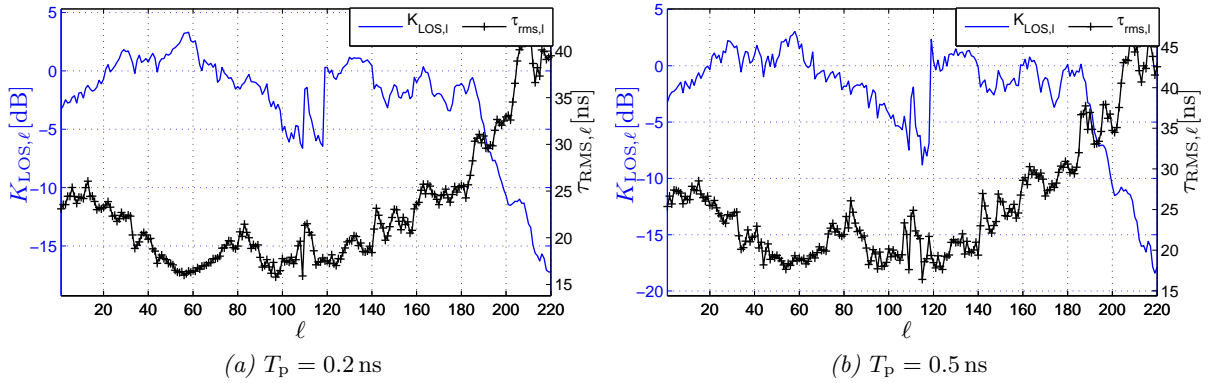


Figure 8.7: Instantaneous channel parameters $\tau_{\text{RMS},\ell}$ and $K_{\text{LOS},\ell}$ as defined in (2.4) and (2.5) for positions $\ell = 1, \dots, 220$ of the corridor scenario (see Section A.4). Anchor 3 is used for two pulse durations $T_p = 0.2$ ns and $T_p = 0.5$ ns.

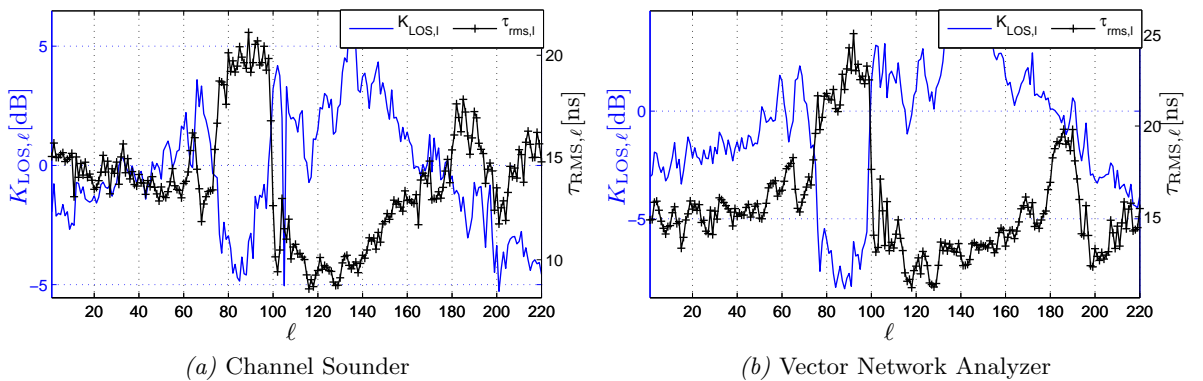


Figure 8.8: Instantaneous channel parameters $\tau_{\text{RMS},\ell}$ and $K_{\text{LOS},\ell}$ as defined in (2.4) and (2.5) for the seminar room (see Section A.5). Anchor 1 and agent 2 have been used with a pulse duration of $T_p = 0.5$ ns at a center frequency $f_c = 7$ GHz. Left plot shows M-sequence channel sounder measurements (see Section A.2.2), right plot for the Vector Network Analyzer (see Section A.2.1).

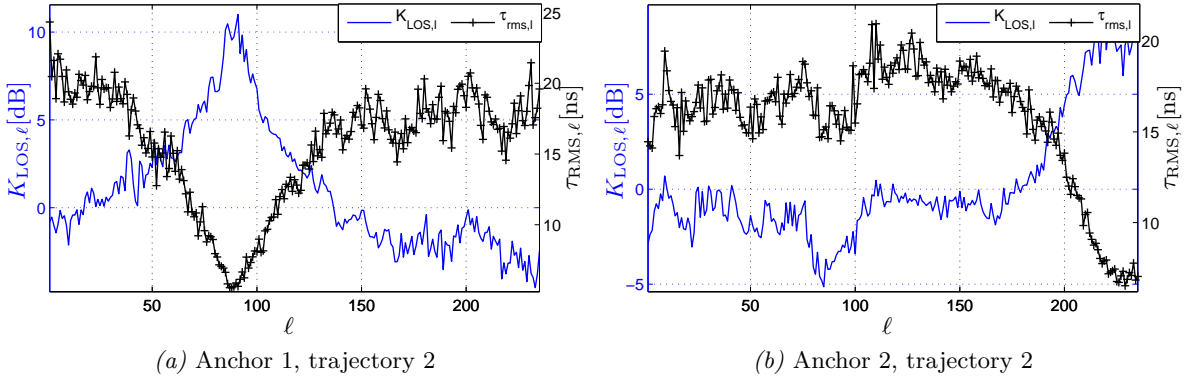


Figure 8.9: Instantaneous channel parameters $\tau_{\text{RMS},\ell}$ and $K_{\text{LOS},\ell}$ as defined in (2.4) and (2.5) for the demonstration room scenario in Graz (see Section A.5.2). Anchor 1 and 2 are used on trajectory 2 with a pulse duration of $T_p = 0.5$ ns at a center frequency of $f_c = 7$ GHz.

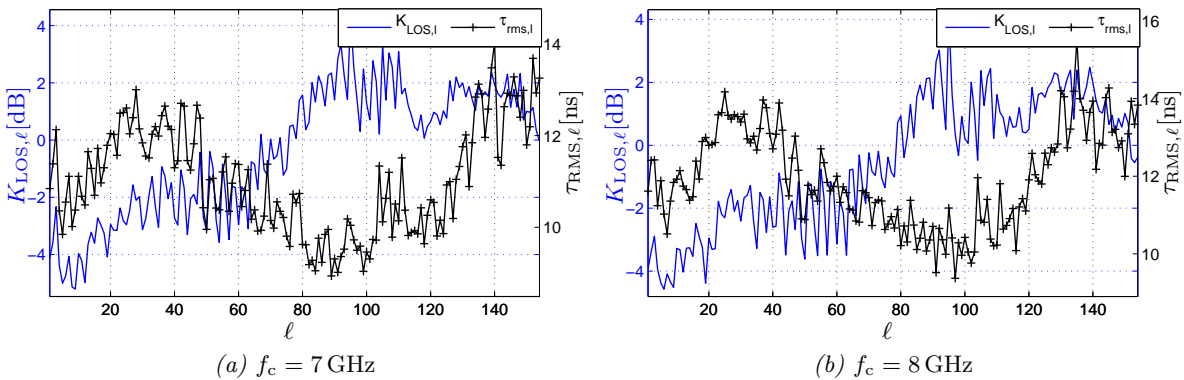


Figure 8.10: Instantaneous channel parameters $\tau_{\text{RMS},\ell}$ and $K_{\text{LOS},\ell}$ as defined in (2.4) and (2.5) for the demonstration room scenario in Montbéliard (see Section A.5.3). Anchor 1 and agent 1 have been used with a pulse duration of $T_p = 0.2$ ns at center frequencies of $f_c = 7$ GHz (left plot) and $f_c = 8$ GHz (right plot).

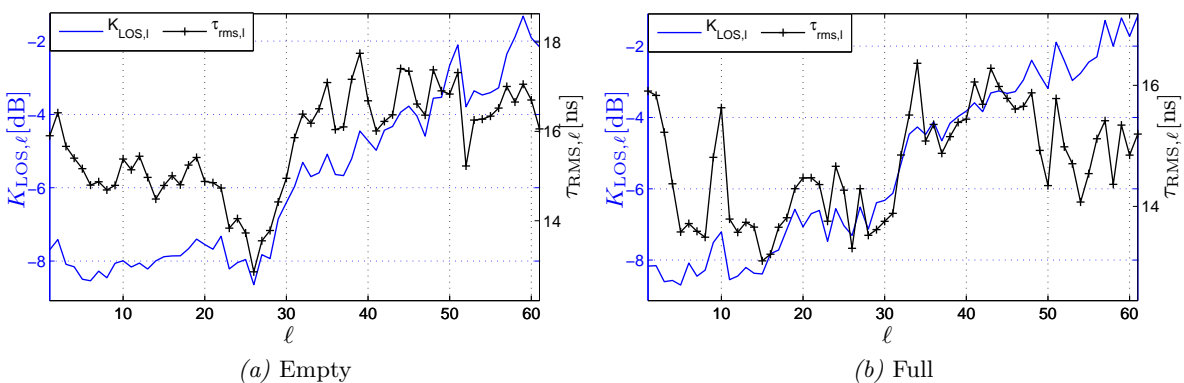


Figure 8.11: Instantaneous channel parameters $\tau_{\text{RMS},\ell}$ and $K_{\text{LOS},\ell}$ as defined in (2.4) and (2.5) for the laboratory room scenario (see Section A.6). Anchor 1 has been used with a pulse duration of $T_p = 0.5$ ns at a center frequency of $f_c = 7$ GHz. The left plot uses the measurements in the empty room, for the right plot, a lot of measurement equipment was inside.

8.3 SINR and CRLB Estimation and Performance Results

8.3.1 PEB and Performance in Demonstration Room

Fig. 8.12 contains a comparison of the PEB estimated using 60 points on trajectory 1 in the demonstration room in Graz (see Appendix A.5.2). Also the tracking performance using the EKF-DA presented in Section 5.2.2 is shown. A pulse duration of $T_p = 1$ ns is used at a center frequency of $f_c = 8$ GHz. Fig. 8.12a shows the PEB according to (3.11), for Fig. 8.12b, (3.16) is used, i.e. the EFIM just considering the MPCs that are not in contiguous clusters. Fig. 8.12c shows the quantitative difference of these two PEBs using CDFs over the whole room. Regions in which contiguous clusters exist are observable in 8.12b. However, along the trajectory, such a region is visited only at the end, in the vicinity of $\mathbf{a}_1^{(2)}$, shown as a close-up in Fig. 8.12d. Here, the ellipse according to (3.16) can better predict the performance of the EKF-DA.

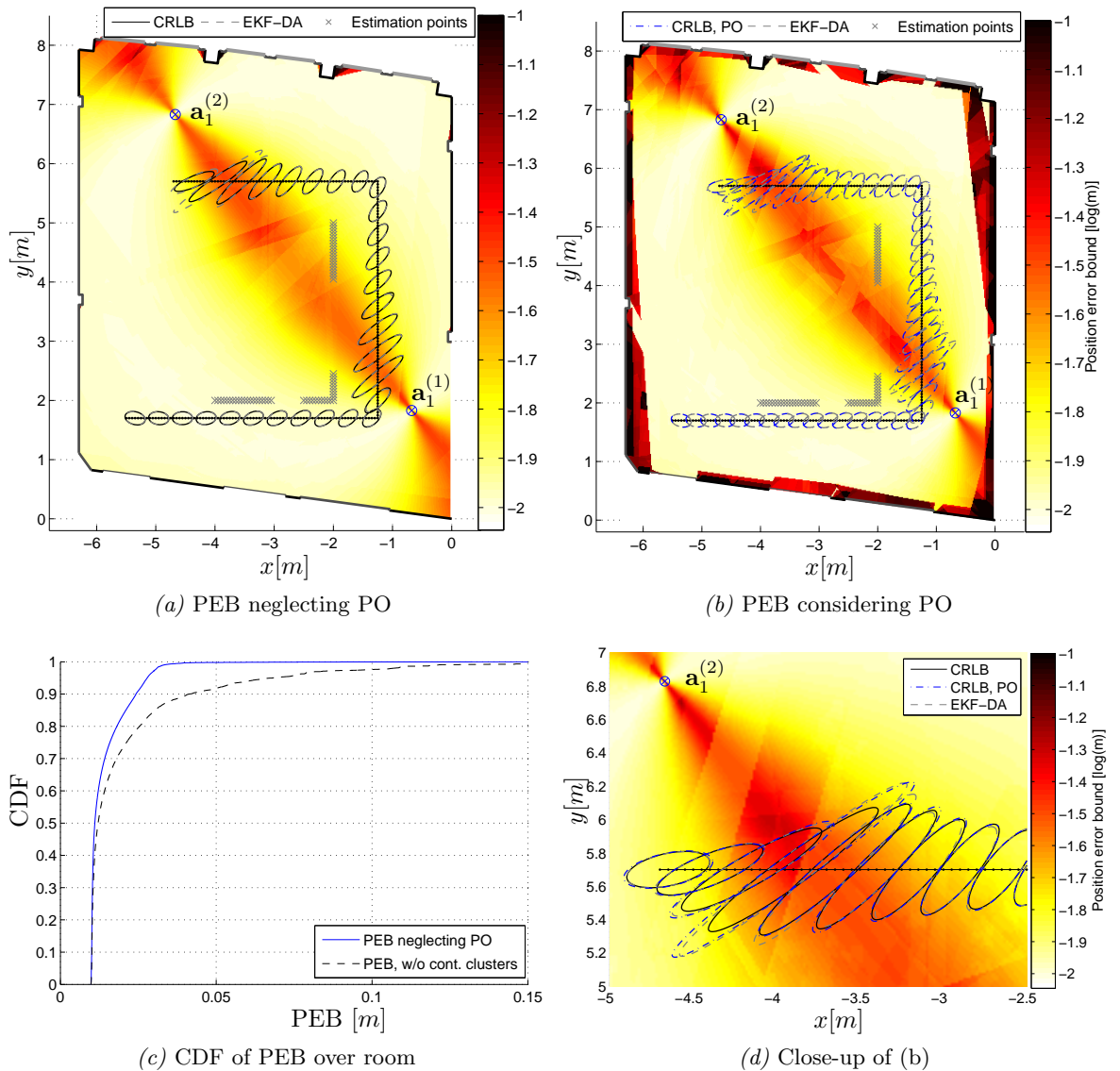


Figure 8.12: PEB for demonstration room scenario using $T_p = 1$ ns, $f_c = 8$ GHz and VAs up to order 2. The grey crosses are the 60 estimation points for the SINR. The black ellipse denotes the CRLB at some points of trajectory 2, for the blue ellipse, the CRLB in (3.16) is used, excluding MPC clusters. The grey ellipses denote the covariance matrix of the EKF-DA using estimated measurements noise model (5.13). All ellipses are enlarged by a factor of 20.

8.3.2 PEB, Performance and SINR Analysis in Seminar Room

Figs. 8.13-8.16 show different estimated PEBs and tracking results for the seminar room scenario explained in Appendix A.5. A pulse duration of $T_p = 1$ ns is used at a center frequency of $f_c = 7$ GHz, except for the single anchor scenario in Fig. 8.16, where $T_p = 0.5$ ns. VAs up to order three have been considered.

In general, a larger PEB can be observed in the region between the anchors, which is typical for a two anchor scenario [T8]. It is caused by the bad geometric constellation between the anchors. This effect gets more pronounced by the fact that the LOS components usually have the largest SINR of all MPCs (see e.g. Fig. 8.17 and [T8]). Interestingly, a simple model of the SINRs (without estimating them) can not reproduce this behavior realistically, as shown in [T8].

In terms of the tracking performance, the EKF is in general very close to the according CRLB, as confirmed by a comparison of its estimation error covariance matrix to the uncertainty ellipse provided by the EFIM, e.g. in Fig. 8.13. In the region between the anchors, the EKF-DA cannot reach the CRLB. This is due to the bad geometry as explained above. However, a conventional measure like HDOP cannot predict this³⁶, an awareness of the MPC SINRs is required.

In Fig. 8.14, the PEB according to (3.16) is shown, i.e. excluding MPCs that are in contiguous clusters. A peculiarity of this result is that the SINR estimation is done for points on the same trajectory as on which the performance evaluation of the EKF-DA is performed. On the upper right side of the trajectory there is a region where (3.16) predicts a significant impairment due to path overlap. The EKF-DA however is not impaired by the occurrence of path overlap since it can still associate one estimated MPC within the cluster to its set of expected VAs at the respective positions. Hence, the CRLB is overly *pessimistic*³⁷ here, as it considers all information from the cluster to be unusable. Information metrics for MPCs within clusters and their estimation hence remain an important topic for further research.

Fig. 8.15 shows the PEB neglecting path overlap estimated on 60 points of trajectory 1. Also here, the EKF-DA performance on trajectory 2 is very close to the CRLB, and the impairments in the NLOS region with respect to Anchor 1 behind the pillar on the left side are visible. In general, the bounds estimated using trajectories 1 or 2 agree well qualitatively. Quantitative differences are due to differences in the estimated SINRs in different regions of the room.

Fig. 8.16 shows the PEB neglecting path overlap for a single anchor scenario using only Anchor 2. Here, the pulse duration is decreased to $T_p = 0.5$ ns to allow for more usable MPCs. Estimation is done for 60 points on trajectory 1, results are shown on both trajectories. Geometry plays a larger role in this case, as the whole configuration of VAs is determined by just one anchor and the floor plan. It should be noted that there are a few situations where the covariance ellipse of the EKF-DA is smaller than the CRLB. This only happens when the EKF is slightly off track, i.e. biased. In such cases, the CRLB is not a valid lower bound. However, the plotted EKF error ellipse is always centered on the true position, to facilitate a comparison with the CRLB.

Some of the individual MPCs that contribute to the PEBs shown in Fig. 8.16 are analyzed in terms of their SINRs and EC in Fig. 8.17. Fig. 8.17a shows the MPCs for Anchor 1, Fig. 8.17b the ones for Anchor 2, where the latter are the basis for the PEB in Fig. 8.16. A subset of the 60 signals used for the SINR estimation is shown together with the estimated amplitude tracks. The EC value that is shown is the mean per-VA-EC over these 60 points. It is clearly visible that the LOS component provides the most significant position-related information, leading to the main orientation of the uncertainty ellipses in the PEB. Important reflectors are the windows (which are metal-coated) and the blackboard. An interesting observation, which is valid also in other scenarios, is that later arriving reflections, such as double and triple reflections between the windows, can have large SINRs. This is not indicated by their mean EC. However, at

³⁶ These results are not shown, the HDOP for this case is always less than 2, indicating excellent geometry.

³⁷ It should be stressed that this is due to a model mismatch between the CRLB and the estimator in this case.

comparably large delays also the power density of the DM is already decreased, allowing for large SINRs.

Fig. 8.17a shows similar information for Anchor 1 and some of the occurring reflections. Here, also an MPC which is heavily impaired by DM is shown, the double reflection between lower wall and blackboard. The DM influence leads to large fluctuations in the amplitude track and thus to a low SINR. An awareness to this can significantly improve positioning performance as such a measurement can be weighted accordingly.

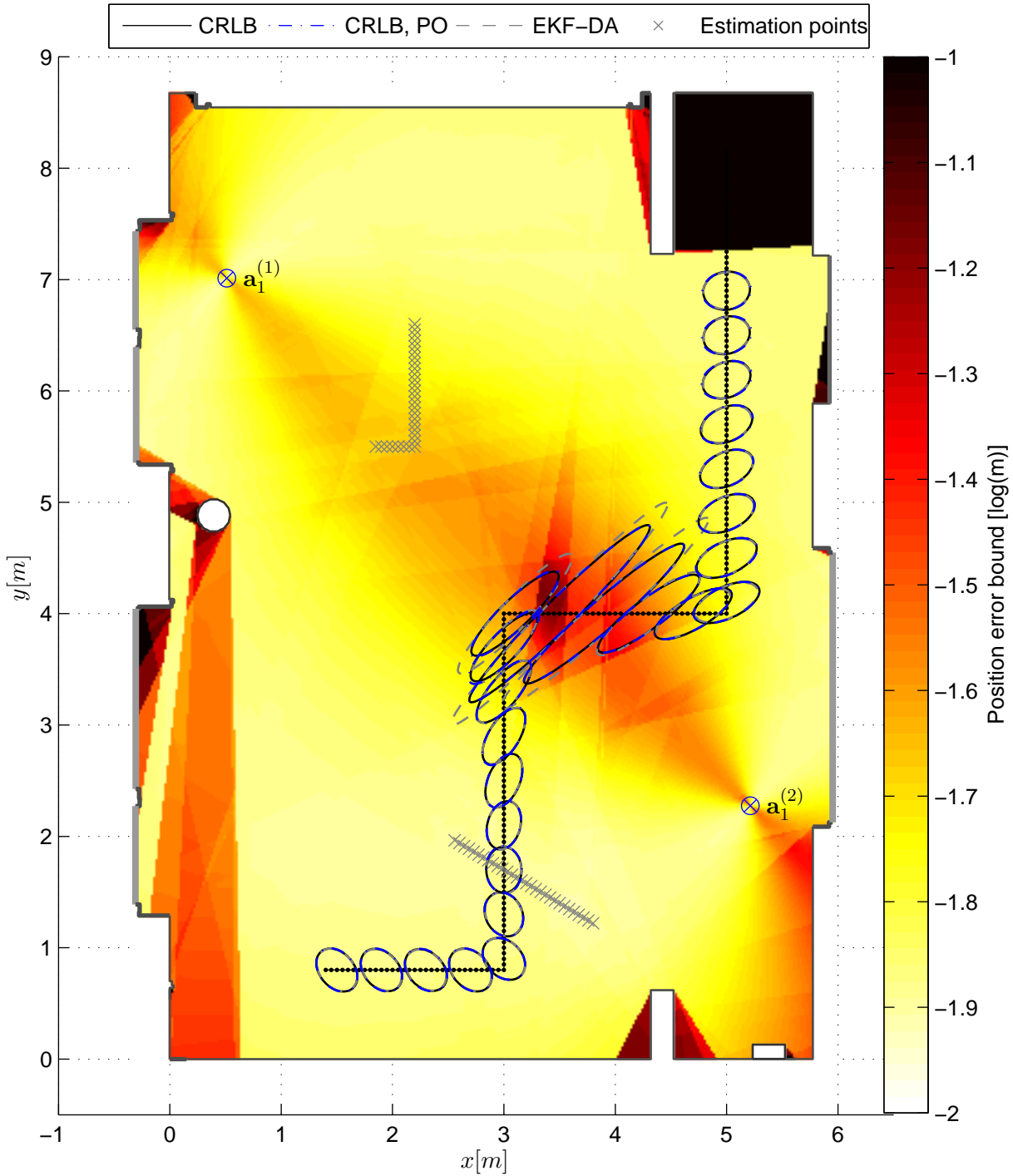


Figure 8.13: PEB using estimated SINRs and (3.11) (neglecting path overlap) over the seminar room scenario explained in Appendix A.5 with the VNA measurements, $T_p = 1$ ns and $f_c = 7$ GHz. The grey crosses are the 60 estimation points for the SINR. The black ellipse denotes the CRLB at some points of trajectory 1, for the blue ellipse, the CRLB in (3.16) is used, excluding MPC clusters. The grey ellipses denote the estimation error covariance matrix of the EKF-DA using estimated measurements noise model (5.13). All ellipses are enlarged by a factor of 20 for better perceptibility.

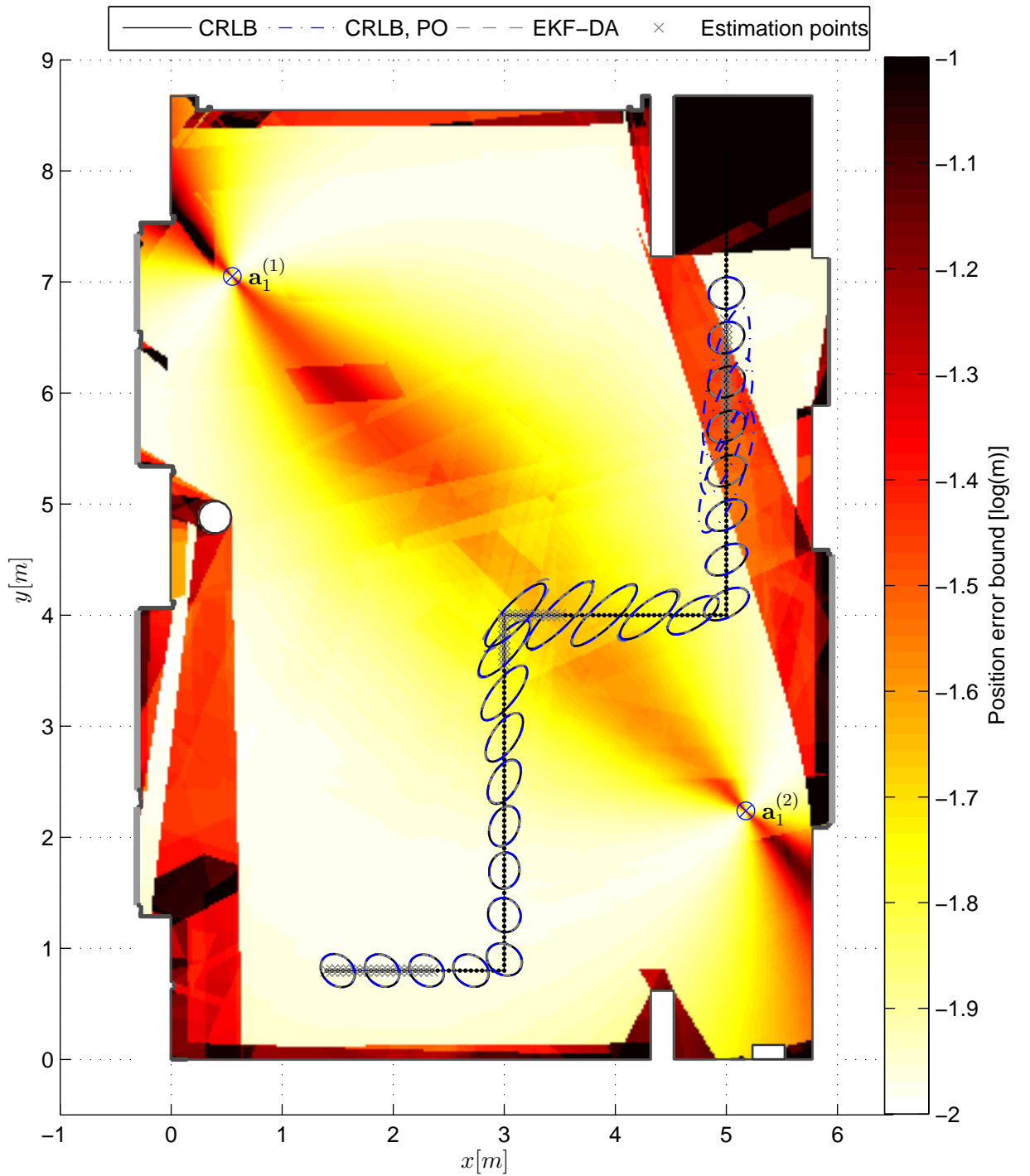


Figure 8.14: PEB using estimated SINRs and (3.16) (excluding MPC clusters) over the seminar room scenario explained in Appendix A.5 with the VNA measurements, $T_p = 1$ ns and $f_c = 7$ GHz. The grey crosses are the 60 estimation points for the SINR. The black ellipse denotes the CRLB at some points of trajectory 1, for the blue ellipse, the CRLB in (3.16) is used, excluding MPC clusters. The grey ellipses denote the estimation error covariance matrix of the EKF-DA using estimated measurements noise model (5.13). Compared to the previous Fig. 8.13, the estimation is done using 60 points on trajectory 1. All ellipses are enlarged by a factor of 20 for better perceptibility.

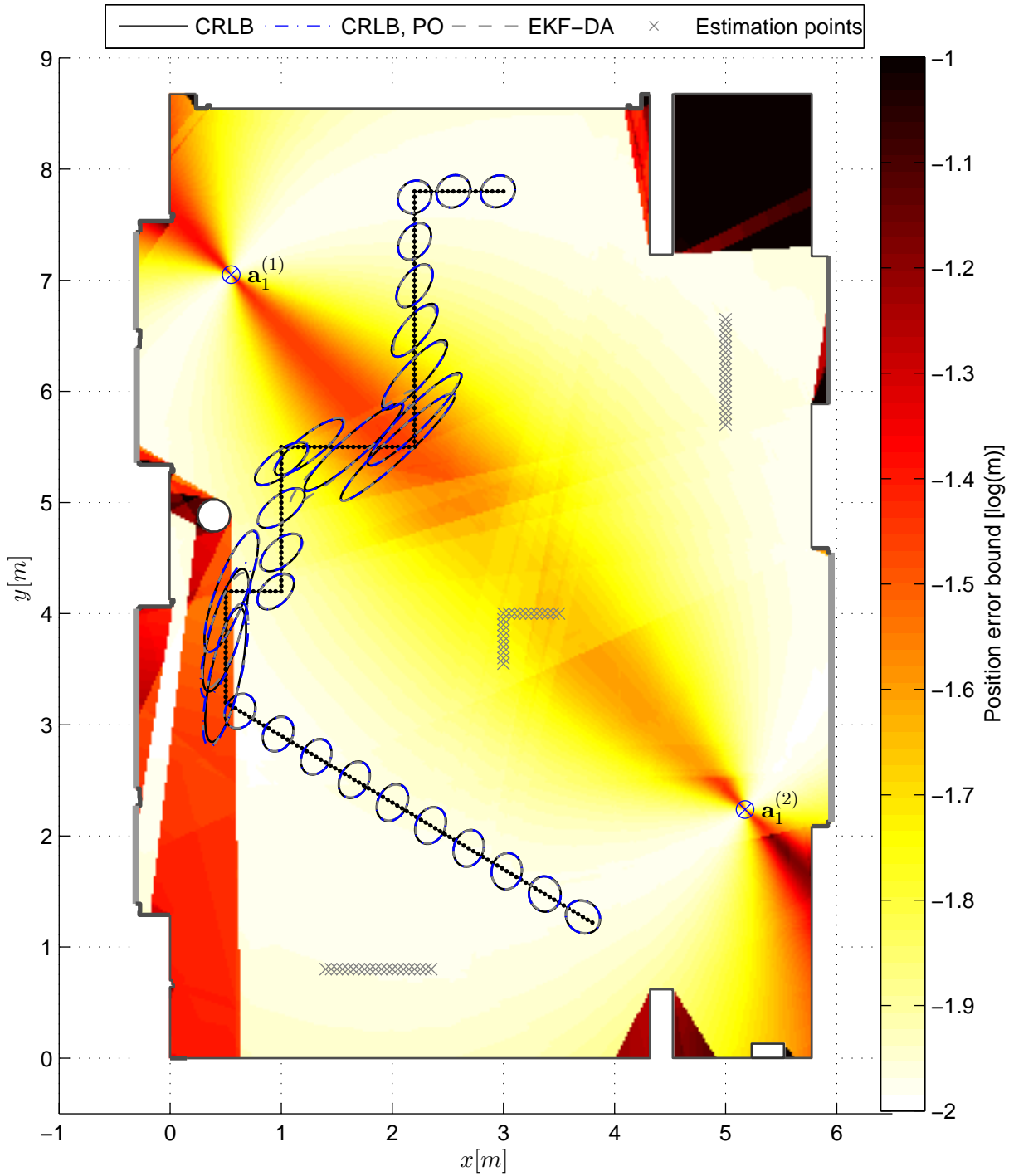


Figure 8.15: PEB using estimated SINRs and (3.11) (neglecting path overlap) over the seminar room scenario explained in Appendix A.5 with the VNA measurements, $T_p = 1$ ns and $f_c = 7$ GHz. The grey crosses are the 60 estimation points for the SINR. The black ellipse denotes the CRLB at some points of trajectory 2, for the blue ellipse, the CRLB in (3.16) is used, excluding MPC clusters. The grey ellipses denote the estimation error covariance matrix of the EKF-DA using estimated measurements noise model (5.13). All ellipses are enlarged by a factor of 20 for better perceptibility.

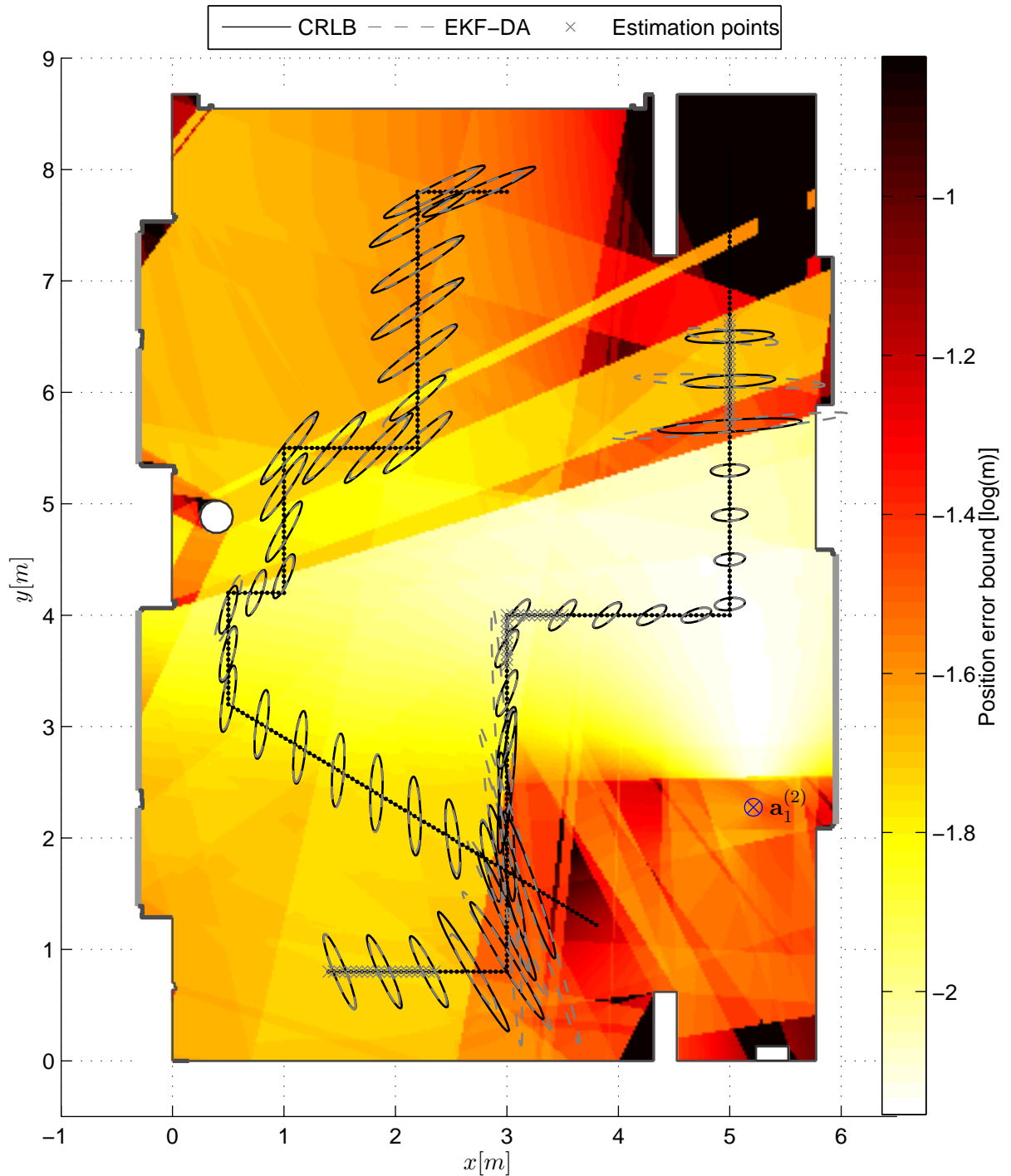
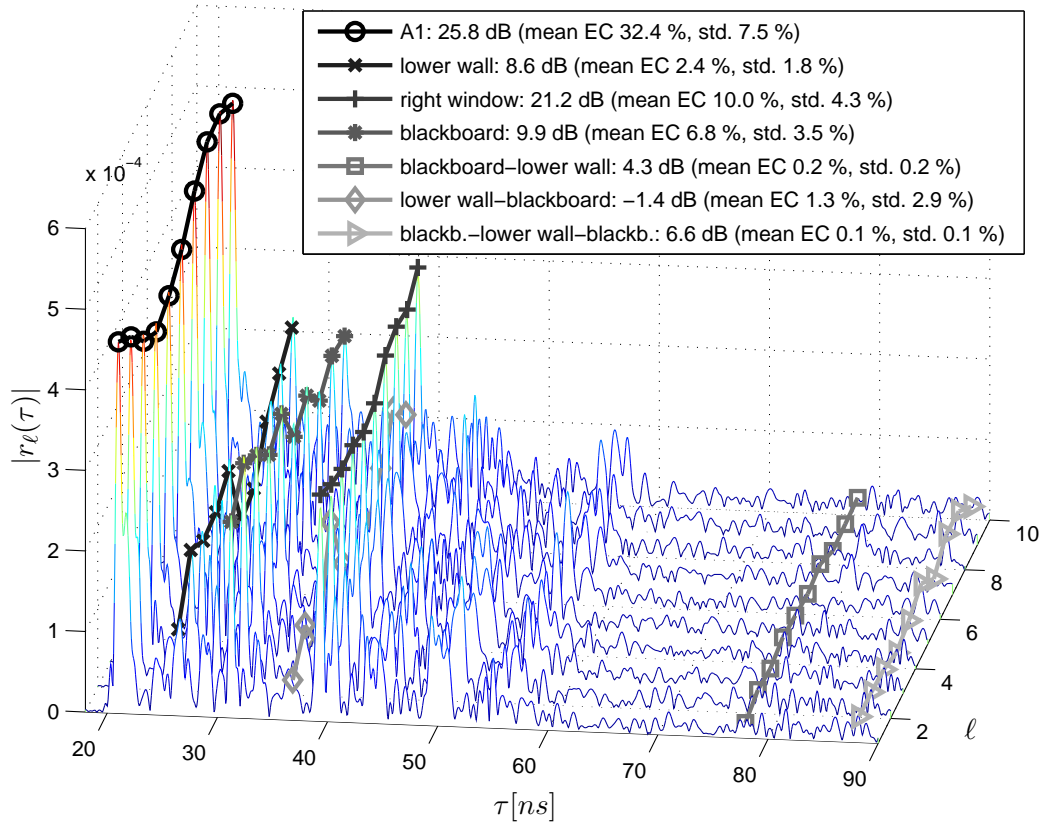
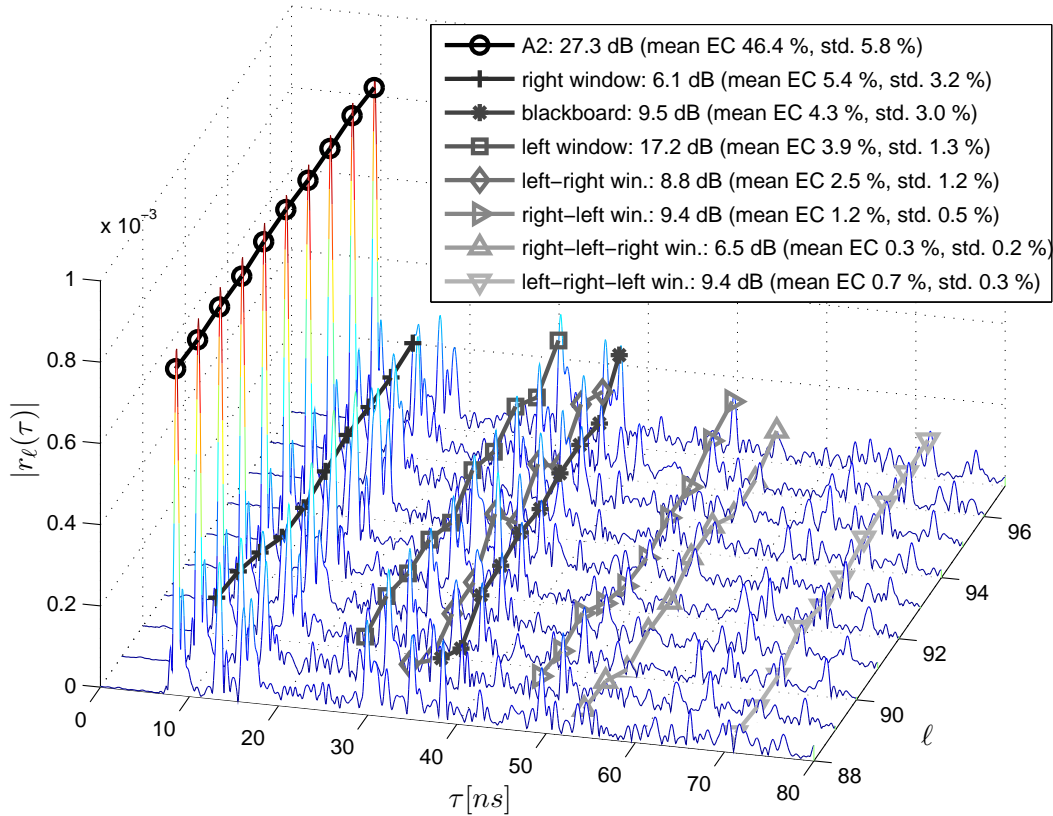


Figure 8.16: PEB using estimated SINRs and (3.11) (neglecting path overlap) over the seminar room scenario explained in Appendix A.5 with the VNA measurements, $T_p = 0.5 \text{ ns}$ and $f_c = 7 \text{ GHz}$, only Anchor 2 is used. The grey crosses are the 60 estimation points for the SINR. The black ellipse denotes the CRLB at some points of trajectory 2. The grey ellipses denote the estimation error covariance matrix of the EKF-DA using estimated measurements noise model (5.13). All ellipses are enlarged by a factor of 20 for better perceptibility.



(a) Anchor 1



(b) Anchor 2

Figure 8.17: Estimated SINRs over the estimation points on trajectory 1 indicated in Fig. 8.15 in the seminar room scenario explained in Appendix A.5 with the VNA measurements. Anchor 1 is used for the top plot, Anchor 2 for the lower one, with $T_p = 0.5$ ns and $f_c = 7$ GHz. Amplitude tracks are shown for a subset of the estimation points. Besides the SINR, also the mean EC and its standard deviation over all estimation points is indicated.

8.3.3 PEB and SINR Analysis in the Laboratory Room

As another exemplary case study of using the SINR estimates to predict the tracking performance, we use the Laboratory room measurements explained in Appendix A.6. We show single-anchor performances for both anchors and compare this with the estimated PEBs. To get an insight on propagation phenomena that lead to the performance results, we present SINR estimation results for anchors using the full and empty room. Due to the small room, we use a short pulse duration of $T_p = 0.2$ ns at a center frequency of $f_c = 6.85$ GHz to reduce PO. VAs up to order three are considered. All uncertainty ellipses are enlarged by a factor of 50 for better visibility.

In Fig. 8.18, the PEB neglecting PO is compared for the four configurations using (3.11). The energy capture analysis of the full and empty room in Fig. 8.6 did not show significant differences. In terms of the PEB, differences are observable due to the SINRs of the MPCs. By only looking at the PEB, it is not immediately clear where they come from. Comparing the two anchors, some change originates from the visibility of some important reflections. An example is the the whiteboard at the lower right side of the room (see floor plan in Fig. A.10), which is visible as a first-order reflection for Anchor 2, but not for Anchor 1.

To investigate which reflections are prominent in an environment, the SINRs can be used estimated using (4.8). Figs. 8.19-8.22 show some of the signals used for estimation (i.e. a subset of the 21 points indicated in Fig. 8.18) together with amplitude tracks of important reflections.

For Anchor 1 (Figs. 8.19 and 8.20) we observe a very large SINR of the LOS component, stemming from its very stable amplitude evolution over the estimation points. This is the main reason for the orientation of the uncertainty ellipses. An important difference is the SINR of the door, which interestingly is larger for the full room. This may be explained by different local behavior of the DM, caused by the presence of the laboratory equipment. Despite the fact that the equipment is mostly made of metal, it seems to attenuate certain parts of the DM. It also partly blocks the right wall, leading to a large difference of the amplitude of the corresponding MPC. The SINR for the right wall in the full room scenario is still reasonable, as this path is well separated from others at the shown points. An interesting observation is that also higher-order reflections like the second-order reflection on window and door (from the agent's perspective) and also the third-order reflection on window, right wall and whiteboard are significant and carry much position-related information.

For Anchor 2 (Figs. 8.21 and 8.22), the SINR of the LOS component is significantly lower than for Anchor 1. Especially for the empty room, a large variation in its amplitude is observed, which is not solely due to the distance. Although this point is not entirely clear for us, we assume an influence of the antenna pattern which is not completely isotropic. This causes a less pronounced orientation of the uncertainty ellipses. For Anchor 2, a first-order reflection on the whiteboard, which is metallic and rather smooth, is possible, leading to the most significant reflection. The most important difference comparing the empty and full room is that many reflections that occur on the right side of the room have no SINR estimates for the full room scenario. This is due to the fact that the laboratory equipment (see floor plan in Fig. A.10) strongly influences their paths, leading to unusable SINR estimates³⁸. These MPCs are then not used for the PEB computation. For the EKF-DA, they are not part of the set of VAs, and can thus not be used (see Fig. 5.1).

It has to be noted that despite the large bandwidth used, some possibly important reflection could not be estimated in this room. This is due to the rather small room dimensions, leading to many path overlap situation. In these, the SINRs can not be estimated using the presented method, as the SINR is not defined in path overlap cases. The investigation of an MPC performance metric for path overlap situations is an important topic for further research.

³⁸ In cases where large amplitude variations occur on the estimation segments, the SINR estimate in (4.8) can become complex and thus is discarded, see [T4].

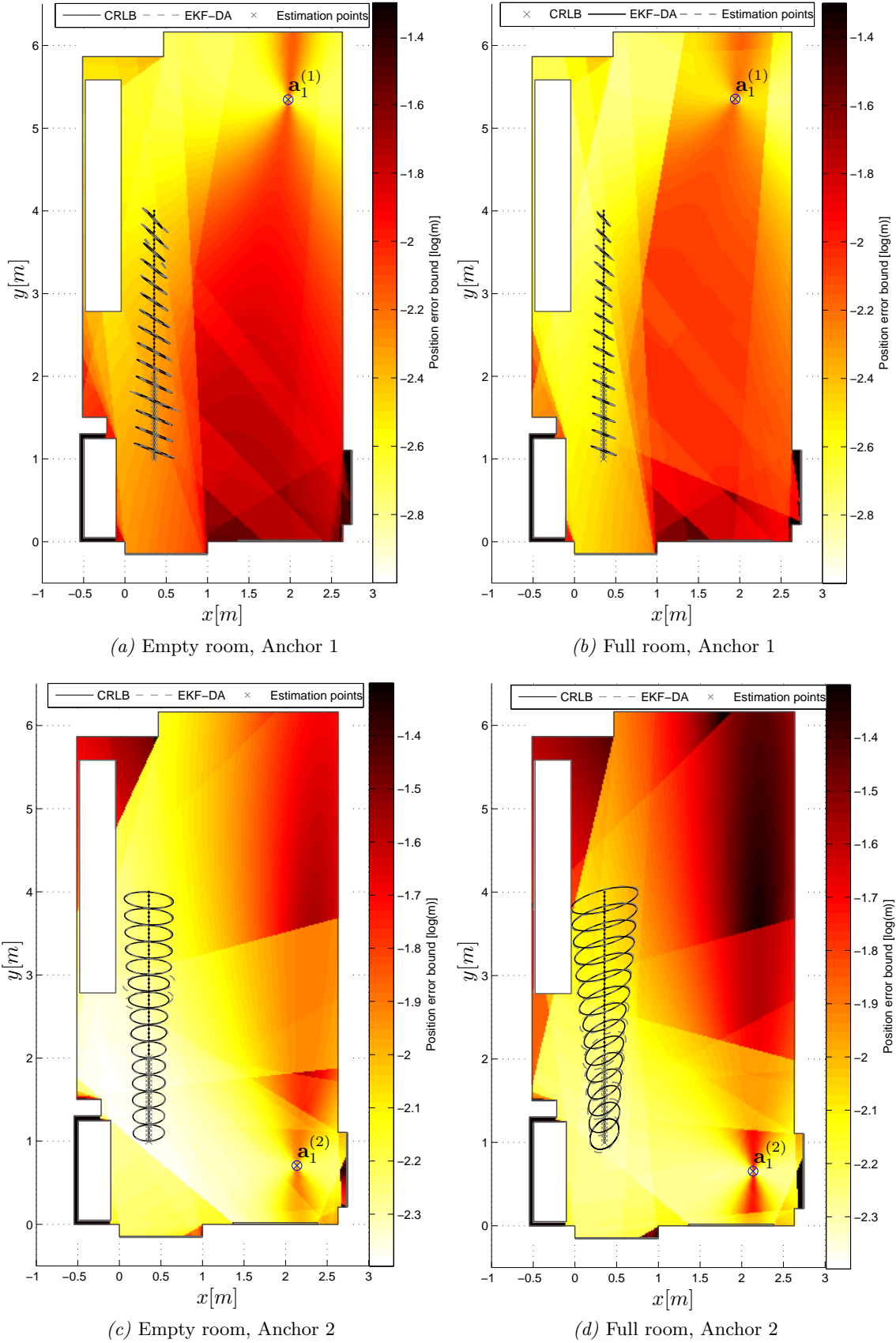


Figure 8.18: PEB for full and empty laboratory room scenario using $T_p = 0.2$ ns, $f_c = 6.85$ GHz, Anchor 1 (top row) or Anchor 2 (bottom row) and VAs up to order 3. The grey crosses are the 21 estimation points for the SINR. The black ellipse denotes the 50-fold CRLB at some points of the trajectory. The grey ellipses denote the 50-fold covariance matrix of the EKF-DA using estimated measurements noise model (5.13).

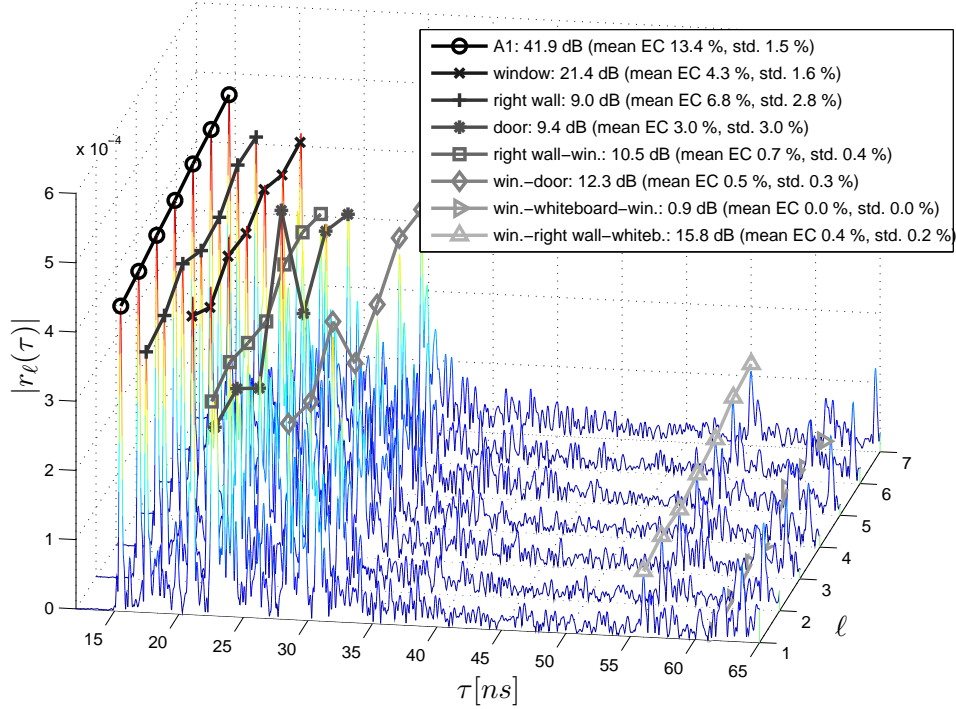


Figure 8.19: SINR estimation in the Laboratory Room (empty using Anchor 1, according to PEB in Fig. 8.18a) explained in Appendix A.6. Seven of the 21 used estimation signals are shown as examples. The gray amplitude tracks indicate the basis for the SINR estimation. The legend shows estimated SINRs together with the mean EC (over all 21 estimation points, respectively).

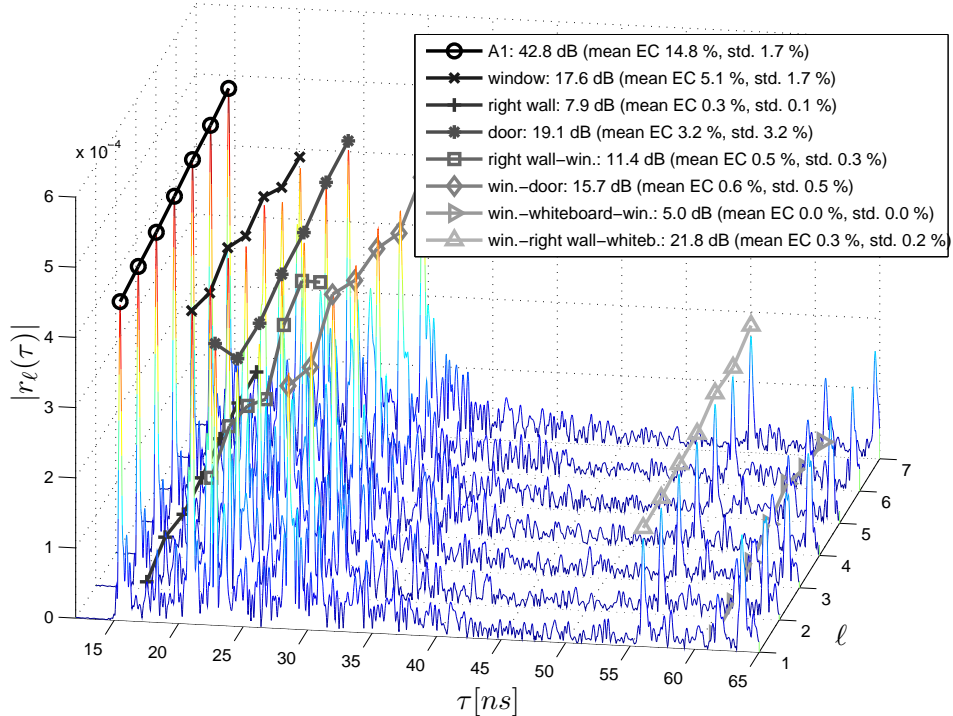


Figure 8.20: SINR estimation in the Laboratory Room (full using Anchor 1, according to PEB in Fig. 8.18b) explained in Appendix A.6. Seven of the 21 used estimation signals are shown as examples. The gray amplitude tracks indicate the basis for the SINR estimation. The legend shows estimated SINRs together with the mean EC (over all 21 estimation points, respectively).

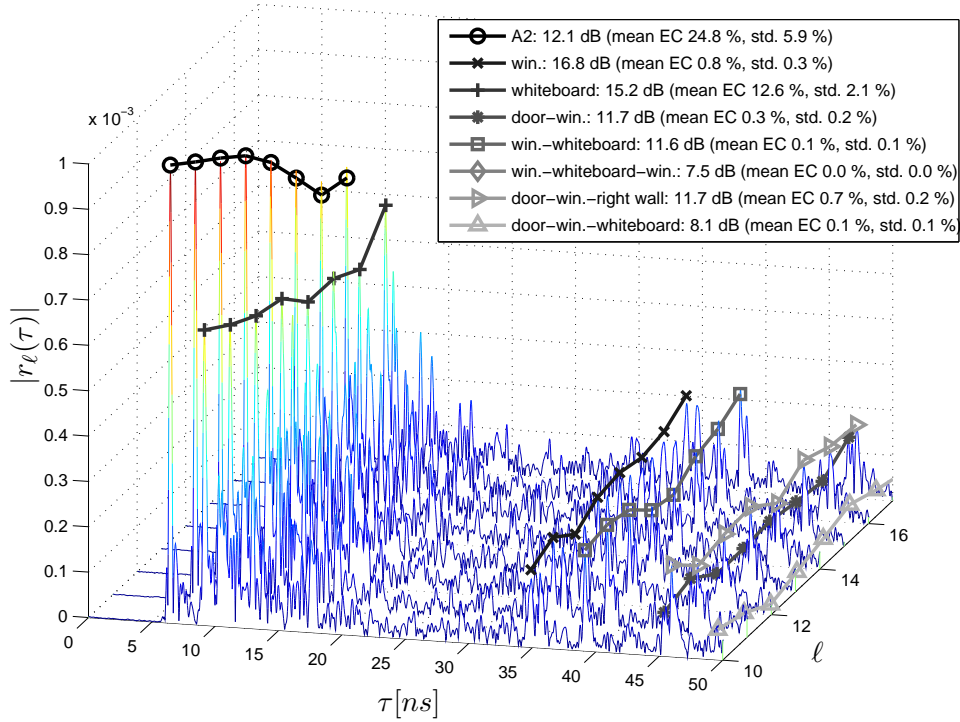


Figure 8.21: SINR estimation in the Laboratory Room (empty using Anchor 2, according to PEB in Fig. 8.18c) explained in Appendix A.6. Seven of the 21 used estimation signals are shown as examples. The gray amplitude tracks indicate the basis for the SINR estimation. The legend shows estimated SINRs together with the mean EC (over all 21 estimation points, respectively).

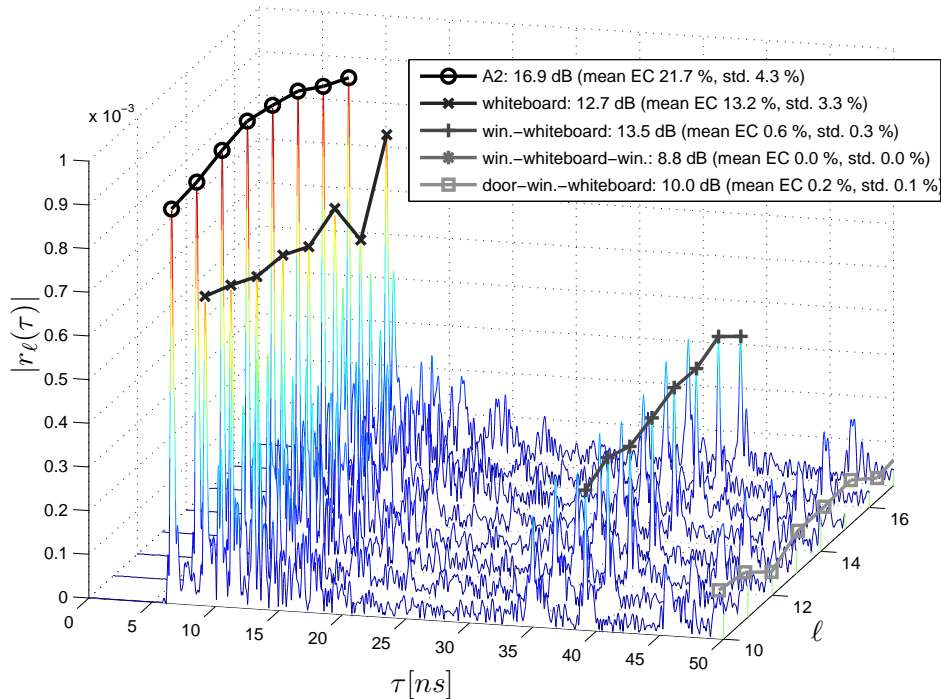


Figure 8.22: SINR estimation in the Laboratory Room (full using Anchor 2, according to PEB in Fig. 8.18d) explained in Appendix A.6. Seven of the 21 used estimation signals are shown as examples. The gray amplitude tracks indicate the basis for the SINR estimation. The legend shows estimated SINRs together with the mean EC (over all 21 estimation points, respectively).

8.4 Chapter Conclusions

This chapter presented additional measurement-based results for concepts in this thesis. Using different measurement scenarios explained in Appendix A, results are discussed for the EC and SINRs of deterministic MPCs. Furthermore, the PEB is evaluated for these SINRs and compared with the tracking performance of the EKF-DA. The conclusions in the papers comprising this thesis can be reproduced and confirmed in other scenarios. It has been shown that the channel analysis methods developed are useful to evaluate the relevant propagation effects in an environment. In all considered scenarios, the reflected MPCs carry a relatively large fraction of the signal energy. The average behavior of deterministic MPCs in terms of their energy ratio to the diffuse multipath is analyzed and used to compute performance bounds for multipath-assisted positioning. In this way, the performance of corresponding tracking algorithms can be understood in detail.

Part III

Included Papers

UWB Sequential Monte Carlo Positioning using Virtual Anchors

Paul Meissner*, Thomas Gigl^{*,o} and Klaus Witrisal*

*Graz University of Technology, Graz, Austria. Email: {paul.meissner, thomas.gigl, witrisal}@tugraz.at

^oCISC Semiconductor, Design and Consulting GmbH, Austria

Abstract—We present a novel UWB indoor localization concept that performs the position estimation with a set of virtual anchor nodes, generated from a single physical anchor and floor plan information. Using range estimates to the virtual anchors, we perform multilateration to estimate the position of an agent. Previous work has shown the general applicability of this concept. In this contribution, we use a moving agent to exploit the correlation in successive positions using state-space concepts. A motion model for the agent and the measurement likelihood function allow for the use of the powerful framework of Bayesian state estimation. With this concept, we can propagate prior information on the agent position from one time step to the next. The statistical model for the ranging to the virtual anchors accounts for several imperfections, which lead to multimodal and heavy-tailed measurement distributions. We show how modified versions of the Kalman filter as well as a particle filter can account for these imperfections and yield accurate and robust position estimates. In a typical indoor pedestrian motion scenario, we can achieve an accuracy of about 45 cm for 90% of the estimates.

I. INTRODUCTION

In previous work [1], we have shown how an agent can be localized using ultra-wideband (UWB) radio signals transmitted between the agent and a single anchor node at a known location. Our approach exploits the multipath components (MPCs) of the UWB signal, which result from signal reflections at e.g. the room walls. Using given floor plan information, these MPCs can be mapped to virtual anchors (VAs), which are mirror images of the anchor with respect to the room walls, or other reflecting surfaces. Fig. 1 shows a scenario with VAs corresponding to single and double wall reflections. The locations of the VAs can be easily computed with the help of the floor plan. From the UWB channel impulse response (CIR), range estimates to the VAs can be obtained. The position of the agent can then be computed from these range estimates using statistical techniques.

As we have shown in [1], the availability of prior information about the agents position results in a potentially accurate and robust position estimator. In this contribution, we consider a moving agent, like the one shown in Fig. 1. The sequence of its positions will be correlated in time. Using appropriate techniques like state-space motion models and the corresponding estimation techniques, we can propagate

This work was partly supported by the Austrian Science Fund (FWF) within the National Research Network SISE project S10604-N13 and by the Austrian Research Promotion Agency (FFG) under grant number 814560 (COMAR).

978-1-4244-5864-6/10\$26.00 © IEEE

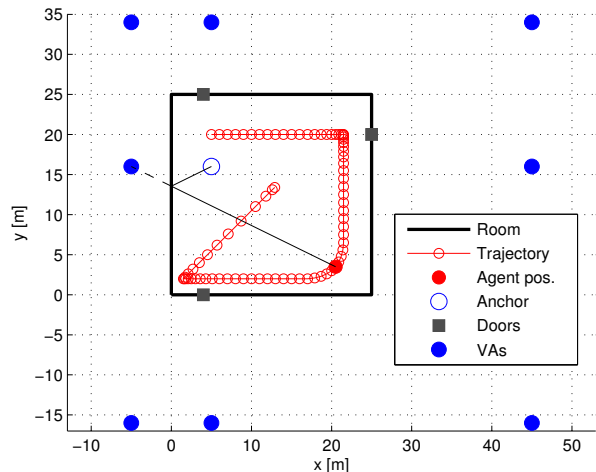


Fig. 1. Indoor positioning scenario with example room geometry and movement trajectory. There is only one physically existing anchor node, VA locations can be computed from the floor plan. Single- and double-reflection VAs are shown. The length of the single-reflection path from the anchor to the agent along the left wall equals the agents distance to the respective VA.

position knowledge from one time step to the next. In this manner, previous position estimates can be used as prior knowledge.

We show that the ubiquitous standard Kalman filter [2] is not useful for our approach, as our statistical models can either be multimodal or show heavy tails. There are numerous variants of the Kalman filter that account for such scenarios, e.g. [3], [4]. We will use a modified version of the Kalman filter that allows to alleviate measurement outliers. This filter needs a good and robust initialization, for which we propose a variant of the Gaussian sum filter [3]. To make full use of our specified statistical models, we use Bayesian filtering techniques [5]–[7]. Such techniques have often been successfully applied for localization, e.g. in [8] for tracking in UWB radar sensor networks.

We make explicit use of signal reflections together with floor plan information. The latter is often used only to truncate the search area, while e.g. in [9] such information is also used to discard invalid particle paths in a Bayesian filtering context. Reflected signal paths are often only seen as impairments that can lead to biased range estimates in non-line-of-sight (NLOS) scenarios. There is few work that actually exploits this information: [10] uses NLOS paths, with the need to estimate

not only range-, but also angular information of these paths, which leads to a potentially complex receiver. Single-bounce paths are also used in [11], where in addition to the angular parameters, also the Doppler shift is estimated. For an UWB link with single antennas on both link ends, [12] proposes an algorithm for anchor-less localization, but with an assumed LOS situation and a fixed number of multipaths. The concept of virtual anchors is also used in [13], where the reflections result in new nodes at unknown locations that contribute in the location estimation through cooperation. In [14], reflections from an UWB signal are used for imaging purposes, which corresponds to the well-known simultaneous localization and mapping problem.

The extraction of multipath components is a key step of our approach and is as such still ongoing work [15]. However, for MPC extraction, a wealth of publications exists, e.g. [16], [17]. Our approach combines the knowledge of the floor plan with the information embedded in the structure of the CIR to turn one anchor node into a set of VAs that provides rich localization information.

This paper is organized as follows: Section II introduces the mathematical and statistical models that are used, Section III discusses in detail the state-space estimation algorithms that were adapted to our problem. Finally, Section IV presents performance results and Section V draws conclusions and mentions important future and ongoing work.

Throughout the paper, column vectors are boldface and lowercase, matrices are boldface and uppercase, \mathbf{x}^T denotes the transposition of the vector \mathbf{x} and $\hat{\mathbf{x}}_k$ indicates an estimate of \mathbf{x}_k at the discrete time step k . A multivariate normal distribution for the random vector \mathbf{x} with mean vector \mathbf{m} and covariance matrix Σ is denoted by $\mathcal{N}(\mathbf{x}|\mathbf{m}, \Sigma)$

II. LOCALIZATION USING VIRTUAL ANCHORS

Using UWB signals, many of the reflected signal paths within a room are resolvable. For example, Fig. 2 shows an UWB CIR measured in a very recent campaign. It is well-known that such a CIR consists of a sum of delayed and scaled (and possibly distorted) copies of a transmitted pulse [18], which is well visible. A key step of our approach is to extract the delays of the MPCs, that correspond to the VAs from such a CIR. Using these delays, we can perform multilateration to estimate the agents position.

A. Static location estimation using VAs

The result of the MPC extraction step is a vector \mathbf{z} containing range estimates to the VAs. As discussed in detail in [1], we have to take several possible imperfections of this step into account: First, \mathbf{z} can contain entries that are not caused by an MPC (false positive detections), second, some reflected paths could be missed by the detection and third, we do not assume that the entries are mapped to the corresponding VAs. Because of these imperfections, we call \mathbf{z} a pseudodistance vector.

We have shown that a probabilistic model for one entry z_i of the pseudodistance vector \mathbf{z} can be given as a likelihood

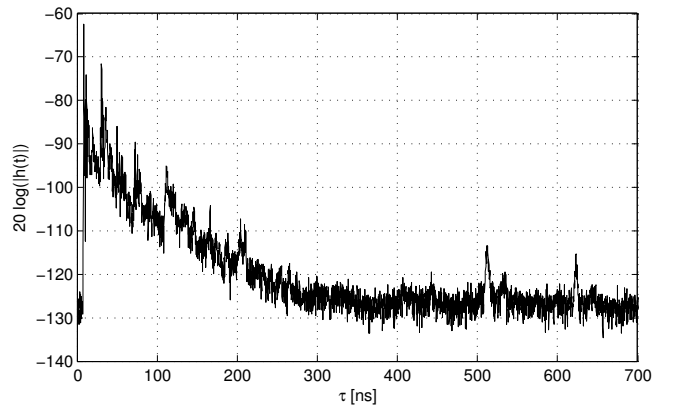


Fig. 2. Example for an UWB impulse response from a recent measurement campaign. Reflected paths are well visible as peaks over the noise floor.

function parameterized with the position \mathbf{p}

$$p_{z_i|\mathbf{p}}(z_i|\mathbf{p}) = P_{VA} \frac{1}{\sum_{n=1}^{N_{VA}} v_n} \sum_{n=1}^{N_{VA}} v_n \mathcal{N}(z_i | \|\mathbf{p} - \mathbf{p}_n\|, \sigma_n^2) + (1 - P_{VA}) p_{z_i, \overline{VA}|\mathbf{p}}(z_i|\mathbf{p}) \quad (1)$$

where P_{VA} is the probability that a z_i corresponds to a VA and v_n is the probability that the n -th VA at position \mathbf{p}_n is visible. N_{VA} is the number of VAs that are taken into account. Here, we use the direct signal path as well as single and double reflections, hence $N_{VA} = 9$. The PDF $p_{z_i, \overline{VA}|\mathbf{p}}(z_i|\mathbf{p})$ is the distribution of a z_i that resulted from a false detection. We select this PDF as a uniform distribution between zero and a maximum range value that is larger than the possible domain of VA-matched z_i . The distance estimates to the VAs follow a normal distribution around their true values $\|\mathbf{p} - \mathbf{p}_n\|$ with a variance σ_n^2 .

Assuming statistical independence of the N pseudodistances z_i , the joint likelihood function of \mathbf{z} can be expressed as

$$p_{\mathbf{z}|\mathbf{p}}(\mathbf{z}|\mathbf{p}) = \prod_{i=1}^N p_{z_i|\mathbf{p}}(z_i|\mathbf{p}) \quad (2)$$

An example for the log-likelihood $\ln(p_{\mathbf{z}|\mathbf{p}}(\mathbf{z}|\mathbf{p}))$ is shown in Fig. 3. We can observe that this functions shows a multimodal behavior, which is a result of the imperfections that it accounts for. A maximum-likelihood (ML) location estimate is given by

$$\hat{\mathbf{p}}_{ML} = \begin{bmatrix} \hat{p}_x \\ \hat{p}_y \end{bmatrix}_{ML} = \arg \max_{\mathbf{p}} p_{\mathbf{z}|\mathbf{p}}(\mathbf{z}|\mathbf{p}) \quad (3)$$

Performance results in [1] have shown that using this ML technique results in a potentially accurate, but not very robust estimator, as it contains large outliers. This is confirmed by Fig. 4, which shows a histogram of the ML position estimation error in the x -direction, $\text{Err}_{\hat{p}_x, ML} = p_{x, RX} - \hat{p}_{x, ML}$. We can observe that the estimator is unbiased but follows a heavy-tailed distribution. Assuming availability of prior information on the agents position substantially increased the robustness. The next subsection explains how to actually obtain this prior information.

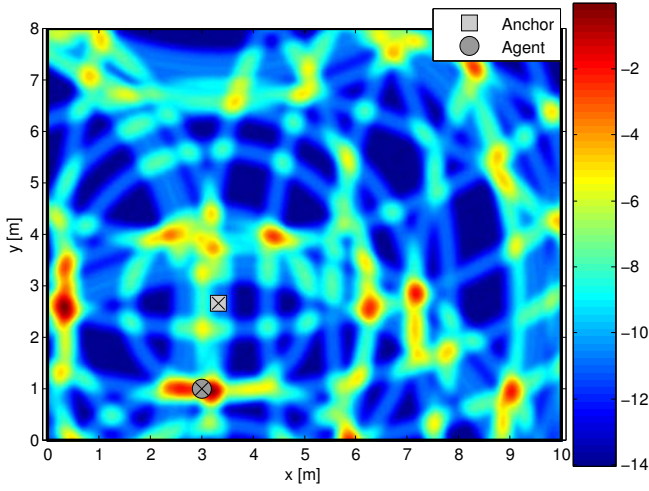


Fig. 3. Plot of measurement log-likelihood $\ln(p_{\mathbf{z}|\mathbf{p}}(\mathbf{z}|\mathbf{p}))$ for one specific realization of \mathbf{z} containing 5 VA-matched z_i and 5 false detections. In this case, the likelihood function is multimodal and the ML estimation chooses the wrong mode near $\mathbf{p} = [0.5, 2.5]^T$.

B. Localization of a moving agent

Let us assume we want to track the position of a moving agent in a room with known geometry. For the mathematical description, we will use a standard state-space model of the movement. We will consider a two-dimensional discrete-time model with time index k and a sampling time of ΔT . The state vector of the mobile agent at time k is defined as $\mathbf{x}_k = [p_x, p_y, v_x, v_y]^T$; it contains position and velocity in x and y directions. In general, a state-space model is defined by the two equations

$$\mathbf{x}_{k+1} = f_k(\mathbf{x}_k, \boldsymbol{\omega}_k) \quad (4)$$

$$\mathbf{y}_k = h_k(\mathbf{x}_k, \boldsymbol{\nu}_k) \quad (5)$$

where (4) is called the system- or state-propagation equation. It maps a state vector from one time step to the next, where $\boldsymbol{\omega}_k$ denotes the process noise [2]. The state vector itself is only accessible via the function $h_k(\mathbf{x}_k)$, which is therefore called the measurement equation. The vector $\boldsymbol{\nu}_k$ is the measurement noise.

A possible scenario is shown in Fig. 1. A movement like this can be described with a well-known linear dynamical motion model [19], [20]

$$\mathbf{x}_{k+1} = \underbrace{\begin{bmatrix} 1 & 0 & \Delta T & 0 \\ 0 & 1 & 0 & \Delta T \\ 0 & 0 & 1 & 0 \\ 0 & 0 & 0 & 1 \end{bmatrix}}_{\mathbf{F}} \mathbf{x}_k + \underbrace{\begin{bmatrix} \frac{\Delta T^2}{2} & 0 \\ 0 & \frac{\Delta T^2}{2} \\ \Delta T & 0 \\ 0 & \Delta T \end{bmatrix}}_{\mathbf{G}\mathbf{a}_k = \boldsymbol{\omega}_k} \mathbf{a}_k \quad (6)$$

where the function $f_k(\mathbf{x}_k) = f(\mathbf{x}_k)$ is linear and time-invariant. The vector \mathbf{a}_k contains acceleration noise in x and y directions and is transformed in position and velocity noise components via multiplication with the matrix \mathbf{G} . This can be interpreted as process noise in the linear system. It can also

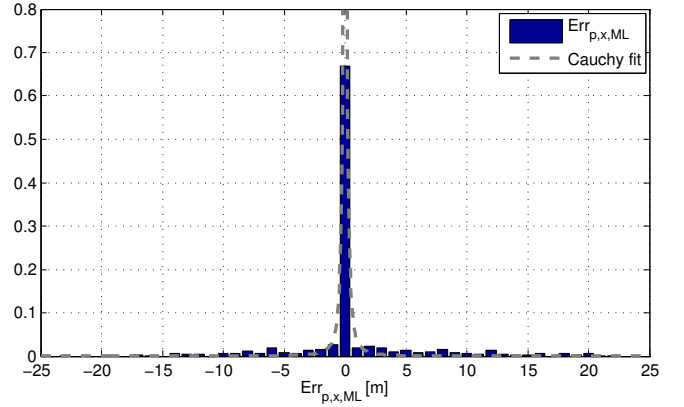


Fig. 4. Normalized histogram of position error in the x coordinate of the ML-estimate. The histogram indicates that this error follows a heavy-tail distribution. The grey dashed line is a fit of a Cauchy distribution to the ML error in the x -direction. The y -direction is distributed analogously.

be used as a deterministic driving input to the system, e.g. we used it to generate several different motion trajectories.

Concerning the measurement equation, we use two different types of measurements in this paper: First, we can take the ML position estimate at time step k , $\hat{\mathbf{p}}_{k,ML}$ from (3) as an input to a state-space filter. Second, we can directly take the pseudodistances in \mathbf{z} . Both possibilities require some discussion, which follows next.

1) *Maximum likelihood estimates as measurements*: In this case we define the measurements as $\mathbf{y}_k = \hat{\mathbf{p}}_{k,ML}$. Then we can write (5) as

$$\mathbf{y}_k = \underbrace{\begin{bmatrix} 1 & 0 & 0 & 0 \\ 0 & 1 & 0 & 0 \end{bmatrix}}_{\mathbf{H}} \mathbf{x}_k + \boldsymbol{\nu}_k \quad (7)$$

which, together with (6) is a linear state-space model, for which a standard Kalman filter would be applicable.

A Kalman filter is the optimal estimator in the minimum mean squared error sense for such a linear model if the noise terms are Gaussian. But a look at Fig. 4 suggests that this is not the case. A probabilistic model of the measurement error could be a sharply peaked unimodal, but heavy-tailed distribution. Approximating $\boldsymbol{\nu}_k$ as a zero-mean Gaussian noise term facilitates computations but fails to capture the large outliers. More appropriate heavy-tailed distributions can be obtained using the family of α -stable distributions [21], for which the Cauchy distribution is a special case that has a closed-form PDF. Dropping the time index, a bivariate isotropic Cauchy distribution over the vector $\boldsymbol{\nu}$ with location parameter vector $\mathbf{m} = [m_x, m_y]^T$ and width parameter β is denoted as $\mathcal{C}(\boldsymbol{\nu}|\mathbf{m}, \beta)$ and has the PDF [22]

$$p(\boldsymbol{\nu}) = \frac{\beta}{2\pi} [(v_x - m_x)^2 + (v_y - m_y)^2 + \beta^2]^{-3/2}. \quad (8)$$

Here, the width parameter β is linked to the interquartile range [23] and the location parameters m_x and m_y are medians in x - and y -direction. Fig. 4 contains a fit of a Cauchy distribution

to $\text{Err}_{\hat{\mathbf{p}},x,\text{ML}}$ where $m_x = 0$ and β is chosen as half the interquartile range of the error samples. We can also extend our noise model with the knowledge of the room dimensions. In this case, the distribution is a truncated bivariate isotropic Cauchy distribution which is defined as

$$\bar{\mathcal{C}}(\boldsymbol{\nu}|\mathbf{m}, \beta) = \begin{cases} Z \cdot \mathcal{C}(\boldsymbol{\nu}|\mathbf{m}, \beta) & |\nu_x| \leq d_x \text{ and } |\nu_y| \leq d_y \\ 0 & \text{otherwise.} \end{cases} \quad (9)$$

where d_x and d_y are the dimensions of the rectangular room. The normalization constant Z ensures that $\bar{\mathcal{C}}(\cdot)$ is a proper PDF. As this is not important for the cases where we will actually use this distribution, we will drop the factor Z .

2) *Pseudodistance vector as measurement*: If we define the measurements as the pseudodistance vector, i.e. $\mathbf{y}_k = \mathbf{z}_k$, we do not end up at a deterministic closed-form measurement equation such as (7). This is due to the possible imperfections of the MPC-extraction discussed in Section II-A. If we have an estimate of the state vector $\hat{\mathbf{x}}_k$ available, then we can rate the plausibility of its position entries $\hat{\mathbf{p}}_k = \mathbf{H}\hat{\mathbf{x}}_k = [\hat{p}_x, \hat{p}_y]^T$ via the likelihood function given in (2) and (1). Hence, a likelihood for the measurements, given a position estimate $\hat{\mathbf{x}}_k$ can be given as

$$p(\mathbf{y}_k|\hat{\mathbf{x}}_k) = p_{\mathbf{z}|\mathbf{p}}(\mathbf{z}_k|\mathbf{p} = \mathbf{H}\hat{\mathbf{x}}_k) \quad (10)$$

We observe that in this case there is no deterministic measurement equation $h_k(\cdot)$. This is the consequence of a lack of a mapping of the z_i to the VAs, and makes the application of Kalman-filter-like schemes impossible. Instead, we resort to Bayesian state-space estimation concepts and implement them using Particle filters. Those can deal with a purely probabilistic description of the measurements. Also, it is well-known that particle filters perform better than Kalman filters if the PDF of the measurements is multimodal in the domain of the state vector. As confirmed by Fig. 3, we have to deal with such a scenario.

A third possible choice concerning the measurements is to again take the pseudodistances and perform a mapping of its entries to the VAs. Then an extended Kalman filter using the range measurements would be applicable. Such a mapping scheme is subject of ongoing research.

III. STATE SPACE ESTIMATORS

In the previous section we have shown that the virtual-anchor-based localization problem can be formulated as a standard state-space estimation problem. A block diagram of the overall system is shown in Fig. 5. The MPC extraction estimates a vector of distances to the VAs from the received UWB signal $r_k(t)$. This vector is processed by the static VA-based position estimation block, that computes the measurement likelihood function for \mathbf{z}_k and an ML estimate. Both are passed to the state-space estimator that either uses the ML-estimate or \mathbf{z}_k directly as its measurements. The different algorithms that can be used in the latter block are the subject of this subsection.

The state-space estimation problem can be solved using recursive Bayesian state estimation. Our aim is to estimate

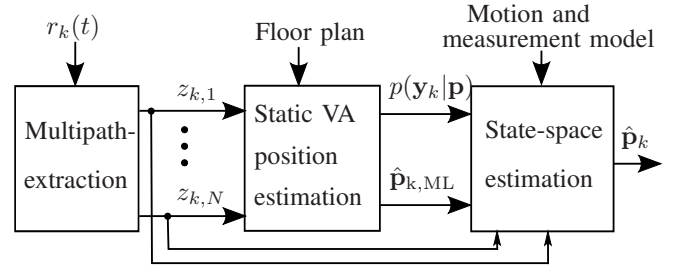


Fig. 5. Conceptual localization scheme at time k using multipath extraction from the received signal $r_k(t)$, subsequent computation of the likelihood as a function of the position, followed by a state-space estimator. The latter can use either the ML-estimate or the likelihood function plus the pseudodistances as measurements.

the posterior distribution of the state vector \mathbf{x}_k , given all measurements up to and including time k . Denoting the latter set of measurements as \mathbf{Y}_k , this posterior PDF is written as $p(\mathbf{x}_k|\mathbf{Y}_k)$. It is well-known [2], [6], [7], that this problem can be solved using a sequence of prediction/update calculations. In the prediction step, we calculate the *a-priori* estimate of the PDF of \mathbf{x}_k

$$p(\mathbf{x}_k|\mathbf{Y}_{k-1}) = \int p(\mathbf{x}_k|\mathbf{x}_{k-1})p(\mathbf{x}_{k-1}|\mathbf{Y}_{k-1})d\mathbf{x}_{k-1} \quad (11)$$

which is the PDF of the state vector before taking the current measurement \mathbf{y}_k into account. Equation (11) is known as the Chapman-Kolmogorov equation. In principle, it forms the new a-priori PDF of the state by using the transition density $p(\mathbf{x}_k|\mathbf{x}_{k-1})$ together with the posterior PDF from the previous time step $p(\mathbf{x}_{k-1}|\mathbf{Y}_{k-1})$ and marginalizing out the previous state vector.

At the time k , the new measurement is available and we can calculate the posterior PDF in the update step

$$p(\mathbf{x}_k|\mathbf{Y}_k) = \frac{p(\mathbf{y}_k|\mathbf{x}_k)p(\mathbf{x}_k|\mathbf{Y}_{k-1})}{\int p(\mathbf{y}_k|\mathbf{x}_k)p(\mathbf{x}_k|\mathbf{Y}_{k-1})d\mathbf{x}_k}. \quad (12)$$

Here, we need to evaluate the measurement likelihood $p(\mathbf{y}_k|\mathbf{x}_k)$ as well as the a-priori PDF from the prediction step. Both the transition density in the prediction step and the measurement likelihood in the update step can be obtained using probabilistic descriptions of (4) and (5) using the PDFs of the respective noise terms. To start the recursion, we need to select an initial guess of the state vector PDF $p(\mathbf{x}_0|\mathbf{Y}_0) = p(\mathbf{x}_0)$.

In theory, (11) and (12) give access to the full posterior PDF of the state vector. In practice, both equations can be solved analytically only for special cases, e.g. if the model and the measurement equation are linear and the noise terms are Gaussian. Then, the Kalman-filter is the optimal state-space estimator. In many other cases, we need to calculate approximations of the posterior PDF of the state. One possibility is to use a set of N_p candidate state vectors, called *particles*, at which (11) and (12) are evaluated. The state-space estimators that we use in our localization scheme are the subject of the next section.

A. Kalman filter with measurement refinement

Using a standard Kalman filter with the motion model in (6) and the ML-estimates of the position as measurements, i.e. (7), does not give satisfying results. Although both state-propagation and measurement equations are linear, the measurement noise is non-Gaussian as it contains large outliers.

We propose a modification of the standard Kalman filter that exploits the correlation of successive agent positions on a trajectory like shown in Fig. 1. For prediction and update phases, we use the standard Kalman filter equations [2]. The KF assumes that the PDF of the state vector is Gaussian and recursively estimates mean and covariance. We denote a-priori estimates with a minus and a-posteriori estimates with a plus in the superscript. The matrix $\mathbf{P}_k = \mathbb{E}\{(\mathbf{x}_k - \hat{\mathbf{x}}_k)(\mathbf{x}_k - \hat{\mathbf{x}}_k)^T\}$ is the estimation error covariance matrix and \mathbf{Q}_k and \mathbf{R}_k are the covariance matrices of process and measurement noise, respectively. Then, the KF equations are

$$\hat{\mathbf{x}}_k^- = \mathbf{F}\hat{\mathbf{x}}_{k-1}^+ \quad (13)$$

$$\mathbf{P}_k^- = \mathbf{F}\mathbf{P}_{k-1}^+\mathbf{F}^T + \mathbf{Q}_{k-1} \quad (14)$$

for the prediction phase of the Kalman filter, and

$$\mathbf{K}_k = \mathbf{P}_k^- \mathbf{H}^T (\mathbf{H}\mathbf{P}_k^- \mathbf{H}^T + \mathbf{R}_k)^{-1} \quad (15)$$

$$\mathbf{P}_k^+ = (\mathbf{I} - \mathbf{K}_k \mathbf{H}) \mathbf{P}_k^- (\mathbf{I} - \mathbf{K}_k \mathbf{H})^T + \mathbf{K}_k \mathbf{R}_k \mathbf{K}_k^T \quad (16)$$

$$\hat{\mathbf{x}}_k^+ = \hat{\mathbf{x}}_k^- + \mathbf{K}_k (\mathbf{y}_k - \mathbf{H}\hat{\mathbf{x}}_k^-) \quad (17)$$

for the update phase.

Our variant of the Kalman filter modifies the measurement \mathbf{y}_k given in (7) to reduce the outliers. Under the assumption that \mathbf{x}_{k-1}^+ represents a relatively "good" estimate of the state vector, we can expect that \mathbf{x}_k will be in the vicinity of it, bounded by the finite velocity of the agent. Hence we define a Gaussian position prior centered at the predicted position $\hat{\mathbf{p}}_k^- = \mathbf{H}\hat{\mathbf{x}}_k^-$ as

$$p_k(\mathbf{p}) = \mathcal{N}(\mathbf{p} \mid [\hat{p}_{x,k}^-, \hat{p}_{y,k}^-]^T, \sigma_p^2). \quad (18)$$

The prior variance σ_p^2 is a design parameter that should be chosen such that it allows for a movement with the expected maximum of the velocity. The actual measurement used in the update phase of the KF is then obtained by replacing the ML-position estimate with a MAP-estimate

$$\mathbf{y}_k = \arg \max_{\mathbf{p}} p_k(\mathbf{p}) p_{\mathbf{z}|\mathbf{p}}(\mathbf{z}|\mathbf{p}) \quad (19)$$

where the prior attenuates incorrect maxima of the multimodal measurement likelihood function of the pseudodistance vector.

The assumption of a reasonably good estimate from the previous time step boils down to a careful initialization of the algorithm with proper $\hat{\mathbf{x}}_0^+$ and \mathbf{P}_0^+ . An outline of the algorithm is described in Table I.

B. Initialization – Gaussian sum filter

In the KF with measurement refinement, a correct initialization of the algorithm is crucial, as the prediction using the initial state vector defines the mean of the first position prior. In practice, the initialization using this algorithm can be

TABLE I
KALMAN FILTER WITH MEASUREMENT REFINEMENT

```

@k = 0 do: Choose initial estimates  $\hat{\mathbf{x}}_0^+$  and  $\mathbf{P}_0^+$ 
for all k > 0 do
    procedure KALMANREF( $\mathbf{x}_{k-1}^+, \mathbf{P}_{k-1}^+$ )
        Predict  $\hat{\mathbf{x}}_k^-$  and  $\mathbf{P}_k^-$  using (13) and (14)
        Set up position prior  $\mathcal{N}(\mathbf{p} \mid [\hat{p}_{x,k}^-, \hat{p}_{y,k}^-]^T, \sigma_p^2)$ 
        Select refined measurement  $\mathbf{y}_k$  according to (19)
        Calculate  $\hat{\mathbf{x}}_k^+$  and  $\mathbf{P}_k^+$  as in (15), (16) and (17)
        return  $\hat{\mathbf{p}}_k = \mathbf{H}\hat{\mathbf{x}}_k^+$ 
    end procedure
end for
    
```

done in the following way: Instead of following just one state trajectory hypothesis, we use multiple weighted hypotheses. This can be done using the concept of a Gaussian sum filter (GSF) [3], where the state vector posterior PDF is represented by a Gaussian mixture of the form

$$p(\hat{\mathbf{x}}_k^+) = \sum_{i=1}^M a_{k,i} \mathcal{N}(\mathbf{x}_k \mid \hat{\mathbf{x}}_{k,i}^+, \mathbf{P}_{k,i}^+). \quad (20)$$

In principle, this is equivalent to a bank of M parallel Kalman filters, where we will use our modified KF from the previous section. To choose the weights $a_{k,i}$, we look at the *innovation* process of each KF. It is defined as the term in the brackets on the right hand side of (17)

$$\mathbf{r}_{k,i} = \mathbf{y}_{k,i} - \mathbf{H}\hat{\mathbf{x}}_{k,i}^- \quad (21)$$

According to theory [2], this should be a zero-mean Gaussian white noise process with covariance matrix $\mathbf{H}\mathbf{P}_{k,i}^- \mathbf{H}^T + \mathbf{R}_{k,i}$. Hence, a relative confidence measure of the estimate of each KF can be computed as

$$\beta_{k,i} = \mathcal{N}(\mathbf{r}_{k,i} \mid \mathbf{0}, \mathbf{H}\mathbf{P}_{k,i}^- \mathbf{H}^T + \mathbf{R}_{k,i}). \quad (22)$$

Subsequently the weights $a_{k,i}$ are obtained as in [3]

$$a_{k,i} = \frac{a_{k-1,i} \beta_{k,i}}{\sum_{j=1}^M a_{k-1,j} \beta_{k,j}}. \quad (23)$$

The original motivation of the GSF was to represent a non-Gaussian state vector PDF by a combination of all M KFs using (20). Our intention is to just represent M state vector hypotheses and find the one closest to the true trajectory with the help of the $a_{k,i}$. Simulations showed that the KFs that are initialized rather far away from the true trajectory have quickly decaying weights and could in principle also be discarded after the initialization phase. To draw our state vector estimate, we do not combine the KFs, we just take the $\hat{\mathbf{x}}_{k,i}^+$ with the maximum corresponding weight.

The algorithm is outlined in Table II. It can handle the initialization problem as follows: At $k = 0$, the M initial state vectors are chosen. We identify two scenarios, depending on our prior knowledge. The first case corresponds to a scenario where we do not know anything about the initial agent position, so we choose the initial positions randomly, according to a uniform distribution bounded by the room dimensions. The initial velocities are set to zero. In the second

TABLE II
 GAUSSIAN SUM FILTER

```

@k = 0 do
for all i = 1..M do
    Set  $a_{0,i} = 1/M$ 
    Choose initial estimates  $\hat{\mathbf{x}}_{0,i}^+$  and  $\mathbf{P}_{0,i}^+$ 
end for
for all k > 0 do
    procedure GSF( $\{\mathbf{x}_{k-1,i}^+, \mathbf{P}_{k-1,i}^+, a_{k-1,i}\}_{i=1}^M, M$ )
        for all i = 1..M do
            Perform KALMANREF( $\mathbf{x}_{k-1,i}^+, \mathbf{P}_{k-1,i}^+$ )
        end for
        Update weights  $\{a_{k,i}\}_{i=1}^M$  using (23)
        Select  $i_{\max} = \arg \max_i \{a_{k,i}\}$ 
        return  $\hat{\mathbf{p}}_k = \mathbf{H}\hat{\mathbf{x}}_{k,i_{\max}}^+$ 
    end procedure
end for
    
```

case, we assume that we are monitoring movement within a room and we set the initial positions equal to the known locations of the room doors, where M equals the number of doors. The initial velocities can be selected such that they point in a direction orthogonal to the corresponding wall and inside the room, to represent the entry through this door.

C. Particle filter

Both the KF with refined measurements and the GSF are variants of the Kalman filter, that treat the measurement noise as Gaussian. Although the measurement refinement procedure should decrease the influence of large outliers of the ML-estimate, it does not model the measurement noise term correctly as we have seen in Section II-A. Also, we still want to obtain a state-space estimator that uses the pseudodistance vector \mathbf{z}_k and the associated likelihood function (2) directly. Both objectives can be handled using particle filters, which are an implementation of the recursive Bayesian state estimator in (11) and (12) using Monte Carlo techniques. Therefore, they belong to the family of sequential Monte Carlo algorithms [6], [7].

A PF uses a set of N_p particles (candidate state vectors) and corresponding weights. Our chosen PF variant corresponds to a sampling-importance-resampling (SIR) PF, where resampling is performed at every time step. After the update phase at each time step k the particles are distributed according to the state posterior PDF $p(\mathbf{x}_k | \mathbf{Y}_k)$. The set of a-priori particles, obtained by using (4) at time k , is denoted as $\{\hat{\mathbf{x}}_{k,i}^-\}_{i=1}^{N_p}$ and the set of weights as $\{w_{k,i}\}_{i=1}^{N_p}$. In the update phase, the measurement \mathbf{y}_k is taken into account. This is done by evaluating the likelihood of the measurement, given each particle. These likelihoods are the weights of the particles, which are then normalized such that they sum up to one. The last step is the resampling of the particles, which results in the posterior particles, which are denoted by a plus in the superscript. The resampling is done by drawing the particles with replacement from the multinomial distribution over the a-priori particles, with probabilities given by the weights. After resampling, the weights are reset to a value of $1/N_p$.

The advantage of using a PF is, that it allows for a more appropriate statistical modeling of noise PDF and measurement likelihood function. These statistical descriptions have been outlined in Section II-B. We now briefly discuss the different phases of our PF, an algorithm outline is found in Table III.

1) *Initialization phase:* The initialization of the PF can be done similar to the GSF in the previous subsection: One possibility is to select the position entries of the initial particles uniformly distributed within the room, with the velocities at zero. Another possibility is to sample the positions of the initial particles from a mixture of M (equal to the number of doors) truncated bivariate Gaussians, each one centered at the position of one of the room doors. In simulations, choosing the door initialization did not lead to a considerable gain in performance. The PF was able to rapidly lock on the trajectory also with the complete random initialization.

2) *Prediction phase of the PF:* At each time step k , a set of new a-priori particles $\{\hat{\mathbf{x}}_{k,i}^-\}_{i=1}^{N_p}$ is obtained by passing the posterior particles from $k-1$ through the state propagation equation (4). Here, the linear motion model (6) is used and the noise term \mathbf{a}_k is a zero-mean Gaussian with covariance $\mathbf{I}\sigma_a^2$. Hence, the a-priori particles are distributed as

$$\hat{\mathbf{x}}_{k,i}^- \sim \mathcal{N}(\mathbf{x}_{k,i}^- | \mathbf{F}\hat{\mathbf{x}}_{k-1,i}^+, \sigma_a^2 \mathbf{G}\mathbf{G}^T), \quad i \in \{1 \dots N_p\} \quad (24)$$

i.e. they follow a Gaussian distribution, from which they can be sampled conveniently. The variance σ_a^2 has to be chosen large enough such that a change in movement with the highest expected acceleration is possible.

3) *Update phase: ML measurements and Cauchy likelihood:* As we have seen in Fig. 4, the measurement noise term can be modeled using a truncated bivariate isotropic Cauchy distribution $\bar{\mathcal{C}}(\cdot)$ for $\mathbf{y}_k = \hat{\mathbf{p}}_{k,\text{ML}}$. Using the PF, we can easily model this behavior. The weights of the particles are computed as the value of $\bar{\mathcal{C}}(\cdot)$ centered at the ML-estimate evaluated at the position coordinates of the particles

$$w_{k,i} = \bar{\mathcal{C}}(\mathbf{H}\hat{\mathbf{x}}_{k,i}^- | \hat{\mathbf{p}}_{k,\text{ML}}, \beta). \quad (25)$$

This distribution differs from the definition in (9) in the truncation: Here, $\bar{\mathcal{C}}(\cdot)$ is only non-zero if both x and y coordinates of the particle are within the room. With this definition, particles outside the room are automatically discarded as their weight will be zero and therefore also the probability of resampling. The width β is a design parameter that can be chosen as outlined in section II-B1.

4) *Update phase: Pseudodistance measurements and likelihood model:* Here, $\mathbf{y}_k = \mathbf{z}_k$ and the likelihood function for the particles is given in (2) and (1)

$$w_{k,i} = p_{\mathbf{z}|\mathbf{p}}(\mathbf{z}_k | \mathbf{H}\hat{\mathbf{x}}_{k,i}^-). \quad (26)$$

Also this function is zero for a position coordinate outside the room.

5) *Location estimation using the posterior particles:* The next step is to resample the particles according to their weights. The step results in the posterior particles, that are distributed according to the state vector posterior PDF. Hence, any desired

TABLE III
PARTICLE FILTER WITH ML-POSITION- OR
PSEUDODISTANCE-MEASUREMENTS

```

@k = 0 do Select initial set of particles  $\{\hat{\mathbf{x}}_{0,i}^+\}_{i=1}^{N_p}$ 
for all k > 0 do
    procedure PF( $\{\mathbf{x}_{k-1,i}^+\}_{i=1}^{N_p}, \hat{\mathbf{p}}_{k,\text{ML}}, \mathbf{z}_k$ )
        for all i = 1 ≤ Np do
            Sample a-priori particle  $\hat{\mathbf{x}}_{k,i}^-$  according to (24)
            if  $\mathbf{y}_k = \hat{\mathbf{p}}_{k,\text{ML}}$  then ▷ ML-estimates
                Evaluate weight  $w_{k,i}$  as in (25)
            else if  $\mathbf{y}_k = \mathbf{z}_k$  then ▷ pseudodistances
                Evaluate weight  $w_{k,i}$  as in (26)
            end if
        end for
        Normalize weights
        Resample particles to get  $\{\hat{\mathbf{x}}_{k,i}^+\}_{i=1}^{N_p}$ 
        return  $\hat{\mathbf{p}}_k = \text{median}(\{\mathbf{H}\hat{\mathbf{x}}_{k,i}^+\}_{i=1}^{N_p})$ 
    end procedure
end for
    
```

estimate can be approximated. In performance simulations, we observed that the median of each component yields satisfying results. This is due to the fact that the median is more robust to clouds of particles that correspond to outliers than the mean. Such outliers can be the result of particles that are resampled at wrong modes of the multimodal range likelihood function. Choosing the median of the posterior distribution corresponds to a minimization of the absolute error [24].

IV. PERFORMANCE RESULTS

For performance simulations, we selected typical indoor localization scenarios. A scenario consists of a trajectory, that is a sequence of agent positions and velocities, as well as a given room geometry and the position of the single anchor node. One is the trajectory shown in Fig. 1, the other one is shown in Fig. 6. The scenarios represent indoor pedestrian movement at varying velocity. In these simulations, the anchor node is used and denoted as the transmitter (TX), but the roles of TX and receiver (RX) can of course also be reversed.

The parameters of the statistical model for the pseudodistance vector in (1) have been set as follows: We chose $P_{VA} = 0.5$, which means that we expect half of the z_i in one MPC-extraction process to be false detections. The visibilities of the VAs v_n are chosen such that the LOS path, the single reflection VAs and the double reflection VAs are visible with probabilities of 0.8, 0.5 and 0.3, respectively. It should be noted, that the actual visibilities are drawn independently for each position of the RX, which could correspond to a scenario with lots of additional scatterers like furniture or moving people. Correlation of the visibilities over time are subject of current research. The standard deviation of the distance estimates to the VAs, σ_n has been selected as 10 cm.

Fig. 7 shows the CDF of the position estimation error $\text{Err}_{\hat{\mathbf{p}}} = \|\mathbf{p}_{\text{RX}} - \hat{\mathbf{p}}\|$ for 50 simulated runs over the trajectory shown in Fig. 6. On average, the PF with the pseudodistance measurements shows the best performance. About 90% of the estimates are within 43 cm. Also its error floor is small and is just due to the random initialization. The other estimators

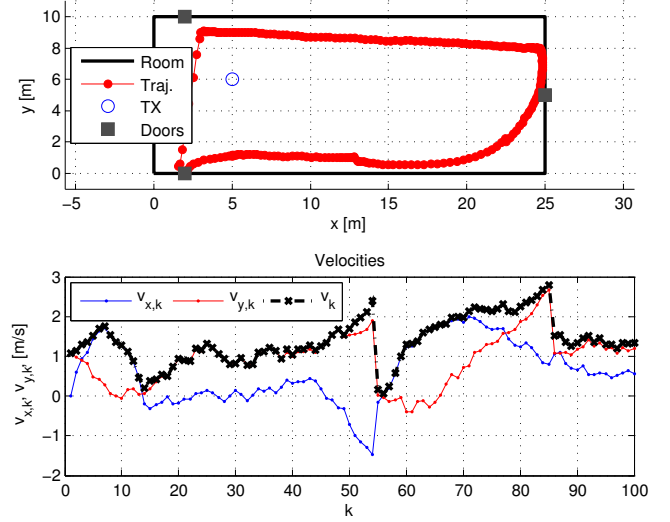


Fig. 6. Indoor pedestrian motion scenario. Top plot shows the sequence of 245 positions in the room and the lower plot shows the velocity components for $k \leq 100$. A pedestrian enters the room through the door in the south-west and then walks along the walls with varying velocity, including some stops. This could model a maintenance worker or a visitor in a museum gallery.

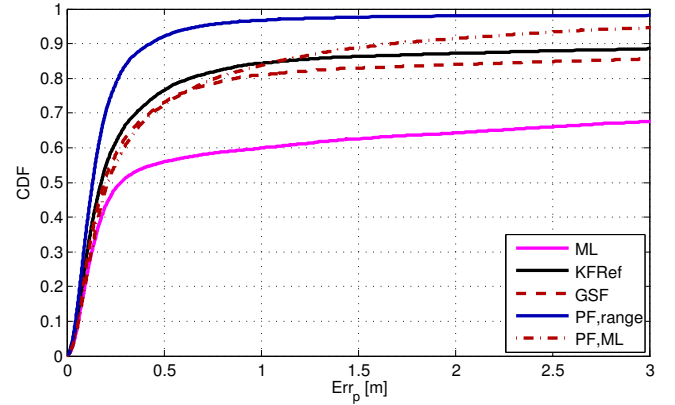


Fig. 7. CDF of the position errors for 50 runs over the trajectory in Fig. 6. The average behaviour of the estimators can be observed.

show a substantially better performance than the ML-estimate, on which all of them are based. Their error floor is caused by occasional divergence of the KF and the GSF. It is well-known that Kalman filters can diverge if model assumptions do not hold, which in our case corresponds to the non-Gaussian measurement noise. In this scenario, five of the 50 runs showed diverging results. In case of the PF with ML-measurements, the error floor is caused by the fact that this estimator is still influenced by the ML-outliers, though much less than a standard KF. Taking the pseudodistances as measurements is seemingly the best way to deal with the multimodality of the likelihood function (2). This is due to the fact that the decision for the correct mode is here in the responsibility of the tracking algorithm, and not the ML-estimation based on just the current time step.

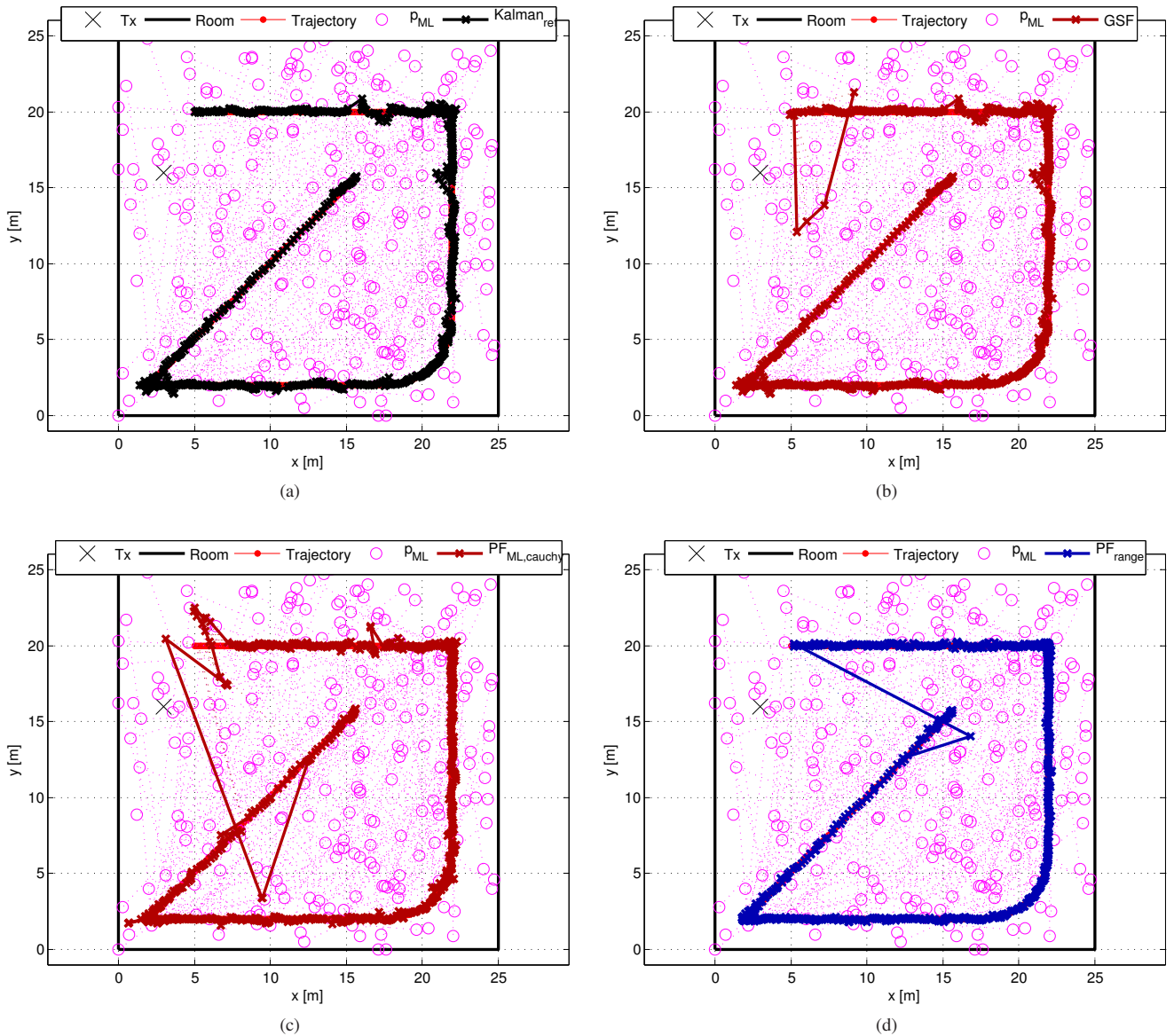


Fig. 8. Performance results for the four state-space filters over the trajectory from Fig. 1, starting point is in the north-west. Magenta circles are outliers of the ML-estimates ($\text{Err}_{\text{PML}} > 1$ m). The dotted lines connect the ML-estimates to their respective true positions. (a) Kalman filter with measurement refinement and perfect initialization. (b) Gaussian sum filter with $M = 10$ uniformly random selected components. (c) Particle filter with ML-estimates and Cauchy error model and $N_p = 2000$ particles. (d) Particle filter with pseudodistances and $N_p = 2000$ particles.

A comparison of all four estimators for the scenario in Fig. 1 can be found in Fig. 8 and 9. This scenario supports the previous results from e.g. Fig. 7, i.e., KF with measurement refinement and GSF show similar performance. The KF is initialized here with the true initial state vector, while the GSF draws $M = 5$ random initial state vectors. It converges quickly to the correct trajectory. The PF with the ML-estimates as measurements is again more influenced by their outliers than the one using pseudodistances. Both PFs use $N_p = 2000$ particles. Increasing this number leads to better robustness. Concerning the initialization, both PFs use particles that are randomly drawn according to a uniform distribution within

the room. Both converge to the true trajectory, the PF using pseudodistances is considerably faster. Looking at the error CDFs in Fig. 9 confirms the ability of the state-space methods to enhance both accuracy and also to a large extent the reliability in terms of avoiding the error floor.

An additional comparison of the proposed estimators can be found in Fig. 10 and Fig. 11. This trajectory consists of movement with longer stop phases. It can also illustrate the initialization phases of the different filters. In Fig. 10, the performance of the GSF is shown. The door positions are known via the floor plan. Therefore, $M = 3$ and the corresponding initial Gaussian position hypotheses are placed at the door positions. This leads to a very quick convergence.

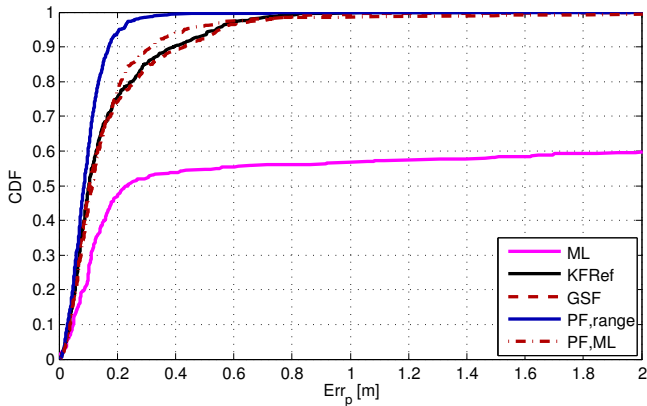


Fig. 9. CDF of the position error for the scenario shown in Fig. 8. All estimators show accurate and robust performance, even though the ML estimation shows a large percentage of outliers. For the PF using the pseudodistances, 80% of the estimators are within 15 cm. For the other estimators, this value is at about 25 cm.

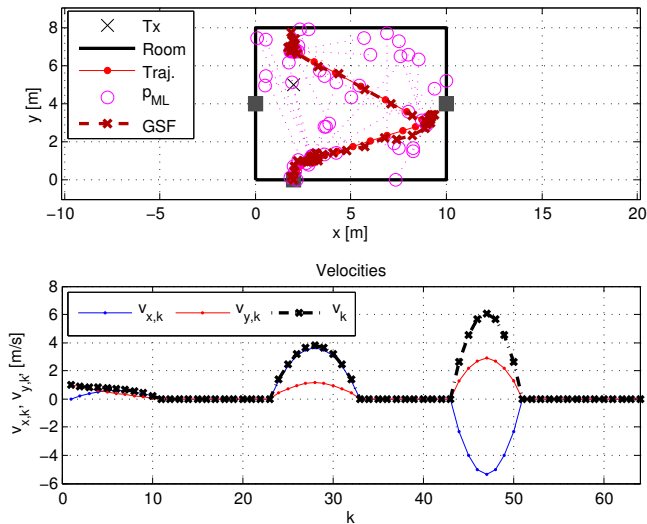


Fig. 10. Localization scenario with three doors and the Gaussian sum filter, starting point is the door at the south. The bottom plot shows the velocities for this scenario. Inbetween rather fast movements, there are also longer stop phases.

It should be mentioned, that in a case where the first few ML-estimates are outliers that come to lie in the vicinity of an incorrect initialization point, the GSF will be impaired and the convergence will take severely longer. Fig. 11 illustrates the excellent initialization capabilities of the PF, here the one with pseudodistance measurements. The comparison is between an initialization of all particles uniformly across the room and the initialization with truncated Gaussians at the doors. Both converge fast to the correct trajectory, the latter is a bit faster taking about 3 time steps while the uniformly initialized PF takes 7 time steps. A further advantage of the PF is its robustness to dynamic movement. It is difficult to optimize the fixed state noise variance parameter for KF and

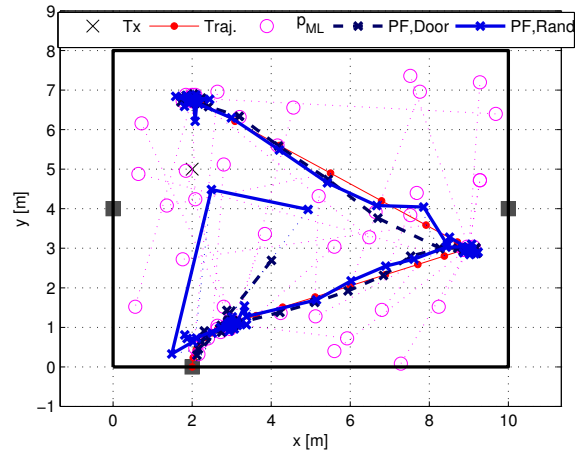


Fig. 11. Localization scenario like in Fig. 10. The solid blue line shows the performance of the PF with pseudodistance measurements and $N_p = 2000$ for a random initialization of the particles uniformly across the room. The dashed line denotes the same PF where $N_p/3$ particles are initialized corresponding to a truncated bivariate Gaussian centered at each door, respectively.

GSF, because a trade-off between fast movement and stop phases has to be found. For the PF, this is not a problem due to the median operation on the posterior particles, which makes the PF also robust in stop phases.

V. CONCLUSIONS AND FUTURE WORK

We have demonstrated an indoor positioning concept exploiting the reflections of UWB radio signals with virtual anchors. Using several tracking algorithms, we have shown by simulations that this approach can deliver both accurate and robust location estimation, taking into account several possible measurement impairments. We have introduced specialized variants of popular state-space estimators to account for the impairments in our statistical models. Most importantly, we address multimodality or heavy-tail behavior in our measurement likelihood functions, which both are known to substantially impair standard state-space methods. The performance has been demonstrated by simulations for indoor pedestrian movement trajectories. Also the problem of initialization of the state-space approaches has been treated by discussing possibilities to initialize the estimators at user-chosen points of interest, e.g. room doors.

Future work will deal with the validation and extension of our statistical measurement model through the analysis of recently measured UWB channels along reference trajectories. Also, we will extend our statistical models to include the virtual anchors, their locations and their visibility in the tracking process.

REFERENCES

- [1] P. Meissner, C. Steiner, and K. Witrisal, "UWB Positioning with Virtual Anchors and Floor Plan Information," in *Proc. 7th Workshop on Positioning, Navigation and Communication, WPNC 2010*, 2010.
- [2] D. Simon, *Optimal State Estimation*, 1st ed. Wiley, 2006.

- [3] D. Alspach and H. Sorenson, "Nonlinear Bayesian estimation using Gaussian sum approximations," *Automatic Control, IEEE Transactions on*, vol. 17, no. 4, pp. 439 – 448, aug 1972.
- [4] C. Masreliez and R. Martin, "Robust bayesian estimation for the linear model and robustifying the Kalman filter," *Automatic Control, IEEE Transactions on*, vol. 22, no. 3, pp. 361 – 371, jun 1977.
- [5] D. Fox, J. Hightower, L. Liao, and D. Schulz, "Bayesian Filtering for Location Estimation," *Pervasive Computing*, 2003.
- [6] O. Cappe, S. Godsill, and E. Moulines, "An Overview of Existing Methods and Recent Advances in Sequential Monte Carlo," *Proceedings of the IEEE*, vol. 95, no. 5, pp. 899 –924, may 2007.
- [7] M. Arulampalam, S. Maskell, N. Gordon, and T. Clapp, "A tutorial on particle filters for online nonlinear/non-Gaussian Bayesian tracking," *Signal Processing, IEEE Transactions on*, vol. 50, no. 2, pp. 174 –188, feb 2002.
- [8] M. Chiani, A. Giorgetti, M. Mazzotti, R. Minutolo, and E. Paolini, "Target detection metrics and tracking for UWB radar sensor networks," in *Ultra-Wideband, 2009. ICUWB 2009. IEEE International Conference on*, 9-11 2009, pp. 469 –474.
- [9] Widyawan, M. Klepal, and S. Beauregard, "A Backtracking Particle Filter for fusing building plans with PDR displacement estimates," in *Positioning, Navigation and Communication, 2008. WPNC 2008. 5th Workshop on*, march 2008, pp. 207 –212.
- [10] H. Miao, K. Yu, and M. Juntti, "Positioning for NLOS Propagation: Algorithm Derivations and Cramer-Rao Bounds," *Vehicular Technology, IEEE Transactions on*, vol. 56, no. 5, pp. 2568 –2580, sept. 2007.
- [11] K. Papakonstantinou and D. Slock, "Direct Location Estimation using Single-Bounce NLOS Time-Varying Channel Models," in *Vehicular Technology Conference, 2008. VTC 2008-Fall. IEEE 68th*, 21-24 2008, pp. 1 –5.
- [12] V. La Tosa, B. Denis, and B. Uguen, "Maximum Averaged Likelihood Estimation Tree for Anchor-Less Localization Exploiting IR-UWB Multipaths," in *Vehicular Technology Conference (VTC 2010-Spring), 2010 IEEE 71st*, 16-19 2010, pp. 1 –5.
- [13] Y. Shen and M. Win, "On the use of multipath geometry for wideband cooperative localization," in *Global Telecommunications Conference, 2009. GLOBECOM 2009. IEEE*, 30 2009-dec. 4 2009, pp. 1 –6.
- [14] J. Seitz, M. Schaub, O. Hirsch, R. Zetik, T. Deissler, R. Thoma, and J. Thielecke, "UWB feature localization for imaging," in *Proc. IEEE International Conference on Ultra-Wideband ICUWB 2008*, vol. 2, Sep. 10–12, 2008, pp. 199–202, geometry/TOA based feature mapping.
- [15] K. Hausmair, K. Witrisal, P. Meissner, C. Steiner, and G. Kail, "SAGE Algorithm for UWB Channel Parameter Estimation," in *COST 2100 Management Committee Meeting*, Feb. 2010.
- [16] T. Santos, J. Karedal, P. Almers, F. Tufvesson, and A. Molisch, "Modeling the ultra-wideband outdoor channel: Measurements and parameter extraction method," *Wireless Communications, IEEE Transactions on*, vol. 9, no. 1, pp. 282 –290, january 2010.
- [17] B. Fleury, M. Tschudin, R. Heddergott, D. Dahlhaus, and K. Ingeman Pedersen, "Channel parameter estimation in mobile radio environments using the SAGE algorithm," *Selected Areas in Communications, IEEE Journal on*, vol. 17, no. 3, pp. 434 –450, mar 1999.
- [18] A. F. Molisch, "Ultra-wide-band propagation channels," *Proc. IEEE*, vol. 97, no. 2, pp. 353–371, Feb. 2009.
- [19] T. Liu, P. Bahl, and I. Chlamtac, "Mobility modeling, location tracking, and trajectory prediction in wireless ATM networks," *Selected Areas in Communications, IEEE Journal on*, vol. 16, no. 6, pp. 922 –936, aug 1998.
- [20] B. Dong and X. Wang, "Adaptive Mobile Positioning in WCDMA Networks," *EURASIP Journal on Wireless Communications and Networking*, vol. 3, pp. 343–353, 2005.
- [21] P. Georgiou, P. Tsakalides, and C. Kyriakakis, "Alpha-stable modeling of noise and robust time-delay estimation in the presence of impulsive noise," *Multimedia, IEEE Transactions on*, vol. 1, no. 3, pp. 291 –301, sep. 1999.
- [22] G. Tsihrintzis and C. Nikias, "Incoherent receivers in alpha-stable impulsive noise," *Signal Processing, IEEE Transactions on*, vol. 43, no. 9, pp. 2225 –2229, sep 1995.
- [23] T. S. Ferguson, "A representation of the symmetric bivariate cauchy distribution," *The Annals of Mathematical Statistics*, vol. 33, no. 4, pp. pp. 1256–1266, 1962. [Online]. Available: <http://www.jstor.org/stable/2237984>
- [24] S. Kay, *Fundamentals of Statistical Signal Processing: Estimation Theory*. Prentice Hall Signal Processing Series, 1993.

Analysis of an Indoor UWB Channel for Multipath-Aided Localization

Paul Meissner, Daniel Arnitz, Thomas Gigl and Klaus Witrisal

Graz University of Technology, Graz, Austria, Email: {paul.meissner, daniel.arnitz, thomas.gigl, witrisal}@tugraz.at

Abstract—We present a detailed analysis of an indoor UWB channel measurement campaign. The focus is on the modeling of the deterministic part of the multipath channel using a-priori known relevant reflections and scatterers, found from an available floor plan. Our approach uses virtual signal sources, whose locations and visibilities can be calculated using simple ray-launching techniques. The channel analysis steps exploit these results, using an effective multipath cancellation method that introduces virtually no artifacts. We show that the corresponding multipath-components can explain up to 90 % of the UWB channel impulse responses in terms of energy capture. This is important for multipath-aided indoor localization, which provides robust position fixes using a single base station only.

I. INTRODUCTION

For indoor localization, time-of-arrival (ToA) based systems using (ultra)-wideband (UWB) signals are favorable, due to their fine delay resolution. In indoor scenarios, the large number of interacting objects like walls or furniture usually results in dense multipath channels, i.e. the channel impulse response (CIR) at a specific position consists of many specular reflections as well as diffuse scattered components [1]. If a floor plan is available, signal paths reflected of the room walls can be mapped to virtual signal sources [2], which are mirror images of the base station with respect to the corresponding reflecting surface, so-called *virtual anchors* (VAs). Using statistical models for range estimates to these virtual nodes, we have achieved robust algorithms for indoor localization and tracking in [3].

This contribution presents the results of a recently performed indoor UWB channel measurement campaign. Our localization algorithms are based on the fact that the UWB channel gives access to the specular reflections associated to the geometry of virtual sources [4]. It is important to know if these, usually few, expected multipath-components (MPCs) are important features of the channel and if they can be identified. We answer the former question by cancelling these expected MPCs from the CIRs obtained in our measurements with a time-domain method, i.e. a search-and-subtract approach [5]. A multipath template signal is generated at a position within a room with the help of the known distances to the virtual sources [2]. In the method presented in this paper, an additional pulse-shaping step is proposed that reduces artifacts of the MPC-cancellation. The amount of energy contained in the cancelled MPCs can be quantified by energy capture, which is also an important measure for the design of Rake receivers [6].

This work was partly supported by the Austrian Science Fund (FWF) within the National Research Network SISE project S10604-N13.

We show that using the few expected reflections allows for a large fraction of the energy to be accounted for. In comparison to other results in the literature, e.g. [7], we achieve high energy capture values for relatively low numbers of considered MPCs. This shows that geometry and position-related prior information can make search-and-subtract approaches very effective.

The approach presented here involves ray-tracing-steps. Ray-tracing is a valuable, but computationally demanding tool in both localization and channel analysis [8]. Our aim is a complexity tradeoff: We do not use ray-tracing techniques to accurately predict amplitudes and delays of possible signal paths at a specific location, but rather use it beforehand to compute and investigate potential reflectors and scatterers.

The rest of this paper is organized as follows: Section II describes the measurement campaign and the geometric computations that are needed. In Section III we describe the channel analysis and MPC cancellation method. Results are discussed in Section IV and Section V draws conclusions.

II. MEASUREMENT AND GEOMETRIC MODELING

Our measurement campaign was motivated by the intended application of indoor localization and tracking of a moving agent, as described in [3]. To this end, we measured the UWB channel along an example trajectory as can be seen in Fig. 1. This route consists of 381 points with a spacing of 10 cm, covering a total distance of 38 m. The measurements were performed in the frequency domain using a Rhode & Schwarz ZVA-24 vector network analyzer. At each position \mathbf{p}_k , the complex channel transfer function $H_k(f)$ is measured at 7501 frequency points over the frequency range from 3.1 to 10.6 GHz. This results in a maximum resolvable delay of approx. 1 μ s (or approx. 300 m path delay), and a delay resolution of 0.133 ns (or 4 cm path resolution). In performance evaluations, we will also restrict the bandwidth to 2 GHz (the range from 6 – 8 GHz), resulting in a delay resolution of 0.5 ns (or 15 cm path resolution). Transmitter and receiver antennas were placed at a height of 1.5 m.

The measurement location is the ground floor of our lab. This is an atrium style hallway of an office building, whose outer walls, marked with black lines in the floor plan, are made of concrete. Concerning geometry and building materials, the environment could be classified as semi-industrial. As can be seen in the floor plan, there are large reflective windows in the area of the initial part of the trajectory, shown as grey lines in the floor plan. Inbetween these windows are narrow

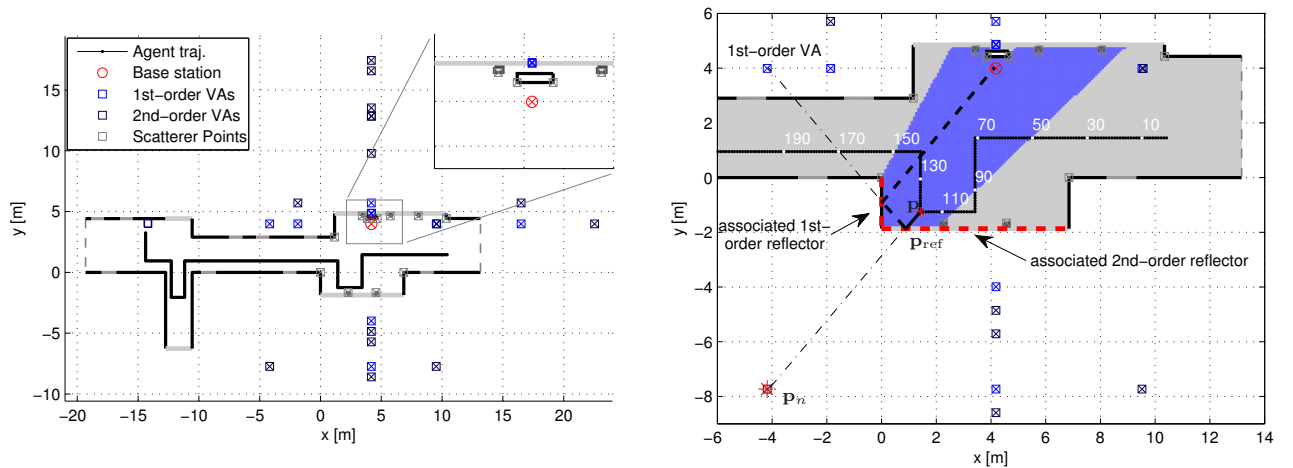


Fig. 1. Left plot shows floor plan, agent trajectory and considered VAs for the measurement scenario. The right plot shows an example for the calculated expected visibility region (in blue) of a specific second-order VA together with its associated reflecting surfaces (marked in red). Also shown is an example signal path (dashed black line, dash-dotted lines indicate “virtual paths” to the VAs) from point \mathbf{p} to the BS. Indices of some trajectory points are given for orientation, as they are occasionally used in the text.

metal pillars, which we expect to be visible as point scatterers (see also the zoom in Fig. 1). Doors are made of metal and also shown as grey line segments. The building consists of three floors, which are not separated by ceilings. Nevertheless, there are bridges connecting the two sides on the upper floors, which consist of both concrete and metal. The dashed lines at the right and left side of the floor plan are just delimiting the area we take into account for analysis. The building extends several meters to the right and several tens of meters to the left. Stationary channel conditions were ensured during the measurements.

TABLE I
MEASUREMENT PARAMETERS

Parameter	Value	Comment
Frequency range	3.1 – 10.6 GHz	full measurement BW
	6 – 8 GHz	offline bandlimitation
Trajectory parameters	381 points	
	10 cm spacing	
Frequency points	7501	over full bandwidth

For the moving agent, we used a Skycross SMT-3TO10M UWB antenna mounted on a tripod, at a height of 1.5 m. At the base station, which was at the same height, we used a custom-made coin antenna, made of 2 5 Euro-cent coins [9]. Both antennas have approximately uniform horizontal gain patterns. Floor plan, as well as agent and base station positions, were measured manually using a laser distance meter.

Having the floor plan and the position of the base station available, we can compute the possible positions of VAs. For first-order wall reflections, the VAs are simply mirror images of the BS at the corresponding reflective surface, which we call the associated reflector. Second-order VAs can be obtained by mirroring the first-order VAs at the associated second-order

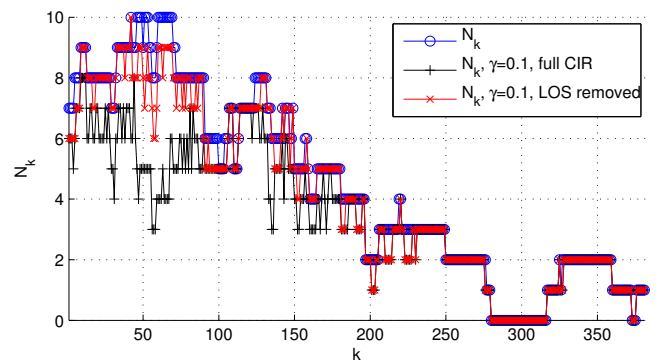


Fig. 2. Number of geometrically visible VAs N_k over the trajectory (blue line). The other lines show the number of significant MPCs from VAs, according to the threshold decision discussed in Section III-B, with $\gamma = 0.1$. For the black line, the threshold is computed using the full CIR, for the red line, the LOS component has been removed.

reflectors. Although this procedure can be repeated for higher orders, we restrict ourselves to second-order VAs and some additional scatterers in this work. Another model restriction is given by the 2D-modeling. Although the environment contains potential scatterers and reflectors at different heights than the antennas as mentioned previously, we want to show the suitability of a 2D-model, which is computationally much less demanding. The only exception is the inclusion of the floor reflection, which can be incorporated easily.

Naturally, the building geometry restricts the region, in which a certain reflection is possible. This is taken into account by computing visibility regions of VAs, which is discussed here. As an example, the geometric visibility of a second-order VA at a position \mathbf{p}_n from an agent position \mathbf{p} can be computed as follows (see also right plot in Fig. 1): First, we test if the line from \mathbf{p} to \mathbf{p}_n intersects the associated second-

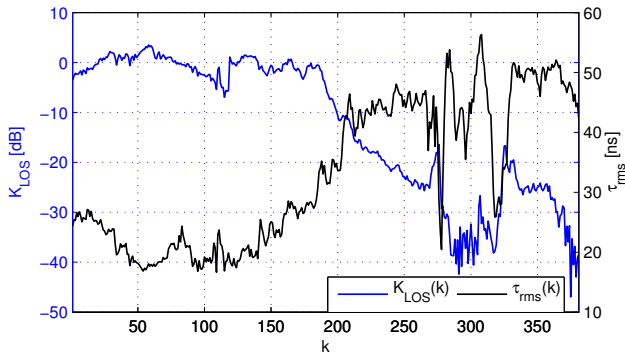


Fig. 3. Instantaneous K-factor w.r.t. the LOS component K_{LOS} and RMS delay spread τ_{rms} over the trajectory.

order reflecting surface in a point \mathbf{p}_{ref} . We also have to make sure, that out of all intersection points of this line with any objects known from the floor plan, \mathbf{p}_{ref} is the one closest to \mathbf{p} , such that the path from the point to the surface is not blocked. If these conditions do not hold, \mathbf{p} is not a valid “target” for this reflection and the VA is not visible. Otherwise, we have to test whether \mathbf{p}_{ref} is a valid “target” for a first-order reflection at the associated first-order segment of the second-order VA, which can be done using the corresponding first-order VA. This recursive ray-launching could be generalized to higher-order VAs as well and is repeated until the base station is reached.

For each VA that is taken into account, the visibility can be precomputed for a sufficiently dense grid of points within the floor plan. Fig.1 contains an example for the computed visibility region of the second-order VA associated to the large window and the adjacent wall. At each step k of the trajectory, the set of expected visible virtual anchors, denoted by \mathcal{V}_k , can then simply be looked up in the computed visibilities. The number of expected visible VAs at time-step k is then denoted as $|\mathcal{V}_k| = N_k$. The blue line in Fig. 2 shows N_k over all 381 measured trajectory positions.

III. CHANNEL ANALYSIS METHOD DESCRIPTION

A. Channel model and parameters

In the following, we use the channel model

$$h_k(\tau) = \sum_{l=1}^L \alpha_{k,l} \delta(\tau - \tau_{k,l}) + \nu_k(\tau) + n_k(\tau) \quad (1)$$

for the UWB-CIR at time step k , corresponding to position \mathbf{p}_k . This model decomposes the channel in three major parts. The first one is a sum over L deterministic, specular reflections, modeled with complex-valued amplitudes $\alpha_{k,l}$ and time delays $\tau_{k,l}$. The signals $\nu_k(\tau)$ and $n_k(\tau)$ model the diffuse scattered parts and the measurement noise, respectively. We expect that at a position \mathbf{p}_k , the set of visible VAs \mathcal{V}_k can be used to model a part of the deterministic reflections.

The measurements are the position-variant channel transfer functions (CTF) $H_k(f)$ along the trajectory. An inverse discrete Fourier transform (IDFT) is used for the transformation

to time domain. To reduce the leakage effect, and to support the MPC cancellation process, which will be described in the next section, we use a Parzen window function in frequency domain prior to the IDFT, hence

$$h_k(\tau) = \frac{1}{N_f} \sum_{f=f_{\min}}^{f_{\max}} H_k(f) W(f) e^{j2\pi f \tau}. \quad (2)$$

Note that both f and τ are defined as equally spaced discrete values. In time domain, the ideal CIR in (1) is convolved with the impulse response of the window function $w(\tau)$, which can be understood as a pulse shaping step. In (2), f_{\min} and f_{\max} denote upper and lower band edge and N_f is the number of frequency points. The values for τ are selected at a higher resolution as given by the measurement bandwidth, similar to the work in [5]. The upper part of Fig. 5 contains the 381 obtained CIRs $h_k(\tau)$ from our measurements.

Due to the geometric separation of successive agent positions, which is relatively large compared to the wavelength at the upper band edge, no spatial averaging was performed. Hence, we can not use an average power delay profile to compute channel parameters like the RMS-delay spread τ_{rms} and the K-factor with respect to the line-of-sight (LOS)-component [10]. But as these parameters are valuable for the analysis of an UWB channel, we evaluate the instantaneous values of these parameters along the trajectory, as shown in Fig. 3. We note that despite the clear LOS scenario, the K-factor is positive only on the points closest to the base station. This indicates the presence of strong MPCs that can easily bias a localization system whenever the LOS path is blocked. For positions around $k = 300$, the agent is in an occluded corridor, hence the CIRs in that region show an extremely low SNR (see Figs. 1 and 5). Therefore, the corresponding channel parameter estimates are highly unreliable.

B. MPC estimation and cancellation

In order to evaluate the relevance of the MPCs that can be attributed to the VAs, we need to detect them in the CIRs and afterwards remove their influence. To this end, we calculate the vector of expected MPC delays at position \mathbf{p}_k as

$$\tilde{\tau}_k = [\tilde{\tau}_{k,1}, \dots, \tilde{\tau}_{k,N_k}] = \frac{1}{c} [d(\mathbf{p}_1, \mathbf{p}_k), \dots, d(\mathbf{p}_{N_k}, \mathbf{p}_k)] \quad (3)$$

where the function $d(\cdot)$ denotes the Euclidean distance. We expect that due to uncertainties in the floor plan and/or the placement of the MS, these distances are imperfect. In Fig. 4, the entries of $\tilde{\tau}_k$ are shown as vertical dashed black lines, illustrating some minor geometric errors.

In the sequential cancellation procedure, a cleaned CIR $\tilde{h}_{k,l}(\tau)$ is computed for each MPC, where l is the MPC index with $l \in \{1, \dots, N_k\}$. The initial cleaned CIR is the measured one, $\tilde{h}_{k,0}(\tau) = h_k(\tau)$. To cancel the l -th MPC, we first calculate an estimate of the true delay of the respective expected MPC $\hat{\tau}_{k,l}$, starting from the corresponding $\tilde{\tau}_{k,l}$. We use a narrow uncertainty window of width $T = 0.5$ ns, or approx. 15 cm, around the expected delays. Within this

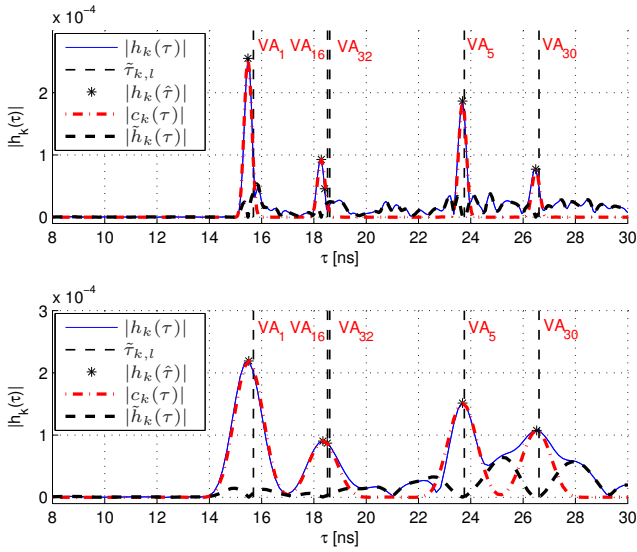


Fig. 4. Example of the MPC-cancellation procedure at position $k = 92$ for a bandwidth of 7.5 GHz (upper plot) and 2 GHz (lower plot), zoomed view.

window, we search for the maximum amplitude of the CIR. The corresponding delay is our estimate $\hat{\tau}_{k,l}$

$$\hat{\tau}_{k,l} = \arg \max_{\tau \in [\hat{\tau}_{k,l} - T/2, \hat{\tau}_{k,l} + T/2]} |h_k(\tau)|. \quad (4)$$

With the estimated $\hat{\tau}_{k,l}$, we generate a template signal for the l -th MPC at position \mathbf{p}_k

$$c_{k,l}(\tau) = \frac{\tilde{h}_{k,l}(\hat{\tau}_{k,l})}{N_f} \sum_{f=f_{\min}}^{f_{\max}} W(f) e^{j2\pi f(\tau - \hat{\tau}_{k,l})}. \quad (5)$$

The template consists of the impulse response of the window $W(f)$, shifted to the estimated delay of the l -th MPC and scaled by the complex amplitude of the current cleaned CIR at the estimated delay. This signal is then used to calculate the CIR cleaned from all expected MPCs up to the l -th

$$\tilde{h}_{k,l}(\tau) = \tilde{h}_{k,l-1}(\tau) - c_{k,l}(\tau). \quad (6)$$

The overall cleaned CIR is then $\tilde{h}_k(\tau) = \tilde{h}_{k,N_k}(\tau)$, and the overall template signal at \mathbf{p}_k consisting of the contributions from expected reflections is the sum

$$c_k(\tau) = \sum_{l=1}^{N_k} c_{k,l}(\tau). \quad (7)$$

Fig. 4 contains an example for this procedure at $k = 92$ for both bandwidths. One can see that the MPCs are cancelled without introducing noticeable distortions elsewhere. The higher the bandwidth, the more “local” the cancellation is, i.e. at a lower bandwidth, the estimated MPC (the template signal) also contains other parts of the CIR that happen to be within the window impulse response.

In addition to the geometric mismatch, we also take possible impairments of the visibilities of the VAs into account. For example, at a position \mathbf{p}_k , an expected MPC might not be

visible (i.e. its amplitude is very low) due to fading or other effects. Hence, we want to determine which of the expected VAs \mathcal{V}_k are actually *significant*. This is done using a threshold $A_{\gamma,k}$, which is defined as a value inbetween the maximum of $|h_k(\tau)|$ and the noise floor

$$A_{\gamma,k} = \gamma \cdot (\max\{|h_k(\tau)|\} - \langle |n_k(\tau)| \rangle) + \langle |n_k(\tau)| \rangle. \quad (8)$$

The noise floor is computed as the time average of the noise part, $\langle n_k(\tau) \rangle$, where $n_k(\tau)$ is obtained as the part of the CIR before the LOS component. An MPC at $\tau = \hat{\tau}_{k,l}$ is then defined as significant, if $|h_k(\hat{\tau}_{k,l})| \geq A_{\gamma,k}$. In strong LOS situations this threshold can be relatively high and restrictive, i.e. it will exclude reflections that are clearly distinguishable from the noise floor. Therefore we also use an alternative threshold that is computed in the same way as in (8), but where the maximum amplitude is taken from the CIR with the LOS component removed.

IV. PERFORMANCE RESULTS

We performed the described method over the whole trajectory in order to evaluate the relevance of the part of the UWB channel that can be attributed to the known VAs. Measured CIRs and obtained template signals $c_k(\tau)$ can be seen in Fig. 5. It can be observed that the paths along the trajectory corresponding to VA-caused reflections are matched well.

To obtain a quantitative analysis of the results, we use the concept of energy capture [6]. The energy of the CIR at position \mathbf{p}_k is defined as

$$E_k = \int |h_k(\tau)|^2 d\tau \quad (9)$$

where the integration is performed over the whole measured CIR. With a similar definition for the energy of the cleaned CIR \tilde{E}_k , the energy capture at position \mathbf{p}_k is then defined as

$$EC_k = 1 - \frac{\tilde{E}_k}{E_k}. \quad (10)$$

Fig. 6 shows EC_k for both bandwidths over the trajectory. We can see that the MPCs caused by the expected VAs carry a large amount of the energy contained in the CIRs. In general, the energy capture is higher for the lower bandwidth. This is explained with the fact that the template of, say, the l -th MPC, $c_{k,l}(\tau)$, contains not only the corresponding deterministic reflection, but also diffuse parts at that delay as well as possibly other deterministic reflections. As also confirmed qualitatively by Fig. 4, this effect is more pronounced at lower bandwidths, where the duration of the window impulse response $w(\tau)$ is longer. The high bandwidth shows an average energy capture of 47% for the entire trajectory, while at the lower bandwidth we achieve 52%. In roughly the first 180 positions, which according to Fig. 1 might be the operating area for this base station, the average energy capture is almost 70% for the high bandwidth, and 76% for the lower one. We also emphasize the model restriction to second-order reflections as well as to the 2D plane, which does not seem to play a major role, considering the high amount of energy capture that is obtained.

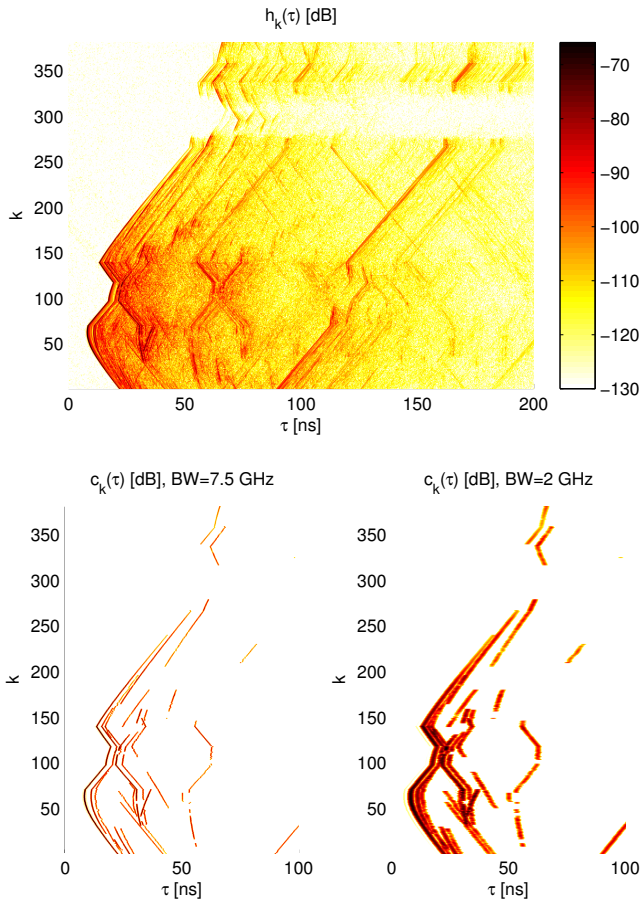


Fig. 5. Measured CIRs over the trajectory (top) and extracted template signals (bottom). Lower left plot shows the templates for the full and lower right plot for the reduced bandwidth. Template plots are zoomed on the τ -axis.

Fig. 2 shows the number of expected and significant VAs over the trajectory, using the threshold decision in (8) and the large bandwidth. The threshold $A_{\gamma,k}$ is computed with $\gamma = 0.1$. If the full CIR is used, many VAs are considered insignificant, especially in the region of high expected VA density. A look at Fig. 3 reveals that this effect is most pronounced in strong LOS situations. Therefore, and because we focus on the deterministic reflections, the use of the alternative threshold that is computed with the LOS-removed CIR is well suited for this analysis. Results show that the number of expected and significant VAs match well. For multipath-aided localization, it is important to note that the mean number of significant VAs in the operating area of the BS (again the first 180 positions) using $A_{\gamma,k}$ with the LOS-removed CIR is 6.82. This is clearly sufficient for 2D localization.

The influence of the insignificant VAs on the energy capture is negligible. For Fig. 6, all expected VAs have been taken into account. If EC_k is calculated with just the significant MPCs and $A_{\gamma,k}$ using the full CIR, the maximum penalty in energy capture is only 1.8% for the high bandwidth, and 1.9% for

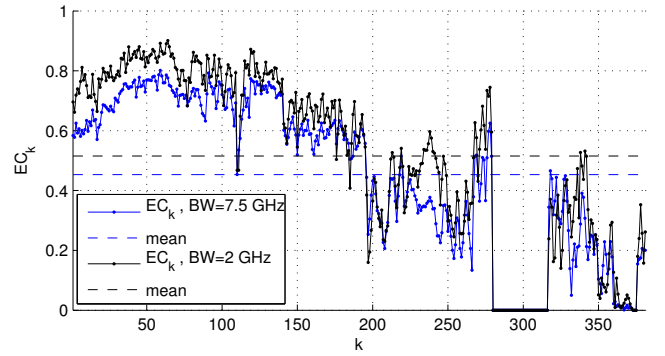


Fig. 6. Energy capture EC_k over the trajectory for the full (blue) and the reduced bandwidth. Horizontal dashed lines are corresponding averages.

the low one. This emphasizes again that the MPCs caused by the significant VAs are reliable channel features.

V. CONCLUSION AND OUTLOOK

We have presented an analysis of a measurement campaign of an indoor UWB channel. A floor plan was used to calculate a set of virtual signal sources plus their expected visibilities. The obtained geometric information was the basis of the channel analysis. We also presented an MPC cancellation method that introduces virtually no artifacts. This work acts as feasibility study for our previously proposed multipath-aided indoor localization algorithms, as it shows that the specular reflections caused by walls and scatter points are relevant features of the channel. Ongoing work includes the refinement of the estimation of the arrival times of the expected MPCs and of course the localization algorithms based on this data.

REFERENCES

- [1] A. F. Molisch, "Ultra-Wide-Band Propagation Channels," *Proc. IEEE*, vol. 97, no. 2, pp. 353–371, Feb. 2009.
- [2] J. Kunisch and J. Pamp, "An ultra-wideband space-variant multipath indoor radio channel model," in *Ultra Wideband Systems and Technologies, 2003 IEEE Conference on*, pp. 290 – 294.
- [3] P. Meissner, T. Gigl, and K. Witrisal, "UWB Sequential Monte Carlo Positioning using Virtual Anchors," in *Proc. 2010 International Conference on Indoor Positioning and Indoor Navigation, IPIN, Zurich, 2010*.
- [4] Y. Shen and M. Win, "On the Use of Multipath Geometry for Wideband Cooperative Localization," in *Global Telecommunications Conference, 2009. GLOBECOM 2009. IEEE*, 30 Dec. 2009, pp. 1–6.
- [5] T. Santos, J. Karedal, P. Almers, F. Tufvesson, and A. Molisch, "Modeling the ultra-wideband outdoor channel: Measurements and parameter extraction method," *Wireless Communications, IEEE Transactions on*, vol. 9, no. 1, pp. 282–290, January 2010.
- [6] M. Win and R. Scholtz, "Characterization of ultra-wide bandwidth wireless indoor channels: A communication-theoretic view," *Selected Areas in Communications, IEEE Journal on*, vol. 20, no. 9, pp. 1613–1627, Dec. 2002.
- [7] J. Karedal, S. Wyne, P. Almers, F. Tufvesson, and A. Molisch, "A Measurement-Based Statistical Model for Industrial Ultra-Wideband Channels," *Wireless Communications, IEEE Transactions on*, vol. 6, no. 8, pp. 3028–3037, 2007.
- [8] L. Zwirrello, M. Janson, C. Ascher, U. Schwesinger, G. Trommer, and T. Zwick, "Localization in industrial halls via ultra-wideband signals," in *Positioning Navigation and Communication (WPNC), 2010 7th Workshop on*, pp. 144–149.
- [9] C. Krall, "Signal processing for ultra wideband transceivers," PhD thesis, Graz Univ. of Techn. (Austria), 2008.
- [10] A. Molisch, *Wireless Communications*. John Wiley & Sons, 2005.

Performance Bounds for Multipath-assisted Indoor Navigation and Tracking (MINT)

Klaus Witrisal and Paul Meissner

Graz University of Technology, Inffeldgasse 12, A-8010 Graz, Austria, email: Witrisal@tugraz.at

Abstract—The MINT (multipath-assisted indoor navigation and tracking) problem exploits the geometry of deterministic multipath components (MPCs) for robust indoor positioning in line-of-sight (LOS) and non-LOS situations. It assumes a known room layout and can thus easily make use of signals reflected by the walls, for instance. In this paper, the Cramér-Rao lower bound of the positioning error is derived for this problem. This requires a novel channel model, where diffuse multipath is modeled as a colored Gaussian process that influences the effective SNR of deterministic MPCs. The adverse effect of path overlap is demonstrated and discussed. Computational results show the three-fold importance of a large signal bandwidth. The bandwidth reciprocal (i.e. the pulse duration) multiplies the error standard deviation—a fundamental result well-known from AWGN channels. But it also multiplies the effective power of the interfering diffuse multipath and gives rise to additional path overlap. A minimum bandwidth of 1 GHz seems appropriate and sufficient.

I. INTRODUCTION

Indoor positioning based on ultra-wideband (UWB) radio signals remains a challenging problem, in particular due to error induced by non-line-of-sight (NLOS) propagation conditions. This problem has received growing attention in recent years. Suggested solutions include the detection of NLOS, advanced tracking algorithms, cooperation between agents, and exploiting reflected multipath components (MPCs).

The latter also has the potential advantage of reducing the required infrastructure. For example, in [1], [2], a single physical anchor node has been assumed. Considering a known floorplan, a set of virtual anchors (VAs) is obtained by mirroring the anchor in the walls, thus allowing for a solution of the positioning problem (cf. Fig 1 below). Unfortunately, the unknown association of MPCs to VAs results in a rather large error floor. Tracking and cooperation have been shown to greatly improve the robustness [2], [3].

The above outlined problem has been termed multipath-assisted indoor navigation and tracking (MINT). Its solution requires novel tracking algorithms accounting for the geometry at hand, online channel analysis for extracting deterministic MPCs, and data association for mapping MPCs to hypothesized signal sources. It bears similarity to the simultaneous localization and mapping (SLAM) problem [4]–[6]. However, we have to deal with a signal source that typically has no angle resolution¹ and is heavily affected by diffuse multipath, which makes the feature detection and data association much more challenging. On the other hand, our assumption of a known

floorplan is a very reasonable one when considering scenarios with fixed anchor nodes.

In this paper, we derive the Cramér-Rao lower bound (CRLB) for the MINT problem. Our derivations partly follow those found in [7], [8] but also go back to the classic text by van Trees [9]. In particular, we propose a novel stochastic approach for modeling diffuse multipath, in contrast to previous work on this topic in [7], [10]–[12]. In [12], a multipath-aided positioning scenario has been analyzed as well. However, the authors assume *no* prior knowledge of the room layout. For this reason, cooperation was needed to make use of deterministic multipath.

This paper is organized as follows. Section II introduces the signal and channel model. The derivation of the CRLB and a discussion on path overlap is found in Section III. Computational results are presented in Section IV, followed by conclusions and recommendations for future work.

II. SIGNAL AND CHANNEL MODEL

A baseband signal $s(t)$ is transmitted from a fixed anchor node² at position \mathbf{p}_1 . It gets reflected and scattered by the environment. In particular, we assume $K - 1$ deterministic reflections at flat surfaces that can be mapped to virtual transmitter nodes located at fixed positions $\{\mathbf{p}_k = [x_k, y_k]^T\}$, $k = 2, \dots, K$.

The mobile agent at position $\mathbf{p} = [x, y]^T$ receives the complex-valued baseband signal

$$r(t) = \sum_{k=1}^K \alpha_k s(t - \tau_k) + \int_{-\infty}^{\infty} s(\lambda) \nu(t - \lambda) d\lambda + w(t) \quad (1)$$

which comprises K deterministic MPCs with amplitudes $\{\alpha_k\} \in \mathbb{C}$ and propagation delays $\tau_k = \frac{1}{c} \|\mathbf{p} - \mathbf{p}_k\|$, where c is the propagation velocity. We assume the energy of $s(t)$ is normalized to one; hence the path amplitudes define the energy received from each deterministic MPCs. Furthermore, $s(t) \in \mathbb{R}$, i.e. the transmitted signal has a symmetric spectrum. The second term of (1) models diffuse multipath. We assume uncorrelated scattering, and hence model this part by a stochastic process $\nu(t)$ with ACF

$$K_\nu(\tau, u) = \mathbb{E}\{\nu(\tau)\nu^*(u)\} = S_\nu(\tau)\delta(\tau - u) \quad (2)$$

where $S_\nu(\tau)$ is the delay power spectrum [13] of the diffuse multipath. This model implies that the diffuse part is quasi

¹Assuming—for simplicity—single-antenna terminals.

²Note that the anchor can as well be the receiver node, turning a navigation-type scenario into an object-tracking-type scenario.

stationary because it neglects spatial variations of $S_\nu(\tau)$. Hence these derivations will apply within a suitably defined “local area” with a diameter of several wavelengths. Finally, $w(t)$ denotes AWGN with double-sided PSD of $N_0/2$.

III. CRAMÉR RAO LOWER BOUND ON POSITION ERROR

The goal of MINT is estimating the agent’s position \mathbf{p} from the received waveform (1), exploiting knowledge of the VA positions $\{\mathbf{p}_k\}$, in presence of diffuse multipath and AWGN. The propagation delays $\{\tau_k\}$ relate to geometric information, while the path-amplitudes $\{\alpha_k\}$ are nuisance parameters. We will apply the chain rule to derive the CRLB of the position error (cf. [7], [8]). I.e., the Fisher information matrix (FIM) \mathbf{J}_θ of the parameter vector $\theta = [\mathbf{p}^\top (\alpha^R)^\top (\alpha^I)^\top]^\top$ is computed from the FIM of a parameter vector $\psi = [\boldsymbol{\tau}^\top (\alpha^R)^\top (\alpha^I)^\top]^\top$, where vectors α^R and α^I are the real and imaginary components of the MPC amplitudes $\{\alpha_k\}$ respectively, and $\boldsymbol{\tau}$ stacks the delays $\{\tau_k\}$. We get

$$\mathbf{J}_\theta = \mathbf{T} \mathbf{J}_\psi \mathbf{T}^\top \quad (3)$$

with the Jacobian

$$\mathbf{T} = \frac{\partial \psi}{\partial \theta}. \quad (4)$$

Finally, the FIM can be computed from the likelihood function $f(\mathbf{r}|\psi)$ of the received signal $r(t)$ (denoted as \mathbf{r}) conditioned on parameter vector ψ ,

$$\mathbf{J}_\psi = \mathbb{E}_{\mathbf{r}|\psi} \left\{ \left[\frac{\partial}{\partial \psi} \ln f(\mathbf{r}|\psi) \right] \left[\frac{\partial}{\partial \psi} \ln f(\mathbf{r}|\psi) \right]^\top \right\}. \quad (5)$$

A. Likelihood Function of Received Signal

According to (1), the stochastic process $\nu(t)$ representing diffuse multipath is convolved by the TX signal $s(t)$, written as $w_c(t) = s(t) * \nu(t)$. Hence it is present as a colored additive noise process. Let’s assume a Gaussian model is suitable for the diffuse multipath—a usual assumption for narrowband and conventional wideband channels, but not necessarily for UWB. Then a whitening operation can be applied to $r(t)$ to arrive at a tractable likelihood function.

We first need the correlation function $K_n(t, u)$ of the additive noise, which can be decomposed into the discrete component

$$K_w(t, u) = \mathbb{E}\{w(t)w^*(u)\} = N_0\delta(t - u) \quad (6)$$

and the continuous component

$$\begin{aligned} K_c(t, u) &= \mathbb{E}\{w_c(t)w_c^*(u)\} \\ &= \int_{-\infty}^{\infty} S_\nu(\tau)s(t - \tau)s(u - \tau)d\tau, \end{aligned} \quad (7)$$

resulting in $K_n(t, u) = K_w(t, u) + K_c(t, u)$. Then the likelihood function is [9, eq. (4.153)]

$$\begin{aligned} f(\mathbf{r}|\psi) &\propto \\ &\exp \left\{ \frac{2}{N_0} \iint_0^{T_0} \Re \left[r(t) Q_n(t, u) \sum_{k=1}^K \alpha_k^* s(u - \tau_k) \right] dt du \right. \end{aligned}$$

$$\left. - \frac{1}{N_0} \iint_0^{T_0} \sum_{k'=1}^K \alpha_{k'} s(t - \tau_{k'}) \times Q_n(t, u) \sum_{k=1}^K \alpha_k^* s(u - \tau_k) dt du \right\} \quad (9)$$

where $[0, T_0]$ is the observation interval and $Q_n(t, u)$ is the inverse kernel for $K_n(t, u)$ satisfying

$$N_0\delta(z - v) = \int_0^{T_0} K_n(x, z)Q_n(v, x)dx. \quad (10)$$

We proceed with the reasonable assumption that the TX signal has perfect autocorrelation properties for integer multiples of the bandwidth reciprocal T_s . We can then approximate³ the received signal by using the Karhunen-Loève expansion with the orthonormal basis functions $\varphi_i(t) = s(t - iT_s)$, $i = 0, 1, \dots, N$. Next, we write (8) as

$$K_c(t, u) \approx T_s \sum_{i=0}^N S_\nu(iT_s) s(t - iT_s) s(u - iT_s) \quad (11)$$

and find

$$\begin{aligned} Q_n(t, u) &= \delta(t - u) \\ &- \sum_{i=0}^N \frac{T_s S_\nu(iT_s)}{T_s S_\nu(iT_s) + N_0} s(t - iT_s) s(u - iT_s). \end{aligned} \quad (12)$$

Due to the autocorrelation properties of $s(t)$, we obtain for $\int s(t - iT_s) s(t - \tau) dt$ samples of a fractionally delayed pulse at time $iT_s = \tau$. We hence get for the $\int(\cdot) du$ in (9)

$$\int_0^{T_0} Q_n(t, u) \sum_{k=1}^K \alpha_k^* s(u - \tau_k) du \approx \sum_{k=1}^K w_k^2 \alpha_k^* s(t - \tau_k) \quad (13)$$

where $w_k^2 = N_0/(N_0 + T_s S_\nu(\tau_k))$ is a weight factor accounting for the influence of diffuse multipath.⁴ With this equation, we arrive at a standard likelihood function (cf. e.g. [7]), but with path amplitudes reduced by the weights w_k ,

$$\begin{aligned} f(\mathbf{r}|\psi) &\propto \exp \left\{ \frac{2}{N_0} \int_0^{T_0} \Re \left[r(t) \sum_{k=1}^K w_k^2 \alpha_k^* s(t - \tau_k) \right] dt \right. \\ &\left. - \frac{1}{N_0} \int_0^{T_0} \sum_{k'=1}^K \alpha_{k'} s(t - \tau_{k'}) w_{k'}^2 \sum_{k=1}^K \alpha_k^* s(t - \tau_k) dt \right\}. \end{aligned} \quad (14)$$

B. Equivalent FIM and Position Error Bound

With (14) in (5), we get the FIM of ψ . The appendix shows the elements of this matrix. Matrix \mathbf{T} is composed of four submatrices,

$$\mathbf{T} = \begin{bmatrix} \mathbf{H}_{2 \times K} & \mathbf{0}_{2 \times 2K} \\ \mathbf{0}_{2K \times K} & \mathbf{I}_{2K \times 2K} \end{bmatrix} \quad (15)$$

³This expansion is exact for signal with a block spectrum, where T_s is the sampling interval for critical sampling. For practical pulses some bandwidth extension is needed, which results in a violation of the sampling theorem.

⁴Again equality holds for signals having a block spectrum.

whose size is indicated by the subscripts. Its first subblock \mathbf{H} accounts for the geometry; its k -th column is found to be $\frac{1}{c}[\cos \phi_k, \sin \phi_k]^T$ (cf. [7], [8]), where angle ϕ_k is the angle from the k -th VA to the agent, i.e. $\phi_k = \tan^{-1} \frac{y-y_k}{x-x_k}$.

To compute the position error bound (PEB) we need the upper left 2×2 submatrix of the inverse of \mathbf{J}_θ . This can be obtained from blockwise inversion as

$$[\mathbf{J}_\theta^{-1}]_{2 \times 2} = \mathbf{J}_p^{-1} = \left(\mathbf{H} \mathbf{\Lambda}_A \mathbf{H}^T - \mathbf{H} \mathbf{\Lambda}_B \mathbf{\Lambda}_C^{-1} \mathbf{\Lambda}_B^T \mathbf{H}^T \right)^{-1} \quad (16)$$

where $\mathbf{\Lambda}_A$, $\mathbf{\Lambda}_B$, and $\mathbf{\Lambda}_C$ are subblocks of \mathbf{J}_ψ defined in the appendix. Matrix \mathbf{J}_p is called equivalent FIM (EFIM) [7]. The PEB is defined as the square root of the trace of \mathbf{J}_p^{-1} .

Expression (16) simplifies when we assume no path overlap (i.e. orthogonality) between signals from different VAs. In this case, $\mathbf{\Lambda}_B = \mathbf{0}$ and $\mathbf{\Lambda}_A$ will be diagonal and we can write

$$\mathbf{J}_p = \mathbf{H} \mathbf{\Lambda}_A \mathbf{H}^T = \frac{8\pi^2 \beta^2}{c^2} \sum_{k=1}^K \text{SINR}_k \mathbf{J}_r(\phi_k) \quad (17)$$

where β^2 is the effective (mean square) bandwidth of $s(t)$,

$$\text{SINR}_k := w_k^2 \frac{|\alpha_k|^2}{N_0} = \frac{|\alpha_k|^2}{N_0 + T_s S_\nu(\tau_k)} \quad (18)$$

is the signal-to-interference-plus-noise ratio (SINR) of the k -th MPC, and

$$\mathbf{J}_r(\phi) = \begin{bmatrix} \cos^2(\phi) & \cos \phi \sin \phi \\ \cos \phi \sin \phi & \sin^2 \phi \end{bmatrix}$$

is called ranging direction matrix (cf. [7]), a rank-one matrix with an eigenvector in direction of ϕ .

Valuable insight is gained from (17) and (18). In particular,

- Each VA (i.e. each deterministic MPC) adds some positive term to the EFIM in direction of ϕ_k and hence reduces the PEB in direction of ϕ_k .
- The SINR_k determines the intensity of this contribution (cf. ranging intensity information (RII) in [7]). It is limited by diffuse multipath as quantified by coefficient w_k ; an effect that scales with pulse duration T_s (cf. (18)).
- The effective bandwidth β^2 scales the EFIM. Any increase corresponds to a decreased PEB.

C. Effect of Path Overlap

In presence of path overlap—a particularly important situation for the problem at hand, as deterministic MPCs corresponding to VAs may of course arrive at (nearly) equal delays—the subtractive part of (16) has to be considered and $\mathbf{\Lambda}_A$ is no longer diagonal. This problem was extensively studied in [7]. It has been shown that the RII is reduced towards zero and—surprisingly—that this effect is independent of the path amplitudes.⁵ Assuming prior knowledge about the path delays and gains, the effect of path overlap can be reduced [7]. The model (1) introduced in this paper does not show an equally severe impact of path overlap in case of diffuse multipath. Only an SNR-loss is evident, cf. (18).

⁵In [7], a real-valued baseband model has been used for the received signal, in contrast to the complex baseband model (1) employed here. Therefore the influence of the phase angle of the path amplitudes has not been investigated, an issue that has to be explored in future work.

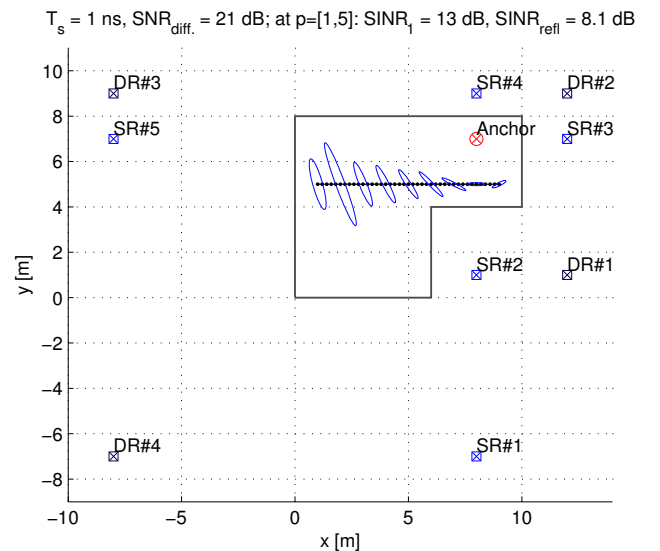


Fig. 1. Example scenario and position error bound along several points of a straight trajectory. The ellipses denote the ten-fold standard deviation.

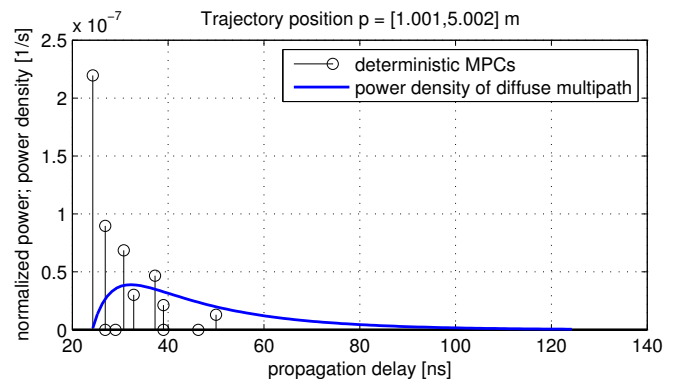


Fig. 2. Illustration of the channel model for trajectory position (1,5). Invisible MPCs are shown at zero power.

IV. COMPUTATIONAL RESULTS

Computational results are shown for the simple test scenario illustrated in Fig. 1. One physical anchor is present, which yields five possible first-order reflections (denoted as “SR: single reflection”) and four second-order reflections (“DR: double reflection”). The corresponding channel model is shown in Fig. 2 for agent position $\mathbf{p} = [1, 5]^T$ at the very left of the trajectory.⁶ Deterministic MPCs correspond to the physical anchor, first-order VAs number 3, 4, and 5, and double reflections number 2, 3, and 4. The system parameters were chosen for the purpose of supporting the analysis rather than based upon actual physical propagation models or measurements.⁷ We use the free-space pathloss model for a carrier frequency of 7 GHz to account for the distance dependence of the path amplitudes and add 3 dB for first-order and 6 dB for second-order reflections. The diffuse part is modeled by a fixed

⁶The trajectory was actually shifted 2 mm to the right and 1 mm up to avoid numeric instabilities due to exactly equal path delays.

⁷Recent experimental work reported in [14] gives related computational results based on an extensive channel measurement campaign.

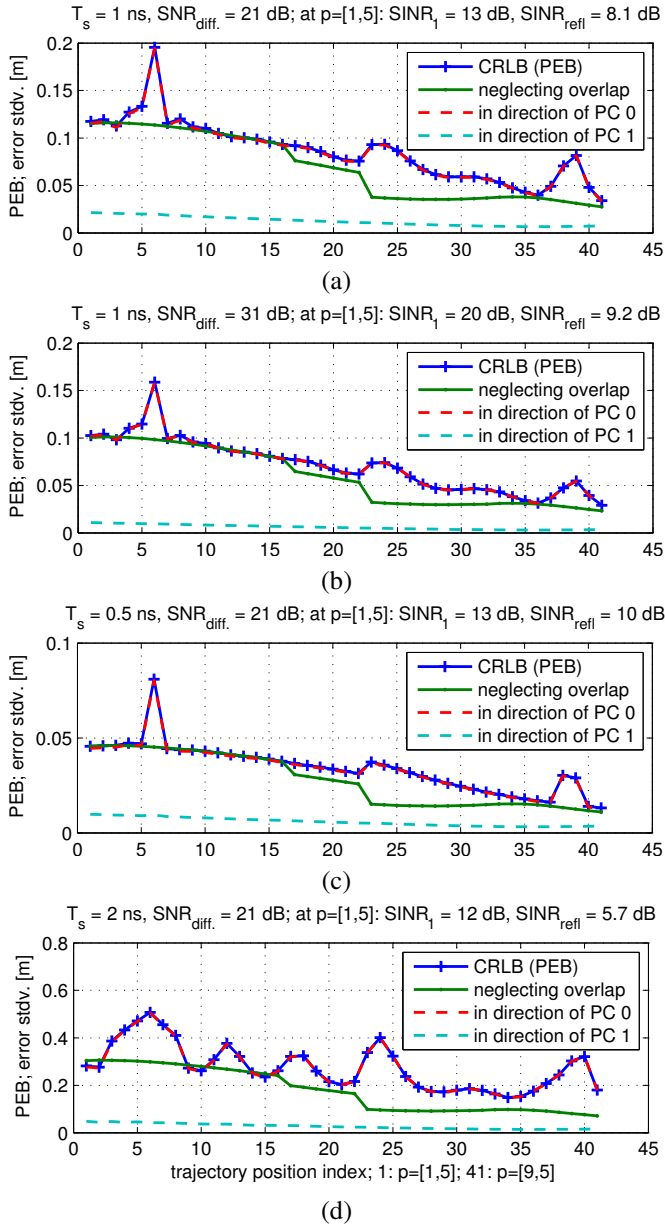


Fig. 3. Position error bound along the trajectory for various system parameters. (b): Ten-fold SNR w.r.t (a); (c): Double bandwidth w.r.t. (a); (d): Half bandwidth w.r.t. (a).

double-exponential function, cf. [15, eq. (9)], which accounts for lower path arrival rates at small excess delay. Its parameters are $\Omega_1 = 1.16 \times 10^{-6}$, $\gamma_1 = 20$ ns, $\gamma_{\text{rise}} = 5$ ns, and $\chi = 0.98$, where Ω_1 denotes the total power of the diffuse multipath. The power ratio of deterministic to diffuse MPCs is at -4 dB at position $\mathbf{p} = [1, 5]^T$. The SNR for the diffuse multipath is at a constant 21 dB throughout the room. The SINR_1 of the LOS component is at 13 dB while the *total* SINR of *all reflected*, deterministic MPCs is at just 8.1 dB due to the strong interference by diffuse multipath. (Both values apply at $\mathbf{p} = [1, 5]^T$). The transmitted signal was modeled as having a raised-cosine ACF $R_s(\tau)$ with roll-off factor $R = 0.6$ and pulse duration T_s of 0.5, 1, or 2 ns.

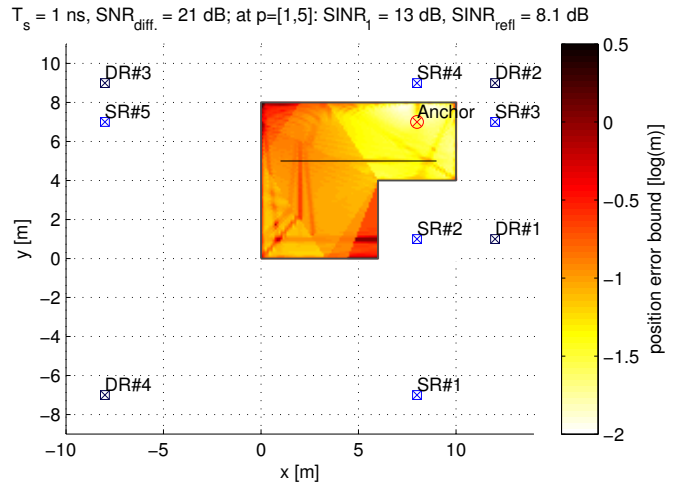


Fig. 4. Logarithm (base 10) of the position error bound across the floorplan.

Fig. 1 shows error ellipses computed from (16) for several positions along the trajectory. The ellipses denote the ten-fold PEB decomposed geometrically, i.e. the ten-fold error standard deviation. Fig. 3(a) gives quantitative results for the same parameter settings. It compares the PEB computed from the complete EFIM (16) and from (17) which neglects path overlap. It also shows the error components in direction of the major (PC0) and minor (PC1) semi-axes of the error ellipses.

The error is clearly lower in direction of the *physical* anchor node, because signals from *virtual* anchors are heavily affected by diffuse multipath. A significant reduction of the error is seen when approaching the anchor. This expected behavior is not monotonous, however. At Position 6, for example, we observe a step increase of the error that can be attributed to path overlap. The distances to SR#3 and SR#5 are equal at this position, as well as the distances to DR#2 and DR#3. From position 17, DR#1 becomes visible at equal distance to DR#2, leading again to a deviation between the two results due to path overlap. The deviation increases further from position 23, where SR#2 gets visible at equal distance to SR#4.

Figs. 3(b)–(d) analyze the error bound for various parameter settings. In Fig. 3(b), the SNR was increased by 10 dB, which clearly reduces the variance in direction of PC1. However the variance in direction of PC0 is influenced only slightly, because the system operates at a working point where diffuse multipath causes an error floor for signals from (reflected) VAs. The positive effect of an increased bandwidth is seen from Fig. 3(c) w.r.t. Fig. 3(a). Doubling the bandwidth, the overall error bound is reduced by a factor greater than two. This is due to a two-fold effect: An overall scaling of the CRLB with the effective bandwidth (cf. (17)), and a reduction of the limiting impact of diffuse multipath, as seen from (18). Finally, for Fig. 3(d) the bandwidth was reduced by a factor of two w.r.t. Fig. 3(a). Here also the increased influence of path overlap is evident. From this result, a minimum bandwidth of 1 GHz seems desirable for the MINT approach.

In Fig. 4, the position error bound is shown across the

floorplan. For most of the area, the CRLB is below 10 cm. The complete room can be served by a single physical anchor, even though the anchor is not visible from all locations. Again, the adverse effect of symmetries is clearly seen. Note that their position can be moved in some cases by shifting the physical anchor. Other symmetries, for instance along the walls, cannot be avoided.

V. CONCLUSIONS

The CRLB on the position error has been derived for the ‘‘MINT’’ problem, a multipath-assisted indoor positioning approach using UWB signals. For this purpose, a novel, stochastic channel model has been formulated to account for diffuse multipath interfering with deterministic reflections that are to be exploited.

Analysis and computational results demonstrate the potential advantage of exploiting deterministic multipath and point at the key parameters influencing the performance. Path overlap diminishes the ranging information by the corresponding (virtual) anchors, since orthogonality of their signals can only be achieved through different propagation delays. Therefore, the geometry of the (virtual) anchor nodes has a two-fold importance in this scenario. It effects the geometric dilution of precision and it determines the amount of path overlap. Similarly, the impact of signal bandwidth is a multiple one. As in conventional positioning schemes, it directly scales the error bound of the ranging estimates. But it also scales the power of the interfering diffuse multipath and the amount of path overlap.

There remains a great need for experimental verification of this work, however. Firstly the novel channel model has to be parameterized and validated using measurement results. Secondly, the applicability and usefulness of the CRLB has to be analyzed. A significant impact of diffuse multipath is mostly observed at low to medium path SINRs. The CRLB is known to be a loose bound under such working conditions. The presented models may also lead towards new and improved position estimators for MINT.

ACKNOWLEDGEMENTS

This work was supported by the Austrian Science Fund (FWF) within the National Research Network SISE, project S10604-N13, and by the Austria Research Promotion Agency (FFG) within KIRAS PL3, grant nb. 832335 ‘‘LOBSTER’’.

APPENDIX

Computation of the Fisher information matrix (FIM)

We compute the FIM \mathbf{J}_ψ of the auxiliary parameter vector $\psi = [\tau^T (\alpha^R)^T (\alpha^I)^T]^T$ using (5) and (14). We closely follow the notation of [7]. The FIM is decomposed according to the subvectors of ψ into

$$\mathbf{J}_\psi = \begin{bmatrix} \mathbf{\Lambda}_A & \mathbf{\Lambda}_B^R & \mathbf{\Lambda}_B^I \\ (\mathbf{\Lambda}_B^R)^T & \mathbf{\Lambda}'_C & \mathbf{0} \\ (\mathbf{\Lambda}_B^I)^T & \mathbf{0} & \mathbf{\Lambda}'_C \end{bmatrix} = \begin{bmatrix} \mathbf{\Lambda}_A & \mathbf{\Lambda}_B \\ \mathbf{\Lambda}_B^T & \mathbf{\Lambda}_C \end{bmatrix}. \quad (19)$$

Its elements are defined as

$$\begin{aligned} [\mathbf{\Lambda}_A]_{k,k'} &= \mathbb{E}_{\mathbf{r}|\psi} \left\{ -\frac{\partial^2 \ln f(\mathbf{r}|\psi)}{\partial \tau_k \partial \tau_{k'}} \right\} \\ &= \frac{2}{N_0} \Re \{ \alpha_k \alpha_{k'}^* \} w_k^2 \frac{\partial^2 R_s(\tau_k - \tau_{k'})}{\partial \tau_k \partial \tau_{k'}} \\ [\mathbf{\Lambda}_B^R]_{k,k'} &= \mathbb{E}_{\mathbf{r}|\psi} \left\{ -\frac{\partial^2 \ln f(\mathbf{r}|\psi)}{\partial \tau_k \partial \alpha_{k'}^R} \right\} \\ &= \frac{2}{N_0} \alpha_k^R w_k^2 \frac{\partial R_s(\tau_k - \tau_{k'})}{\partial \tau_k} \\ [\mathbf{\Lambda}_B^I]_{k,k'} &= \mathbb{E}_{\mathbf{r}|\psi} \left\{ -\frac{\partial^2 \ln f(\mathbf{r}|\psi)}{\partial \tau_k \partial \alpha_{k'}^I} \right\} \\ &= \frac{2}{N_0} \alpha_k^I w_k^2 \frac{\partial R_s(\tau_k - \tau_{k'})}{\partial \tau_k} \\ [\mathbf{\Lambda}'_C]_{k,k'} &= \mathbb{E}_{\mathbf{r}|\psi} \left\{ -\frac{\partial^2 \ln f(\mathbf{r}|\psi)}{\partial \alpha_k^R \partial \alpha_{k'}^R} \right\} = \mathbb{E}_{\mathbf{r}|\psi} \left\{ -\frac{\partial^2 \ln f(\mathbf{r}|\psi)}{\partial \alpha_k^I \partial \alpha_{k'}^I} \right\} \\ &= \frac{2}{N_0} w_k^2 R_s(\tau_k - \tau_{k'}) \end{aligned}$$

where $R_s(\tau) = \int_{-\infty}^{\infty} s(t)s(t-\tau)dt$.

REFERENCES

- [1] P. Meissner, C. Steiner, and K. Witrisal, ‘‘UWB positioning with virtual anchors and floor plan information,’’ in *Workshop on Positioning, Navigation and Communication, WPNC*, Dresden, Germany, Mar. 2010.
- [2] P. Meissner and K. Witrisal, ‘‘Multipath-Assisted Single-Anchor indoor localization in an office environment,’’ in *International Conference on Systems, Signals and Image Processing (IWSSIP)*, Vienna, Austria, Apr. 2012.
- [3] S. Van de Velde, H. Wymeersch, P. Meissner, K. Witrisal, and H. Steendam, ‘‘Cooperative multipath-aided indoor localization,’’ in *IEEE Wireless Commun. and Networking Conf., WCNC*, 2012.
- [4] H. Durrant-Whyte and T. Bailey, ‘‘Simultaneous localization and mapping: part I,’’ *Robotics & Automation Magazine, IEEE*, vol. 13, no. 2, pp. 99–110, June 2006.
- [5] T. Bailey and H. Durrant-Whyte, ‘‘Simultaneous localization and mapping (SLAM): part II,’’ *Robotics & Automation Magazine, IEEE*, vol. 13, no. 3, pp. 108–117, Sept. 2006.
- [6] T. Deissler and J. Thielecke, ‘‘UWB SLAM with Rao-Blackwellized Monte Carlo data association,’’ in *Intern. Conf. on Indoor Positioning and Indoor Navigation, IPIN*, Zurich, Switzerland, Sept. 2010.
- [7] Y. Shen and M. Win, ‘‘Fundamental limits of wideband localization; Part I: A general framework,’’ *IEEE Trans. Inform. Theory*, vol. 56, no. 10, pp. 4956–4980, Oct. 2010.
- [8] H. Godrich, A. Haimovich, and R. Blum, ‘‘Target localization accuracy gain in MIMO radar-based systems,’’ *IEEE Trans. Inform. Theory*, vol. 56, no. 6, pp. 2783–2803, June 2010.
- [9] H. L. van Trees, *Detection, Estimation, and Modulation Theory, Part I: Detection, Estimation, and Linear Modulation Theory*. John Wiley & Sons, 2001.
- [10] Y. Qi, H. Suda, and H. Kobayashi, ‘‘On time-of-arrival positioning in a multipath environment,’’ in *IEEE Vehicular Technology Conference, VTC*, vol. 5, Sept. 2004, pp. 3540 – 3544 Vol. 5.
- [11] Y. Shen and M. Win, ‘‘Effect of path-overlap on localization accuracy in dense multipath environments,’’ in *IEEE International Conference on Communications, ICC*, May 2008, pp. 4197–4202.
- [12] —, ‘‘On the use of multipath geometry for wideband cooperative localization,’’ in *IEEE Global Telecommun. Conf., GLOBECOM*, 2009.
- [13] P. Bello, ‘‘Characterization of randomly time-variant linear channels,’’ *IEEE Trans. Commun.*, vol. 11, pp. 360–393, 1963.
- [14] P. Meissner and K. Witrisal, ‘‘Analysis of Position-Related information in measured UWB indoor channels,’’ in *European Conf. on Antennas and Propagation, EuCAP*, Prague, Czech Republic, Mar. 2012.
- [15] J. Karedal, S. Wyne, P. Almers, F. Tufvesson, and A. F. Molisch, ‘‘A measurement-based statistical model for industrial ultra-wideband channels,’’ *IEEE Trans. Wireless Commun.*, vol. 6, no. 8, pp. 3028–3037, Aug. 2007.

Analysis of Position-Related Information in Measured UWB Indoor Channels

(Convened Session)

Paul Meissner and Klaus Witrisal

Graz University of Technology, Graz, Austria, Email: {paul.meissner, witrisal}@tugraz.at

Abstract—Conventional radio-based indoor localization systems often only make use of the direct signal path between an agent and the anchor nodes. Therefore, performance can deteriorate in non-line-of-sight situations, even though reflected multipath-components carry useful location-dependent information. Using ultra-wideband signals, these components become resolvable. Bringing together previously obtained results on the Cramér-Rao bound on the position error and measurement data along a reference trajectory, we present a methodology for quantifying the position-related information contained in UWB indoor channels. An explicit model for the diffuse part of the channel enables to evaluate its importance realistically. Experimental results verify prior theoretical work. Important parameters and their influence on the system performance are discussed.

I. INTRODUCTION

For multilateration-based indoor localization, ultra-wideband (UWB) signals are the method of choice, especially due to the fact that the line-of-sight component can be separated from the reflected multipath components (MPCs). In non-line-of-sight (NLOS) situations however, these systems can still show large errors due to biased range estimates. Proposed solutions try to e.g. identify and discard NLOS measurements, which implies loosing all geometric information that is embedded in the reflected components. In prior work (see [1] and references therein), we proposed an indoor localization method that explicitly makes use of multipath propagation by mapping MPCs to *virtual anchors* (VAs) that are positioned according to a known floor plan.

Recently, we have derived the Cramér-Rao lower bound (CRLB) for this multipath-assisted indoor navigation and tracking (MINT) scenario [2]. In contrast to other work on this topic, like [3] and [4], we explicitly model diffuse multipath (DM) using a stochastic process. With this, we are able to evaluate the influence of DM on the localization performance, which is important as the density of diffuse components can be high in indoor scenarios. The often-used model for the UWB channel as a sum of reflected copies of the transmit signal plus noise seems to be inappropriate for this purpose. This paper aims at a verification of these theoretical results using data from an extensive indoor measurement campaign [5].

This work was partly supported by the Austrian Science Fund (FWF) within the National Research Network SISE project S10604-N13, and by the Austria Research Promotion Agency (FFG) within KIRAS PL3, grant nb. 832335 “LOBSTER”

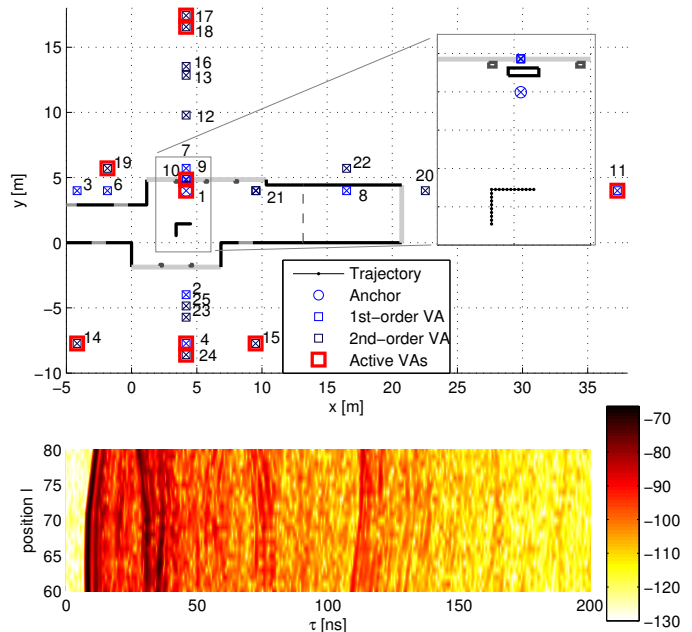


Fig. 1. Scenario used in this paper (upper plot). Black lines represent concrete walls, gray lines depict large windows and metal doors. Only the VAs marked in red are visible from the trajectory. On the right side, a close-up of the anchor area is shown. The lower plot shows the CIRs over the trajectory at a bandwidth of 2 GHz.

We present a framework for the quantification of position-related information in UWB channel measurements. The results are used to verify the theoretical work in [2]. Also, they provide important performance considerations for localization schemes making use of multipath propagation, like [6] or [7], for example.

II. SCENARIO AND SIGNAL MODEL

Fig. 1 shows the scenario that is analyzed in this paper and where the measurement campaign was performed [5]. The position of the single anchor node \mathbf{p}_1 is mirrored with respect to the reflecting surfaces using the known floor plan. This results in VA nodes at positions $\mathbf{p}_k = [x_k, y_k]^T$, $k = 2, \dots, K$ [8]. These can be exploited for multipath-assisted indoor navigation and tracking (MINT) [2].

The UWB channel was measured at 381 points, spaced by 10 cm with a Rhode & Schwarz ZVA-24 vector network analyzer over a frequency range of 3.1-10.6 GHz. Using pulse

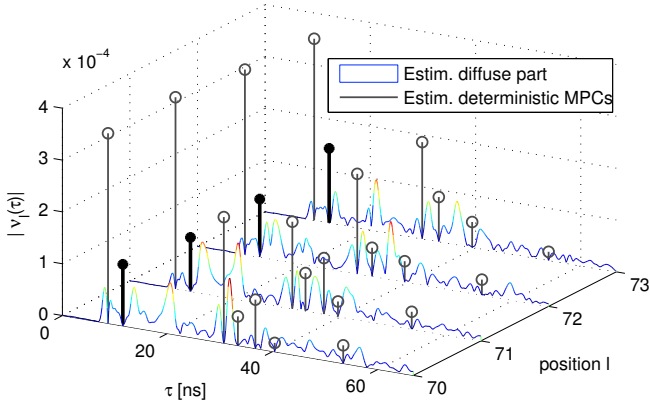


Fig. 2. Decomposition of measured CIRs as in [5] into deterministic MPCs (black lines) and diffuse multipath (colored lines) at certain points of the trajectory and a bandwidth of 2 GHz. The bold line marks the MPC from VA 10, whose tail was used to extract the data for Fig. 3.

shaping with a “transmit signal” $s(t)$, the signal at position \mathbf{p}_l is modeled as [2]

$$r_l(t) = \sum_{k=1}^{K_l} \alpha_{k,l} s(t - \tau_{k,l}) + n_l(t) \quad (1)$$

which consists of K_l deterministic MPCs with amplitudes $\{\alpha_{k,l}\} \in \mathbb{C}$ and propagation delays $\tau_{k,l} = \frac{1}{c} \|\mathbf{p}_l - \mathbf{p}_k\|$, where c is the propagation velocity. We assume that these MPCs are caused by specular reflections at flat surfaces, i.e. they are modeled by the VAs. The noise term $n_l(t)$ consists of both measurement noise, $w_l(t)$, and the convolution of the transmit signal with the DM, which is modeled by a random process $\nu_l(t)$, i.e.

$$n_l(t) = \int_{-\infty}^{\infty} s(\lambda) \nu_l(t - \lambda) d\lambda + w_l(t). \quad (2)$$

Here, $w_l(t)$ denotes additive white Gaussian noise with two-sided power spectral density $N_0/2$. The lower part of Fig. 1 shows the measured channel impulse responses (CIRs) along the trajectory. We can observe the structure of the deterministic components, that bears information for localization [9].

The aim of this paper is a verification of the results on the performance bounds for MINT [2] using the measured CIRs along the trajectory. One major challenge in this regard is the lack of sufficiently many (and densely spaced) measurement points to reliably estimate channel statistics. E.g., in [2], uncorrelated scattering is assumed, which means that the process $\nu_l(t)$ is modeled by an ACF $K_{\nu_l}(\tau, u) = E\{\nu_l(\tau)\nu_l^*(u)\} = S_{\nu}(\tau)\delta(\tau - u)$. According to this model, the power delay profile $S_{\nu}(\tau)$ does not consider spatial variations as it does not depend on the position l . However, it is clear that in the scenario in Fig. 1, visibility regions of the VAs and hence propagation characteristics change severely, even over a distance of just a few meters [5]. Hence, we restrict our analysis to only $L = 21$ measurement positions \mathbf{p}_l for $l = L_1, \dots, L_2$ (see Fig. 1, for comparison with [5], $L_1 = 60$

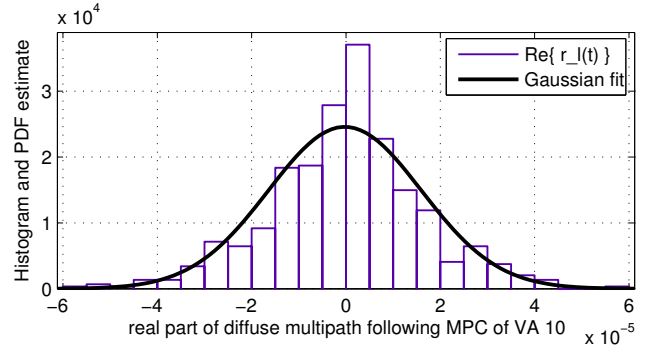


Fig. 3. Histogram of the real part of $r_l(t)$ for a bandwidth of 2 GHz. Here, t is restricted to a region of 2 ns after the deterministic signal part caused by VA 10, i.e. its diffuse tail (c.f. Fig. 2). The black line shows a Gaussian fit.

and $L_2 = 80$), and stack the corresponding measurements in the vector

$$\mathbf{r}_{L_1:L_2}(t) = [r_{L_1}(t), \dots, r_{L_2}(t)]^T. \quad (3)$$

III. BOUNDS ON THE POSITION ERROR

In [2], the Cramér-Rao lower bound on the position error for multipath-assisted localization has been derived by blockwise inversion of the Fisher information matrix (FIM) \mathbf{J}_{θ} [3] for the parameter vector $\boldsymbol{\theta}_l = [\mathbf{p}^T (\boldsymbol{\alpha}^R)^T (\boldsymbol{\alpha}^I)^T]^T$ that contains the position and the real and imaginary components of the MPC amplitudes $\alpha_{k,l}$. The equivalent FIM (EFIM) [3] for the position \mathbf{p} has been derived as

$$\mathbf{J}_{\mathbf{p}_l} = \frac{8\pi^2 \beta^2}{c^2} \sum_{k=1}^{K_l} \text{SINR}_{k,l} \mathbf{J}_{\mathbf{r}}(\phi_{k,l}) \quad (4)$$

where no path overlap, i.e. orthogonality of the signals from different VAs, is assumed. Ref. [2] also derives $\mathbf{J}_{\mathbf{p}_l}$ for path overlap situations. As we will discuss below, this situation leads to considerable practical difficulties, and is not considered here. In (4), β^2 is the effective bandwidth of $s(t)$ and $\mathbf{J}_{\mathbf{r}}(\phi)$ is the ranging direction matrix [3], with one eigenvector in the direction $\phi_{k,l}$, which is the angle from \mathbf{p}_k to \mathbf{p}_l . The signal-to-interference-plus-noise ratio (SINR) of the k -th MPC at position \mathbf{p}_l is

$$\text{SINR}_{k,l} := w_{k,l}^2 \frac{|\alpha_{k,l}|^2}{N_0} = \frac{|\alpha_{k,l}|^2}{N_0 + T_s S_{\nu}(\tau_{k,l})}. \quad (5)$$

In (5), the influence of the individual terms of the CIR (c.f. (1)) is shown: The weights w_k account for the influence of DM via its power delay profile $S_{\nu}(\tau)$. We observe that the DM is scaled by T_s , the bandwidth inverse. Again we note that with limited measurement points, $S_{\nu}(\tau)$ or a reliable estimate of it will not be available, and due to the 10 cm spacing of the \mathbf{p}_l , the spatial variation can not be neglected. Hence, instead of estimating $\text{SINR}_{k,l}$ for each \mathbf{p}_l , we will estimate an average SINR_k for each VA, restricted to our measurement set in $\mathbf{r}_{L_1:L_2}(t)$.

IV. ESTIMATION OF POSITION-RELATED PARAMETERS

For the contribution of one deterministic MPC at the position \mathbf{p}_l , the log-likelihood function that results in the EFIM in (4) can be expressed as [2]

$$\ln f(r_l(t)|\boldsymbol{\theta}_{k,l}) \propto \frac{2}{N_0} \int_0^T \Re [r_l(t)\alpha_{k,l}w_{k,l}^2s(t-\tau_{k,l})] dt - \frac{1}{N_0} \int_0^T [\alpha_{k,l}w_{k,l}s(t-\tau_{k,l})]^2 dt \quad (6)$$

where $\boldsymbol{\theta}_{k,l} = [\mathbf{p}_k^T \alpha_k^R \alpha_k^I]^T$, T is the observation interval and the delay $\tau_{k,l}$ depends on the respective VA position \mathbf{p}_k as

$$\tau_{k,l}(\mathbf{p}_k) = \frac{1}{c} \|\mathbf{p}_l - \mathbf{p}_k\|. \quad (7)$$

Equation (6) is the log of the likelihood ratio of a signal $s(t)$, parameterized by $\boldsymbol{\theta}_{k,l}$, in Gaussian noise [10]. The scaling factors $w_{k,l}$ result from a whitening operation used to account for the colored noise in $\nu_l(t)$ [2].

To evaluate the suitability of a Gaussian model for the noise term $n_l(t)$ given in (2), we use the channel analysis method in [5]. We subtract the influence of the deterministic MPCs caused by the VAs from $r_l(t)$. The remaining signal is an estimate for the combined noise term $\hat{n}_l(t)$ [11]. Fig. 2 shows the procedure for several trajectory positions and a bandwidth of 2 GHz. We observe that the DM is often especially pronounced after deterministic MPCs, i.e. those show a “diffuse tail” associated to them [12]. These components seem to carry significant energy which severely influences multipath-assisted localization schemes [1].

Although elaborate statistical modeling is out of the scope of this paper, we exemplarily analyze $\hat{n}_l(t)$ for a certain part of the channel. For this purpose, we extract $\hat{n}_l(t)$ for a range of 2 ns after the MPC from VA 10 (marked in Fig. 2). A histogram of its real part, together with an ML-fit of a Gaussian distribution, is shown in Fig. 3. Although both a slight concentration of values in the vicinity of zero and outliers with quite large values can be observed, a zero-mean Gaussian model might be a reasonable assumption.

A. Maximum-Likelihood Localization of VAs

We assume that in a realistic scenario, the floorplan is not known exactly and therefore, the VA positions \mathbf{p}_k are subject to uncertainty. Hence, as a first step in the data extraction process, we re-estimate the locations of the VAs according to the model in (6). In a small region around the geometrically expected VA position \mathbf{p}_k , we search for the VA position that provides a best fit to the received signal. For each candidate point $\tilde{\mathbf{p}}_k$ within this region, we construct a template signal

$$\tilde{s}_{k,l}(t) = \tilde{a}_k s(t - \tilde{\tau}_{k,l}(\tilde{\mathbf{p}}_k)) \quad \text{with } \|s(t)\| = 1 \quad (8)$$

where $\|s(t)\|$ denotes the norm of $s(t)$. The complex amplitude of the template, \tilde{a}_k , is kept constant with respect to l , as it is a nuisance parameter in this estimation. Assuming

noncoherent processing, we choose \tilde{a}_k as the mean of the absolute value of $r_l(\tilde{\tau}_{k,l})$ over the trajectory, i.e.

$$\tilde{a}_k = \frac{1}{L} \sum_{l=L_1}^{L_2} |r_l(\tilde{\tau}_{k,l})| \quad (9)$$

where $\tilde{\tau}_{k,l}$ is the expected delay according to the floorplan. Assuming independent measurements at different trajectory positions, the log-likelihood function is given as

$$\ln f(\mathbf{r}_{L_1:L_2}(t)|\mathbf{p}_k) \propto \frac{2}{N_0} \sum_{l=L_1}^{L_2} \int_0^T |r_l(t)\tilde{s}_{k,l}(t)| dt - \frac{1}{N_0} \int_0^T |\tilde{s}_{k,l}(t)|^2 dt. \quad (10)$$

It is important to restrict the computation of (10) to those measurement positions \mathbf{p}_l where the k -th VA is expected to be visible, and where additionally no path overlap with any other VA occurs. The latter is important because this processing allows no “distribution” of MPC energy to different sources at the same delay. However, in the selected part of the trajectory, path overlap only occurs for some positions between VAs 15 and 24, if a bandwidth of 2 GHz or below is used. The ML estimate of the position of the k -th VA is then computed as

$$\hat{\mathbf{p}}_k = \arg \max_{\tilde{\mathbf{p}}_k} \ln f(\mathbf{r}_{L_1:L_2}(t)|\tilde{\mathbf{p}}_k) \quad \text{where } \|\tilde{\mathbf{p}}_k - \mathbf{p}_k\| \leq \tilde{d} \quad (11)$$

where \tilde{d} is the radius of the uncertainty region around the expected \mathbf{p}_k and is chosen as 20 cm.

B. Estimation of Path Amplitudes and SINR for VAs

In this step, the complex amplitudes of the MPCs are estimated. To this end, we project the received signal onto the energy-normalized transmit signal, shifted to the ML estimate $\hat{\tau}_{k,l} = \tau_{k,l}(\hat{\mathbf{p}}_k)$ of its respective path delay, i.e. $\hat{s}_{k,l}(t) = s(t - \hat{\tau}_{k,l})$. The projection is then

$$\hat{a}_{k,l} = \int_0^T r_l(t)\hat{s}_{k,l}^*(t) dt. \quad (12)$$

With the assumptions that $s(t) \approx 0$ for $|t| > T_s$, no path overlap, and that the ML estimate of the delay is exact, i.e. $\hat{\tau}_{k,l} = \tau_{k,l}$, this reduces to

$$\hat{a}_{k,l} = \alpha_{k,l} + \int_0^T [s(t) * \nu_l(t) + w_l(t)] \hat{s}_{k,l}^*(t) dt = \alpha_{k,l} + \nu_{k,l} + w_{k,l} \quad (13)$$

where $*$ denotes convolution. Hence, the estimated amplitude $\hat{a}_{k,l}$ is a sum of the true amplitude $\alpha_{k,l}$ and the projections of the DM and the noise on the estimated template for the k -th MPC. As there is no way of finding these components individually based on observing $\hat{a}_{k,l}$ without additional knowledge, we proceed by directly estimating the corresponding average SINR $_k$ for the k -th VA.

For this, we assume that the deterministic amplitude $\alpha_{k,l} = \alpha_k$, i.e. it is constant over the L measurement points. This implies that all variations in $\hat{a}_{k,l}$ are caused by DM and noise.

TABLE I
 SINR_k FOR DIFFERENT BANDWIDTHS

VA Index	SINR _k [dB]		
	W = 7.5 GHz	W = 2 GHz	W = 1 GHz
1	24.56	24.27	23.42
4	13.05	7.85	2.31
10	19.03	15.48	1.93
11	14.61	5.8	5.94
14	5.24	2.47	0.51
15	2.7	3.24	−∞
17	6.0	4.04	3.83
18	14.38	7.27	4.95
19	6.37	−∞	−∞
24	9.03	−∞	3.99
tot. SINR _{refl}	26.09	17.9	12.27

To allow this assumption, we correct the deterministic distance dependence of the $\hat{a}_{k,l}$ by multiplying them with a factor $f_{\text{corr},k} = \sqrt{F_k(l_0)/F_k(l)}$, where $F_k(l)$ is the Friis equation for the free space loss between the VA at \mathbf{p}_k and the position \mathbf{p}_l . The position \mathbf{p}_{l_0} is the one closest to the average distance between \mathbf{p}_k and all \mathbf{p}_l .

As $\hat{a}_{k,l}$ consists of the deterministic complex amplitude α_k , which is superimposed by Gaussian noise, it is reasonable to model its absolute value as $|\hat{a}_{k,l}| \sim \text{Rice}(s = |\alpha_k|, \sigma^2)$, where σ^2 denotes the variance of the noise. We observe that the Ricean K-factor, $s/2\sigma^2$, is a reasonable estimate for SINR_k.

The estimated complex amplitudes $\hat{a}_{k,l}$ can be written as

$$\hat{a}_{k,l} = \alpha_k e^{j\psi_{k,l}} + N_l \quad \text{where } N_l \sim \mathcal{CN}(0, 2\sigma^2) \quad (14)$$

where the random variable N_l denotes contributions from DM and noise. Multiplying (14) with $e^{-j\psi_{k,l}}$ yields

$$\hat{a}_{k,l} e^{-j\psi_{k,l}} = \alpha_k + N_l e^{-j\psi_{k,l}} = X_1 + jX_2 \quad (15)$$

where

$$X_1 \sim \mathcal{N}(\Re\{\alpha_k\}, \sigma^2) \quad \text{and} \quad X_2 \sim \mathcal{N}(\Im\{\alpha_k\}, \sigma^2). \quad (16)$$

Hence, the random variable $Y = |\hat{a}_{k,l}|^2$ will follow a non-central χ^2 -distribution with $n = 2$ degrees of freedom [13], whose parameter s^2 is the sum of the means of the underlying Gaussians, i.e. $s^2 = \mathbb{E}\{X_1\}^2 + \mathbb{E}\{X_2\}^2 = |\alpha_k|^2$. Mean and variance of Y are given as

$$\mathbb{E}\{Y\} = n\sigma^2 + s^2 \quad (17)$$

$$\text{var}\{Y\} = 2n\sigma^4 + 4\sigma^2 s^2 \quad (18)$$

which means that s^2 and σ^2 and hence the desired estimate for the SINR_k can be computed from moment estimates of (17) and (18), which we denote with $m_{1,Y}$ and $m_{2,Y}$, respectively. We obtain

$$\text{SINR}_k \approx \frac{1}{\frac{m_{1,Y}}{\sqrt{m_{1,Y}^2 - m_{2,Y}}} - 1} \quad (19)$$

where we observe that the estimate of SINR_k can be complex if the variance of the observed $|\hat{a}_{k,l}|^2$ is high. As in these cases the true SINR would be very low, we set it to zero.

V. RESULTS

We performed the steps described in the previous sections over the $L = 21$ trajectory points shown in Fig. 1. The analysis is performed at three different bandwidths, the full FCC bandwidth of $W = 7.5$ GHz between 3.1 and 10.6 GHz, $W = 2$ GHz and $W = 1$ GHz. The latter two both start at 6 GHz. It should be noted that the estimates for e.g. (19) are based on at most $L = 21$ samples, which is due to the previously discussed limitations of the measurement campaign. However, the presented methodology can be used as a framework for future campaigns, as the results below show its validity in principle.

Table I shows the estimated SINR_k for the individual VAs. SINR_{refl} indicates the total SINR of all reflected (i.e. all but the LOS) MPCs. As expected from the geometry, we observe a high SINR₁, which corresponds to the LOS anchor. For $W =$

7.5 GHz, the SINR_k is high for most VAs, which is due to the fact that their contributions are well resolvable in the received signals. This mostly carries over to $W = 2$ GHz (observe the bandwidth dependence in (5)), but only to a lesser extent to $W = 1$ GHz. Although we exclude path overlap situations in this work, some interference from closely spaced pulses $s(t)$ is visible for e.g. VAs 1 and 10. SINR₁₀ is significantly lower for this bandwidth, as the corresponding pulse is already distorted by the LOS component which causes the re-localization of the respective VA to be erroneous. Hence, path overlap situations are identified as an especially important issue for future work.

Fig. 4 shows the position error bound (PEB), i.e. the square root of the trace of $\mathbf{J}_{\mathbf{p}_l}^{-1}$ over the measurement points. The beneficial influence of bandwidth is clearly visible. As in [2], the CRLB is decomposed into orthogonal (principal) components (PC). We see that most of the expected position error can be attributed to one direction (PC0), while in direction of PC1, low errors are expected (c.f. Fig. 5). Over the analyzed part of the trajectory, the PEB is seen to be roughly constant. For $W = 2$ GHz, we observe an increase at \mathbf{p}_{72} , where VA 15 becomes invisible, increasing the PEB in the corresponding direction.

Fig. 5 finally shows the ten-fold position error standard deviation ellipses for some points on the trajectory. The results are extrapolated for positions \mathbf{p}_l with $l > 80$, i.e. the previously estimated SINR_k is used. The geometry dependence is clearly shown, as the bound in direction to the physical anchor is very low. At position \mathbf{p}_{95} , VA 11 is no longer visible, and the remaining VAs are all located on a vertical line through the anchor. The resulting geometric dilution of precision is well predicted by the CRLB. An additional comparison is done with an Extended Kalman Filter (EKF) algorithm presented in [1]. This EKF can rely on perfect data association (DA) of MPCs to VAs. Analysis of its estimation error covariance matrix reveals a good match with the CRLB, which further verifies its usefulness for performance analysis and prediction of multipath-assisted indoor localization.

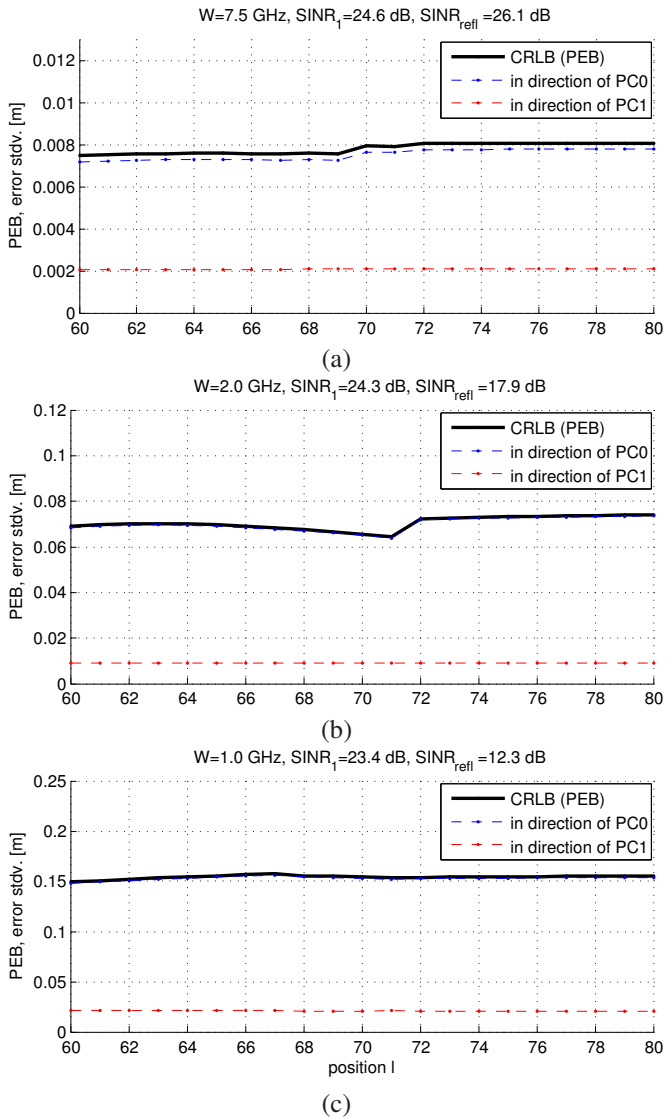


Fig. 4. CRLB over the trajectory for different bandwidths

VI. CONCLUSION AND OUTLOOK

We have presented a framework to quantify position-related information in measured UWB channels. As multipath propagation can be used to enhance accuracy and robustness of localization systems, we have shown how to evaluate the usefulness of different multipath components resulting from specular reflections. Results verify previous theoretical work on the Cramér-Rao bound for multipath-aided localization and provide important performance considerations for corresponding localization schemes. The beneficial influence of a high bandwidth has been shown and the influence of the geometry was emphasized. The presented methodology is potentially valuable in planning both localization systems and measurement campaigns. It is furthermore suitable to compare localization capability in different environments and frequency bands.

Future work most importantly has to address the path over-

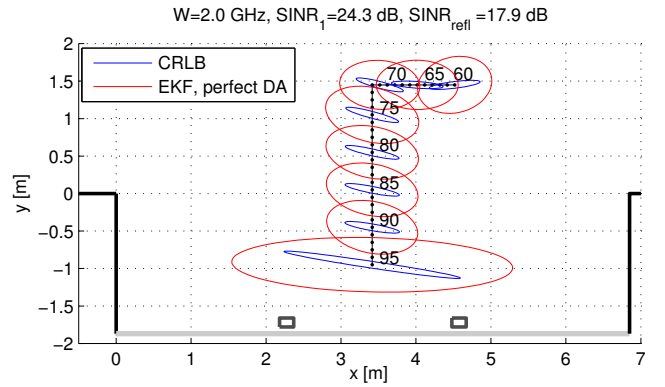


Fig. 5. Ten-fold error standard deviation ellipses for the CRLB (blue) and an EKF with perfect data association (DA) [1] for certain trajectory points and a bandwidth of 2 GHz. After about p_{90} , only VAs on a vertical line through the anchor are visible, which increases the error in x -direction.

lap problem, which was not considered here. Path overlap as one of the major issues for practical system requires additional algorithms to evaluate contributions and interference from multiple (virtual) anchors. Also, further parameterization and validation of the channel model has to be done, as the limited amount of closely spaced measurements did not allow for this here. Furthermore, coherent processing potentially provides additional gains in performance and has to be investigated.

REFERENCES

- [1] P. Meissner and K. Witrals, "Multipath-assisted single-anchor indoor localization in an office environment," in *19th International Conference on Systems, Signals and Image Processing, IWSSIP 2012*, 2012, accepted.
- [2] K. Witrals and P. Meissner, "Performance Bounds for Multipath-aided Indoor Navigation and Tracking (MINT)," in *International Conference on Communications (ICC)*, 2012, accepted.
- [3] Y. Shen and M. Win, "Fundamental limits of wideband localization - part i: A general framework," *Information Theory, IEEE Transactions on*, vol. 56, no. 10, pp. 4956–4980, 2010.
- [4] H. Godrich, A. Haimovich, and R. Blum, "Target Localization Accuracy Gain in MIMO Radar-Based Systems," *Information Theory, IEEE Transactions on*, vol. 56, no. 6, pp. 2783–2803, june 2010.
- [5] P. Meissner, D. Arnitz, T. Gigl, and K. Witrals, "Analysis of an Indoor UWB Channel for Multipath-Aided Localization," in *2011 IEEE International Conference on Ultra-Wideband (ICUWB 2011)*, 2011.
- [6] V. La Tosa, B. Denis, and B. Uguen, "Joint Anchor-less Tracking and Room Dimensions Estimation through IR-UWB Peer-to-peer Communications," in *2011 IEEE International Conference on Ultra-Wideband (ICUWB 2011)*, 2011.
- [7] T. Deissler and J. Thielecke, "UWB SLAM with Rao-Blackwellized Monte Carlo data association," in *Indoor Positioning and Indoor Navigation (IPIN), 2010 International Conference on*, sept. 2010, pp. 1–5.
- [8] P. Meissner, T. Gigl, and K. Witrals, "UWB Sequential Monte Carlo Positioning using Virtual Anchors," in *Proc. 2010 International Conference on Indoor Positioning and Indoor Navigation, IPIN, Zurich*, 2010.
- [9] H. Durrant-Whyte and T. Bailey, "Simultaneous localization and mapping: Part I," *IEEE Robotics Automation Magazine*, vol. 13, no. 2, pp. 99–110, Jun. 2006.
- [10] H. Van Trees, *Detection, Estimation, and Modulation Theory, Part I*. John Wiley & Sons, 2001.
- [11] T. Santos, F. Tufvesson, and A. Molisch, "Modeling the ultra-wideband outdoor channel: Model specification and validation," *Wireless Communications, IEEE Transactions on*, vol. 9, no. 6, pp. 1987–1997, 2010.
- [12] J. Kunisch and J. Pamp, "An ultra-wideband space-variant multipath indoor radio channel model," in *Ultra Wideband Systems and Technologies, 2003 IEEE Conference on*, 2003, pp. 290–294.
- [13] J. G. Proakis and M. Salehi, *Digital Communications*, 5th ed. McGraw-Hill, 2008.

Multipath-Assisted Single-Anchor Indoor Localization in an Office Environment

(Invited Paper)

Paul Meissner and Klaus Witrisal

Graz University of Technology, Graz, Austria, Email: {paul.meissner, witrisal}@tugraz.at

Abstract—Multipath propagation is one of the key problems for indoor localization systems. Strong multipath components can cause range estimates to anchor nodes to be severely biased. If a floor plan is available, reflected signal paths can be used effectively by mapping them to virtual anchors. We show how to make use of the rich localization information provided by just one anchor node. Using tracking algorithms both with and without data association, we achieve accurate and robust localization, which is verified in an indoor environment using measured data at ultra-wide bandwidths. With an extended Kalman filter and data association, a position error of 22 cm is obtained for 90 % of the estimates at a bandwidth of 2 GHz.

I. INTRODUCTION

In prior work [1], we have introduced a multipath-assisted indoor localization and tracking scheme. Using a known floor plan, a single physical anchor node can be turned into a set of virtual anchors (VAs). Using ultra-wideband (UWB) signals, reflected signal paths are resolvable and provide rich localization information [2], [3]. In this contribution, we verify the performance of the scheme using measured data in an indoor environment. The results confirm the excellent accuracy observed in simulations previously and help to identify major influences on the system performance.

Signal reflections are also exploited in [4], but with the restriction to rectangular rooms and single reflections. In [5], VAs are used whose locations are unknown and exploited via cooperation. If reflected signal paths are used as measurement inputs for tracking algorithms like extended Kalman filters (EKFs) [6], the association of range estimates to features in the environment may be unknown. In this case, data association (DA) is necessary [7]. In [8], this is done by finding the nearest neighbor and most probable DAs. In our contribution, we show how the DA can be solved using optimal sub-pattern assignment [9], i.e. finding the subset of measurements that optimally fits to the expected environmental features. The associated measurements can be used as input for an EKF. As a direct comparison with our prior work in [1], a particle filter that can deal with complete lack of DA is also evaluated.

This paper is organized as follows: Section II introduces the scenario, the measurements and the geometric modeling, Section III deals with the extraction of multipath components (MPCs). Tracking algorithms are introduced in Section IV,

This work was partly supported by the Austrian Science Fund (FWF) within the National Research Network SISE project S10604-N13, and by the Austria Research Promotion Agency (FFG) within KIRAS PL3, grant nb. 832335 “LOBSTER”

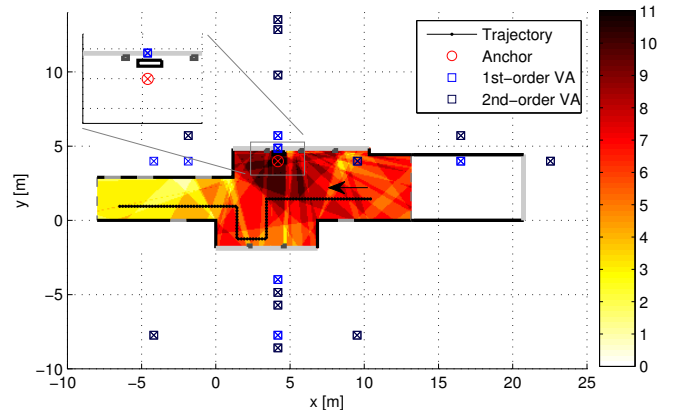


Fig. 1. Scenario with trajectory of a moving agent and physical as well as some of the virtual anchor nodes, with the number of expected virtual anchors N_k in color. The upper-left corner shows a close-up of the base station area.

their performance is discussed in Section V and Section VI draws conclusions.

II. SCENARIO, MEASUREMENTS AND MODELING

The indoor scenario is shown in Fig. 1. It is the ground floor of a multi-storey office building, in which our laboratory is situated. Black lines represent concrete walls, the gray ones are large windows and metal doors. The building further extends several tens of meters to the left. We performed channel measurements over the shown trajectory consisting of 220 points spaced by 10 cm. At each point, the UWB channel was measured with a Rhode & Schwarz ZVA-24 vector network analyzer over a frequency range of 3.1 – 10.6 GHz. The obtained channel transfer functions are transformed to time domain via an inverse discrete Fourier transform. An outline of this procedure and a more detailed description and analysis of the measurement campaign can be found in [2].

Our aim is to localize and track a moving agent node with the help of just a single base station together with the signal reflections in the building walls [1]. Assuming that these MPCs are resolvable in the channel impulse response (CIR), they can be mapped to VAs, which are mirror images of the anchor node with respect to the corresponding reflecting surface. Hence, if the floor plan is known, one physically existing anchor can be turned into a set of VAs usable for localization. The set of all VAs over the whole floor plan is denoted as

$$\mathcal{A} = \{\mathbf{a}_i : i = 1, \dots, N_{VA}\}. \quad (1)$$

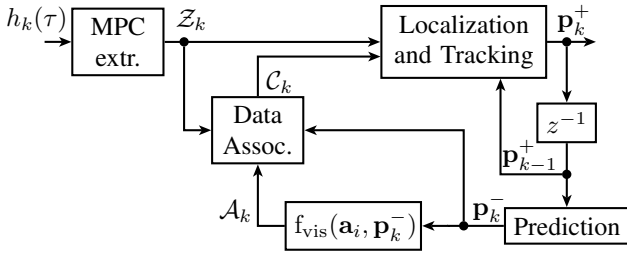


Fig. 2. Overview of localization and tracking scheme.

The geometric visibility region of the i -th VA, which is at position \mathbf{a}_i , can be pre-computed using ray-tracing, as outlined in [2]. In this contribution, this is denoted with a function

$$f_{\text{vis}}(\mathbf{a}_i, \mathbf{p}) = \begin{cases} 1, & \text{if VA } \mathbf{a}_i \text{ is visible at } \mathbf{p} \\ 0, & \text{else.} \end{cases} \quad (2)$$

Evaluating this function for all VAs at the k -th position \mathbf{p}_k yields the set of expected visible VAs at this position, which is denoted as

$$\mathcal{A}_k = \{\mathbf{a}_{k,1}, \dots, \mathbf{a}_{k,N_k}\} = \{\mathbf{a}_i : f_{\text{vis}}(\mathbf{a}_i, \mathbf{p}_k) = 1\}. \quad (3)$$

Hence, \mathcal{A}_k is only a subset of \mathcal{A} with cardinality $|\mathcal{A}_k| = N_k$. Fig. 1 shows N_k over the floor plan, where single- and double-reflections are taken into account in the construction of \mathcal{A} . We observe a potential challenge for multipath-assisted localization: The set of anchors that can be used for position estimation rapidly changes over the area. Hence, an agent moving through the scenario needs some awareness of the currently valid set of VAs to perform location estimation.

III. MULTIPATH EXTRACTION AND LOCALIZATION

Fig. 2 shows the conceptual layout of our proposed multipath-assisted localization scheme. Localization and tracking algorithms use range estimates to the VAs, which are delivered by an MPC-extraction step. As this step is performed without any location information, it extracts the arrival times of the M_k largest local maxima from the CIR.

The UWB CIR $h_k(\tau)$ is modeled as

$$h_k(\tau) = \sum_{l=1}^{L_k} \alpha_{k,l} \delta(\tau - \tau_{k,l}) + \nu_k(\tau) + n_k(\tau). \quad (4)$$

It consists of L_k MPCs caused by deterministic reflections, with corresponding amplitudes $\alpha_{k,l}$ and delays $\tau_{k,l}$. The signal $\nu_k(\tau)$ models diffuse scattered components and $n_k(\tau)$ is the measurement noise. We expect that at position \mathbf{p}_k , the VAs in \mathcal{A}_k are responsible for a part of the deterministic reflections, i.e. $N_k \leq L_k$. Results in [2] show that these MPCs carry a significant part of the energy of the CIR, which justifies our choice to extract the arrival times of the local maxima.

The set of M_k estimated path delays is denoted as $\mathcal{Z}_k = \{z_{k,1}, \dots, z_{k,M_k}\}$, where $z_{k,i} = c\tau_{k,i}$ and c is the propagation velocity. Of course \mathcal{Z}_k does not only contain range estimates to the VAs in \mathcal{A}_k , but also entries that are due to noise or

diffuse scattered components, i.e. clutter. The quality of \mathcal{Z}_k is determined by its distance to the ground truth \mathcal{D}_k , which is the set of distances to the expected VAs at \mathbf{p}_k , i.e.

$$\mathcal{D}_k = \{d_{k,1}, \dots, d_{k,N_k}\} = \{d(\mathbf{a}_i, \mathbf{p}_k) : \mathbf{a}_i \in \mathcal{A}_k\} \quad (5)$$

where $d(\mathbf{a}_i, \mathbf{p}_k)$ is simply the Euclidean distance between the VA \mathbf{a}_i and the point \mathbf{p}_k . However, as both \mathcal{Z}_k and \mathcal{D}_k are sets of usually different cardinality, no straightforward distance measure is available. Instead, we resort to a popular *multi-target miss-distance*, the optimal sub-pattern assignment (OSPA) metric [9]. For $M_k \geq N_k$, which can be ensured by filling up \mathcal{Z}_k with dummy clutter, it is defined as

$$d_{\text{OSPA}}(\mathcal{D}_k, \mathcal{Z}_k) = \left[\frac{1}{M_k} \left(\min_{\pi \in \Pi_{M_k}} \sum_{i=1}^{N_k} d^{(d_c)}(d_{k,i}, z_{k,\pi_i})^p + d_c^p (M_k - N_k) \right) \right]^{1/p} \quad (6)$$

where Π_{M_k} is the set of permutations of positive integers up to M_k . The function $d^{(d_c)}(x, y) = \min(d_c, d(x, y))$, i.e. an arbitrary distance metric $d(\cdot)$ that is cut off at a $d_c > 0$, which is a design parameter. The first part of the metric, the sum, is the cumulative distance over the optimal sub-pattern assignment of \mathcal{Z}_k to \mathcal{D}_k , i.e. where N_k entries of \mathcal{Z}_k are assigned optimally to the entries of \mathcal{D}_k . The Hungarian algorithm is used for this assignment [10]. For the remaining $M_k - N_k$ entries of \mathcal{Z}_k , d_c is assigned as penalty distance.

IV. TRACKING AND DATA ASSOCIATION

The motion of the agent is modeled with a standard discrete-time linear state-space model as in [1]

$$\mathbf{x}_{k+1} = \begin{bmatrix} 1 & 0 & \Delta T & 0 \\ 0 & 1 & 0 & \Delta T \\ 0 & 0 & 1 & 0 \\ 0 & 0 & 0 & 1 \end{bmatrix} \mathbf{x}_k + \begin{bmatrix} \frac{\Delta T^2}{2} & 0 \\ 0 & \frac{\Delta T^2}{2} \\ \Delta T & 0 \\ 0 & \Delta T \end{bmatrix} \mathbf{n}_{a,k} \quad (7)$$

where the state vector $\mathbf{x}_k = [p_x, p_y, v_x, v_y]_k^T$ contains position and velocity components in x - and y -direction, ΔT is the update interval and $\mathbf{n}_{a,k}$ is acceleration noise. For range-based tracking using the VAs, we use \mathcal{Z}_k as measurement input for the tracking algorithm at time-step k . However, the association of the entries of \mathcal{Z}_k to the VAs is unknown [7]. Therefore, we introduce a set \mathcal{C}_k of correspondence variables [6], whose i -th entry $c_{k,i}$ is defined as

$$c_{k,i} = \begin{cases} j, & \text{if } z_{k,i} \text{ corresponds to VA } \mathbf{a}_j \ (j = 1, \dots, N_{\text{VA}}) \\ 0, & \text{if } z_{k,i} \text{ corresponds to clutter.} \end{cases} \quad (8)$$

A. Extended Kalman filter with data association (EKF-DA)

If \mathcal{C}_k is available, state-space estimation can be performed by e.g. an EKF using the linear motion model and a linearized observation model [6] based on the associated entries of \mathcal{Z}_k and the corresponding VAs. As the well-known EKF equations are used, we concentrate on the description of the DA here. Fig. 2 depicts the general scheme: Assuming

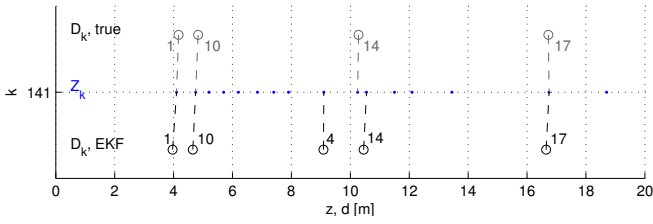


Fig. 3. Example for the DA for a bandwidth of 2 GHz at $k = 141$, zoomed view on x -axis. Upper part shows the genie-aided DA, lower part the DA based on the estimated position. Due to the position error, the EKF expects a different set \mathcal{D}_k . For the VA at \mathbf{a}_4 , a clutter measurement is associated, for \mathbf{a}_{14} , the wrong measurement is associated.

the EKF is already on track at time step k , the predicted position \mathbf{p}_k^- is computed using the motion model (7) and the previous posterior estimate \mathbf{p}_{k-1}^+ . Using $f_{\text{vis}}(\mathbf{a}_i, \mathbf{p}_k^-)$, the set of expected VAs \mathcal{A}_k , and subsequently the expected delays \mathcal{D}_k are estimated.

Inspired by the definition of the OSPA metric, the DA is done using optimal sub-pattern assignment between \mathcal{D}_k and \mathcal{Z}_k , which is reflected in the first part of (6)

$$\boldsymbol{\pi}_{\text{opt}} = \arg \min_{\boldsymbol{\pi} \in \Pi_{M_k}} \sum_{i=1}^{N_k} d^{(d_c)}(d_{k,i}, z_{k,\pi_i})^p. \quad (9)$$

The first N_k entries of $\boldsymbol{\pi}_{\text{opt}}$ contain the indices of those entries of \mathcal{Z}_k that have been optimally assigned to \mathcal{D}_k . For some entries of \mathcal{D}_k , we will probably have $d^{(d_c)}(d_{k,i}, z_{k,\pi_{\text{opt},i}}) = d_c$, i.e. this expected distance has an assigned measurement, but the difference between measurement and expected distance is larger or equal to the cutoff distance. We expect that by using UWB signals, the estimated path delays will be quite accurate, provided that they are detected. Hence, we select a certain d_c that may depend on the bandwidth and reject the corresponding assignments as outliers. Formally, the DA is expressed by setting the correspondence variables as

$$c_{k,i} = \begin{cases} j, & \text{if } \pi_j = i \text{ and } d^{(d_c)}(d_{k,j}, z_{k,i}) < d_c \\ 0, & \text{else} \end{cases} \quad (10)$$

B. Extended Kalman filter with genie-aided data association (EKF-GADA)

It is well-known that erroneous DA can lead to catastrophic failures of Kalman filters. Hence we propose a genie-aided DA procedure that can act as a benchmark for other trackers. The only difference to the DA procedure explained in Sec. IV-A is that here the set of expected path delays \mathcal{D}_k is calculated based on the true position \mathbf{p}_k .

C. Particle filter without data association

We compare the performance of the EKF with a particle filter-based tracker (PF) that was introduced in [1]. This filter has the advantage of not requiring DA. N_p particles are initially selected randomly over the floor plan. In each time-step, they are propagated through the motion model (7) and subsequently weighted and resampled according to their

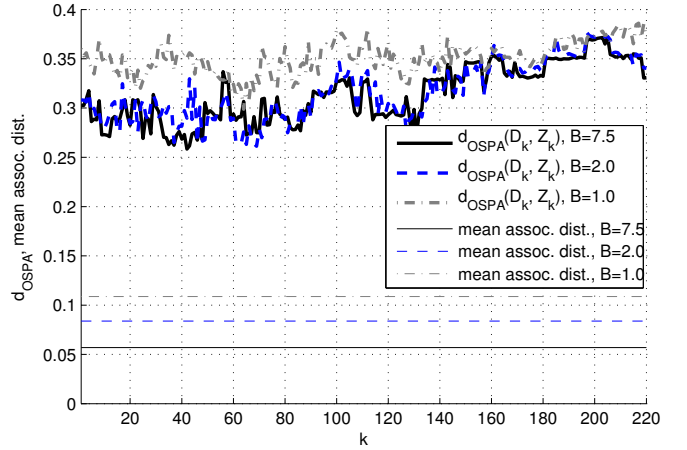


Fig. 4. OSPA metric over the trajectory for different bandwidths as well as mean distance of associated path delays.

likelihood with respect to the current measurement. For a particle at \mathbf{p}_k and a range estimate $z_{k,i}$, the likelihood is

$$p(z_{k,i} | \mathbf{p}_k) = P_{VA} \sum_{n=1}^{N_{VA}} P_{v,n} f_{\text{vis}}(\mathbf{a}_n, \mathbf{p}_k) p(z_{k,i} | \mathbf{p}_k, c_{k,i} = n) + (1 - P_{VA}) p(z_{k,i} | \mathbf{p}_k, c_{k,i} = 0) \quad (11)$$

where $P_{v,n}$ is the visibility probability of the n -th VA and P_{VA} is the probability that $z_{k,i}$ is caused by any of the VAs. The likelihood is a sum over all possible causes of $z_{k,i}$, i.e. over all VAs visible at \mathbf{p}_k and also the possibility that $z_{k,i}$ is clutter. The corresponding conditional densities of $z_{k,i}$ are selected as Gaussian with mean equal to the true distance in the first case, and as uniform over the range from zero to a maximum range value in the latter case. Treating \mathcal{Z}_k as a random vector, the joint likelihood of all measurements is calculated as the product of the individual likelihoods (11). This assumes that the $z_{k,i}$ are independent, which is a simplification resulting in severe multimodality, as discussed in [1].

V. PERFORMANCE RESULTS

The performance of the proposed tracking algorithms is evaluated over the scenario in Fig. 1. We selected the full bandwidth of $B = 7.5$ GHz as well as bandwidths of 2 GHz and 1 GHz, where the frequency range of the reduced bandwidths starts at 6 GHz. For the MPC-extraction, the $M_k = 20$ largest local maxima are extracted from $|h_k(\tau)|$, using the subtraction method discussed in [2]. The EKFs are provided with a perfect initialization. In practice, initialization can be handled using a Gaussian sum filter, as described in [1].

Fig. 3 shows an example for the DA procedure for $B = 2$ GHz at a point on the trajectory. The cutoff distance has been chosen as $d_c = 0.4$ m. Although the true position \mathbf{p}_k and the EKFs estimate of it are just 14 cm apart, the set of expected VAs differ. This leads to an erroneous detection of the VA at \mathbf{a}_4 , where a clutter measurement is within the cutoff distance. Also the association for VA \mathbf{a}_{14} is wrong due to the

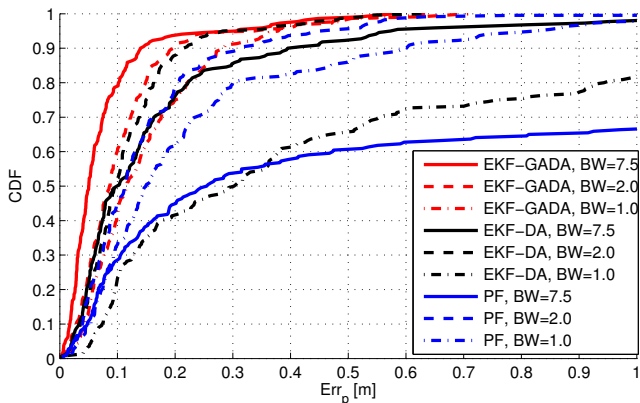


Fig. 5. CDFs of the position error for the proposed tracking algorithms and different bandwidths.

slight position error. This erroneous example has been chosen on purpose to highlight potential error sources, in general the DA based on optimal sub-pattern assignment works stable with a sensitivity tunable via the choice of d_c .

Fig. 4 shows the OSPA metric defined in (6) over the trajectory for all bandwidths and $d_c = 0.4$ m. It can be observed that for $B = 7.5$ GHz and $B = 2$ GHz, the OSPA distance qualitatively shows similar behavior. For $B = 1$ GHz, the distance is larger, which is partly because of the higher probability of path overlap [3]. Using the optimal sub-pattern assignment, a measurement can only be assigned to one VA, whereas it might be caused by multiple ones. Due to the fact the MPC extraction returns the 20 largest local maxima and the mean N_k is around 5.6, the cardinality error dominates the metric. Therefore, also the mean distance over the trajectory of the associated sub-pattern is shown, as this also corresponds to the objective function for the DA in (9). Here, the beneficial influence of a high bandwidth is clearly visible.

The performance of the tracking algorithms is compared in Fig. 5, which shows CDFs of the position error. The influence of bandwidth is interesting: The EKF-GADA does not suffer from erroneous associations and can thus make use of the large bandwidth that also results in low probability of path overlap. The latter is problematic for the EKF-DA at $B = 1$ GHz, as every measurement can only be associated once, causing increased sensitivity to miss-associations. For the EKF-DA at $B = 2$ GHz, a promising 90% of the estimates are within 22 cm. For the higher bandwidth, the DA gets trickier: The MPC extraction returns more clutter around the true MPCs, as at this bandwidth, diffuse tails of some MPCs can be resolved. For the PF at this bandwidth, this clutter leads to pronounced maxima of the multimodal likelihood function in the vicinity of the true position. This can draw the PF estimate away from the true trajectory. For the lower bandwidths, this effect is less pronounced and the PF offers reasonable performance.

Qualitatively, the performance is shown in Fig. 6 for $B = 2$ GHz. For this case, the EKF-DA approaches the EKF with genie-aided DA. Near the end of the trajectory, all filters are

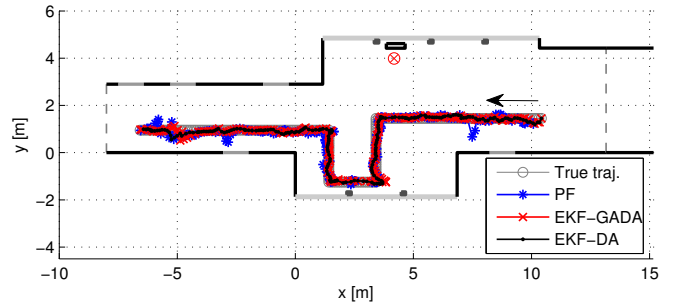


Fig. 6. Performance of proposed algorithms over scenario for BW=2 GHz.

drawn away from the trajectory, as in this region, only two VAs are visible. All the filters can again lock on the trajectory once the double reflection between the corridor walls becomes visible. Also the influence of geometric dilution of precision is visible at the second bend of the trajectory. Both EKFs tend to the wrong direction initially and the variance in x -direction increases. This is due to the fact that in this region, only VAs on a vertical line through the anchor are visible, providing little information in x -direction [3].

VI. CONCLUSION AND OUTLOOK

We have presented an indoor localization scheme with only a single base station that effectively makes use of multipath propagation. Using a known floor plan and the concept of virtual anchors, excellent performance can be achieved with tracking algorithms, also in the absence of data association information. Data association based on optimal sub-pattern assignment can further improve the accuracy, even if the clutter rate is high. In future work, tracking of the multipath components themselves will be used to significantly reduce clutter and to help in resolving path overlap problems.

REFERENCES

- [1] P. Meissner, T. Gigl, and K. Witrisal, "UWB Sequential Monte Carlo Positioning using Virtual Anchors," in *Proc. 2010 International Conference on Indoor Positioning and Indoor Navigation, IPIN, Zurich*, 2010.
- [2] P. Meissner, D. Arnitz, T. Gigl, and K. Witrisal, "Analysis of an Indoor UWB Channel for Multipath-Aided Localization," in *2011 IEEE International Conference on Ultra-Wideband (ICUWB 2011)*, 2011.
- [3] K. Witrisal and P. Meissner, "Performance Bounds for Multipath-aided Indoor Navigation and Tracking (MINT)," in *International Conference on Communications (ICC)*, 2012, accepted.
- [4] V. La Tosa, B. Denis, and B. Uguen, "Joint Anchor-less Tracking and Room Dimensions Estimation through IR-UWB Peer-to-peer Communications," in *2011 IEEE International Conference on Ultra-Wideband (ICUWB 2011)*, 2011.
- [5] Y. Shen and M. Win, "On the Use of Multipath Geometry for Wideband Cooperative Localization," in *Global Telecommunications Conference, 2009. GLOBECOM 2009. IEEE*, 2009, pp. 1–6.
- [6] S. Thrun, W. Burgard, and D. Fox, *Probabilistic Robotics*. MIT, 2006.
- [7] Y. Bar-Shalom and T. Fortmann, *Tracking and Data Association*. Academic Press, 1988.
- [8] T. Deissler and J. Thielecke, "UWB SLAM with Rao-Blackwellized Monte Carlo data association," in *Indoor Positioning and Indoor Navigation (IPIN), 2010 International Conference on*, sept. 2010, pp. 1–5.
- [9] D. Schuhmacher, B.-T. Vo, and B.-N. Vo, "A Consistent Metric for Performance Evaluation of Multi-Object Filters," *Signal Processing, IEEE Transactions on*, vol. 56, no. 8, pp. 3447–3457, 2008.
- [10] J. Munkres, "Algorithms for the Assignment and Transportation Problems," *Journal of the Society for Industrial and Applied Mathematics*, vol. 5, no. 1, pp. pp. 32–38, 1957.

Accurate and Robust Indoor Localization Systems using Ultra-wideband Signals

Paul Meissner*, Erik Leitinger*, Markus Fröhle*, and Klaus Witrisal*

*Graz University of Technology, Austria; E-mail: paul.meissner@tugraz.at

Abstract—Indoor localization systems that are accurate and robust with respect to propagation channel conditions are still a technical challenge today. In particular, for systems based on range measurements from radio signals, non-line-of-sight (NLOS) situations can result in large position errors. In this paper, we address these issues using measurements in a representative indoor environment. Results show that conventional tracking schemes using high- and a low-complexity ranging algorithms are strongly impaired by NLOS conditions unless a very large signal bandwidth is used. Furthermore, we discuss and evaluate the performance of multipath-assisted indoor navigation and tracking (MINT), that can overcome these impairments by making use of multipath propagation. Across a wide range of bandwidths, MINT shows superior performance compared to conventional schemes, and virtually no degradation in its robustness due to NLOS conditions.

a Ph.D. student and Research Engineer at Delft University of Technology. Currently, he is an Associate Professor at the Signal Processing and Speech Communication Laboratory (SPSC), Graz University of Technology. His research interests are in signal processing for broadband and UWB wireless communications, propagation channel modeling, and (indoor) positioning. Prof. Witrisal served as co-chair of the MTT/COM Society of the IEEE Austria Section, TPC co-chair of the Workshop on Positioning, Navigation, and Communications (WPNC) 2011, and as a TPC member in numerous conferences and workshops. He is a co-chair of the first IEEE ICC Workshop on Advances in Network Localization and Navigation (ANLN) 2013 and an associate editor of the IEEE Communications Letters.

BIOGRAPHIES

Paul Meissner was born in Graz, Austria, in 1982. He received his M.Sc. degree (with distinction) in Telematics from Graz University of Technology, Austria, in 2009. Since then, he is working towards the PhD degree at Graz University of Technology. His research interests include statistical signal processing, indoor localization, UWB systems and channel analysis as well as wireless communications.

Erik Leitinger was born in Graz, Austria, in 1985. He received the Dipl.-Ing. degree in electrical engineering (with distinction) from the Graz University of Technology, Austria, in 2012. Since February 2012 he is working as PhD Student at Graz University of Technology at the Signal Processing and Speech Communication Laboratory. His research interests are UWB wireless communications, indoor-positioning, estimation theory, Bayesian inference and statistical signal processing.

Markus Fröhle received his M.Sc. degree (with distinction) in Telematics from Graz University of Technology, Austria, in 2012. He is currently pursuing his Ph.D. degree at the Signal Processing and Speech Communication Laboratory also at Graz University of Technology. His main research interests are UWB indoor positioning, machine learning and statistical signal processing.

Klaus Witrisal received the Dipl.-Ing. degree in electrical engineering from Graz University of Technology, Graz, Austria, in 1997, the Ph.D. degree (cum laude) from Delft University of Technology, Delft, The Netherlands, in 2002, and the Venia Docendi (Habilitation) from Graz University of Technology in 2009. From 1997 to 2001, he was

I. INTRODUCTION

Indoor localization systems face many difficulties when they are to be deployed in practice [1]. Optical systems might become unusable in emergency situations due to fire and smoke; signal strength based systems are sensitive to fading effects; fingerprinting systems need dedicated training phases; etc. Range-measurement-based systems using radio signals, which are in the focus of this paper, offer advantages like the capability of being integrated in existing radio devices such as smartphones, the potential of low-power implementations and moderate infrastructure requirements. However, they face challenging performance impairments caused by propagation effects like strong reflections or diffuse scattering.

To counter these impairments, a large signal bandwidth is beneficial for two main reasons: First, the temporal resolution and therefore the attainable accuracy is increased. Second, the line-of-sight (LOS) path can be separated from other signal parts easier, which improves the robustness, i.e. the percentage of cases in which the attainable accuracy can be achieved. For these reasons, systems using ultra-wideband (UWB) signals are promising candidates for both accurate and robust indoor localization [2].

In this paper, we examine the performance of a conventional range-based UWB indoor localization and tracking system in a representative indoor environment with several anchor nodes. Using channel measurements along a reference trajectory, mimicking the walking path of a pedestrian user, we show the dependence of the robustness and accuracy of the localization on changing propagation conditions. The LOS path is estimated

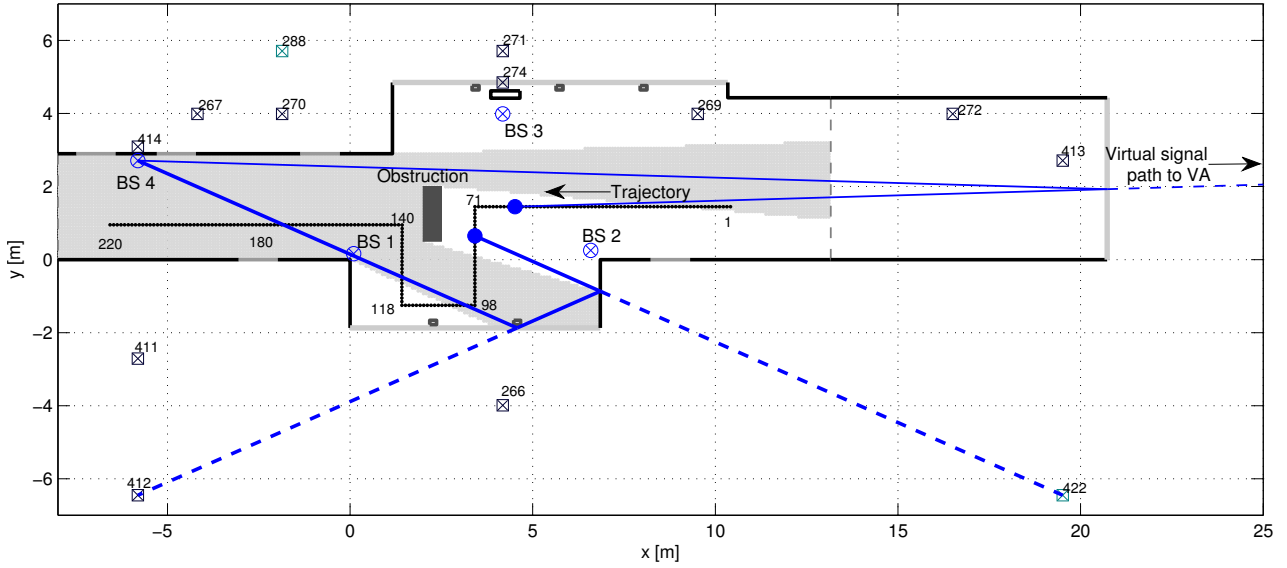


Figure 1: Indoor tracking scenario considered in this paper. The black dotted line illustrates the user's trajectory in the scenario, selected position indices are given to allow easier interpretation of later results. Blue circled crosses are the base stations, while black and grey squares with crosses denote some few illustrative VAs for BSs 3 and 4. The area shaded in light gray denotes the geometric visibility region of the LOS path of BS 4, illustrating the NLOS region caused by the hypothetical obstruction in the center that is used for performance evaluations. Additionally, the thin and bold blue lines show two example propagation paths that can be modeled by VAs and that are potentially visible in the NLOS region.

using the maximum-likelihood method as well as using a low-complexity ranging algorithm. These estimates are provided as inputs to an extended Kalman filter (EKF), which tracks the user's position. The presence of strong reflections in the measurement signal can lead to a large bias in the estimate of the propagation delay of the direct path between user and anchor. This is especially true in non-LOS (NLOS) situations, where the direct path is blocked. Overall, a degradation of the robustness of the system is the result.

Usual countermeasures are to detect such situations based on signal statistics and discard the corresponding measurements [3], [4]. In advanced schemes like [5], [6], machine learning techniques are used to mitigate the range bias in NLOS situations. However, these approaches discard position-related information that is inherent in the geometric structure of reflected MPCs. The usefulness of this information has been shown in [7]–[10].

We have shown in previous work [9]–[11] that by using additional floor plan information, these reflected signal paths can be used for localization. Extracting these paths from the channel measurements and associating them to the floor plan, signal reflections can be seen as direct signals coming from virtual anchor (VA) nodes. In this way, one physically existing anchor node is turned into a set of virtual anchors, and NLOS situations no longer render this anchor useless for localization. This scheme, which we call multipath-assisted indoor navigation and tracking (MINT), can thus deliver the desired robustness with respect to the propagation conditions. However, the effect of diffuse scattering is especially pronounced in

indoor environments due to the presence of objects like, e.g., furniture. This makes the extraction of the reflected components from the measurements and the required data association challenging. To highlight these issues in a practical setting, this paper extends our previous work in [11] with the use of multiple base stations, a detailed performance analysis of the proposed algorithms and a comparison to standard tracking schemes employed in indoor localization.

The key contributions of this work are:

- We show the performance and the robustness issues of a conventional, EKF based tracking system with respect to channel conditions. This is done in a representative indoor environment using measured signals.
- Making explicit use of multipath, robustness and accuracy can be increased. We discuss an implementation of the proposed MINT approach and examine its performance. Results show the excellent robustness of MINT with respect to NLOS situations.
- The results obtained highlight general practical considerations for indoor localization systems, i.e. the importance of a large bandwidth and propagation channel conditions is shown.

This paper is organized as follows: Section II explains the scenario, the measurement campaign and the geometrical modeling of the environment. A short overview over performance bounds for MINT is given in Section III, while Section IV discusses channel estimation and

ranging algorithms. Tracking is explained in Section V and a detailed discussion of results is given in Section VI.

II. SCENARIO, MEASUREMENTS, AND GEOMETRIC MODELING

Fig. 1 shows the scenario used in this paper. It is the ground floor of a large three-storey building with open ceilings in the corridor areas in all but the uppermost floors. Walls are made of reinforced concrete (shown as black outer lines) and doors (shown in grey) are made of metal. The long grey outer lines on the upper and lower side are large windows with some metal pillars in-between. We placed four base stations (BSs) at known locations and measured the UWB channel between them and a moving agent. The latter was moved along a trajectory consisting of 220 points spaced by 10 cm. The obstruction shown near the center of the corridor has not been present in the measurements. It is introduced artificially in the performance evaluations to show the influence of NLOS scenarios on the localization, c.f. Section VI.

A. Geometric Modeling of the Environment

If a floor plan of the building is available, the BS positions \mathbf{a}_i , $i = 1, \dots, 4$, can be mirrored with respect to reflecting surfaces like walls to obtain so-called first-order virtual anchors (VAs) at positions \mathbf{a}'_i . Using these, the procedure can be repeated to obtain second-order VAs \mathbf{a}''_i , and so on. The visibility regions of these VAs, i.e. the regions where the corresponding reflections are possible, can be computed by ray tracing as explained in [12]. If the corresponding MPCs are detectable at the moving agent, they can be associated to the VAs and used for localization. Fig. 1 shows a subset of VAs for BSs 3 and 4 together with two example signal paths.

In an analogous manner to [11], the overall set of VAs for the i -th BS is denoted as

$$\mathcal{A}^{(i)} = \{\mathbf{a}_j : j = 1, \dots, N_{\text{VA}}^{(i)}\}. \quad (1)$$

Here, the superscript indicating the VA order has been dropped as it is not important in the upcoming discussion. A function $f_{\text{vis}}(\mathbf{a}_j, \mathbf{p})$ determines the visibility of the j -th VA at a position \mathbf{p} , i.e.

$$f_{\text{vis}}(\mathbf{a}_j, \mathbf{p}) = \begin{cases} 1, & \text{if VA } \mathbf{a}_j \text{ is visible at } \mathbf{p} \\ 0, & \text{else.} \end{cases} \quad (2)$$

The set of expected visible VAs at a specific position \mathbf{p}_ℓ can then be computed evaluating (2) for all VAs in (1)

$$\mathcal{A}_\ell^{(i)} = \{\mathbf{a}_{\ell,1}, \dots, \mathbf{a}_{\ell,K_\ell^{(i)}}\} = \{\mathbf{a}_j : f_{\text{vis}}(\mathbf{a}_j, \mathbf{p}_\ell) = 1\}. \quad (3)$$

In the following, we omit the BS index i wherever it should be clear from the context that the respective quantity exists for all BSs.

It can be seen from (3) that a set of anchor nodes significantly larger than the set of BSs can potentially be used for localization. We call this approach *multipath-assisted indoor navigation and tracking* (MINT). However, the challenges are as manifold as the potential gains:

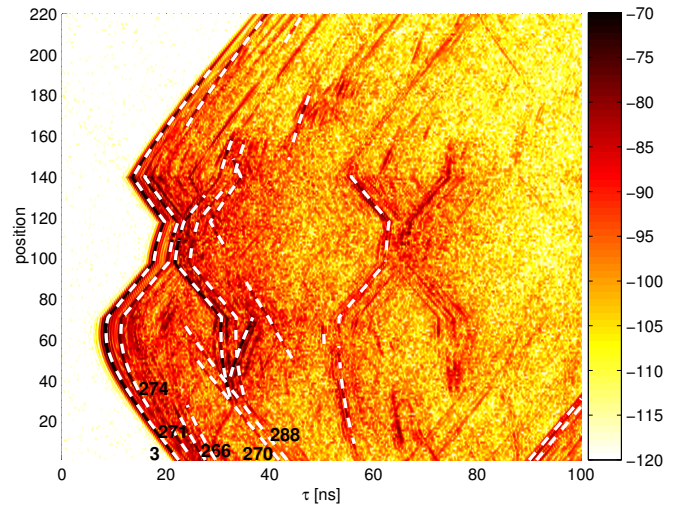


Figure 2: Received signals $r_\ell(t)$ in logarithmic scaling over the trajectory for BS 3. The white dashed lines indicate expected delay paths of MPCs modeled by VAs up to order two, computed by geometric ray-tracing. Indices of some of the VAs shown in Fig. 1 are given.

First, the MPCs corresponding to the VAs need to be detected in the signal received at the agent, which depends on influences such as e.g. material parameters or reflection angles. Second, together with deterministic MPCs, also some scattered, non-specular components will cause a certain level of clutter in the measurements. Third, the detected MPCs need to be associated to the VAs to make their position-related information accessible. Summarizing, a moving agent needs to perform detection of MPCs in the presence of possibly strong diffuse multipath and noise as well as subsequently a robust data association procedure to infer its location.

B. Channel Measurements

Measurements were performed in the frequency domain with a vector network analyzer (VNA) over the full FCC bandwidth from 3.1 to 10.6 GHz. These measurements have also been used in [10]–[12]. The discrete frequency representation of the channel's transfer function at position \mathbf{p}_ℓ is denoted as $H_\ell[k]$. Using a frequency spacing of Δf , it corresponds to a Fourier series (FS) of a time-domain channel impulse response (CIR) $h_\ell(\tau)$. This CIR is periodic with a period of $\tau_{\text{max}} = 1/\Delta f$, which is the maximum resolvable delay. The FS representation allows an arbitrarily fine time resolution $\Delta\tau$ to be achieved. Using an IFFT with size $N_{\text{FFT}} = \lceil (\Delta f \Delta\tau)^{-1} \rceil$, the time domain equivalent baseband signal is obtained as

$$r_\ell(t) = \text{IFFT}_{N_{\text{FFT}}} \{H_\ell[k]S[k]\} e^{-j2\pi(f_c - f_0)t}. \quad (4)$$

In (4), $S[k]$ is the discrete frequency domain representation of a raised-cosine pulse $s(t)$ with pulse duration T_p and roll-off factor β_R [13]. It is used to cut out the desired band of the signal as well as to filter it to facilitate an MPC estimation algorithm. The frequencies f_c and f_0 are the desired center frequency and the lower band edge of the extracted band, respectively. This procedure is similar to

[14]. Examples for $r_\ell(\tau)$ obtained in this way are shown in Fig. 2 for BS 3 over the trajectory.

III. CHANNEL INFLUENCE ON LOCALIZATION

The received signal at the ℓ -th trajectory position \mathbf{p}_ℓ , corresponding to the processing in (4), is modeled as [9]

$$r_\ell(t) = \sum_{k=1}^{K_\ell} \alpha_{k,\ell} s(t - \tau_{k,\ell}) + s(t) * \nu_\ell(t) + w_\ell(t). \quad (5)$$

It consists of a sum of K_ℓ deterministic MPCs, scaled and shifted by the complex amplitudes $\alpha_{k,\ell}$ and propagation delays $\tau_{k,\ell}$, respectively. The signal $\nu_\ell(t)$ is a stochastic process modeling the diffuse multipath (DM), i.e. diffuse scattering at rough surfaces and other propagation mechanisms that are not captured by the specular part of the channel. It is observed at the agent as a convolution with the transmit pulse $s(t)$. Finally, $w_\ell(t)$ denotes additive white Gaussian noise (AWGN) with two-sided power spectral density $N_0/2$.

We expect that the deterministic part of $r_\ell(t)$ can be modeled by the set of VAs \mathcal{A}_ℓ . In [9], we have derived the Cramér-Rao lower bound (CRLB) on the position error for the MINT scheme, based on the received signal $r_\ell(t)$. It is given as the inverse of the equivalent Fisher Information matrix (EFIM) [8]. If all K_ℓ deterministic MPCs are orthogonal at \mathbf{p}_ℓ , i.e. there is no path overlap in the delay domain, the EFIM can be decomposed as

$$\mathbf{J}_{\mathbf{p}_\ell} = \frac{8\pi^2\beta^2}{c^2} \sum_{k=1}^{K_\ell} \text{SINR}_{k,\ell} \mathbf{J}_r(\phi_{k,\ell}) \quad (6)$$

where β denotes the effective (RMS) bandwidth of $s(t)$ and c is the speed of light. The decomposition is instructive since it separates the channel's influence from the geometry of the VAs. The former is given by the signal-to-interference-plus-noise-ratio (SINR) of the deterministic MPCs. For the k -th MPC at position \mathbf{p}_ℓ , it is defined as [9]

$$\text{SINR}_{k,\ell} = \frac{|\alpha_{k,\ell}|^2}{N_0 + T_p S_{\nu,\ell}(\tau_{k,\ell})}. \quad (7)$$

Here, interference is understood as the contribution of the DM, which is given by the power delay profile (PDP) of the DM, $S_{\nu,\ell}$ at the delay $\tau_{k,\ell}$ of the respective MPC, scaled with the pulse duration. This PDP is defined as the second central moment of the DM process $\nu_\ell(t)$.

The influence of the geometry is accounted for by the ranging direction matrix $\mathbf{J}_r(\phi_{k,\ell})$ [8], [9], which is defined as

$$\mathbf{J}_r(\phi_{k,\ell}) = \begin{bmatrix} \cos^2(\phi_{k,\ell}) & \cos(\phi_{k,\ell}) \sin(\phi_{k,\ell}) \\ \cos(\phi_{k,\ell}) \sin(\phi_{k,\ell}) & \sin^2(\phi_{k,\ell}) \end{bmatrix}. \quad (8)$$

This matrix has one eigenvector pointing in the direction $\phi_{k,\ell}$, the angle from the VA at \mathbf{a}_k to position \mathbf{p}_ℓ . The SINR in (7) is used in the performance evaluations to emulate changes of propagation conditions caused by the artificial obstruction that is shown in Fig. 1.

IV. CHANNEL ESTIMATION AND RANGING

Conventional time-of-arrival (ToA) localization requires an estimate of the time-of-flight of the signal from the BS to the agent. This process is called ranging [15]. In this work, we consider two different ranging algorithms, maximum likelihood (ML) and jump-back search-forward (JBSF). The former is computationally intensive since it requires channel estimation, while the latter is a popular low-complexity algorithm. The MINT approach requires range estimates to all the MPCs that are modeled by VAs, i.e., an estimation of the deterministic part of the UWB channel as for ML ranging.

A. Channel Estimation and ML Ranging

It has been shown that the MPCs corresponding to the VAs can carry a large fraction of the energy of the received signal [12], hence we extract those K_ℓ MPCs that result in the minimum energy of the difference signal

$$\{\hat{\tau}_{k,\ell}\} = \arg \min_{\{\tau_{k,\ell}\}} \int_T \left| r_\ell(t) - \sum_{k=1}^{K_\ell} \hat{\alpha}_{k,\ell} s(t - \hat{\tau}_{k,\ell}) \right|^2 dt \quad (9)$$

where T is the observation interval. Of course the parameter \hat{K}_ℓ should be related to K_ℓ in (5). However, without the knowledge of the position, a value has to be chosen that allows for the extraction of the geometrically relevant paths over the entire scenario. The choice of this parameter will be discussed in Section VI-B.

For this work, we assume a separable channel, i.e. there is no overlap between deterministic MPCs. In this case, (9) can be performed path-per-path. The amplitudes $\alpha_{k,\ell}$ are nuisance parameters to this estimation and can be obtained by a projection of the unit-energy pulse $s(t)$, shifted to the estimated delay $\hat{\tau}_{k,\ell}$, onto the received signal

$$\hat{\alpha}_{k,\ell} = \int_T r_\ell^*(t) s(t - \hat{\tau}_{k,\ell}) dt \quad (10)$$

where $*$ denotes complex conjugation. With the separable channel assumption, this procedure is similar to [16].

For MINT, the set of estimated arrival times in (9), converted to distances, constitutes the measurement input to the tracking algorithms. Additionally, a data association (DA) scheme is necessary, which will be described in Section V-A. For ML ranging, only the propagation delay of the first arriving path, the LOS path, is interesting and can be obtained from (9) as

$$\hat{\tau}_{\text{LOS},\ell}^{(\text{ML})} = \min\{\hat{\tau}_{k,\ell}\}. \quad (11)$$

B. Jump-back Search-forward (JBSF) Ranging

If real-time localization is desired, a channel estimation like (9) might not be feasible. JBSF is a threshold-based ranging algorithm that also works for low-complexity receiver structures like energy detectors [15]. Backwards from the maximum of the received signal at delay τ_{max} , a search-back window of length τ_{sb} is defined.

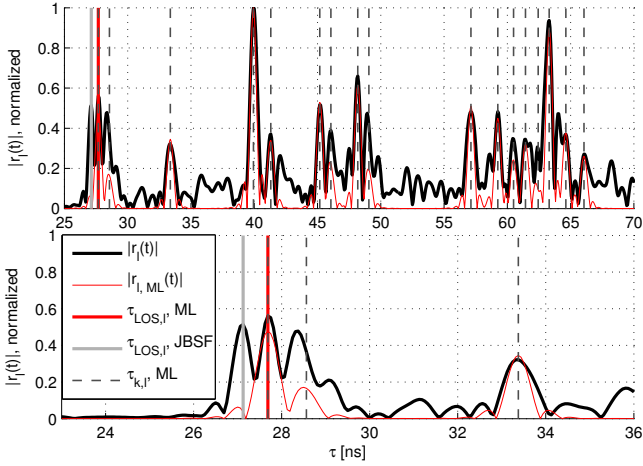


Figure 3: Exemplary ranging results for BS 4 and position $l = 120$ (c.f. Fig. 1), using $T_p = 0.5$ ns. The lower plot is a close-up. The black line denotes the received signal, while the red signal illustrates the reconstruction using the ML channel estimator. The latter also provides estimates for the MPC arrival times $\tau_{k,l}$ (grey dashed lines), where the ML range estimate (in red) is the minimum of these. Here, JBSF (light grey) outperforms ML due to path overlap. The simplified implementation of the ML channel estimator assumes a separable channel and only detects the larger second component.

The JBSF range estimate is the minimum delay within this window that exceeds a certain threshold

$$\hat{\tau}_{\text{LOS},\ell}^{(\text{JBSF})} = \min\{\hat{\tau} : \tau_{\text{max}} - \tau_{\text{sb}} \leq \hat{\tau} \leq \tau_{\text{max}}, |r_\ell(\hat{\tau})| \geq A_\xi\}. \quad (12)$$

The choice of the threshold A_ξ is usually based on the noise level.

An illustrative example for the channel estimation and ranging algorithms is given in Fig. 3. In this case, the LOS path is not separable from the rest of the channel. Since the amplitude of the second arriving MPC is larger, it is detected in an earlier iteration of the ML estimator. Due to the separable channel assumption, the ML estimator is constrained not to estimate any MPCs within one T_p of already detected ones, hence the LOS path is not detected. However, the LOS component is above the threshold of JBSF and within its search-back window, so JBSF can outperform the ML estimator in this case.

V. TRACKING AND DATA ASSOCIATION

The conventional tracking schemes based on ranging and the MINT approach are both implemented in this work using extended Kalman filters (EKFs) [17], [18] employing linearized observation equations for the estimated path delays. As in [11], we use a simple constant-velocity state-space model of the moving agent node. Stacking the position $\mathbf{p} = [p_x, p_y]^T$ and velocity $\mathbf{v} = [v_x, v_y]^T$ in the state vector $\mathbf{x} = [\mathbf{p}^T, \mathbf{v}^T]^T$ the model reads

$$\begin{aligned} \mathbf{x}_{\ell+1} &= \mathbf{F}\mathbf{x}_\ell + \mathbf{G}\mathbf{n}_{\mathbf{a},\ell} \\ &= \begin{bmatrix} 1 & 0 & \Delta T & 0 \\ 0 & 1 & 0 & \Delta T \\ 0 & 0 & 1 & 0 \\ 0 & 0 & 0 & 1 \end{bmatrix} \mathbf{x}_\ell + \begin{bmatrix} \frac{\Delta T^2}{2} & 0 \\ 0 & \frac{\Delta T^2}{2} \\ \Delta T & 0 \\ 0 & \Delta T \end{bmatrix} \mathbf{n}_{\mathbf{a},\ell}. \end{aligned} \quad (13)$$

Here, ΔT is the update interval and $\mathbf{n}_{\mathbf{a},\ell}$ denotes the driving process noise, which allows for motion at non-constant velocity. The measurement inputs for the conventional tracking scheme using EKFs are either the ML or JBSF ranging estimates. Using (11) or (12), ranging is performed to each of the four BSs. The entries of the vector of distance estimates are obtained as $z_\ell^{(i)} = c\hat{\tau}_{\text{LOS},\ell}^{(\text{ML},i)}$ or $z_\ell^{(i)} = c\hat{\tau}_{\text{LOS},\ell}^{(\text{JBSF},i)}$, where i is the BS index.

A. MINT Using EKF with Data Association (DA)

For the MINT scheme implemented using an EKF, the MPC estimation in (9) only results in an unordered set of distance estimates, i.e. $\mathcal{Z}_\ell^{(i)} = c \cdot \{\hat{\tau}_{k,\ell}^{(i)}\}$, where the cardinality of the set is $|\mathcal{Z}_\ell^{(i)}| = \hat{K}_\ell^{(i)}$. To obtain a suitable input for the observation equations of the EKF, a DA scheme is necessary. As the association to the BS is known, we only consider the DA for one BS and drop the index i . After the DA, all associated distance estimates are stacked into one measurement vector.

The employed DA approach is the same as used in [11] and is just shortly re-sketched here. We introduce a set \mathcal{C}_ℓ of correspondence variables [19], whose n -th entry $c_{\ell,n}$ represents the association of the n -th entry of \mathcal{Z}_ℓ and is defined as

$$c_{\ell,n} = \begin{cases} j, & \text{if } z_{\ell,n} \text{ corresponds to VA } \mathbf{a}_j \ (j = 1, \dots, N_{\text{VA}}) \\ 0, & \text{if } z_{\ell,n} \text{ corresponds to clutter.} \end{cases} \quad (14)$$

Using the predicted position of the EKF, \mathbf{p}_ℓ^- , the set of expected visible VAs \mathcal{A}_ℓ can be computed using (2) and (3). From this, the set of expected path lengths, denoted as \mathcal{D}_ℓ , can be obtained by calculating the Euclidean distances $d(\mathbf{a}_j, \mathbf{p}_\ell^-)$ between all VAs $\mathbf{a}_j \in \mathcal{A}_\ell$ and the position \mathbf{p}_ℓ^- . The task of the DA is now to match the two sets \mathcal{Z}_ℓ and \mathcal{D}_ℓ in an optimum way.

The approach used is optimal sub-pattern assignment [20]. Noting that the cardinality of \mathcal{D}_ℓ is K_ℓ (c.f. (3)) and assuming that $\hat{K}_\ell \geq K_\ell$, which can always be ensured by filling up \mathcal{Z}_ℓ with dummy clutter, we search the sub-pattern of \mathcal{Z}_ℓ that fits best to the set \mathcal{D}_ℓ . Using a distance function $d^{(dc)}(\cdot)$, that simply saturates at the cut-off distance d_c , this is expressed as

$$\boldsymbol{\pi}_{\text{opt}} = \arg \min_{\boldsymbol{\pi} \in \Pi_{\hat{K}_\ell}} \sum_{i=1}^{K_\ell} d^{(dc)}(d_{\ell,i}, z_{\ell,\pi_i}). \quad (15)$$

Here, $\Pi_{\hat{K}_\ell}$ is the set of permutations of positive integers up to \hat{K}_ℓ and the vector $\boldsymbol{\pi}_{\text{opt}}$ holds the permutation with the minimum cumulative distance in the sense of the cutoff distance function $d^{(dc)}(\cdot)$. Hence, the first K_ℓ entries of $\boldsymbol{\pi}_{\text{opt}}$ contain the indices of those entries of \mathcal{Z}_ℓ that have been optimally assigned to \mathcal{D}_ℓ .

As a last step in the DA process, we reject those measurements for which $d^{(dc)}(d_{\ell,i}, z_{\ell,\pi_{\text{opt},i}}) = d_c$, i.e. those that have been assigned at a distance greater or equal than the cutoff distance. This is done to have a mechanism to tune the DA to the uncertainty in the MPC delay estimates. As UWB signals are used, if an

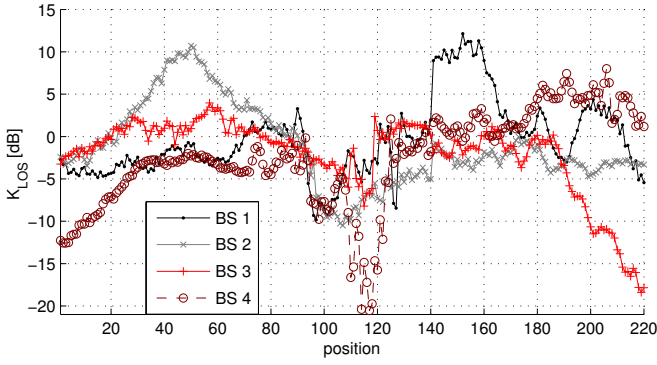


Figure 4: Instantaneous K-factor with respect to the LOS component K_{LOS} for all BSs over the trajectory using a pulse duration $T_p = 0.5$ ns.

MPC is detectable at all, its delay will have a relatively small uncertainty that depends on the used pulse duration T_p and the inaccuracies of the floor plan. Hence, the correspondence variables in (14) are obtained as

$$c_{\ell,n} = \begin{cases} j, & \text{if } \pi_j = n \text{ and } d^{(d_c)}(d_{\ell,j}, z_{\ell, \pi_{\text{opt}}, n}) < d_c \\ 0, & \text{else.} \end{cases} \quad (16)$$

The optimal sub-pattern assignment can be efficiently implemented using the Munkres algorithm [21].

B. Genie-aided Data Association (GADA) for Evaluation

The DA discussed above depends crucially on the EKF's predicted position \mathbf{p}_{ℓ} . To enable an evaluation of the localization performance where the errors due to false DA are mostly eliminated, we use a so-called genie-aided version of the DA (GADA). The GADA relies on the true position \mathbf{p}_{ℓ} for performing the DA, i.e. in the calculation of the set \mathcal{D}_{ℓ} . This can be used to benchmark the usefulness of the MPC delay estimates for localization using MINT.

VI. RESULTS

This section illustrates the accuracy and robustness of the proposed indoor tracking algorithms for the scenario in Fig. 1. A first rough evaluation of the propagation conditions can be obtained by evaluating the K-factor with respect to the LOS component, i.e. the ratio of its energy to the energy of the rest of the CIR. It is estimated using (9) and (10), where only the LOS component is subtracted from $r_{\ell}(t)$, i.e.

$$\hat{K}_{\text{LOS},\ell} = \frac{|\hat{\alpha}_{\text{LOS},\ell}|^2}{\int_T |r_{\ell}(t) - \hat{\alpha}_{\text{LOS},\ell} s(t - \hat{\tau}_{\text{LOS},\ell})|^2 dt} \quad (17)$$

where we note that the pulse $s(t)$ is energy-normalized.

Fig. 4 shows $\hat{K}_{\text{LOS},\ell}$ for all BSs over the trajectory, estimated using the original measurements (without the obstruction) with $T_p = 0.5$ ns. Some geometric influences, like the drop in \hat{K}_{LOS} in the NLOS regions of BSs 3 and 4 or the general distance dependence can be easily observed. Other causes of large variations are not immediately intuitive and require more careful inspection of the local propagation conditions. For example, the drop

of K_{LOS} for BS 1 around position 90 is due to strong scattered components from metal pillars within the lower windows, c.f. Fig. 1.

A. Evaluation Setup

The ‘‘obstruction’’ introduced in Fig. 1 is meant to model a change in the propagation environment, e.g. a group of people. As it causes NLOS regions for all BSs, its influence on the tracking performance is interesting. MINT is not aware of this obstruction in its floor plan knowledge. The original channel measurements were performed without this obstruction, hence they need to be modified. For this, we calculate the positions which are now in NLOS due to the changed conditions. At these positions, we reduce K_{LOS} by a factor of 10 dB, which is done by subtracting the LOS component and adding it again with a suitable amplitude and its original phase. To enable a fair comparison with MINT, we also change the amplitudes of all the MPCs affected by the change in visibility conditions. We do so by reducing their SINR (7) also by 10 dB. Note that this factor leaves the LOS component still detectable in most cases, while for the later arriving MPCs it causes an effective loss of the respective component

B. Choice of Parameters

a) Measurement parameters: We perform the performance evaluation for several exemplary signal bandwidths, i.e. the pulse duration of the raised cosine pulse is chosen as $T_p \in \{0.2 \text{ ns}, 0.5 \text{ ns}, 1 \text{ ns}, 2 \text{ ns}, 4 \text{ ns}\}$. The corresponding -3 dB bandwidths are $\{5 \text{ GHz}, 2 \text{ GHz}, 1 \text{ GHz}, 0.5 \text{ GHz}, 0.25 \text{ GHz}\}$. Using a roll-off factor of $\beta_R = 0.5$, the center frequency is always $f_c = 7 \text{ GHz}$, except for $T_p = 0.2 \text{ ns}$ which corresponds to the full measurement bandwidth, hence the overall center frequency $f_c = 6.85 \text{ GHz}$ has to be used. Table 1 contains an overview of all relevant parameters for these setups.

b) EKF parameters: The EKF's measurement noise covariance matrix is $\mathbf{R} = \sigma_z^2 \mathbf{I}$, where \mathbf{I} is the identity matrix. For the variance σ_z^2 , we choose values based on the expected ranging uncertainty, i.e. it is slightly increased with the pulse duration T_p . The same consideration applies for the DA cutoff distance d_c used in (15) and (16). Table 1 lists the values used in the different measurement parameter setups.

The choice of the process noise variance σ_a^2 depends on the maximum velocity in e.g. the x -direction, denoted as $v_{x,\text{max}}$. The process noise, assumed to be Gaussian, should allow movement at this velocity. Hence, we select the 3σ point of the velocity noise as $v_{x,\text{max}}$ and obtain for the corresponding process noise variance in the acceleration domain

$$\sigma_a^2 = \left(\frac{v_{x,\text{max}}}{3\Delta T} \right)^2. \quad (18)$$

In this paper, we choose to model pedestrian motion and set $v_{x,\text{max}} = 1.5 \text{ m/s}$. The update interval is $\Delta T = 0.1 \text{ s}$, resulting in a magnitude of the velocity in x - or y -direction of 1 m/s along straight segments of the trajectory. The

Table 1: Parameters and results for the performance evaluation. For the performance measures, a pair of values is given where the first one indicates the scenario without the obstruction and the second one with the obstruction.

	$T_p = 0.2$ ns	$T_p = 0.5$ ns	$T_p = 1$ ns	$T_p = 2$ ns	$T_p = 4$ ns
Process noise variance σ_a^2 [m^2/s^4]	$\sigma_a^2 = (\frac{v_{x,\max}}{3\Delta T})^2$, covariance matrix $\mathbf{Q} = \sigma_a^2 \mathbf{G}\mathbf{G}^T$, with $v_{x,\max} = 1.5$ m/s				
EKF measurement noise variance σ_z^2 [m^2]	0.01	0.01	0.04	0.04	0.09
DA cutoff distance d_c (MINT) [m]	0.3	0.3	0.5	0.5	0.6
JBSF SB-window [ns]	100				
JBSF threshold ξ [1]	0.4	0.4	0.3	0.3	0.3
Mean number of assoc. MPCs (EKF-GADA) [1]	18.2 / 17.6	18.6 / 18.2	18.3 / 17.9	15.0 / 13.9	11.9 / 10.2
Mean number of assoc. MPCs (EKF-DA) [1]	18.1 / 17.5	18.5 / 18.2	18.2 / 17.7	15.1 / 14.0	11.8 / 10.1
RMS position error MINT (EKF-GADA) [m]	0.03 / 0.032	0.039 / 0.041	0.06 / 0.069	0.076 / 0.083	0.117 / 0.136
RMS position error MINT (EKF-DA) [m]	0.073 / 0.087	0.067 / 0.065	0.118 / 0.197	0.122 / 0.149	0.207 / 0.304
RMS position error EKF, ML ranging [m]	0.05 / 0.052	0.058 / 0.065	0.079 / 0.113	0.129 / 0.149	0.353 / 0.396
RMS position error EKF, JBSF ranging [m]	0.113 / 0.15	0.351 / 0.418	0.243 / 0.297	0.249 / 0.34	0.406 / 0.714
average HDOP MINT (EKF-GADA) [1]	0.41 / 0.39	0.41 / 0.38	0.39 / 0.39	0.43 / 0.43	0.47 / 0.51
average HDOP MINT (EKF-DA) [1]	0.67 / 0.73	0.56 / 0.53	0.56 / 0.65	0.58 / 0.61	0.68 / 0.76
average HDOP EKF, ML ranging [1]	1.19 / 1.21	1.23 / 1.2	1.35 / 1.23	1.09 / 0.96	1.04 / 0.8
average HDOP EKF, JBSF ranging [1]	1.23 / 1.28	1.27 / 1.52	1.56 / 1.49	1.28 / 1.24	1.03 / 1.14

conventional tracking schemes and MINT always use the same σ_z^2 and σ_a^2 for every pulse duration considered.

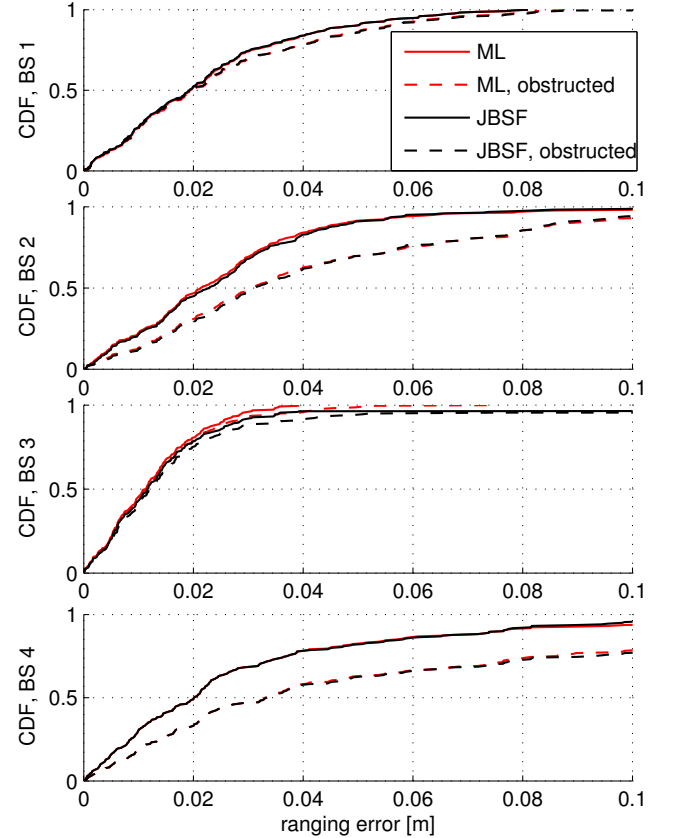
c) *Initialization*: All EKFs are initialized with the correct position and zero velocity. We note that this is a more challenging problem for MINT than for the conventional schemes, since the DA depends on the estimated position. However, we have addressed this problem for a different implementation of MINT in [22] using a Gaussian-sum filter [23]. In this approach, a bank of parallel weighted Kalman filters (KFs) is used to represent multiple initial position hypotheses. After convergence, the KFs with small weights can be discarded. This can also be applied for the MINT implementation in this paper.

d) *Channel estimation and ranging*: The choice of \hat{K}_ℓ in (9), i.e. the number of extracted components, is based on the average number of expected visible VAs in the localization environment. For the performance evaluations, we take into account VAs up to order two and fix $\hat{K}_\ell = \hat{K} = 20$. However, we define a threshold between the noise floor and the maximum amplitude of the received signal, below which no further MPCs are extracted. The noise signal $\hat{w}_\ell(t)$ is estimated from the pre-LOS part of $r_\ell(t)$. Denoting the time average of a signal with $\langle \cdot \rangle$, the threshold is obtained as [12]

$$A_{\gamma,\ell} = \gamma \cdot (\max\{|r_\ell(t)|\} - \langle |\hat{w}_\ell(t)| \rangle) + \langle |\hat{w}_\ell(t)| \rangle. \quad (19)$$

In this paper, $\gamma = 0.1$ is used.

The JBSF ranging threshold A_ξ in (12) is also chosen using a relative threshold ξ , in the same manner as γ in (19). For every pulse duration used, we selected a threshold at which ranging works well in the unobstructed scenario, c.f. Table 1. The length of the search-back window τ_{sb} is chosen for each BS as the maximum distance between the BS and any first-order VA, expressed in ns. This corresponds to the maximum delay difference of the LOS component and any first-order reflection. The reasoning behind this is the assumption that if the LOS component is not the maximum itself, then the maximum will be among the first-order MPCs. A value of 100 ns


 Figure 5: CDFs of the ranging error for ML (red) and JBSF (black) with and without the obstruction for all BSs and $T_p = 1$ ns.

is selected for the geometry in Fig. 1. It approximately corresponds to the excess delay of the reflection path on the far right end of the corridor.

C. Ranging Performance Results

A comparison of the performance of ML and JBSF ranging algorithms in terms of the ranging error CDF

is shown in Fig. 5 with and without the obstruction. A pulse duration of $T_p = 1$ ns has been used for this. The most striking result is that JBSF closely approaches ML ranging for all cases, at a much lower computational complexity. One reason for the good performance of JBSF is the rather low noise level in the VNA measurements. However, when looking at the instantaneous ranging errors over the trajectory (not shown), some isolated outliers of JBSF can be observed. The implications for the localization performance will be discussed in the next subsection.

D. Localization and Tracking Performance Results

Table 1 contains detailed performance results in terms of RMS position error, the mean number of associated MPCs for MINT and the average horizontal dilution of precision (HDOP). The latter value is calculated as the average of the instantaneous HDOP values over the trajectory. These are the ratio of instantaneous position error and RMS ranging error [15], hence they provide snap-shots of the quality of the localization geometry. For MINT, the RMS ranging error is computed from those range estimates that have been associated to VAs by the DA procedure.

Looking at the RMS position error in Table 1 obtained using both ranging methods reveals that the EKF using ML ranging still clearly outperforms the one using JBSF. This behavior would not be suspected by looking at the ranging CDFs alone. The few isolated outliers of JBSF mentioned above cause the gap in localization performance. As this subsection shows, MINT does not show such robustness issues with respect to ranging outages.

Fig. 6 contains the position error CDFs for all considered pulse durations. MINT using EKF-GADA always shows the best performance of all tracking algorithms. Although this is just an upper bound for this implementation of MINT, it shows the potential gain of exploiting multipath propagation. This is not only true for the achieved accuracy, but also for the robustness with respect to difficult propagation conditions, since MINT using EKF-GADA shows almost no performance loss for the obstructed scenario. Also with realistic DA, MINT is able to overcome impairments caused by the obstruction better than the conventional approaches. The conventional approaches show significant performance impairments, especially when the pulse duration is increased.

Only for pulse durations of $T_p = 0.2$ ns and $T_p = 1$ ns, MINT with DA can not provide a performance gain. In the first case, the channel estimation can resolve very closely spaced MPCs that are challenging for the DA due to their clustered structure. In the second case, interference by pulse overlap situations causes the detection of several MPCs to fail. Since neither the channel estimation (9) nor the DA as proposed here can deal with path overlap situations, this is identified as an important topic for future research.

An unexpected result is obtained for $T_p = 4$ ns, which, corresponding to a -3 dB bandwidth of 250 MHz, is no longer UWB by definition [24]. Although MINT generally

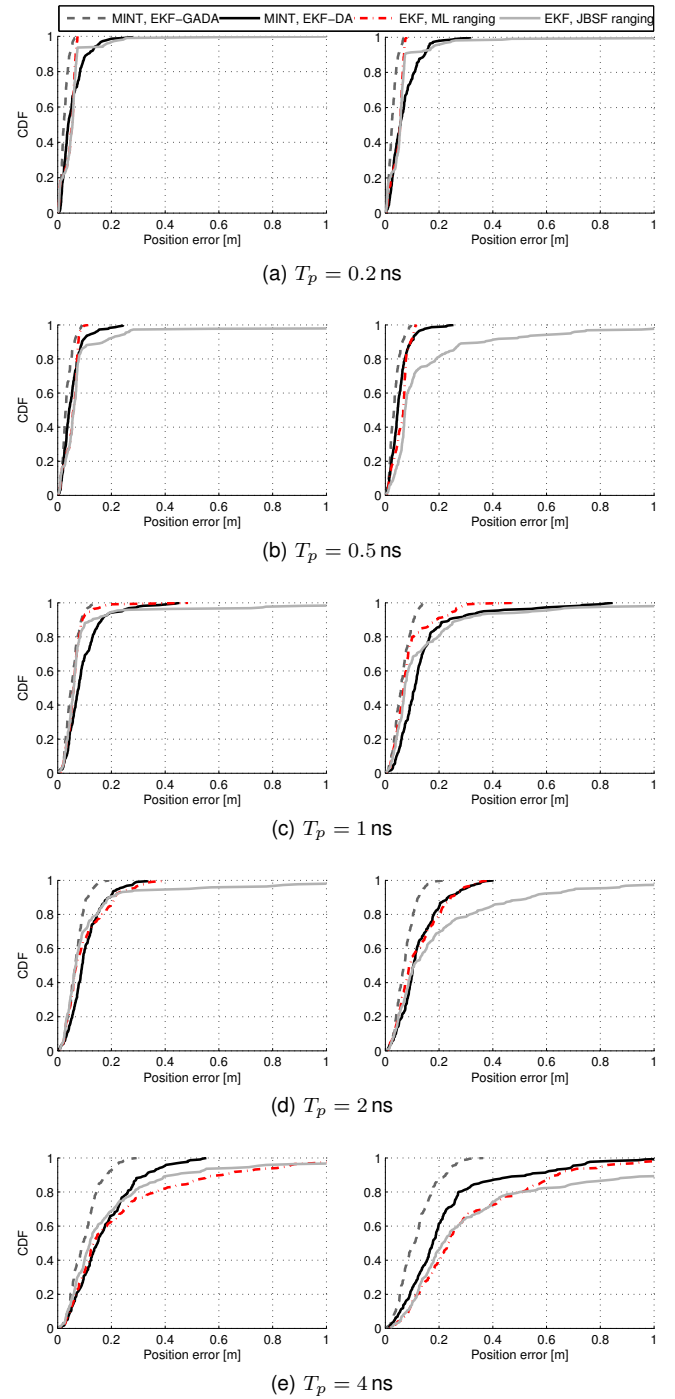


Figure 6: CDFs of the position error over the trajectory for all considered pulse durations T_p . The left column shows runs without the obstruction (c.f. Fig. 1), in the right column, signals have been modified according to the obstruction.

benefits from a large bandwidth, it can yield the largest performance and robustness gain here. The conventional tracking schemes show outliers due to very large ranging biases, while MINT still exploits information from some MPCs, although their number decreases significantly (c.f. Table 1). The mentioned large ranging biases are also the reason for the lower HDOP in the obstructed scenario

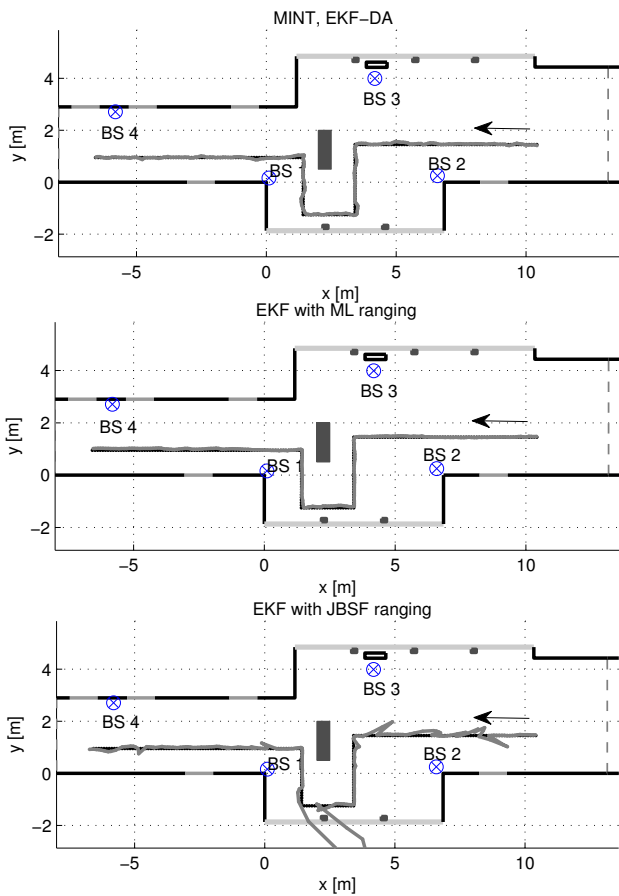


Figure 7: Tracking results for the NLOS scenario and $T_p = 0.5$ ns. The three plots show the estimated trajectories using MINT with the EKF and data association, and EKFs using ML and JBSF ranging, respectively.

in these parameter setups. Furthermore, it should be noted that in terms of the RMS position error, MINT using the EKF-DA always outperforms the conventional EKF approach using JBSF ranging.

An illustrative example for $T_p = 0.5$ ns and the NLOS scenario is shown in Figs. 7 and 8. The estimated trajectories of the agent node are displayed in Fig. 7. While MINT and the EKF using ML range estimates can both follow the trajectory well, the EKF employing JBSF ranging is severely impaired by the NLOS regions of BSs 1 and 4 (at the start of the trajectory), BS 4 (around position 120, c.f. Fig. 1) and BS 3 and 2 (near the end of the trajectory). As Fig. 8 confirms, in the first two of these NLOS regions, rather large values of the instantaneous HDOP occur. This highlights the bad geometry for conventional schemes when there are ranging outages. For MINT, most of the HDOP values along the trajectory are below one, indicating excellent geometry for localization. This is due to the large set of virtual BSs spanned by the VAs (c.f. (6) and (8)).

VII. CONCLUSION AND FUTURE WORK

We have presented a comparison of conventional indoor UWB ranging and tracking schemes and an im-

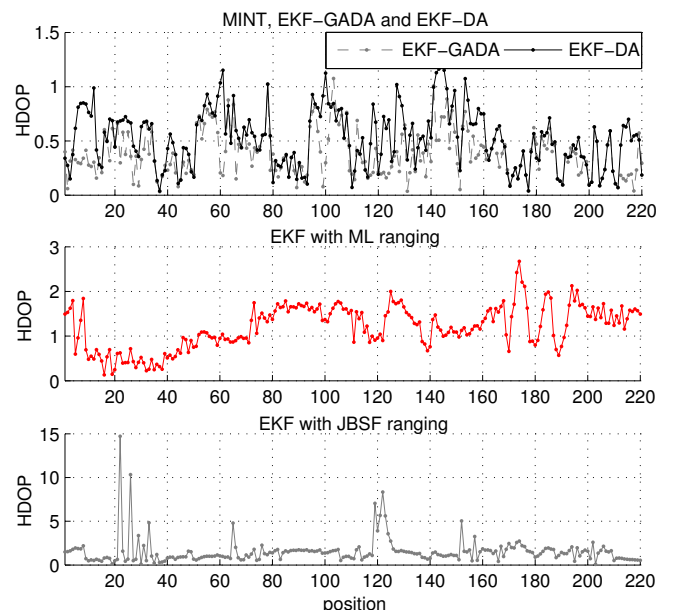


Figure 8: Tracking results for the NLOS scenario and $T_p = 0.5$ ns. The plots illustrate the HDOP for the tracking algorithms used.

plementation of the proposed MINT approach using data from a measurement campaign in a representative indoor environment. The influence of NLOS situations on the accuracy and robustness of these systems has been investigated. Results confirm the potentials of MINT: Using floor plan information, multipath propagation can be efficiently used to obtain position-relevant information in situations where conventional approaches fail. Even at comparably low bandwidths, MINT shows a clear gain in localization performance.

Ongoing and future work includes the modeling of floor plan uncertainties and the combination of localization and channel estimation. The latter can be used to reduce the amount of clutter in the extracted path delay estimates. Also, other implementations of MINT, e.g. using soft classification in the data association, are within the scope of our work.

ACKNOWLEDGMENT

The authors thank Daniel Arnitz and Thomas Gigl for their invaluable help in conducting the channel measurement campaign. This work was partly supported by the Austrian Science Fund (FWF) within the National Research Network SISE project S10610, and by the Austria Research Promotion Agency (FFG) within KIRAS PL3, grant no. 832335 “LOBSTER”.

REFERENCES

- [1] R. Mautz, “Overview of Current Indoor Positioning Systems,” *Geodesy and Cartography*, vol. 35, pp. 18–22, 2009.
- [2] S. Gezici and H. Poor, “Position estimation via ultra-wide-band signals,” *Proceedings of the IEEE*, vol. 97, no. 2, pp. 386–403, feb. 2009.

- [3] J. Borras, P. Hatrack, and N. B. Mandayam, "Decision theoretic framework for NLOS identification," in *IEEE Vehicular Technology Conference (VTC)*, 1998, 1998.
- [4] S. Gezici, H. Kobayashi, and V. Poor, "Non-Parametric Non-Line-of-Sight Identification," in *IEEE Vehicular Technology Conference (VTC) 2003*, 2003.
- [5] H. Wymeersch, S. Marano, W. Gifford, and M. Win, "A Machine Learning Approach to Ranging Error Mitigation for UWB Localization," *IEEE Transactions on Communications*, vol. 60, pp. 1719–1728, 2012.
- [6] S. Marano and W. Gifford, H. Wymeersch, and M. Win, "NLOS identification and mitigation for localization based on UWB experimental data," *IEEE Journal on Selected Areas in Communications*, vol. 28, no. 7, pp. 1026 –1035, 2010.
- [7] Y. Shen and M. Win, "On the Use of Multipath Geometry for Wideband Cooperative Localization," in *Global Telecommunications Conference, 2009. GLOBECOM 2009. IEEE*, 2009.
- [8] —, "Fundamental Limits of Wideband Localization - Part I: A General Framework," *IEEE Transactions on Information Theory*, pp. 4956 –4980, Oct. 2010.
- [9] K. Witrisal and P. Meissner, "Performance Bounds for Multipath-aided Indoor Navigation and Tracking (MINT)," in *International Conference on Communications (ICC)*, Ottawa, Canada, 2012.
- [10] P. Meissner and K. Witrisal, "Analysis of Position-Related Information in Measured UWB Indoor Channels," in *6th European Conference on Antennas and Propagation (EuCAP)*, Prague, Czech Republic, 2012.
- [11] —, "Multipath-Assisted Single-Anchor Indoor Localization in an Office Environment," in *19th International Conference on Systems, Signals and Image Processing (IWSSIP)*, Vienna, Austria, 2012.
- [12] P. Meissner, D. Arnitz, T. Gigl, and K. Witrisal, "Analysis of an Indoor UWB Channel for Multipath-Aided Localization," in *2011 IEEE International Conference on Ultra-Wideband (ICUWB)*, Bologna, Italy, 2011.
- [13] J. G. Proakis and M. Salehi, *Digital Communications*, 5th ed. McGraw-Hill, 2008.
- [14] T. Santos, J. Karedal, P. Almers, F. Tufvesson, and A. Molisch, "Modeling the ultra-wideband outdoor channel: Measurements and parameter extraction method," *IEEE Transactions on Wireless Communications*, vol. 9, no. 1, pp. 282 –290, Jan. 2010.
- [15] Z. Sahinoglu, S. Gezici, and I. Guvenc, *Position Estimation in Ultrawideband Wireless Systems*. Cambridge University Press, 2008.
- [16] M. Win and R. Scholtz, "Characterization of ultra-wide bandwidth wireless indoor channels: A communication-theoretic view," *IEEE Journal on Selected Areas in Communications*, vol. 20, no. 9, pp. 1613 – 1627, Dec. 2002.
- [17] D. Simon, *Optimal State Estimation*, 1st ed. Wiley, 2006.
- [18] Y. Bar-Shalom and T. Fortmann, *Tracking and Data Association*. Academic Press, 1988.
- [19] S. Thrun, W. Burgard, and D. Fox, *Probabilistic Robotics*. MIT, 2006.
- [20] D. Schuhmacher, B.-T. Vo, and B.-N. Vo, "A Consistent Metric for Performance Evaluation of Multi-Object Filters," *IEEE Transactions on Signal Processing*, vol. 56, no. 8, pp. 3447 –3457, 2008.
- [21] J. Munkres, "Algorithms for the Assignment and Transportation Problems," *Journal of the Society for Industrial and Applied Mathematics*, vol. 5, no. 1, pp. pp. 32–38, 1957.
- [22] P. Meissner, T. Gigl, and K. Witrisal, "UWB Sequential Monte Carlo Positioning using Virtual Anchors," in *Proc. 2010 International Conference on Indoor Positioning and Indoor Navigation, IPIN, Zurich*, 2010.
- [23] D. Alspach and H. Sorenson, "Nonlinear Bayesian estimation using Gaussian sum approximations," *IEEE Transactions on Automatic Control*, vol. 17, no. 4, pp. 439 – 448, Aug. 1972.
- [24] A. F. Molisch, "Ultra-Wide-Band Propagation Channels," *Proc. IEEE*, vol. 97, no. 2, pp. 353–371, Feb. 2009.

On the Use of Ray Tracing for Performance Prediction of UWB Indoor Localization Systems

(Invited Paper)

Paul Meissner¹, Mingming Gan², Francesco Mani³, Erik Leitinger¹,
Markus Fröhle¹, Claude Oestges⁴, Thomas Zemen², and Klaus Witrals¹

¹Graz University of Technology, Austria; ²FTW Forschungszentrum Telekommunikation Wien, Austria;

³COMELEC Department, Telecom ParisTech, France; ⁴ICTEAM, Université catholique de Louvain, Belgium

Abstract—The most important factors impairing the performance of radio-based indoor localization systems are propagation effects like strong reflections or diffuse scattering. To the full extent, these effects can be captured only by time-consuming measurement campaigns. Ray tracing (RT) offers the possibility to predict the radio channel for a certain environment, avoiding the need for measurements. However, it is crucial to include all relevant propagation mechanisms in the RT as well as to validate the obtained results. In this paper, we analyze if sub-band divided RT can yield realistic ultra-wideband channel impulse responses. We use the RT results for performance analysis of multipath-assisted localization, which depends directly upon the above mentioned propagation effects. In particular, it has been shown that the ratio of the signal energies of deterministically reflected paths to interfering diffuse components quantifies the amount of position-related information of deterministic multipath components. Comparison of this ratio to measurement data is thus useful to validate the sub-band divided RT. The results highlight the need for proper modeling of the diffuse multipath, as estimates of this energy ratio using RT are often overly optimistic. However, the obtained localization performance predictions using measurements and RT show general agreement.

I. INTRODUCTION

The performance of indoor localization systems based on radio signals is strongly affected by the propagation channel. Non line-of-sight (NLOS) situations between anchor nodes and the user terminal can cause large biases in range or angle estimation. Channel measurements can help to predict the expectable accuracy in a certain environment, either by using them for modeling the ranging error [1] or to evaluate parametrized performance bounds [2], [3]. However, such measurement campaigns are usually time-consuming and tedious to perform.

An available floor plan of the indoor environment offers several benefits for indoor localization. First, it allows for

The work of P. Meissner, E. Leitinger and K. Witrals was partly supported by the Austrian Science Fund (FWF) within the National Research Network SISE project S10610, and by the Austria Research Promotion Agency (FFG) within KIRAS PL3, grant nb. 832335 “LOBSTER”.

The work of M. Gan and T. Zemen is supported by the Austrian Science Fund (FWF) through grant NFN SISE (S10607) and by the Austrian Competence Center FTW Forschungszentrum Telekommunikation Wien GmbH within project I0. FTW is funded within the program COMET - Competence Centers for Excellent Technologies by BMVIT, BMWFJ, and the City of Vienna. The COMET program is managed by the FFG.

This collaboration was also part of the COST action IC1004 entitled “Cooperative Radio Communications for Green Smart Environments”.

multipath-assisted indoor navigation and tracking (MINT), which maps reflected multipath-components (MPCs) to virtual anchors, i.e. mirror images of the physical anchor nodes with respect to flat surfaces like walls [2], [3]. In this way, it makes use of the geometric structure of MPCs [4], exploiting more information in the received signal than just the direct path. Second, together with electric properties of the building materials, the floor plan can be used for ray tracing (RT) simulations. With RT, realistic channel impulse responses can be obtained [5]. Some RT tools can also provide diffuse multipath (DM) contributions, which model the non-coherent part of the channel. This DM can be very pronounced in indoor environments and can thus impair the localization performance.

The evaluation of the usefulness of signals generated by RT for localization is not trivial. In references like [5], power delay profiles (PDPs) over some geometric areas are used. The large density of specular paths and the averaging process cause PDPs that nicely fit to measured ones. However, for individual signals, the degree of realism in terms of the different propagation mechanisms is unclear. By evaluating the usefulness of a sub-band divided RT tool for the purpose of performance prediction of the MINT approach, the following contributions to this problem are made in this paper:

- The quantification of position-related information of MPCs requires the estimation of the energy ratio of deterministic MPCs and DM. This allows for detailed local evaluation of propagation effects modeled by RT.
- It is shown that despite some limitations, RT can provide reasonable predictions of the localization performance without the need for tedious measurement campaigns.
- Insight is given on important future research directions that allow RT tools to produce more realistic signals.

The paper is organized as follows: Section II introduces the signal models and the measurement environment, in Section III, the RT tool and its configuration are described. The extraction of performance parameters is described in Section IV and Section V discusses the results.

II. SCENARIO, MEASUREMENTS, AND SIGNAL MODEL

The scenario used for both RT and the measurement campaign is illustrated in Fig. 1, while geometry and building materials are described in Sec. III-C. Fig. 1b shows the

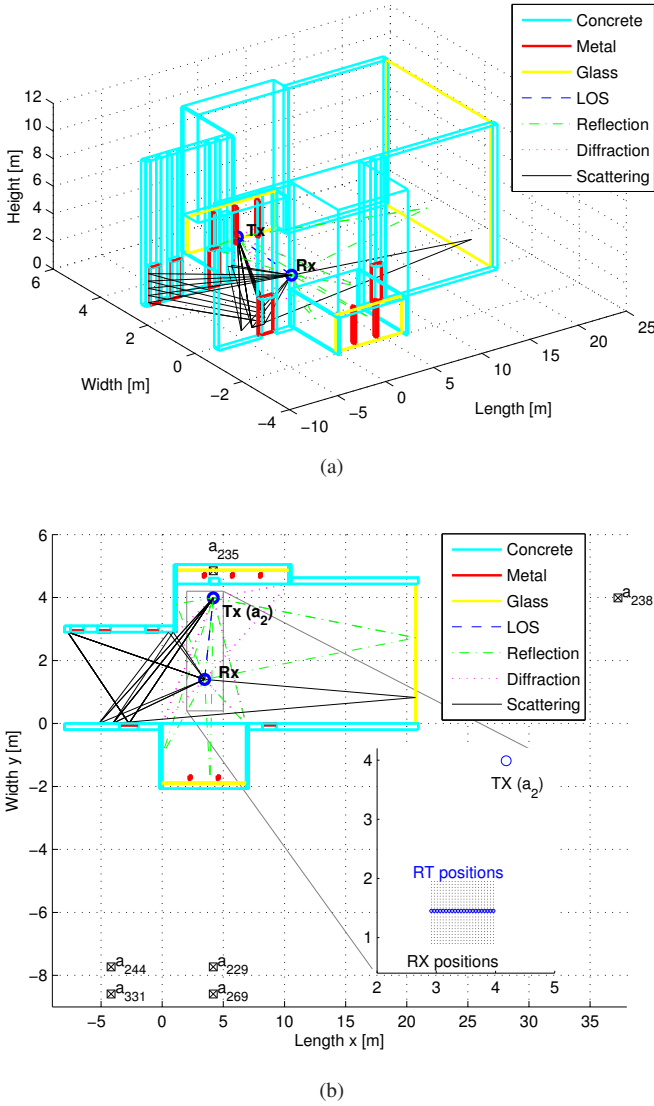


Fig. 1. Pictorial view of the RT scenario considering one Rx position from the grid. (a) 3-D view. (b) 2-D view, including a close-up view of the measurement grid positions together with the positions where RT simulations are available. Also shown are the locations \mathbf{a}_i of the VAs that are analyzed in Section V.

locations of transmitter (Tx) and receiver (Rx) antennas. The latter form a grid of 22×22 points, spaced by 5 cm, covering an area of roughly 1 m^2 . In an indoor localization application, the Tx is usually an anchor node at a known location. For the ray tracing simulations, the middle horizontal line of the grid, marked in blue in Fig. 1b, is used. The UWB channel has been measured using a Rhode & Schwarz ZVA-24 vector network analyzer (VNA) at 7501 frequency points over the frequency range from 3.1 to 10.6 GHz.

Using a transmitted pulse $s(\tau)$, the received signal at the ℓ -th Rx position \mathbf{p}_ℓ is modeled as [2], [3]

$$r_\ell(\tau) = \sum_{k=1}^{K_\ell} \alpha_{k,\ell} s(\tau - \tau_{k,\ell}) + s(\tau) * \nu_\ell(\tau) + w_\ell(\tau). \quad (1)$$

Here, $\alpha_{k,\ell}$ and $\tau_{k,\ell}$ denote the complex amplitude and the

propagation delay of the k -th deterministic, i.e. specular reflected, MPC. The number K_ℓ of deterministic MPCs varies with the position. The noise term $w_\ell(\tau)$ is white Gaussian measurement noise with two-sided PSD $N_0/2$, whereas $\nu_\ell(\tau)$ denotes a random process modeling the DM, filtered by the transmit pulse. We assume that the delays can be modeled geometrically using virtual transmitters (or anchors (VAs)), which are mirror images of the anchor node with respect to reflecting surfaces, given in a floor plan of the environment. The positions of these VAs are denoted as \mathbf{a}_k , resulting in $\tau_{k,\ell} = \frac{1}{c} \|\mathbf{p}_\ell - \mathbf{a}_k\|$ for the corresponding delay, where c is the speed of light. Fig. 1b shows the positions of several VAs.

Both the RT and the measured signals are pulse-shaped with $s(\tau)$, a raised-cosine pulse with pulse duration T_p and roll-off factor β_R . This is done to select a desired frequency band for the analysis and to facilitate a search-and-subtract MPC estimation algorithm. At position \mathbf{p}_ℓ , the set of expected delays to the visible VAs can be computed using ray tracing. Using an algorithm described in Section IV, estimates $\hat{\alpha}_{k,\ell}$ and $\hat{\tau}_{k,\ell}$ of the corresponding complex amplitudes and delays are obtained. Assuming negligible noise $w_\ell(\tau)$, this yields an estimate of the deterministic and the diffuse channel parts [6]

$$\hat{\nu}_\ell(\tau) = r_\ell(\tau) - \hat{r}_{\ell,\text{det}}(\tau) = r_\ell(\tau) - \sum_{k=1}^{K_\ell} \hat{\alpha}_{k,\ell} s(\tau - \hat{\tau}_{k,\ell}). \quad (2)$$

Evaluating (2) at all measurement positions, local power delay profiles (PDPs) of the received signal and the diffuse parts can be estimated. For a center point $\mathbf{p}_{\bar{\ell}}$, the PDP is defined as the expectation with respect to the position of instantaneous PDPs around $\mathbf{p}_{\bar{\ell}}$. Using the L spatially closest points around $\mathbf{p}_{\bar{\ell}}$, defined as the set $\mathcal{P}_{\bar{\ell}}$, an estimate of the local PDP of the DM is obtained as

$$S_{\nu,\bar{\ell}}(\tau_{\text{ex}}) \approx \frac{1}{L} \sum_{\ell \in \mathcal{P}_{\bar{\ell}}} |\hat{\nu}_\ell(\tau + \tau_{1,\ell})|^2. \quad (3)$$

Note that the PDP is defined over the excess delay τ_{ex} . Hence, the LOS propagation delay, denoted as $\tau_{1,\ell}$, has to be compensated prior to the averaging to remove this deterministic effect from the DM. For brevity, we drop the subscript in τ_{ex} where the distinction is clear from the context.

III. RT ANALYSIS

RT is a deterministic propagation prediction tool which has been widely used to simulate indoor channel characteristics for both narrowband and wideband systems. Due to the frequency selective properties of the propagation channel, the channel characteristics may vary significantly within the entire bandwidth of an ultra-wideband (UWB) system. Therefore, a conventional RT implementation at one discrete frequency point, used for narrowband systems, is not sufficient to simulate UWB channels. The usual way to overcome this problem is to use a sub-band divided RT algorithm [7], [8].

A. Conventional RT

The RT algorithm employed in the present work is three-dimensional (3D) and requires the thorough geometrical and

electromagnetic description of the indoor scenario, as well as the radiation properties of the antennas. The propagation mechanisms taken into account are: line-of-sight (LOS), reflection, penetration, diffraction and diffuse scattering. The complex dyadic reflection and penetration coefficients are calculated applying Fresnel formulas [9], while diffraction is implemented using the uniform theory of diffraction (UTD) [10]. The diffuse scattering components aim to model the non-specular part of the channel. The diffuseness can be created in RT by dividing the surfaces into multiple tiles, whose size is determined by recursively dividing the surface until the far field condition is satisfied [11]. A directive scattering pattern model, which assumes that the scattering lobe is steered towards the direction of the specular reflection [12], is used to evaluate the amplitude of the diffuse scattering field. Moreover, based on the assumption that the diffuse scattering rays are incoherent, a uniformly distributed random phase is associated with each diffuse scattering ray [13].

B. Sub-band Divided RT

Applying a sub-band divided RT algorithm to UWB radio channels has already been proposed in [7], [8]. The basic concept is simulating the propagation channels at multiple frequency points, which are the center frequencies of the corresponding sub-bands. It is evident that the accuracy of the sub-band divided RT is related to the number of the sub-bands: the larger this number the better the accuracy, but at the cost of an higher computational effort. Sub-band divided RT can be summarized with the following steps [7], [14]:

- The whole UWB bandwidth is divided into several sub-bands. In each sub-band, constant frequency characteristics can be assumed for all materials and mechanisms.
- Conventional RT is used to obtain the channel impulse response (CIR) at each sub-band center frequency.
- The sub-band frequency responses are calculated by Fourier transforms. Afterwards all frequency responses over different sub-bands are combined into a complete frequency response over the whole UWB bandwidth.
- Finally, the CIR over the entire UWB bandwidth can be obtained by an inverse Fourier transform.

The complete frequency response can be expressed as:

$$H(f) = \sum_{i=1}^N \mathcal{F}\{h_i(\tau)\} \cdot R_i(f), \quad (4)$$

where i is the sub-band index, N is the total number of sub-bands, $\mathcal{F}\{\cdot\}$ is the Fourier transform, $h_i(\tau)$ is the CIR at the i -th sub-band, and $R_i(f)$ is the rectangular window function associated with the i -th sub-band. The complete frequency response $H(f)$ can be compared to the raw measurement data obtained from the VNA. In the following sections, we will use either the complete frequency response $H(f)$ or the measured channel frequency response to do the subsequent analysis.

C. Simulation Configuration

According to the measurement environment, the simulated scenario is built as shown in Fig. 1, where only one Rx

position is shown as an example. The size of the simulated indoor scenario is about $29\text{m} \times 7.1\text{m} \times 10.5\text{m}$. The blocks, including doors, walls and pillars, are made of different materials, such as concrete, metal and glass. A metallic block is considered as a perfect electric conductor (PEC). The values of relative permittivity ε_r and conductivity σ of other materials are: $\varepsilon_r = 6$ and $\sigma = 0.08 \text{ S/m}$ for concrete blocks, and $\varepsilon_r = 5.5$ and $\sigma = 0 \text{ S/m}$ for glass blocks. Since it is difficult to distinguish how the dielectric properties vary with the frequencies, we assume that the dielectric properties in the present work are independent of the frequency within the entire bandwidth of interest. In our simulation, the frequency bandwidth of 7.5 GHz is divided into $N = 15$ sub-bands with 500 MHz each. The transmitting and receiving antennas are assumed to be omnidirectional dipoles.

Fig. 1 also visualizes some of the predicted rays. In this work, the propagation mechanisms taken into account are: LOS, reflection (up to the third order), single diffraction, single bounce scattering, scattering-reflection and reflection-scattering cases. The penetration contribution has been embedded into all other mechanisms. It has been previously mentioned that the subdivision of surfaces in tiles for scattering interaction is related to the wavelength. More obstacles would look rougher at higher frequencies than at the lower frequencies. Hence, the subdivision of one rough surface would be different over different sub-bands. This impacts significantly on the computational effort. Therefore, we assume, for a specific Rx's position, the subdivision of each surface at 6.85 GHz to be valid for all sub-bands. This simplified method leads to results comparable to the one where the subdivision is changed according to the center frequency.

D. Comparison of measurement and RT signals

For comparison, the RT signals have been normalized such that the mean amplitude of their LOS path over the positions equals the corresponding mean of the measured signals. Fig. 2 shows several PDPs, averaged over the positions where RT signals are available. The grey dashed lines indicate the mean excess delays of some specular reflections modeled by the VAs (see Fig. 1b for measurement and VA positions). One can see that these deterministic MPCs are similarly present in the measurements and in the RT signals. A detailed investigation of these MPCs will be done in Section V.

The DM shown in Fig. 2 has been estimated using (2). For the RT, $S_\nu(\tau)$ can also be calculated using the available true $r_{\ell, \text{det}}(\tau)$ and $\nu_\ell(\tau)$. $S_\nu(\tau)$ without the position index ℓ indicates that averaging has been performed over all 22 RT points, i.e. the locality has been eliminated. One can see that the DM generated by RT follows the measured one qualitatively up to an excess delay of about 30 ns. The reason for the gap afterwards is that higher-order propagation mechanisms are not considered by the RT algorithm. This together with the rather large dimensions of the environment make the PDP look rather sparse for an excess delay greater than 30 ns.

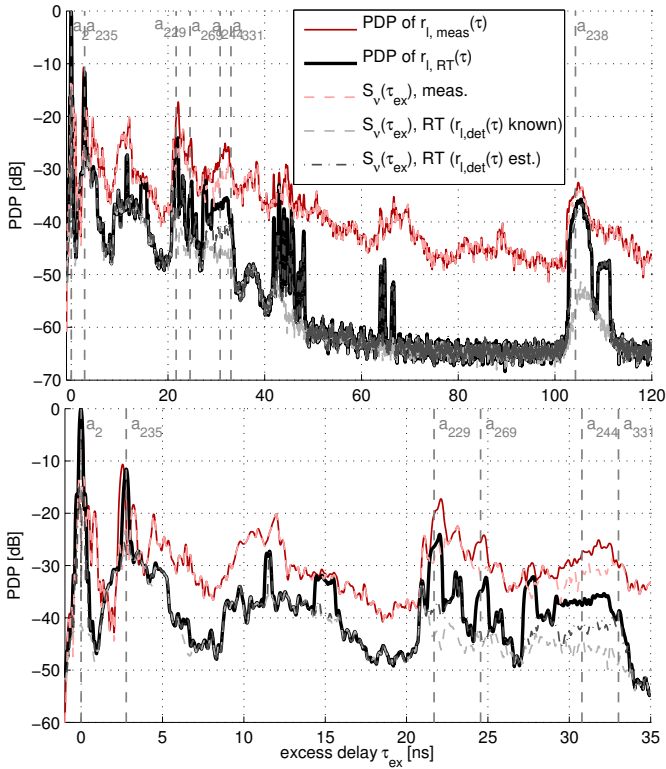


Fig. 2. Comparison of several PDPs: Solid lines denote PDPs of the overall received signal, dashed ones indicate PDPs of the DM. The lower figure provides a close-up view on the excess delay axis. Dashed vertical lines indicate the mean excess delay of the MPCs analyzed in Section V.

In Fig 3, a comparison of the K-factor with respect to the LOS path K_{LOS} and the RMS delay spread τ_{RMS} between measurements and RT is shown. Due to the limited range of delays for which RT provides significant DM, K_{LOS} is considerably higher than for the measurements, while τ_{RMS} is lower. For Figs. 2 and 3, the minimum possible pulse duration $T_p = 0.2$ ns, a roll-off factor of $\beta_R = 0.5$, and $f_c = 6.85$ GHz have been used. However, these observations still allow no direct conclusions on the influence on the localization performance, which is the focus of the next section.

IV. ESTIMATION OF POSITION-RELATED PARAMETERS

As derived in [3], the Cramér-Rao lower bound (CRLB) on the position estimation for MINT is given as the inverse of the equivalent Fisher information matrix (EFIM) [15]

$$\mathbf{J}_{\mathbf{p}_\ell} = \frac{8\pi^2\beta^2}{c^2} \sum_{k=1}^{K_\ell} \text{SINR}_{k,\ell} \mathbf{J}_{\mathbf{r}}(\phi_{k,\ell}). \quad (5)$$

In (5), β denotes the effective (RMS) bandwidth of $s(\tau)$ and it is assumed that no deterministic MPCs overlap in the delay domain. The ranging direction matrix $\mathbf{J}_{\mathbf{r}}(\phi_{k,\ell})$ is defined as

$$\mathbf{J}_{\mathbf{r}}(\phi_{k,\ell}) = \begin{bmatrix} \cos^2(\phi_{k,\ell}) & \cos(\phi_{k,\ell})\sin(\phi_{k,\ell}) \\ \cos(\phi_{k,\ell})\sin(\phi_{k,\ell}) & \sin^2(\phi_{k,\ell}) \end{bmatrix}. \quad (6)$$

It indicates the geometric information of the k -th MPC, as it has one eigenvector pointing in the direction $\phi_{k,\ell}$, the angle

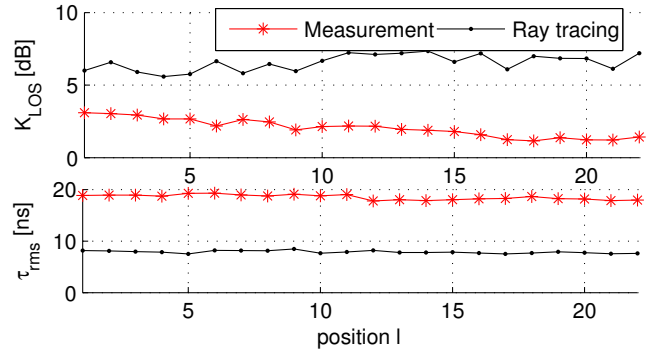


Fig. 3. K-factor with respect to the LOS component and RMS delay spread of measured (red) and RT signals (black).

from the VA at \mathbf{a}_k to position \mathbf{p}_ℓ . This information is weighted by the $\text{SINR}_{k,\ell}$ of the k -th MPC, defined as

$$\text{SINR}_{k,\ell} = \frac{|\alpha_{k,\ell}|^2}{N_0 + T_p S_{\nu,\ell}(\tau_{k,\ell} - \tau_{1,\ell})}. \quad (7)$$

Eq. (7) quantifies local effects of the deterministic and diffuse parts of the channel in the delay domain. We therefore use it to evaluate the suitability of RT for performance prediction, i.e. the computation of the CRLB for a geometrically defined environment. We observe that the estimation of the SINRs depends to a great extent on the level of channel knowledge, i.e. the availability of the local PDP of the DM $S_{\nu,\ell}(\tau)$.

A. Estimation of the instantaneous $\text{SINR}_{k,\ell}$ – PDP available

The availability of grid measurements allows for a local PDP estimation $\hat{S}_{\nu,\ell}(\tau)$ using (2) and (3). For RT, the provided channel decomposition into deterministic MPCs and DM enables the calculation of the “true” $S_{\nu}(\tau)$, which is used for all RT positions. With this and estimated path amplitudes as described in the previous section, a direct evaluation of (7) is possible, yielding an estimate $\widehat{\text{SINR}}_{k,\ell}$. We expect that the RT can provide good ground-truth values for this, while for the measurements, $\widehat{\text{SINR}}_{k,\ell}$ will depend crucially on the local PDP estimate $\hat{S}_{\nu,\ell}(\tau)$.

The subtraction of MPCs in (2) can cause numerical inaccuracies in the evaluation of the PDP of the DM. To prevent this, the local mean value within one T_p of this PDP around the excess delay of the respective path is chosen for the computation of (7). The noise power N_0 is estimated from the pre-LOS portion of the measured signals. To allow for a fair comparison, this quantity is then also used for the SINR estimation of the RT signals, as these do not contain measurement noise.

B. Estimation of the average SINR_k – PDP not available

If densely spaced grid measurements are not available, the local PDP of the DM can not be estimated reliably. For this reason, measurements within some local area, e.g. at M points along a route, have to be evaluated statistically. This renders the estimation of the instantaneous $\text{SINR}_{k,\ell}$ impossible, and gives rise to an average SINR_k . The estimation of this SINR_k

is described in detail in [2], and just shortly re-sketched here. Using the delay $\tilde{\tau}_{k,\ell}$ calculated from geometry, the received signal is projected onto a unit energy template pulse $s(\tau)$

$$\hat{\alpha}_{k,\ell} = \int_0^T r_\ell(\tau) s^*(\tau - \tilde{\tau}_{k,\ell}) d\tau \quad (8)$$

where T is the observation time. Under the assumptions that no path overlap between the k -th and any other MPC occurs, that $\tilde{\tau}_{k,\ell} = \tau_{k,\ell}$, and $s(\tau) \approx 0$ for $|\tau| > T_p$, this reduces to $\hat{\alpha}_{k,\ell} = \alpha_{k,\ell} + \nu_{k,\ell} + w_{k,\ell}$. This is a superposition of the deterministic MPC amplitude, DM, and noise. If both $\nu_\ell(\tau)$ and $w_\ell(\tau)$ are Gaussian processes, $|\hat{\alpha}_{k,\ell}|$ follows a Ricean distribution and the energy samples $|\hat{\alpha}_{k,\ell}|^2$ follow a non-central χ^2 -distribution with two degrees of freedom. Based on the sample mean and variance of $|\hat{\alpha}_{k,\ell}|^2$, denoted as $m_{1,k}$ and $m_{2,k}$ and estimated over the M considered positions, an estimator of SINR_k is [2]

$$\widehat{\text{SINR}}_k = \left(\frac{m_{1,k}}{\sqrt{m_{1,k}^2 - m_{2,k}}} - 1 \right)^{-1}. \quad (9)$$

For this, two additional steps need to be performed. First, as the geometry is not known perfectly, the delays $\tilde{\tau}_{k,\ell}$ have to be re-estimated. This is done using a maximum-likelihood (ML) re-localization of the VAs using data of the M considered points. Second, any variations in $\hat{\alpha}_{k,\ell}$ are inherently attributed to the DM by this estimator. Hence, the estimated amplitudes are corrected by a path-loss factor accounting for the deterministic dependence on the varying distance to the Tx. These procedures are described in detail in [2].

Finally, we note that if the true $S_{\nu,\ell}(\tau)$ was used for the estimation of the instantaneous $\text{SINR}_{k,\ell}$ using (7), then $\widehat{\text{SINR}}_k \approx \frac{1}{M} \sum_\ell \widehat{\text{SINR}}_{k,\ell}$, i.e. evaluated over the same positions, both averages should be equal. The right hand side of this expression is used in performance results where it is called average $\widehat{\text{SINR}}_{k,\ell}$, indicating the difference to (9).

V. RESULTS

For the validation and comparison of the SINR estimates, we selected different exemplary bandwidths and frequency bands from measurement and RT signals. This was done using the pulse shaping approach described in Section II with different pulse durations T_p of the raised-cosine pulse and different center frequencies f_c . The filtered signals were converted to complex baseband. Because of the restriction of the DM in the RT signals to excess delays smaller than 30 ns explained in Section III-D, we restrict the analysis to those deterministic MPCs within this range of delays, except for the VA at \mathbf{a}_{238} , which is the reflection at the far right wall of the corridor (cf. Fig. 1b). For the measurements, the local PDP of the DM is estimated for every point \mathbf{p}_ℓ using (3), where the $L = 15$ spatially closest points are taken into account, while for the RT, the available true $S_\nu(\tau)$ over all 22 points is used.

Fig. 4 shows a comparison of the obtained SINR estimates for different pulse parameters. We note that $\widehat{\text{SINR}}_k$ and $\widehat{\text{SINR}}_{k,\ell}$ obtained by RT and therefore the exact $S_\nu(\tau)$ match

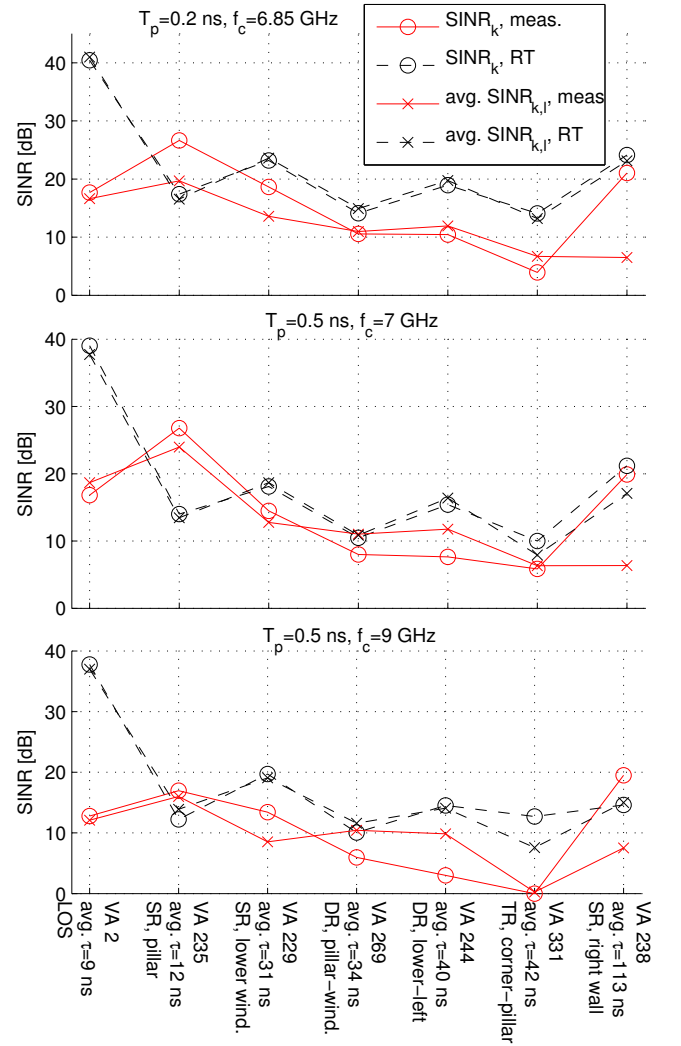


Fig. 4. SINRs for measurements and RT, using different T_p and f_c . Estimates for the mean SINR_k and the instantaneous $\text{SINR}_{k,\ell}$ are shown. SR, DR, and TR denote single-, double-, triple-reflection, respectively. The mean propagation delay over the 22 positions used is indicated.

very well, which validates (9) as estimator for the mean SINR of an MPC.

Concerning the comparison of SINR values for RT and measurements, we notice that although some match well, many values show considerable differences. This has several reasons. First, measurement data show much more variations than the deterministically generated RT data. This can be caused by e.g. physical propagation mechanisms not considered by RT or a simplified representation of the environment geometry in the floor plan. The most obvious discrepancy occurs for the SINR of the LOS path. This is caused by the antenna pattern of the Rx used in the measurements, which deviates by a few dB from omnidirectionality. An unfortunate orientation of the antennas caused the LOS amplitude to decrease when moving towards the Tx along the grid. This additional variation is considered as DM by the SINR estimation. Also, RT does not consider any scattering in the immediate surroundings of

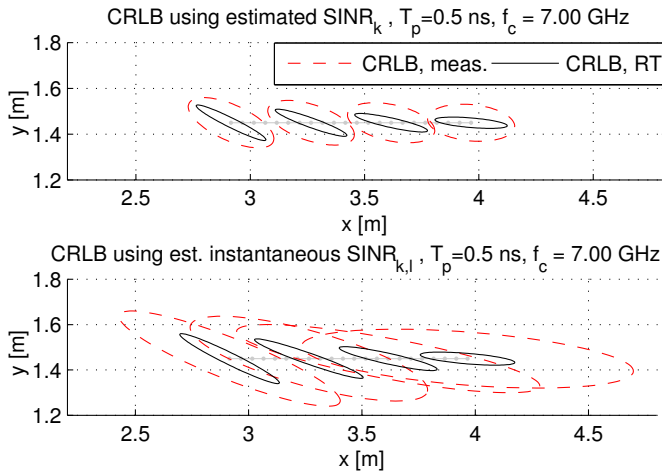


Fig. 5. Standard deviation ellipses for the CRLB over selected positions, enlarged by a factor of 30, to ease perceptibility. Upper plot shows the CRLB using the SINR estimate (9), lower plot uses the instantaneous estimate $\widehat{\text{SINR}}_{k,\ell}$ for the corresponding position. Red dashed ellipses denote results using measured data, for the black ellipses, ray tracing simulations were used.

the antenna, i.e. platform effects, which leads to an underestimation of DM around zero excess delay. The importance of modeling the frequency dependence of material properties is shown e.g. by VA 235 (the pillar above the Tx, cf. Fig 1b). At $T_p = 0.5$ ns, we observe a much higher SINR in the measurements at $f_c = 7$ GHz than at $f_c = 9$ GHz, which is not predicted by the RT.

Additional insights in the estimators can be obtained from VA 238, modeling the reflection on the far right wall. For this, the two SINR estimators differ significantly using the measurements. The right wall is modeled as a single surface, while in reality, it is a more complex structure causing a cluster in the DM. Because this cluster has quite homogeneous amplitude characteristics, $\widehat{\text{SINR}}_k$ according to (9) is large. But as can be seen from Fig. 2, the diffuse cluster is very significant in $S_\nu(\tau)$. This channel knowledge is used by $\widehat{\text{SINR}}_{k,\ell}$, thus reflecting the MPC behavior more realistically.

Fig. 5 shows standard deviation ellipses given by the CRLB, the inverse of the EFIM in (5), for $T_p = 0.5$ ns and a center frequency of $f_c = 7$ GHz. The ellipses are enlarged by a factor of 30 to allow for easier perceptibility. Despite the fact that there are considerable differences in the numeric values of the SINR between measurements and RT, the obtained error ellipses, especially for the mean $\widehat{\text{SINR}}_k$, seem reasonable for performance prediction. The basic orientation of the ellipses is given by the geometry and is the same for measurements and RT. The different SINRs do not cause a change of this orientation. The most obvious deviation is in the direction to the physical anchor, as the LOS path shows the largest error in terms of the SINR estimation.

VI. CONCLUSIONS AND OUTLOOK

In this paper, the use of RT for the analysis of indoor localization has been discussed. We have highlighted the

importance of the diffuse multipath for the localization performance and used a sub-band divided RT tool that is capable of modeling scattered signal paths. The energy ratio of deterministic MPCs and diffuse multipath has been introduced as evaluation method for the degree of realism of the RT signals in a dense indoor environment. At this stage of development, there are still considerable differences in estimated localization performance parameters between measurements and RT. However, the obtained results for the CRLB on the position accuracy show general agreement.

Future work includes a calibration technique for the RT using some limited channel measurements. This could alleviate the need for detailed knowledge of the electrical parameters of the building materials over a large frequency range. Such a calibrated RT tool would enable replacement of time-consuming measurement campaigns by offline RT simulations before installing an indoor localization system.

REFERENCES

- [1] N. Alsindi, B. Alavi, and K. Pahlavan, "Measurement and Modeling of Ultrawideband TOA-Based Ranging in Indoor Multipath Environments," *Vehicular Technology, IEEE Transactions on*, pp. 1046–1058, 2009.
- [2] P. Meissner and K. Witrisal, "Analysis of Position-Related Information in Measured UWB Indoor Channels," in *6th European Conference on Antennas and Propagation (EuCAP)*, Prague, Czech Republic, 2012.
- [3] K. Witrisal and P. Meissner, "Performance Bounds for Multipath-aided Indoor Navigation and Tracking (MINT)," in *International Conference on Communications (ICC)*, Ottawa, Canada, 2012.
- [4] Y. Shen and M. Win, "On the Use of Multipath Geometry for Wideband Cooperative Localization," in *Global Telecommunications Conference, 2009. GLOBECOM 2009. IEEE*, 2009, pp. 1–6.
- [5] G. Tiberi, S. Bertini, W. Malik, A. Monorchio, D. Edwards, and G. Manara, "Analysis of Realistic Ultrawideband Indoor Communication Channels by Using an Efficient Ray-Tracing Based Method," *Antennas and Propagation, IEEE Transactions on*, pp. 777–785, Mar. 2009.
- [6] T. Santos, F. Tufvesson, and A. Molisch, "Modeling the Ultra-Wideband Outdoor Channel: Model Specification and Validation," *Wireless Communications, IEEE Transactions on*, pp. 1987–1997, 2010.
- [7] H. Sugahara, Y. Watanabe, T. Ono, K. Okanoue, and S. Yarnazaki, "Development and experimental evaluations of "RS-2000" - a propagation simulator for UWB systems," in *Ultra Wideband Systems, 2004. Joint with Conference on Ultrawideband Systems and Technologies*, May 2004, pp. 76–80.
- [8] J. Jemai, P. Eggers, G. Pedersen, and T. Kürner, "On the Applicability of Deterministic Modelling to Indoor UWB Channels," in *3rd Workshop on Positioning, Navigation and Communication (WPNC'06)*, 2006.
- [9] S. U. Inan and S. A. Inan, *Electromagnetic Waves*. Prentice Hall, 2000.
- [10] R. Luebbers, "Finite conductivity uniform GTD versus knife edge diffraction in prediction of propagation path loss," *Antennas and Propagation, IEEE Transactions on*, pp. 70–76, Jan. 1984.
- [11] F. Mani, F. Quitin, and C. Oestges, "Accuracy of depolarization and delay spread predictions using advanced ray-based modeling in indoor scenarios," *EURASIP Journal in Wireless Communications and Networking*, 2011.
- [12] V. Degli-Esposti, F. Fuschini, E. M. Vitucci, and G. Falciasecca, "Measurement and Modelling of Scattering From Buildings," *Antennas and Propagation, IEEE Transactions on*, pp. 143–153, Jan. 2007.
- [13] F. Mani, F. Quitin, and C. Oestges, "Directional Spreads of Dense Multipath Components in Indoor Environments: Experimental Validation of a Ray-Tracing Approach," *Antennas and Propagation, IEEE Transactions on*, pp. 3389–3396, July 2012.
- [14] Y. Zhao, Y. Hao, A. Alomainy, and C. Parini, "UWB on-body radio channel modeling using ray theory and subband FDTD method," *Microwave Theory and Techniques, IEEE Transactions on*, pp. 1827–1835, June 2006.
- [15] Y. Shen and M. Win, "Fundamental Limits of Wideband Localization - Part I: A General Framework," *Information Theory, IEEE Transactions on*, pp. 4956–4980, Oct. 2010.

Real-Time Demonstration of Multipath-Assisted Indoor Navigation and Tracking (MINT)

Paul Meissner, Erik Leitinger, Manuel Lafer, and Klaus Witrisal
 Graz University of Technology, Austria; E-mail: paul.meissner@tugraz.at

Abstract—This paper presents an evaluation of a demonstration system for multipath-assisted indoor navigation and tracking (MINT). MINT overcomes the non-line-of-sight problems of range-based indoor localization systems by explicitly using location information of reflected signal components. With the real-time demonstration system, performance evaluations are possible without the need to rely on pre-recorded measurement trajectories or simulated radio channels. Hence, the robustness and accuracy of MINT in different environments can be tested easily and a proof-of-concept in close-to-practical conditions is obtained. Exemplary results in two different rooms highlight the following key findings: The excellent performance of MINT that we reported previously based on pre-recorded measurements can also be obtained with the real-time system, i.e. 5 cm accuracy for 90 % of the estimates at a bandwidth of 2 GHz. Furthermore, the covariance of the position error of the tracking filters matches well with the corresponding Cramér-Rao lower bound (CRLB).

I. INTRODUCTION

Non-line-of-sight (NLOS) situations between anchors and agents are the main reason for errors for radio based indoor localization systems. Enclosed indoor scenarios cause strong specular reflections and also a large level of diffuse (often called dense) multipath (DM). Errors caused by multipath can be dealt with by detecting NLOS situations and mitigating the corresponding range errors [1], [2]. Using the previously introduced *multipath-assisted* indoor navigation and tracking (MINT) approach [3], [4], the specular reflections can be turned into an advantage. Assuming that the floor plan of the environment is known, the travel times of specular multipath-components (MPCs) can be matched to the geometry by introducing *virtual anchors* (VAs, see Fig. 1).

As such a scheme relies heavily on the propagation channel, we have obtained numerous position-resolved channel measurements [5] to evaluate its performance [4], [6]. However, channel measurement campaigns are tedious to perform. A real-time demonstration system, which is discussed in this paper, allows for flexible and rapid evaluation of e.g. novel algorithms for MINT in more realistic conditions. Issues like fast motion changes and signal obstructions can be tested realistically and easily. For indoor localization systems, experimentation is an important way to understand the limitations and implications of the often heterogeneous requirements and environments. A method for precise anchor-free positioning in a specific environment is presented in [7], requiring many

This work was partly supported by the Austrian Science Fund (FWF) within the National Research Network SISE project S10610, and by the Austria Research Promotion Agency (FFG) within KIRAS PL3, grant nb. 832335 “LOBSTER”.

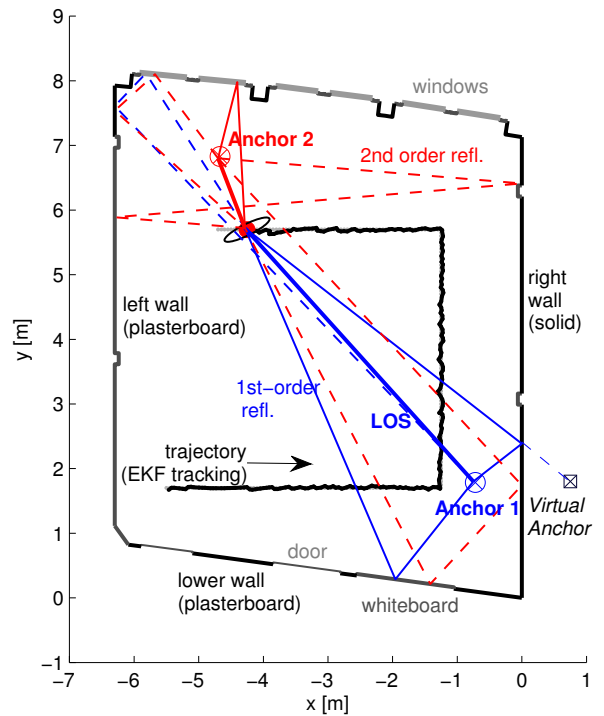


Fig. 1. Setup of the MINT demonstration system in Room 1. The tracking algorithm described in Sec. II is used on a known test trajectory to allow for error computation. Signal contributions from LOS-, first-order-, and second-order reflections are illustrated in bold, thin solid, and thin dashed lines, respectively. Color encodes the anchor number. On the right side, an example for a first-order VA is depicted for Anchor 1.

closely spaced measurements. For the evaluation of cooperative methods, large-scale campaigns are often more appropriate [8], [9], but similarly tedious to perform.

For the MINT demonstration system, it is desirable to compare the performance of different implementations in certain environments. Also, the localization accuracy can be compared to theoretical predictions given by performance bounds that include effects such as path overlap [3] and the DM [6]. The contributions of this paper are:

- We present a proof-of-concept for the MINT approach using a real-time demonstrator, showing excellent accuracy and robustness.
- Using tracking results obtained in two example rooms, we show how estimation of path parameters motivated by theory can be used to predict the performance of the system in an environment and also to improve the

performance.

In the remainder of this paper, Sec. II deals with the scenario, the models and the tracking algorithms, which is a recap from previous work. Section III briefly introduces the hardware of the demo system, while Sec. IV presents the prediction of the expected localization performance based on sample measurements. Finally, detailed results are presented and discussed in Sec. V.

II. SCENARIO, MODEL AND ALGORITHMS

The aim of this paper is to present a real-time demonstration system for the MINT approach [3]. We discussed the specific implementation and its evaluation based on pre-recorded channel measurements in [4] and [6]. In this paper, we therefore restrict the presentation of models and algorithms to a minimum and focus our attention on results obtained with the demonstration system in two exemplary scenarios.

Fig. 1 shows one of the two rooms used in this paper and illustrates the MINT approach itself, using a snapshot of the graphical output of the demonstration system during tracking. Up to $J = 2$ anchors at known positions are placed within a room to track a moving agent. As discussed in detail in [4] and references therein, we use the known floor plan to mirror the anchor coordinates with respect to each reflective surface to calculate the positions of the VAs [10]. The first-order VA corresponding to Anchor 1 and the right wall is illustrated in Fig. 1. The VA is a geometric model for the path delay of the corresponding MPC. Given that the MPC is detectable in the received signal, the VA can in principle be used as if it was a physically existing anchor.

The signal between the j -th anchor and the agent at the ℓ -th position \mathbf{p}_ℓ , is written as [3]

$$r_\ell^{(j)}(t) = \sum_{k=1}^{K_\ell^{(j)}} \alpha_{k,\ell}^{(j)} s(t - \tau_{k,\ell}^{(j)}) + s(t) * v_\ell^{(j)}(t) + w(t) \quad (1)$$

where the $\alpha_{k,\ell}^{(j)}$ and $\tau_{k,\ell}^{(j)}$ are the complex amplitudes and delays of the k -th deterministic MPCs, respectively. The signal $s(t)$ denotes the transmitted pulse. The signals $v_\ell^{(j)}(t)$ and $w(t)$ denote DM and white Gaussian measurement noise, respectively [3]. Especially in indoor environments, DM plays a large role in the detectability of the deterministic MPCs, which will be discussed in more detail later.

The estimation of the arrival times of the deterministic MPCs is done as in [4] using an iterative search-and-subtract implementation of a maximum-likelihood estimator based on the assumption of separable paths, i.e.

$$\{\hat{\tau}_{k,\ell}^{(j)}\} = \arg \min_{\{\tau_{k,\ell}^{(j)}\}} \int_T \left| r_\ell^{(j)}(t) - \sum_{k=1}^{\hat{K}_\ell^{(j)}} \hat{\alpha}_{k,\ell}^{(j)} s(t - \tau_{k,\ell}^{(j)}) \right|^2 dt. \quad (2)$$

The path amplitudes are nuisance parameters and are estimated using the projection of the received signal on a unit energy pulse template shifted to the corresponding delay

$$\hat{\alpha}_{k,\ell}^{(j)} = \int_0^T [r_\ell^{(j)}(t)]^* s(t - \hat{\tau}_{k,\ell}^{(j)}) dt. \quad (3)$$

The number of estimated MPCs $\hat{K}_\ell^{(j)}$ should be chosen corresponding to the number of expected specular paths in an environment.

We focus on the influence of the measurement on the tracking and hence restrict the motion model of the agent to a simple linear Gaussian constant-velocity model

$$\begin{aligned} \mathbf{x}_{\ell+1} &= \mathbf{F}\mathbf{x}_\ell + \mathbf{G}\mathbf{n}_{a,\ell} \\ &= \begin{bmatrix} 1 & 0 & \Delta T & 0 \\ 0 & 1 & 0 & \Delta T \\ 0 & 0 & 1 & 0 \\ 0 & 0 & 0 & 1 \end{bmatrix} \mathbf{x}_\ell + \begin{bmatrix} \frac{\Delta T^2}{2} & 0 \\ 0 & \frac{\Delta T^2}{2} \\ \Delta T & 0 \\ 0 & \Delta T \end{bmatrix} \mathbf{n}_{a,\ell}. \end{aligned} \quad (4)$$

Here, ΔT denotes the sampling time¹ and the state vector \mathbf{x}_ℓ of the agent contains x - and y -position and velocity. The driving acceleration noise term $\mathbf{n}_{a,\ell}$ models motion changes that deviate from this model. The tracking is done as in [4] using an Extended Kalman Filter (EKF) with data association (DA), since the estimated MPC arrival times in (2) are not associated to the VAs. At the position predicted by the EKF, the expected VAs and the corresponding delays (those whose reflection paths are possible) are calculated using pre-computed ray-tracing results. The estimated arrival times from (2) are then matched to these such that the cumulative distance of estimated and expected delays is minimized, using the optimal subpattern assignment approach [11]. Associations at a distance higher than a given maximum ranging uncertainty, the so-called cut-off distance d_c are discarded. The remaining associated delays and corresponding VA positions are then passed to the EKF for the update step, in which a trilateration w.r.t. the associated VAs is performed. We refer the reader to [4] and references therein for a much more detailed description.

III. HARDWARE SETUP AND SIGNAL PREPROCESSING

The receiving and transmitting device used for the real-time system is an M-sequence based UWB channel sounder developed by the German company *Ilmsens*. As there are two RX and one TX channels, the moving agent in the demonstration system is the TX and the anchors are the RXs, but from the view of the algorithms, these roles could also be reversed. The channel sounder is capable of sending and receiving up to 13 signals per channel per second, hence the lowest possible sampling time is $\Delta T = 0.077$ s. On TX and RX sides, self-made dipole-like antennas made of Euro-cent coins are used. They have an approximately uniform radiation pattern in azimuth domain and zeroes in the direction of floor and ceiling. The antennas are connected to the measurement device using cables, and are mounted on tripods. The tripod for the moving TX is equipped with wheels.

The received signal is cross-correlated with the used M-sequence to obtain an estimate of the bandpass channel impulse response $h_\ell^{(j)}(t)$. The channel sounder covers approximately the whole FCC UWB frequency range of 3.1 – 10.6 GHz. To select any desired subband with center frequency f_c and bandwidth B within this range, we use a raised cosine filter with impulse response $s(t)$ with an

¹The difference of time-steps at which measurements are performed.

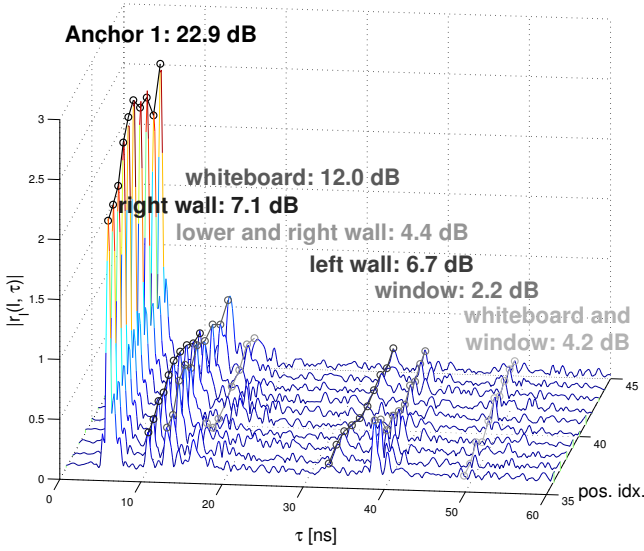


Fig. 2. Received signal from Anchor 1 in Room 1 over a short measurement trajectory (the corner part of the SINR estimation points shown in Fig. 4a) for $T_p = 0.5$ ns and $f_c = 7$ GHz. The estimated SINRs of selected VAs (reflectors) are shown together with the evolution of their path amplitudes.

effective pulse duration $T_p = 1/B$ and a fixed roll-off factor $\beta_R = 0.5$. By downconversion, a received complex baseband signal according to (1) is obtained as

$$r_\ell^{(j)}(t) = \left[h_\ell^{(j)}(t) * s(t) e^{j2\pi f_c t} \right] e^{-j2\pi f_c t}. \quad (5)$$

All signal processing is done on a computer using Matlab, which allows for maximum flexibility. Different levels of graphical output are selectable by the user, such as the visualization of currently used MPCs and their propagation paths as shown in Fig. 1. After setting up an environment, transfer functions of connectors and cables as well as the crosstalk between TX and RX channels are removed with a calibration procedure similar to [12].

IV. PREDICTION OF LOCALIZATION PERFORMANCE

When setting up the demonstration system in an environment, it is beneficial to have a prediction of the expected localization performance available. This can be achieved e.g. using the Cramér-Rao lower bound (CRLB) on the position estimation for MINT, which was derived in [3]. Under the assumption of no path overlap (PO), i.e. the deterministic MPCs in (1) are orthogonal, the equivalent Fisher information matrix (EFIM) [13] on the position is given as

$$\mathbf{J}_{\mathbf{p}_\ell} = \frac{8\pi^2 \beta^2}{c^2} \sum_{j=1}^J \sum_{k=1}^{K_\ell^{(j)}} \text{SINR}_{k,\ell}^{(j)} \mathbf{J}_r(\phi_{k,\ell}^{(j)}), \quad (6)$$

where β denotes the effective (RMS) bandwidth of $s(t)$ and $\text{SINR}_{k,\ell}^{(j)}$ denotes the signal-to-interference-and-noise-ratio of the k -th deterministic MPC at the ℓ -th position. The ranging direction matrix $\mathbf{J}_r(\phi_{k,\ell}^{(j)})$ [13] is defined as

$$\mathbf{J}_r(\phi_{k,\ell}^{(j)}) = \begin{bmatrix} \cos^2(\phi_{k,\ell}^{(j)}) & \cos(\phi_{k,\ell}^{(j)}) \sin(\phi_{k,\ell}^{(j)}) \\ \cos(\phi_{k,\ell}^{(j)}) \sin(\phi_{k,\ell}^{(j)}) & \sin^2(\phi_{k,\ell}^{(j)}) \end{bmatrix}. \quad (7)$$

It indicates the geometric information of the k -th MPC, the angle from the k -th VA to the position \mathbf{p}_ℓ , as it has one eigenvector pointing in the direction $\phi_{k,\ell}^{(j)}$. The $\text{SINR}_{k,\ell}^{(j)}$, which weights this geometric information, is defined as

$$\text{SINR}_{k,\ell}^{(j)} = \frac{|\alpha_{k,\ell}^{(j)}|^2}{N_0 + T_p S_{\nu,\ell}^{(j)}(\tau_{k,\ell}^{(j)})}. \quad (8)$$

It is the ratio of the energy of the k -th MPC to the sum of the noise PSD N_0 and the effective power of the DM at the delay $\tau_{k,\ell}^{(j)}$. The latter is characterized by the power delay profile $S_{\nu,\ell}^{(j)}(\tau)$ of the DM [3].

We observe that the SINRs of deterministic MPCs require knowledge of the PDP of the DM at position ℓ . This requires many closely-spaced measurements around \mathbf{p}_ℓ , which are usually not available. An alternative estimator of the SINR based on a Gaussian model for the DM was derived in [6] and is also used here. In short, it uses a few position-resolved measurements within a region, where the corresponding MPCs are visible. On these, non-overlapping MPCs are estimated as in (2) and corrected for deterministic effects such as path loss and also random effects such as uncertainties in the floor plan. Finally, the estimator is based on the ratio of the estimated deterministic MPC energy to the variations that still remain in the estimated amplitudes after the correction steps.

It is important to note that only position-averaged MPC SINRs can be estimated by this method since statistical moments of the estimated amplitudes need to be computed. We account for this fact by estimating SINR_k globally for each VA, which describes the reliability of the localization information of the respective MPC. Fig. 2 shows several received signals from Anchor 1 in Room 1, using $T_p = 0.5$ ns and $f_c = 7$ GHz. Also shown is the evolution of the estimated amplitudes of selected deterministic MPCs and the estimated SINR values. The trajectory part covers a distance of 45 cm and is part of the SINR estimation points in Room 1 (see Fig. 4a). It can be observed that MPCs with low variations in their amplitudes, such as the LOS, whiteboard and right wall, in general have a large SINR. If there are large variations which cannot be attributed to deterministic effects, the SINR is considerably lower, such as for the window.

The estimated SINRs can be used with (6) to get an EFIM estimate $\hat{\mathbf{J}}_{\mathbf{p}_\ell}$. Note that the only location-dependent effect remaining is the geometry. The ranging direction matrices account for the direction of the information, while the room geometry defines which reflections are visible at \mathbf{p}_ℓ and contribute to the EFIM. The expected localization accuracy for an environment can be quantified by the position error bound (PEB)

$$E\{\|\mathbf{p}_\ell - \hat{\mathbf{p}}_\ell\|\} \geq \text{PEB}(\mathbf{p}_\ell) = \sqrt{\text{Tr}(\mathbf{J}_{\mathbf{p}_\ell}^{-1})}. \quad (9)$$

V. EXAMPLE RESULTS

A. Evaluation Scenarios and Parameters

The two rooms used are shown together with indications of the building materials in Figs. 1 and 5a, respectively. To quantitatively evaluate robustness and accuracy of the MINT

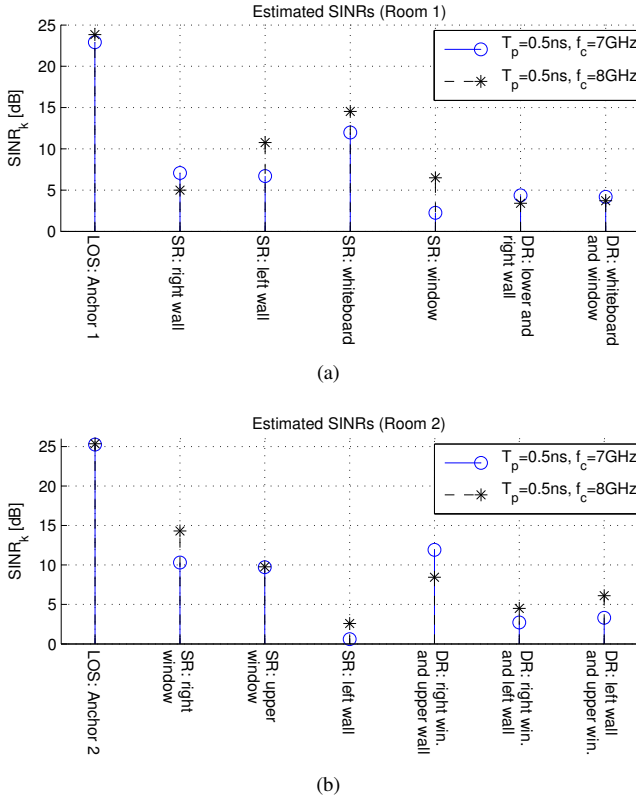


Fig. 3. Exemplary estimated SINRs of deterministic MPCs in Room 1 for Anchor 1 (a) and in Room 2 for Anchor 2 (b). A pulse duration $T_p = 0.5$ ns and two different center frequencies of $f_c = 7$ GHz and $f_c = 8$ GHz were used. SR and DR denote single- and double reflection, respectively.

implementation, one sample trajectory is used in each room, to enable calculation of a position error. The test trajectories consist of 235 points spaced by $\Delta_p = 5$ cm in Room 1, and of 154 points spaced by $\Delta_p = 3$ cm in Room 2. It should be noted that although the evaluation is done only on those trajectories, the results obtained are in close accordance with other results in different environments. As will be shown by the PEB results, they also cover challenging regions in these rooms and the performance accurately reflects the expectations provided by the bounds that are based on the estimated SINRs.

In the motion model, the process noise covariance matrix $\mathbf{Q} = \sigma_a^2 \mathbf{G} \mathbf{G}^T$ is chosen to allow for motion at a given maximum velocity in x - or y -direction, say $v_{x,\max}$. This is obtained by selecting the process noise variance in the acceleration-domain as $\sigma_a^2 = \left(\frac{v_{x,\max}}{3\Delta T}\right)^2$. During real-time operation, only $v_{x,\max}$ has to be chosen. ΔT is measured for every iteration and hence also σ_a^2 is updated, since depending on the chosen level of graphical output, the sampling time is not constant. For the quantitative performance evaluations, we set $v_{x,\max} = \Delta_p / \Delta T$ at e.g. $\Delta T = 1$, to avoid errors that are due to the motion model.

The measurement uncertainty in the EKF can be determined using an approach discussed in [14]. Based on estimates of SINRs as described in Sec. IV, the tracking can be tuned to the reflection properties of the environment. The locations of these measurement points are illustrated in Figs. 4a and 5a. Of course MINT can be used without this information [4]. To

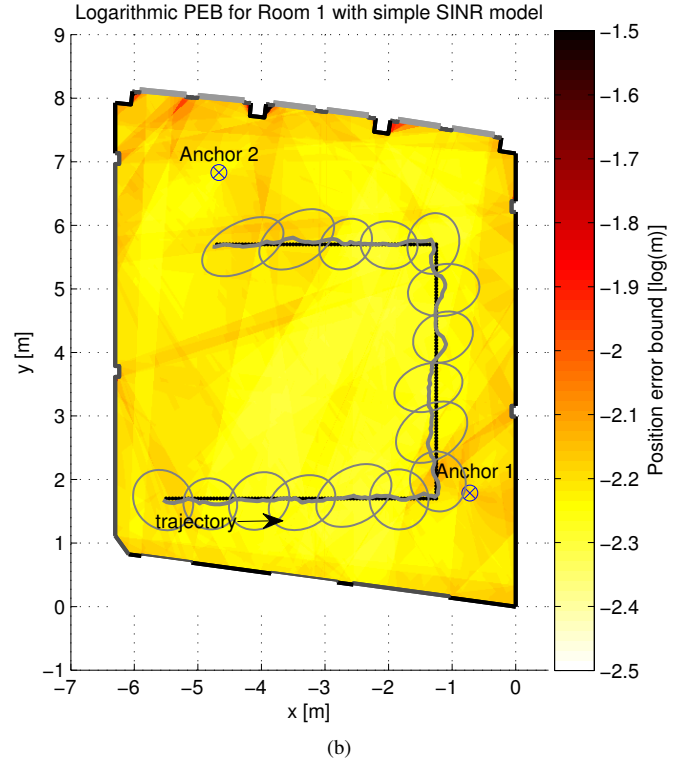
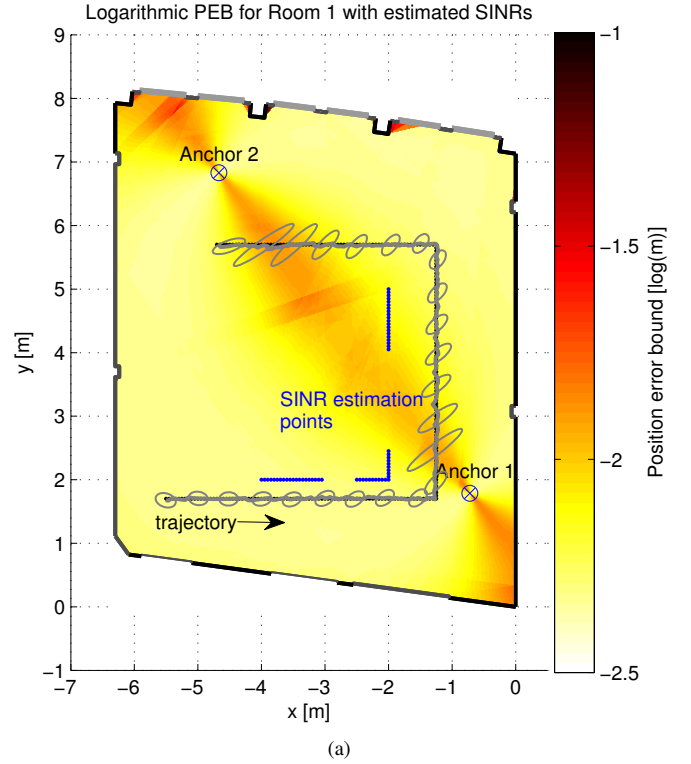


Fig. 4. Logarithmic CRLB for the position error over Room 1 for $T_p = 0.5$ ns and $f_c = 8$ GHz. (a) SINRs are used which have been estimated at the points marked in blue. (b) No SINR knowledge is available, but the mean SINR equals the mean of the estimated ones. Gray lines indicate MINT tracking results (estimated tracks and 40-fold standard deviation ellipses) for the respective scenario. It is evident that the SINRs can be used to obtain a much more realistic performance prediction.

enable a fair comparison, the SINRs for this case are selected as the mean of the estimated ones. The cutoff distance has been chosen as $d_c = 0.12$ m. Initialization of the EKF is done with the true position and zero velocity, since the initialization problem is out of scope of this paper. However, it can be solved using maximization of the likelihood function that is also used to derive the CRLB [15] or with a bank of parallel EKFs.

B. Estimation of the MPC SINRs and the PEB

In both rooms, SINRs of the LOS-component and potential first- and second-order reflections are estimated using the method described in Sec. IV and [6], [14] using 60 position-resolved measurements per room, as indicated in Figs. 4a and 5a. A subset of the obtained SINR results is shown in Fig. 3 for a pulse duration of $T_p = 0.5$ ns and two different center frequencies of 7 and 8 GHz. It can be seen that especially the plasterboard walls provide more information at the higher frequencies. As they represent spatially extended reflectors with large visibility regions, they are potentially important for MINT. Hence, observing the SINRs can give important hints on the optimal frequency range for a given scenario.

Using the geometry, (6), and (9), the CRLB on the position error (neglecting path overlap) can be computed for a scenario. The resulting PEB is illustrated in Figs. 4 and 5 for both rooms, with and without estimated SINRs, but – to allow for a fair comparison – for the same sets of MPCs. In the latter case, a simple model for the SINR is used: For the sake of a fair comparison, the SINRs of (8) are chosen such that their mean equals the mean of the estimated ones. Also, each reflection order decreases the SINR by an example value of 3 dB.

For Room 1, the PEB is shown using MPCs from both anchors. Without knowledge of the MPC SINRs, the PEB mostly encodes the expected visibility regions of the reflections and as such gives only a rough indication of the expected performance. If estimated SINRs are used, we can clearly observe a dilution of precision around the room diagonal, where location information is mostly coming from similar directions. This case is also illustrated in Fig. 1, where the MPCs are shown that the EKF can use in this region. We conclude that awareness of the SINRs gives a clearer picture of the expected performance in a given scenario. It should be noted again that the detrimental effect of path overlap [3] is not reflected by this PEB.

In Room 2, we illustrate the PEB for using only a single anchor (Anchor 2). Exploiting multipath, localization is still possible with MINT. Also here, the SINRs give good performance indications. For example, the visibility regions corresponding to the middle right and the upper window (c.f. Fig. 3b) are visible, which have rather large SINRs.

C. Tracking Results

Fig. 6 shows CDFs of the position error along the trajectories for MINT in both rooms. The evaluations have again been performed with a pulse duration of 0.5 ns and the two center frequencies of 7 and 8 GHz, with and without estimated SINRs. A general advantage is visible in these two rooms at the higher frequency range. According to our experience with

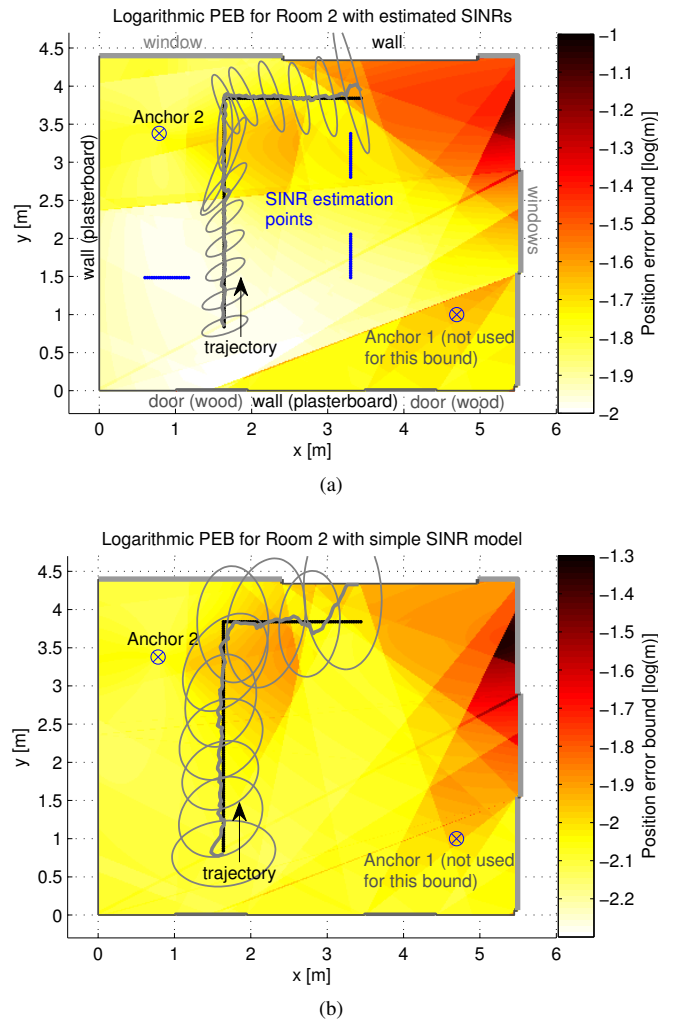


Fig. 5. Logarithmic CRLB for the position error over Room 2 for $T_p = 0.5$ ns and $f_c = 8$ GHz, if only Anchor 2 is used. (a) SINRs are used which have been estimated at the points marked in blue. (b) No SINR knowledge is available, but the mean SINR equals the mean of the estimated ones. Gray lines indicate single-anchor MINT tracking results (estimated tracks and 30-fold standard deviation ellipses).

the demonstration system, we attribute this effect mostly to the higher SINRs of the large plasterboard walls. For the case of no SINR knowledge, the MINT implementation achieves a performance of 13 cm for 90 % of the estimates in Room 1 and 21 cm for 90 % of the estimates in Room 2. With estimated SINRs, 90 % of the position errors are within approximately 5 cm in both rooms, in Room 1 even with the lower center frequency. In Room 2, using the SINRs allows for a similar performance using only a *single* anchor.

Figs. 4 and 5 also contain the tracking results shown in the CDFs in Fig. 6. Furthermore, the (significantly magnified) estimation error standard deviation ellipses of the EKF are indicated at some points. We observe an excellent tracking performance together with a largely reduced variance when estimated SINRs are used. In this case, the error ellipses follow well the predicted PEB and indicate the geometric dilution of precision, especially when the agent is between the two anchors.

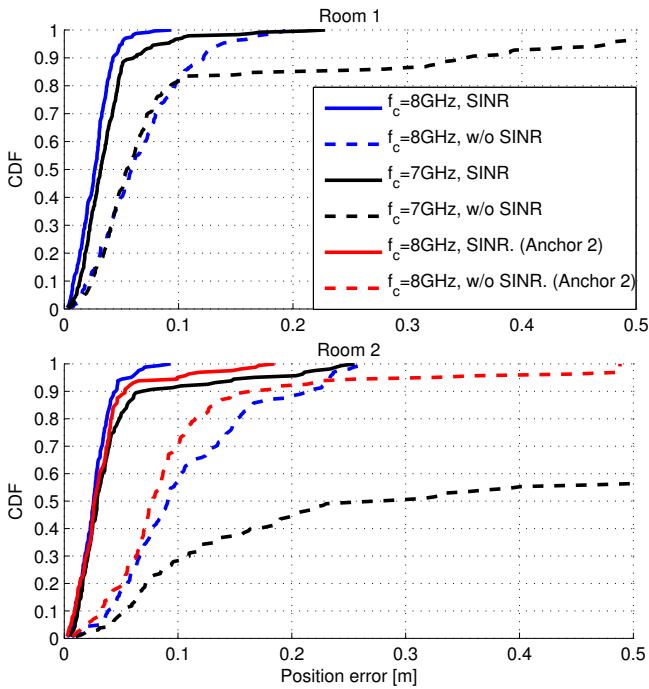


Fig. 6. CDFs of the position error for Room 1 (upper plot) and Room 2 (lower plot). Using the estimated SINRs, similar performance can be obtained in both rooms. Otherwise, the robustness can not always be achieved, especially in challenging environments such as Room 2. As predicted by the SINRs, the higher center frequency is beneficial there. For Room 2, results are also shown for using only a single anchor.

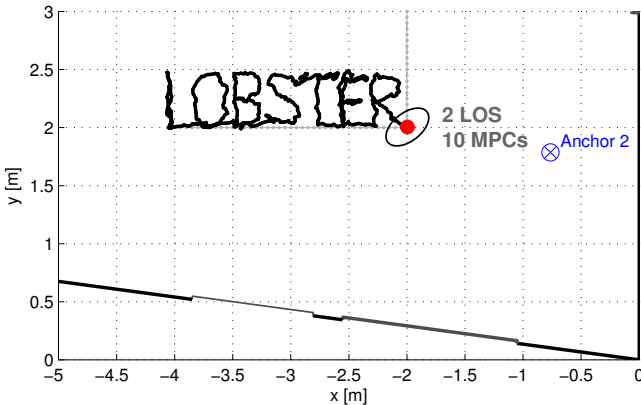


Fig. 7. Exemplary tracking results in Room 1, using estimated SINRs and $T_p = 0.5$ ns and $f_c = 7$ GHz. About 900 time steps were used to write the funding project's name "LOBSTER". The letter height is roughly 0.5 m, which demonstrates that an accuracy well within 10 cm can be achieved robustly.

An exemplary tracking result using SINR estimates is shown in Fig. 7, where the funding project's name "LOBSTER" has been written in letters with a height of approximately 0.5 m. The legibility again demonstrates the good performance.

VI. CONCLUSIONS AND OUTLOOK

We have presented a real-time implementation of the MINT approach in the form of a demonstration system. This system can be used to examine the localization performance and to identify influences on it in different environments. The results

show that the excellent performance of MINT that we have reported previously for measurement campaigns can be reproduced with the real-time implementation. Also, the CRLB on the position error can be estimated using a few measurements. This provides a detailed prediction of the achievable accuracy in some specific environment. The tracking algorithm also benefits from this additional channel awareness, as robustness and accuracy are improved.

The form of the position error bound used in this work is based on the simplifying assumption of no overlap in the deterministic MPCs. The extension of the measurement-based performance prediction to path overlap situations is a crucial step in ongoing research, since path overlap is an important and unavoidable performance impairment. In the current system, the MPC SINRs are estimated from position-resolved measurements that have been performed a-priori. Current work covers online learning of these estimates based on the results of the tracking algorithms.

REFERENCES

- [1] H. Wymeersch, S. Marano, W. Gifford, and M. Win, "A Machine Learning Approach to Ranging Error Mitigation for UWB Localization," *IEEE Transactions on Communications*, vol. 60, pp. 1719–1728, 2012.
- [2] S. Marano and, W. Gifford, H. Wymeersch, and M. Win, "NLOS identification and mitigation for localization based on UWB experimental data," *IEEE Journal on Selected Areas in Communications*, vol. 28, no. 7, pp. 1026–1035, 2010.
- [3] K. Witrisal and P. Meissner, "Performance Bounds for Multipath-aided Indoor Navigation and Tracking (MINT)," in *International Conference on Communications (ICC)*, Ottawa, Canada, 2012.
- [4] P. Meissner, E. Leitinger, M. Froehle, and K. Witrisal, "Accurate and Robust Indoor Localization Systems Using Ultra-wideband Signals," in *European Navigation Conference (ENC)*, Vienna, Austria, 2013. [Online]. Available: <http://arxiv.org/abs/1304.7928>
- [5] P. Meissner, E. Leitinger, M. Lafer, and K. Witrisal, "MeasureMINT UWB database," 2013. [Online]. Available: www.spac.tugraz.at/tools/UWBmeasurements
- [6] P. Meissner and K. Witrisal, "Analysis of Position-Related Information in Measured UWB Indoor Channels," in *6th European Conference on Antennas and Propagation (EuCAP)*, Prague, Czech Republic, 2012.
- [7] Y. Kuang, K. Astrom, and F. Tufvesson, "Single antenna anchor-free UWB positioning based on multipath propagation," in *Communications (ICC), 2013 IEEE International Conference on*, 2013.
- [8] A. Conti, M. Guerra, D. Dardari, N. Decarli, and M. Win, "Network Experimentation for Cooperative Localization," *Selected Areas in Communications, IEEE Journal on*, vol. 30, no. 2, pp. 467–475, 2012.
- [9] B. Denis, R. Raulefs, B. Fleury, B. Uguen, N. Amiot, L. de Celis, J. Dominguez, M. Koldsgaard, M. Laaraiedh, H. Noureddine, E. Staudinger, and G. Steinboeck, "Cooperative and heterogeneous indoor localization experiments," in *Communications Workshops (ICC), 2013 IEEE International Conference on*, 2013.
- [10] J. Kunisch and J. Pamp, "An ultra-wideband space-variant multipath indoor radio channel model," in *Ultra Wideband Systems and Technologies, 2003 IEEE Conference on*, 2003, pp. 290–294.
- [11] D. Schuhmacher, B.-T. Vo, and B.-N. Vo, "A Consistent Metric for Performance Evaluation of Multi-Object Filters," *IEEE Transactions on Signal Processing*, vol. 56, no. 8, pp. 3447–3457, 2008.
- [12] R. Cepeda, S. C. J. Parker, and M. Beach, "The Measurement of Frequency Dependent Path Loss in Residential LOS Environments using Time Domain UWB Channel Sounding," in *Ultra-Wideband, 2007. ICUWB 2007. IEEE International Conference on*, 2007.
- [13] Y. Shen and M. Z. Win, "Fundamental Limits of Wideband Localization - Part I: A General Framework," *IEEE Transactions on Information Theory*, pp. 4956–4980, Oct. 2010.
- [14] P. Meissner, E. Leitinger, and K. Witrisal, "UWB for Robust Indoor Tracking: Weighting of Multipath Components for Efficient Estimation," *IEEE Wireless Communications Letters*, 2014, submitted.
- [15] E. Leitinger, M. Froehle, P. Meissner, and K. Witrisal, "Multipath-Assisted Maximum-Likelihood Indoor Positioning using UWB Signals," in *IEEE ICC 2014 Workshop on Advances in Network Localization and Navigation (ANLN)*, 2014, accepted.

UWB for Robust Indoor Tracking: Weighting of Multipath Components for Efficient Estimation

Paul Meissner, Erik Leitinger, and Klaus Witrisal

Abstract—In a radio propagation channel, deterministic reflections carry important position-related information. With the help of prior knowledge such as a floor plan, this information can be exploited for indoor localization. This letter presents the improvement of a multipath-assisted tracking approach using information about the relevance of deterministic multipath components in an environment. This information is fed to a tracking filter as observation noise model. It is estimated from a few training signals between anchors and an agent at known positions. Tracking results are presented for measurements in a partial non-line-of-sight environment. At a bandwidth of 2 GHz, an accuracy of 4 cm can be achieved for over 90 % of the positions if additional channel information is available. Otherwise, this accuracy is only possible for about 45 % of the positions. The covariance of the estimation matches closely to the corresponding Cramèr-Rao Lower Bound.

I. INTRODUCTION

Robustness and accuracy are key requirements of indoor localization systems. We define robustness as the percentage of cases in which a system can achieve its given potential accuracy. Due to their fine time resolution, range-based ultrawideband (UWB) systems provide accurate distance estimates between anchors and the agent to be localized [1]. However, a non-line-of-sight (NLOS) situation can decrease the robustness due to biased range estimates. We have proposed an approach called multipath-assisted indoor navigation and tracking (MINT) to enhance the robustness [2], [3]. It makes use of the floor plan to associate multipath components (MPCs) to the surrounding geometry.

In this paper, we show how position-related information can be used efficiently as additional prior information. Channel parameters describing the reliability of the reflected MPCs [3], [4] are estimated from a few training signals with an agent at known positions and used in the tracking filter as measurement noise model. For a navigating agent, awareness to the uncertainty of the available information is crucial for the tracking performance both in theoretic [5] and in practical settings [6]. Taking into account diffuse multipath (DM) allows for much more realistic performance indications [7], especially in dense multipath environments.

The main contributions of this letter are:

- We show that a multipath-assisted tracking approach can be made aware of the relevance of specific deterministic MPCs in an environment.
- Using measurements, we show that centimeter-level accuracy can be achieved robustly also in NLOS conditions.

P. Meissner, E. Leitinger and K. Witrisal are with Graz University of Technology, Graz, Austria, email: paul.meissner@tugraz.at.

The authors thank Manuel Lafer for his help in performing the measurements.

Notation: The symbols $*$, $(\cdot)^T$, $(\cdot)^*$, $\mathbb{E}\{\cdot\}$, $\Re\{\cdot\}$, and \mathbf{I}_N denote convolution, transposition, conjugation, expectation, real part, and an identity matrix of dimension N , respectively.

II. TRACKING AND CHANNEL ESTIMATION

A. Signal and Geometry Models

We aim at tracking a mobile agent in an environment with J anchors at known positions. The signal between the j -th anchor and the agent at the position \mathbf{p}_ℓ is modeled as [3]

$$r_\ell^{(j)}(t) = \sum_{k=1}^{K_\ell^{(j)}} \alpha_{k,\ell}^{(j)} s(t - \tau_{k,\ell}^{(j)}) + s(t) * \nu_\ell^{(j)}(t) + w(t). \quad (1)$$

The sets $\{\alpha_{k,\ell}^{(j)}\}$ and $\{\tau_{k,\ell}^{(j)}\}$ are the complex amplitudes and delays of the k -th deterministic MPC, respectively. The signal $s(t)$ denotes the transmitted pulse shape with effective pulse duration T_p . The random process $\nu_\ell^{(j)}(t)$ denotes DM and is modeled as a Gaussian process with auto-covariance $\mathbb{E}\{\nu_\ell^{(j)}(\tau)[\nu_\ell^{(j)}(u)]^*\} = S_{\nu,\ell}^{(j)}(\tau)\delta(\tau - u)$, where $S_{\nu,\ell}^{(j)}(\tau)$ is the power delay profile (PDP) of the DM. The signal $w(t)$ denotes white Gaussian measurement noise with double-sided power spectral density (PSD) of $N_0/2$.

The delays of the $K_\ell^{(j)}$ deterministic MPCs are modeled geometrically using mirror images of the j -th anchor with respect to the corresponding walls, introducing so-called virtual anchors (VAs) [2], [8]. Fig. 1 shows two examples of such VAs. It can be seen that the distance from the agent's position \mathbf{p}_ℓ to the k -th VA at $\mathbf{a}_k^{(j)}$ corresponds to the delay $\tau_{k,\ell}^{(j)} = \frac{1}{c}d_{k,\ell}^{(j)} = \frac{1}{c}\|\mathbf{p}_\ell - \mathbf{a}_k^{(j)}\|$ of the corresponding MPC, where c denotes the speed of light. For the whole scenario, a set $\mathcal{A}^{(j)}$ of all potential VAs of the j -th anchor can be constructed. Higher-order VAs are obtained by mirroring again lower-order VAs with respect to reflectors. Using optical ray-tracing, the set of visible VAs can be computed for position \mathbf{p}_ℓ as

$$\mathcal{A}_\ell^{(j)} = \{\mathbf{a}_{\ell,1}^{(j)}, \dots, \mathbf{a}_{\ell,K_\ell^{(j)}}^{(j)}\} = \{\mathbf{a}_k^{(j)} : f_{\text{vis}}(\mathbf{a}_k^{(j)}, \mathbf{p}_\ell) = 1\} \quad (2)$$

where the ray-tracing is expressed by the function

$$f_{\text{vis}}(\mathbf{a}_k^{(j)}, \mathbf{p}) = \begin{cases} 1, & \text{if VA } \mathbf{a}_k^{(j)} \text{ is visible at } \mathbf{p} \\ 0, & \text{else.} \end{cases} \quad (3)$$

B. Tracking Algorithm

In a first step, the location-dependent parameters, i.e. the arrival times of the deterministic MPCs, are estimated from the received signal modeled by (1). The arrival time estimation

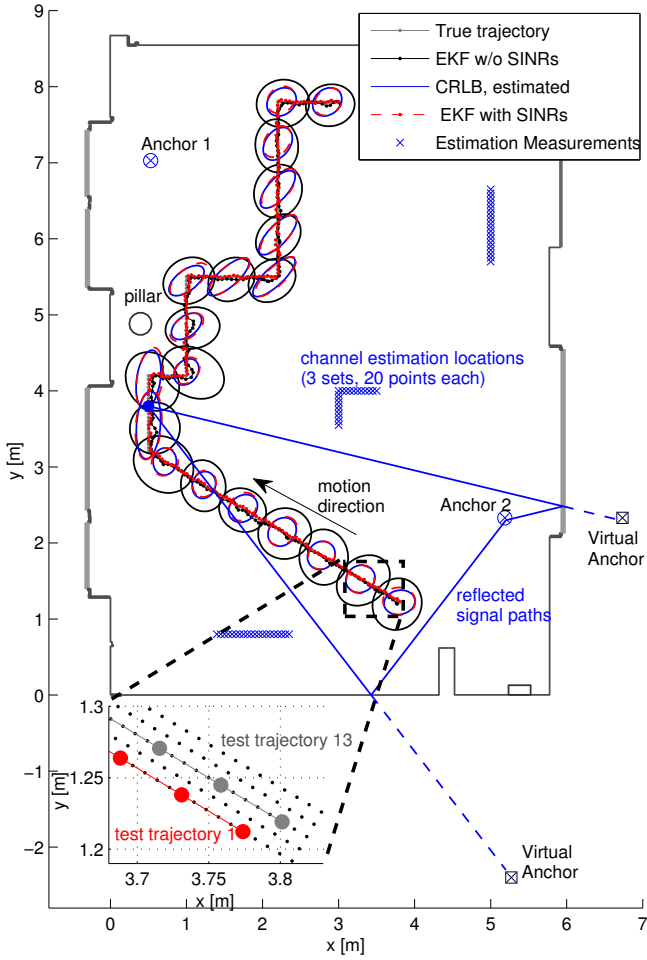


Fig. 1. Floor plan of the evaluation scenario, bold gray lines denote windows and other lines illustrate walls made of different materials. Examples for true and estimated agent trajectories are shown, the former is hidden beneath the others. The bottom contains a close-up of the trajectories, illustrating the 1-cm-spaced grid, out of which 25 5-cm-spaced trajectories are obtained. Two physical anchors are indicated with examples for virtual anchors modeling reflections from walls. Ellipses denote 20-fold standard deviations of the trackers as well as the respective 20-fold CRLB, as described in the text.

at position ℓ is realized as an iterative least-squares approximation of the received signal

$$\hat{\tau}_{k,\ell}^{(j)} = \arg \min_{\tau} \int_0^T \left| r_{\ell}^{(j)}(t) - \hat{r}_{\ell,k-1}^{(j)}(t) - \hat{\alpha}(\tau) s(t - \tau) \right|^2 dt \quad (4)$$

using a template signal $\hat{r}_{\ell,k}^{(j)}(t) = \sum_{k'=1}^k \hat{\alpha}_{k',\ell}^{(j)} s(t - \hat{\tau}_{k',\ell}^{(j)})$ for all MPCs up to the k -th. The path amplitudes are nuisance parameters, estimated using a projection of $r_{\ell}^{(j)}(t)$ onto a unit energy pulse $s(t)$ as

$$\hat{\alpha}(\tau) = \int_0^T [r_{\ell}^{(j)}(t)]^* s(t - \tau) dt; \quad \hat{\alpha}_{k,\ell}^{(j)} = \hat{\alpha}(\hat{\tau}_{k,\ell}^{(j)}). \quad (5)$$

The number of estimated MPCs $\hat{K}_{\ell}^{(j)}$ should be chosen according to the number of expected specular paths in an environment. With the assumptions of separable MPCs and white noise, (4) and (5) correspond to a maximum-likelihood (ML) estimation of the deterministic MPCs.

The tracking is done as in [2] using an EKF with data association (DA), which is necessary since the estimated MPC arrival times in (4) are not associated to the VAs. We choose a simple linear Gaussian constant-velocity motion model

$$\begin{aligned} \mathbf{x}_{\ell+1} &= \mathbf{F}\mathbf{x}_{\ell} + \mathbf{G}\mathbf{n}_{a,\ell} \\ &= \begin{bmatrix} 1 & 0 & \Delta T & 0 \\ 0 & 1 & 0 & \Delta T \\ 0 & 0 & 1 & 0 \\ 0 & 0 & 0 & 1 \end{bmatrix} \mathbf{x}_{\ell} + \begin{bmatrix} \frac{\Delta T^2}{2} & 0 \\ 0 & \frac{\Delta T^2}{2} \\ \Delta T & 0 \\ 0 & \Delta T \end{bmatrix} \mathbf{n}_{a,\ell}. \end{aligned} \quad (6)$$

The state vector \mathbf{x}_{ℓ} of the agent contains position \mathbf{p}_{ℓ} and the velocity vector, and ΔT is the update rate. The driving acceleration noise term $\mathbf{n}_{a,\ell}$ with zero mean and covariance matrix $\mathbf{Q} = \sigma_a^2 \mathbf{G}\mathbf{G}^T$ models motion changes that deviate from the constant-velocity assumption.

For the measurement update of the EKF, the set of expected VAs is calculated for the DA at the predicted position \mathbf{p}_{ℓ}^- using (2) for each anchor, yielding sets $\bar{\mathcal{A}}_{\ell}^{(j)}$. At this time, prior information such as a set $\mathcal{A}^{(j)}$ defining *relevant* VAs can be used to restrict the set of expected VAs, resulting in $\bar{\mathcal{A}}_{\ell}^{(j)} \cap \mathcal{A}^{(j)}$. The corresponding expected path delays are then matched to the estimated arrival times (4) such that the cumulative distance of estimated and expected delays is minimized, yielding sets of associated VAs $\mathcal{A}_{\ell,\text{ass}}^{(j)}$. The association is done using a constrained optimal subpattern assignment approach [2], [9], where the constraint is that associations at a distance larger than a given maximum ranging uncertainty, the so-called cut-off distance d_c , are discarded.

After joining information from all anchors, $\mathcal{A}_{\ell,\text{ass}} = \bigcup_j \mathcal{A}_{\ell,\text{ass}}^{(j)}$, the corresponding distance estimates are stacked in the EKF's measurement input vector which is *modeled* as

$$\mathbf{z}_{\ell} = \left[\dots, \|\mathbf{a}_k^{(j)} - \mathbf{p}_{\ell}\|, \dots \right]^T + \mathbf{n}_{z,\ell}, \quad \mathbf{a}_k^{(j)} \in \mathcal{A}_{\ell,\text{ass}}. \quad (7)$$

The measurement noise $\mathbf{n}_{z,\ell}$ is assumed to be zero-mean multivariate Gaussian. The choice of the measurement noise covariance matrix \mathbf{R}_{ℓ} depends on the amount of prior information. If a-priori estimates of the range estimation uncertainties $\text{var} \{ \hat{d}_{k,\ell}^{(j)} \}$ are available for a set of VAs, then

$$\mathbf{R}_{\ell} = \text{diag} \left\{ \text{var} \left\{ \hat{d}_{k,\ell}^{(j)} \right\} \right\} \quad \forall k, j : \mathbf{a}_k^{(j)} \in \mathcal{A}_{\ell,\text{ass}}. \quad (8)$$

Otherwise, an overall uncertainty σ_d^2 is used, i.e.

$$\mathbf{R}_{\ell} = \sigma_d^2 \mathbf{I}_{|\mathcal{A}_{\ell,\text{ass}}|}. \quad (9)$$

C. Position-Related Information and its Estimation

In [3], we have derived the Cramèr Rao Lower Bound (CRLB) for positioning based on the signal model (1) and the VAs. With the assumption of no path overlap, i.e. the MPCs are orthogonal, the equivalent Fisher information matrix (EFIM) for position \mathbf{p}_{ℓ} [10] is given as

$$\mathbf{J}_{\mathbf{p}_{\ell}} = \sum_{j=1}^J \sum_{k=1}^{K_{\ell}^{(j)}} \mathbf{J}_r(d_{k,\ell}^{(j)}) \mathbf{J}_r(\phi_{k,\ell}^{(j)}). \quad (10)$$

where the ranging direction matrix $\mathbf{J}_r(\phi_{k,\ell}^{(j)})$ determines the direction $\phi_{k,\ell}^{(j)}$ of the information of the k -th MPC, since it

is spanned by the outer product of the unit vector pointing from the k -th VA at $\mathbf{a}_k^{(j)}$ to the agent at \mathbf{p}_ℓ with itself [3]. It is scaled by the Fisher information contained in the signal $r_\ell^{(j)}(t)$ about the path length $d_{k,\ell}^{(j)}$. Its inverse is the CRLB for the variance of an unbiased range estimate $\hat{d}_{k,\ell}^{(j)}$

$$\mathbf{J}_r^{-1}(d_{k,\ell}^{(j)}) = \left(\frac{8\pi^2\beta^2}{c^2} \text{SINR}_{k,\ell}^{(j)} \right)^{-1} \leq \text{var} \left\{ \hat{d}_{k,\ell}^{(j)} \right\}. \quad (11)$$

Here, β denotes the effective (root mean square) bandwidth of $s(t)$ and the signal-to-interference-and-noise-ratio (SINR) of the k -th MPC at \mathbf{p}_ℓ is defined as

$$\text{SINR}_{k,\ell}^{(j)} = \frac{|\alpha_{k,\ell}^{(j)}|^2}{N_0 + T_p S_{\nu,\ell}^{(j)}(\tau_{k,\ell}^{(j)})}. \quad (12)$$

In [4], we have derived an estimator for the average $\text{SINR}_k^{(j)}$, averaged over positions within a confined spatial region in which propagation characteristics such as the PDP of the DM are assumed to be stationary. However, there is only a limited number of MPCs visible within such a region. To increase this number, we use measurements at N_s sets of points $\{\mathbf{p}_\ell : \ell \in \mathcal{P}_i\}$, where \mathcal{P}_i , $i = 1, \dots, N_s$, collects the indices of the points. Within each set, propagation characteristics are again assumed to be stationary and an $\widehat{\text{SINR}}_k^{(j,i)}$ can be estimated. For this, we have to take into account the *observability* of the corresponding VA. We define the subsets

$$\mathcal{P}_k^{(j,i)} = \{ \ell \in \mathcal{P}_i : f_{\text{vis}}(\mathbf{p}_\ell, \mathbf{a}_k^{(j)}) = 1 \wedge |\tau_{k,\ell}^{(j)} - \tau_{k',\ell}^{(j)}| > T_p \forall k' \neq k, \mathbf{a}_{k'}^{(j)} \in \mathcal{A}_\ell^{(j)} \} \quad (13)$$

with cardinality $N_k^{(j,i)}$. The conditions in (13) imply that the k -th VA is visible at \mathbf{p}_ℓ and there is no path overlap [3], [10] with any other VA-modeled MPC.

The overall aim is to take into account the uncertainty of the MPCs in an environment, both w.r.t. the path length estimation and also w.r.t. the position of the VAs, as these are subject to floor plan uncertainties. For the estimation of a *global* range uncertainty of a specific MPC, which is necessary to be useful as a location-independent noise model (8), we propose the weighted mean of the local uncertainties

$$\widehat{\text{var}} \left\{ \hat{d}_k^{(j)} \right\} = \frac{1}{\sum_{i=1}^{N_s} N_k^{(j,i)}} \sum_{i=1}^{N_s} N_k^{(j,i)} \widehat{\text{var}} \left\{ \hat{d}_{k,\ell}^{(j)} : \ell \in \mathcal{P}_k^{(j,i)} \right\}. \quad (14)$$

The $\widehat{\text{var}} \left\{ \hat{d}_{k,\ell}^{(j)} \right\}$ is obtained from an SINR estimate and (11). This and the use of (14) are motivated by assuming the range estimates $\hat{d}_{k,\ell}^{(j)}$ to be Gaussian distributed, which is justified by the fact that (4) is an approximation for the according ML estimator and as such is asymptotically efficient, i.e. $\hat{d}_{k,\ell}^{(j)} \sim \mathcal{N} \left(d_{k,\ell}^{(j)}; \mathbf{J}_r^{-1}(d_{k,\ell}^{(j)}) \right)$.

The VA positions are corrected using a prior $p(\tilde{\mathbf{a}}_k^{(j)})$ for the k -th VA. This leads to the MAP estimate

$$\hat{\mathbf{a}}_k^{(j)} = \arg \max_{\tilde{\mathbf{a}}_k^{(j)}} \ln p(\mathbf{r}^{(j)}(t) | \tilde{\mathbf{a}}_k^{(j)}) + \ln p(\tilde{\mathbf{a}}_k^{(j)}) \quad (15)$$

with a likelihood function that evaluates the contribution of the k -th VA to all estimation signals $\mathbf{r}^{(j)}(t)$ (c.f. [3] but neglecting

the whitening to account for the DM)

$$\ln p(\mathbf{r}^{(j)}(t) | \tilde{\mathbf{a}}_k^{(j)}) \propto \frac{2}{N_0} \sum_{i=1}^{N_s} \sum_{\ell \in \mathcal{P}_k^{(j,i)}} \int_0^T \Re \left\{ [r_\ell^{(j)}(t)]^* \tilde{s}_{k,\ell}^{(j)}(t) \right\} dt - \frac{1}{N_0} \int_0^T |\tilde{s}_{k,\ell}^{(j)}(t)|^2 dt. \quad (16)$$

Here, $\tilde{s}_{k,\ell}^{(j)}(t) = \tilde{\alpha}_{k,\ell}^{(j)} s(t - \tilde{\tau}_{k,\ell}^{(j)})$ is a template signal where $\tilde{\tau}_{k,\ell}^{(j)} = \frac{1}{c} \|\tilde{\mathbf{a}}_k^{(j)} - \mathbf{p}_\ell\|$ and the MPC amplitudes are again nuisance parameters and estimated using (5). The vector of received signals for the estimation is given as

$$\mathbf{r}^{(j)}(t) = [r_{\ell \in \mathcal{P}_1}^{(j)}(t), \dots, r_{\ell \in \mathcal{P}_{N_s}}^{(j)}(t)]^T. \quad (17)$$

With the signal model in (1) and $\hat{m}_{1,k}^{(j,i)}$ and $\hat{m}_{2,k}^{(j,i)}$ denoting estimates of the first and second central moments of the energy samples $|\alpha_{k,\ell}^{(j)}|^2$ for $\ell \in \mathcal{P}_k^{(j,i)}$, the corresponding average SINRs are estimated as [4]

$$\widehat{\text{SINR}}_k^{(j,i)} = \left(\frac{\hat{m}_{1,k}^{(j,i)}}{\sqrt{\hat{m}_{1,k}^{(j,i)2} - \hat{m}_{2,k}^{(j,i)}}} - 1 \right)^{-1}. \quad (18)$$

Those can be used together with (11) and (14) to obtain a range uncertainty for the k -th VA for the given environment.

The SINR estimation described in [4] also performs a correction of deterministic factors such as distance-dependent path-loss. Overall, it leads to sets $\hat{\mathcal{A}}^{(j)}$ of VAs with lower cardinality than $\mathcal{A}^{(j)}$, consisting of re-estimated VA locations obtained in (15).

III. MEASUREMENT SCENARIO

Measurements were obtained along a trajectory of 220 points, spaced by 5 cm, see Fig. 1. Around each point, 25 measurements were performed within a 5 x 5 cm grid, yielding in fact 25 parallel trajectories for the performance analysis.

The channel between the agent on the trajectory and two anchors (see Fig. 1) has been measured with an M-sequence based UWB channel sounder developed by *Imsens*, as also described in [11]. On anchor and agent sides, dipole-like antennas made of Euro-cent coins have been used. They have an approximately uniform radiation pattern in azimuth plane and zeroes in the directions of floor and ceiling. Out of the measured frequency range of 3.1 – 10.6 GHz, a subband with center frequency f_c and bandwidth $B = 1/T_p$ has been selected using filtering with a raised-cosine pulse $s(t)e^{j2\pi f_c t}$ with pulse duration T_p , followed by a downconversion.

IV. RESULTS

For the tracking along the 25 trajectories, a frequency range corresponding to $f_c = 7$ GHz and $T_p = 0.5$ ns has been chosen, which results in a bandwidth of 2 GHz. The process noise variance in the motion model (6) is obtained as in [2] based on selecting a maximum velocity in e.g. the x -direction $v_{x,\text{max}}$, which defines the 3σ point of the noise in velocity domain. The corresponding process noise variance in the acceleration domain is then $\sigma_a^2 = (v_{x,\text{max}}/(3\Delta T))^2$ with $v_{x,\text{max}} = 1$ m/s and $\Delta T = 1$ s in this paper. The DA cutoff distance has been chosen as $d_c = 0.12$ m. VAs up to order two

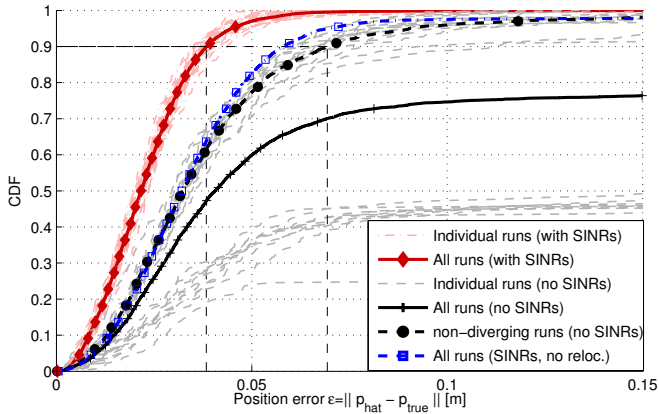


Fig. 2. Performance CDFs for $T_p = 0.5$ ns and $f_c = 7$ GHz. Thin lines show the individual 25 runs over the trajectories in Fig. 1. Red and gray indicate the EKFs with and without estimated SINRs. Bold lines denote the total performance for all runs, the dashed black line indicates the performance without SINRs on all non-diverging runs (15 out of 25).

have been used, and SINR estimation was done using $N_s = 3$ sets of 20 points (Fig. 1). The prior for the VA positions in (15) has been chosen as a uniform distribution within a circle of diameter 10 cm around the calculated VA position. The performance of the EKF is compared for the cases with estimated SINRs (8), and where no such information is available (9). To allow for a fair comparison in the latter case, the overall ranging uncertainty is selected as the mean of the estimated uncertainties, which is $\sigma_d = 0.042$ m.

An exemplary tracking result is illustrated in Fig. 1. In this case, the EKF can track the agent with and without estimated MPC SINRs, also in the NLOS region with respect to Anchor 1 (caused by the concrete pillar on the left side of the room). At every 12-th position, the 20-fold estimation error standard deviation ellipse of the EKF is illustrated. The comparison with the estimated CRLB, given as the inverse of (10), shows a close match to the tracking performance when using the SINRs, which confirms the efficient use of the MPCs. It should be noted that the CRLB shown does not include the motion model, i.e. it is not the posterior CRLB. However, for the chosen process noise variance, which is deliberately larger than the measurement uncertainties, the motion prior does not add significant information, making (10) applicable.

Fig. 2 shows the position error CDFs. It is evident that the channel characterization (red) yields excellent robustness, as all 25 runs have similar performance with 90% of the errors below 4 cm. Without SINR information (black/gray), the robustness is affected, as 10 of 25 runs diverge, mostly in the NLOS region discussed before. The overall CDF for the 15 non-diverging runs (black bold dashed line, circle markers) shows the *potential* performance of MINT without channel information, where 90% of the errors are within 7 cm. The influence of the MAP-re-localization of the VA positions (15) is illustrated by the CDF indicated by the blue dash-dotted curve with square markers. All runs are included, SINRs used, but without the re-localized VA positions. SINR awareness provides robustness, while re-localization improves accuracy.

Fig. 3 illustrates the mean number of associated MPCs,

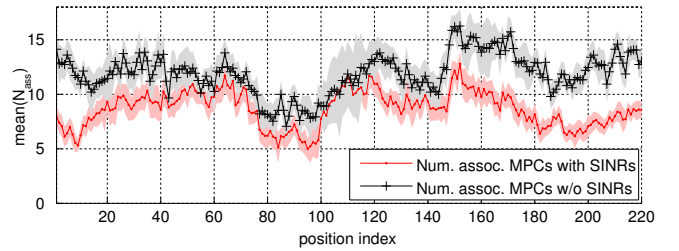


Fig. 3. Mean and standard deviation of the number of associated MPCs used for tracking. The 15 of 25 non-diverging runs are included for the case where no SINRs are available.

$\mathbb{E}\{|\mathcal{A}_{\ell, \text{ass}}|\}$, over all runs using SINRs and the 15 non-diverging runs without SINRs, together with the standard deviation. The additional channel knowledge helps to substantially prune the set of potential VAs to the relevant ones. This leads to less erroneous associations of estimated MPCs to VAs and also reduces the computational complexity.

The results presented here match results in [11], which also includes quantitative results for the SINR estimation in different environments.

V. CONCLUSIONS

We have shown that channel knowledge quantifying the position-related information of deterministic MPCs is a key factor for obtaining accurate and robust indoor localization. By estimating the uncertainty of range estimates corresponding to deterministic MPCs and making this information available to a tracking filter, multipath propagation can be used efficiently. Experimental results have confirmed the advantage, demonstrating excellent performance.

REFERENCES

- [1] D. Dardari, A. Conti, U. Ferner, A. Giorgetti, and M. Z. Win, "Ranging With Ultrawide Bandwidth Signals in Multipath Environments," *Proceedings of the IEEE*, 2009.
- [2] P. Meissner, E. Leitinger, M. Froehle, and K. Witrissal, "Accurate and Robust Indoor Localization Systems Using Ultra-wideband Signals," in *European Navigation Conference (ENC)*, Vienna, Austria, 2013.
- [3] K. Witrissal and P. Meissner, "Performance bounds for multipath-assisted indoor navigation and tracking (MINT)," in *International Conference on Communications (ICC)*, Ottawa, Canada, 2012.
- [4] P. Meissner and K. Witrissal, "Analysis of Position-Related Information in Measured UWB Indoor Channels," in *6th European Conference on Antennas and Propagation (EuCAP)*, Prague, Czech Republic, 2012.
- [5] Y. Shen, S. Mazuelas, and M. Win, "Network Navigation: Theory and Interpretation," *IEEE Journal on Selected Areas in Communications*, 2012.
- [6] A. Conti, D. Dardari, M. Guerra, L. Mucchi, and M. Win, "Experimental Characterization of Diversity Navigation," *IEEE Systems Journal*, 2014.
- [7] N. Decarli, F. Guidi, and D. Dardari, "A Novel Joint RFID and Radar Sensor Network for Passive Localization: Design and Performance Bounds," *IEEE Journal of Selected Topics in Signal Processing*, 2014.
- [8] J. Kunisch and J. Pamp, "An ultra-wideband space-variant multipath indoor radio channel model," in *IEEE Conference on Ultra Wideband Systems and Technologies*, 2003.
- [9] D. Schuhmacher, B.-T. Vo, and B.-N. Vo, "A Consistent Metric for Performance Evaluation of Multi-Object Filters," *IEEE Transactions on Signal Processing*, 2008.
- [10] Y. Shen and M. Z. Win, "Fundamental Limits of Wideband Localization - Part I: A General Framework," *IEEE Transactions on Information Theory*, Oct. 2010.
- [11] P. Meissner, E. Leitinger, M. Lafer, and K. Witrissal, "Real-Time Demonstration System for Multipath-Assisted Indoor Navigation and Tracking (MINT)," in *IEEE ICC 2014 Workshop on Advances in Network Localization and Navigation (ANLN)*, Sydney, Australia, 2014.

Part IV

Appendices

A

Descriptions of Channel Measurement Campaigns

This section describes the various channel measurement campaigns that have been performed during the work on this thesis. These measurements are also publicly available for research purposes [78]. In the following, Section A.2 describes the different measurement setups, i.e. frequency- and time-domain measurements. Section A.3 then discusses the possible options for signal postprocessing, while Sections A.4, A.5, and A.6 contain the detailed descriptions of the various scenarios.

A.1 Overview

The main aim of the measurements campaigns described here is to evaluate the performance of indoor localization and tracking algorithms in realistic scenarios and to gather knowledge of the relevant propagation phenomena. Therefore, measurements are performed along trajectories, that model motion paths of moving agents. Such measurements are done in different representative environments. At each trajectory point, channel measurements with a certain number of fixed anchors are performed.

Table A.1 contains an overview over all measurement campaigns. The different campaigns are divided into frequency- and time-domain measurements. The distinction is based on the measurement device that has been used. For all scenarios, the number of points on the measurement trajectories and their spacing are given. Also, the number of anchors used is indicated, which corresponds to the number of channels measured per trajectory point. For the frequency-domain measurements obtained with a vector network analyzer, the frequency resolution Δf is given. For the case of the time-domain measurements, the number of averages resulting in the measured signal at one trajectory position is given. A detailed discussion of measurement parameters is given in the following Section A.2

Table A.2 shows an overview over published papers using the various measurements.

<i>Frequency domain measurement campaigns – Vector Network Analyzer</i>				
Scenario	# Points	Spacing [cm]	Freq. res. Δf [MHz]	# Anchors
Corridor (Fig. A.4)	381	10	1	6
Corridor, Grid (Fig. A.4)	484	5	1.5	2
Seminarroom, bistatic (Fig. A.6)	2x220	5	5	2
Seminarroom, monostatic (Fig. A.6)	2x220	5	5	0
Lab, equipped (Fig. A.10)	61	5	5	2
Lab, empty	61	5	5	2
<i>Time domain measurement campaigns – M-sequence channel sounder</i>				
Scenario	# Points	Spacing [cm]	# Avg.	# Anchors
Seminarroom, local grids (Fig. A.6)	2x220x25	1	1024	2
Demo room Graz (Fig. A.8)	101, 235	5	33	4
Demo room Montbeliard (Fig. A.9)	154, 161	3	33	2

Table A.1: Available Measurement Campaigns and Parameters

Scenario	Publication	Comments
Corridor (Fig. A.4)	[T6]	Tracking using measurements;
	[T4]	comparison with conventional algorithms
	[T5]	Experimental computation of bounds;
	[T2]	estimation of MPC SINRs
	[147]	Tracking using measurements
	[82]	Energy capture analysis of det. MPCs
Corridor, Grid (Fig. A.4)	[85]	Same, extended results
	[T7]	MPC estimation;
	[T9]	extension of [84] to VA model
Seminarroom (Fig. A.6)	[92]	MPC tracking using PHD filters
	this thesis, Ch. 8	Validation of ray-tracing
Laboratory room (Fig. A.10)		Tracking and channel estimation
Demo room Graz (Fig. A.8)	[T8]	Tracking and channel estimation
Room Montbeliard(Fig. A.9)	[81]	Experimental computation of bounds;
	[T8]	estimation of MPC SINRs
		Description of demonstration system
		Live demonstration
		Description of demonstration system

Table A.2: Overview over publications using the measurement campaigns

A.2 General Measurement Setup

For both frequency- and time-domain measurements, Skycross SMT-3TO10M UWB antennas as well as custom made antennas using Euro-cent coins [148] have been used. The coin antennas have approximately uniform radiation patterns in azimuth domain and zeroes in $\pm 90^\circ$ elevation. The antennas were mounted on tripods in a height of 1.5 – 1.8 m, depending on the scenario. The cables were Huber & Suhner Sucoflex or S-Series cables, which each have an attenuation of approximately 1.1 dB per meter at a frequency of 10 GHz and 1.6 dB per meter at 18 GHz. We follow the usual approach of regarding the antennas as part of the radio channel. The antennas used show only very little distortion of the transmit signal, i.e. they have rather short impulse

responses [149].

For all measurements, the UWB frequency range according to the FCC has been measured, i.e. the range from 3.1 GHz to 10.6 GHz. This corresponds to a wavelength range of 9.67 cm to 2.83 cm. The bandwidth of 7.5 GHz results in a delay resolution of 0.1333 ns and a spatial resolution of 4 cm. For the frequency domain measurements, the frequency resolution Δf has been chosen as shown in Table A.1. It is related to the maximum delay that can be represented unambiguously with these measurements, i.e. $\tau_{\max} = 1/\Delta f$.

A static environment has been ensured in all scenarios, i.e. there have been no moving persons or objects. All floor plans have been measured by hand using a laser distance meter and a tape measure. The two-dimensional representation corresponds to the room dimensions in the height at which the antennas have been mounted. This height was in the range of 1.8 m, but slightly different for the different campaigns. In each campaign, all antennas were at the same height.

A.2.1 Frequency Domain Measurements – Vector Network Analyzer

Frequency-domain measurements have been obtained with a *Rhode & Schwarz ZVA-24* VNA. At the ℓ -th trajectory position, a sampled version $H_\ell[k]$ of the CTF $H_\ell(f)$ is measured with a frequency spacing of Δf as indicated in Table A.1. The VNA has been calibrated up to (but not including) the antennas with a through-open-short-match (TOSM) calibration. A resolution bandwidth of 10 kHz has been used and the transmit power has been set to 15 dBm.

A.2.2 Time Domain Measurements – M-Sequence Radar

Time-domain measurements have been obtained with an *Ilmsens Ultra-Wide Band M-Sequence device* [150]. The measurement principle is correlative channel sounding [100]. A binary code sequence with suitable autocorrelation properties (a large peak-to-off-peak-ratio) is transmitted over the channel. At the receiver, the channel impulse response is recovered using a correlation with the known code sequence.

This M-sequence radar has one transmitter and two receiver ports. Hence, the mobile unit that has been moved along the measurement trajectories was the transmitter, and the two receiver ports have been used as anchors. The transmit power of the M-sequence device in FCC mode is 18 dBm. The employed 12-bit M-sequence has a length of 4095 samples. At the clock rate of 6.95 GHz, this allows for a measurement window of $\tau_{\max} = 589.2$ ns.

A.3 Measurement Post-Processing

A.3.1 Frequency Domain Measurements – Vector Network Analyzer

For the VNA measurements, the major system influences on the measured CTF $H(f)$ have already been removed by the previously mentioned TOSM calibration. This includes cables and connectors, but not the antennas, which are considered as part of the radio channel. In the post-processing, a desired frequency band is first filtered out of the measurement data. This is done using the frequency domain representation of a suitable pulse shape $s(t)$ that is upconverted to the desired center frequency f_c . The baseband signal is obtained by a downconversion.

These steps can be done conveniently using a Fast Fourier Transformation (FFT). The CTF is measured at N_f discrete frequencies $f_k = k\Delta f + f_{\min}$, $k = 0, \dots, N_f - 1$, where f_{\min} is the lowest measured frequency. This sampled CTF $H[k]$ corresponds to a Fourier series representation of the time-domain CIR $h(\tau)$ [T6], which is periodic with a period of τ_{\max} . With f_{\min} and f_c denoting the lower band edge and the center frequency of the extracted band, respectively, and

using an inverse FFT (IFFT) with size $N_{\text{FFT}} = \lceil (\Delta f \Delta \tau)^{-1} \rceil$, where $\Delta \tau$ is the desired delay resolution, the time domain equivalent baseband signal is obtained as

$$r(t) = \text{IFFT}_{N_{\text{FFT}}} \{H[k]S[k]\} e^{-j2\pi(f_c - f_{\text{min}})t}. \quad (\text{A.1})$$

Here, $S[k]$ is the discrete frequency domain representation of the pulse $s(t)$, upconverted to the desired frequency range. This procedure is similar to [84].

A.3.2 Time Domain Measurements – M-Sequence Radar

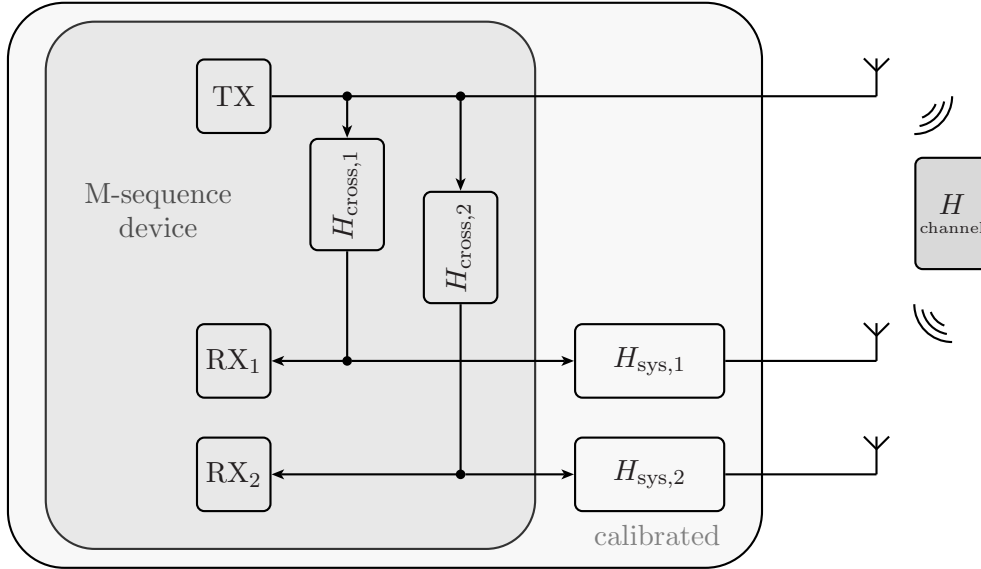


Figure A.1: Calibration setup for time domain measurements

Fig. A.1 shows a block diagram of the measurement setup using the M-Sequence radar. As in the VNA measurements, the measurement system should be calibrated up to (but not including) the antennas. Hence, the influence of the device internal transfer functions and the measurement cables and connectors, combined in the transfer function $H_{\text{sys},i}(f)$ for the i -th RX channel, as well as the crosstalk between TX channel and i -th RX channel, $H_{\text{cross},i}(f)$, have to be compensated. For the further description, we will drop the channel index.

To achieve this, two types of measurements are necessary. First, to determine the crosstalk, the TX antenna is unmounted and the TX port is terminated with a $50\ \Omega$ match and the crosstalk signals are measured. Second, also the RX antennas are unmounted and TX and RX cables are connected back-to-back with an attenuator to avoid nonlinear effects. In this way, $H_{\text{sys}}(f) + H_{\text{cross}}(f)$ is measured to obtain $H_{\text{sys}}(f)$. Using the measurement configuration with all the antennas as depicted in Fig. A.1 yields $H_{\text{meas}}(f) = H(f)H_{\text{sys}}(f) + H_{\text{cross}}(f)$. Hence, a calibrated version of the radio channel transfer function is obtained as

$$H(f) = \frac{H_{\text{meas}}(f) - H_{\text{cross}}(f)}{H_{\text{sys}}(f)}. \quad (\text{A.2})$$

To avoid noise gain, the time-domain representation of the denominator in (A.2) is confined to its significant values using a threshold together with a windowing. Finally, the time-domain signal within the desired frequency range around the center frequency f_c can be computed using a suitable baseband pulse shape $s(t)$ and $h(t)$ as the inverse Fourier transform of $H(f)$ as

$$r(t) = \left[h(t) * s(t) e^{j2\pi f_c t} \right] e^{-j2\pi f_c t} * \delta(t - \tau_{\text{shift}}). \quad (\text{A.3})$$

Here, τ_{shift} is a time shift that accounts for the delays of connectors in the calibration measurements and the antennas, which have not been removed by (A.2). For connectors, this value can be measured using a VNA, for the antennas, it can be computed using the length of the antennas and the propagation velocity in the materials, which is often given in data sheets. This calibration procedure is similar to [151] and is also described in [95].

A.3.3 Pulse Shaping Example

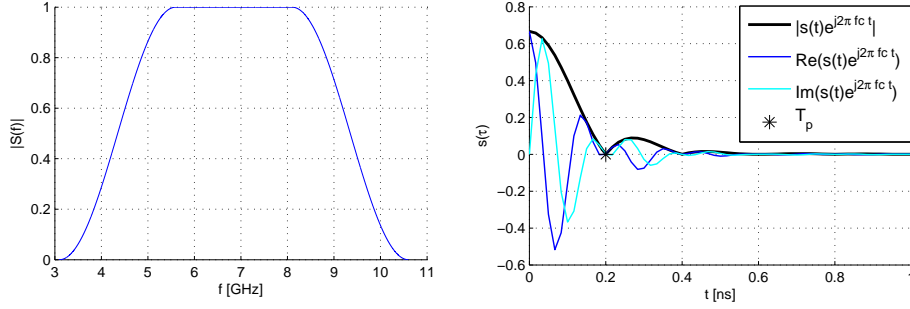


Figure A.2: Example for a pulse-shaping filter used with $T_p = 0.2$ ns and $f_c = 6.85$ GHz.

The example in Fig. A.2 shows a raised-cosine filter with $f_c = 6.85$ GHz, which is the center frequency of the whole measurement bandwidth. The -3 -dB bandwidth of this filter (in pass-band) is given as $B_N = 1/T_p = 5$ GHz. The overall (non-zero, excess) bandwidth is given as $B = (\beta_R + 1)/T_p$ which in this case (roll-off-factor $\beta_R = 0.5$) is the total measurement bandwidth.

Denoting the lower band edge of the measurements as $f_{\text{meas, min}}$ and the upper band edge as $f_{\text{meas, max}}$ (these are the band edges of the actually measured frequency range), we note that the filter parameters have to be chosen such that

$$f_c + \frac{\beta_R + 1}{2T_p} \leq f_{\text{meas, max}} \quad \text{and} \quad f_c - \frac{\beta_R + 1}{2T_p} \geq f_{\text{meas, min}}. \quad (\text{A.4})$$

Assuming that we wish to use the band between $f_c - B_N/2$ and $f_c + B_N/2$, i.e., we select a

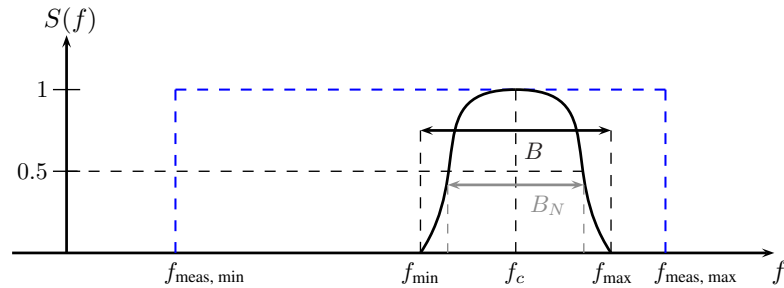


Figure A.3: Pulse-shaping filter parameters.

center frequency f_c and a pulse duration of $T_p = 1/B_N$. Fig. A.3 illustrates this scenario. The roll-off-factor β_R then has to be chosen such that $0 \leq \beta_R \leq 1$ and (A.4) are not violated, as the actual bandwidth B that the filter $S(f)$ will select from the measurement data is of course larger than the chosen B_N . Fig. A.3 shows an illustration of the filter parameters.

A.4 Large-Scale Environment – Corridor

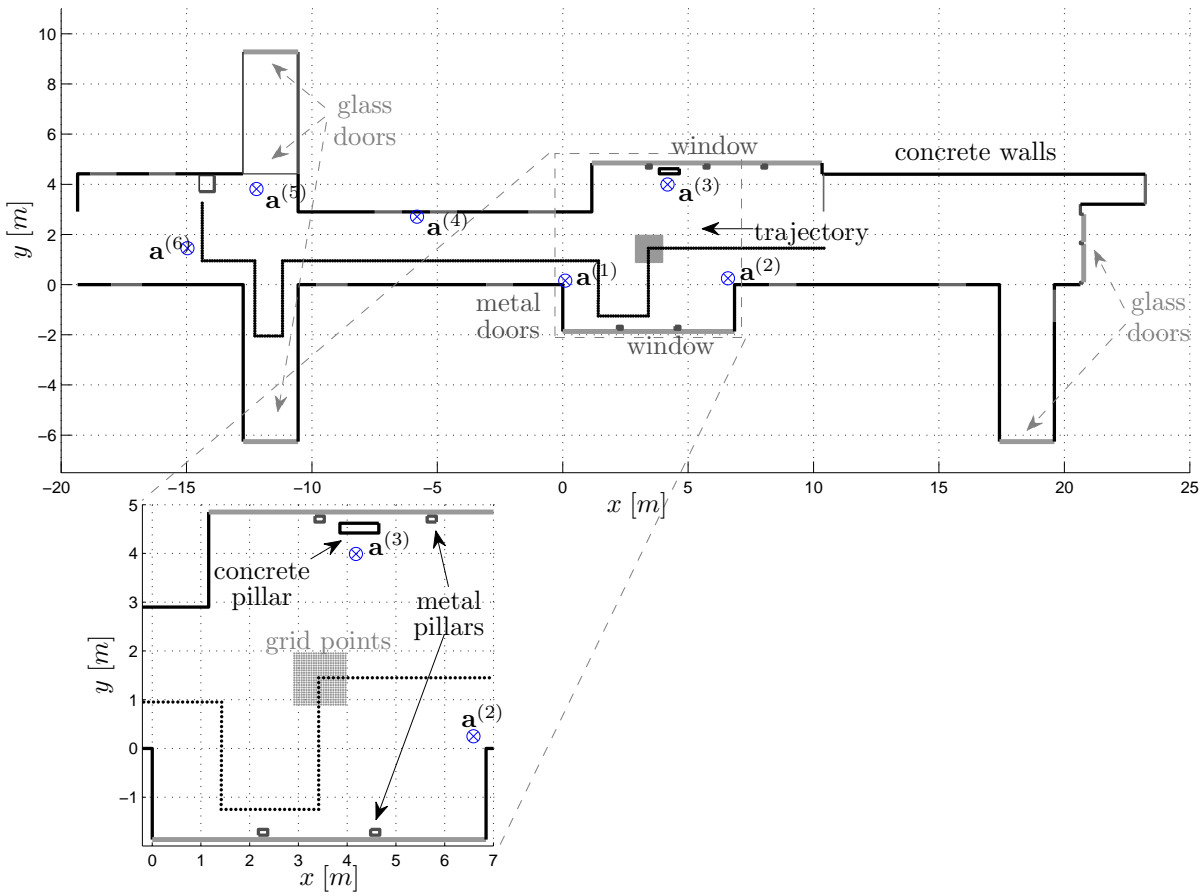


Figure A.4: Large-scale measurement scenario in the corridor of the laboratory. In this scenario, six anchors are available, enabling the use of conventional localization algorithms. Two different measurement setups are used: 1) A trajectory with 381 points spaced by 10 cm, and 2) measurements within a grid of 484 points with 5 cm spacing. For the grid setup, anchors 2 and 3 are available.

A.4.1 Trajectory Measurements

As shown in Figs. A.4 and A.5, these measurements have been obtained in a large corridor in our university building. The mobile was moved over a distance of almost 40 m (381 points, spaced by 10 cm) with measurements to six anchor nodes. Position 1 is at the right side. Mobile and Anchors 1 and 4 were equipped with the Skycross antennas, the other anchors with the coin antennas. All antennas were mounted at a height of 1.5 m.

Different LOS/NLOS conditions over this long distance allow for detailed performance evaluations of tracking algorithms. In this scenario, building walls are made of reinforced concrete and the doors of metal. It is an open, three-storey building with some metal bridges connecting the two sides of the corridor, as seen in Fig. A.5.

A.4.2 Grid Measurements

As shown in Figs. A.4, also grid measurements have been obtained in this scenario to allow for local channel analysis. In an area of roughly 1 m^2 , 484 (22×22) points with a spacing of 5 cm have been obtained to anchors 2 and 3. Position 1 is at the lower left side, position 22 at the

lower right side and position 484 at the upper right side. For the grid measurements, all anchors and the mobile were equipped with the coin antennas and mounted at a height of 1.5 m.



Figure A.5: Photo of corridor scenario, view approximately from the letter “y” in “trajectory” in Fig. A.4.

A.5 Medium-Scale Environments

A.5.1 Seminarroom at Graz University of Technology

Figs. A.6 and A.7 illustrate a seminarroom at our university. As shown, different wall materials are present as well as a solid concrete pillar on the left side, which creates a short NLOS region w.r.t. Anchor 1 and trajectory 2. Two trajectories are measured, also the measurements between the two mobiles are available to evaluate cooperative algorithms. For all anchors and mobiles, the coin antennas were used, mounted at a height of 1.23 m.

In a second measurement run, also monostatic measurements of both mobiles have been obtained, i.e. measurements where TX and RX are at the same location. For this purpose, an antenna setup as shown in the right plot of Fig. A.7 has been used to allow for a low direct coupling between the TX and RX antennas.

Trajectory Measurements – VNA

The trajectory measurements have been performed with the VNA. 2x220 points with 5 cm spacing are available. Also, the 220 measurements between the two mobiles at each trajectory point are available. To obtain an additional set of measurements between the mobiles, the direction of trajectory 2 has been reversed in the monostatic run.

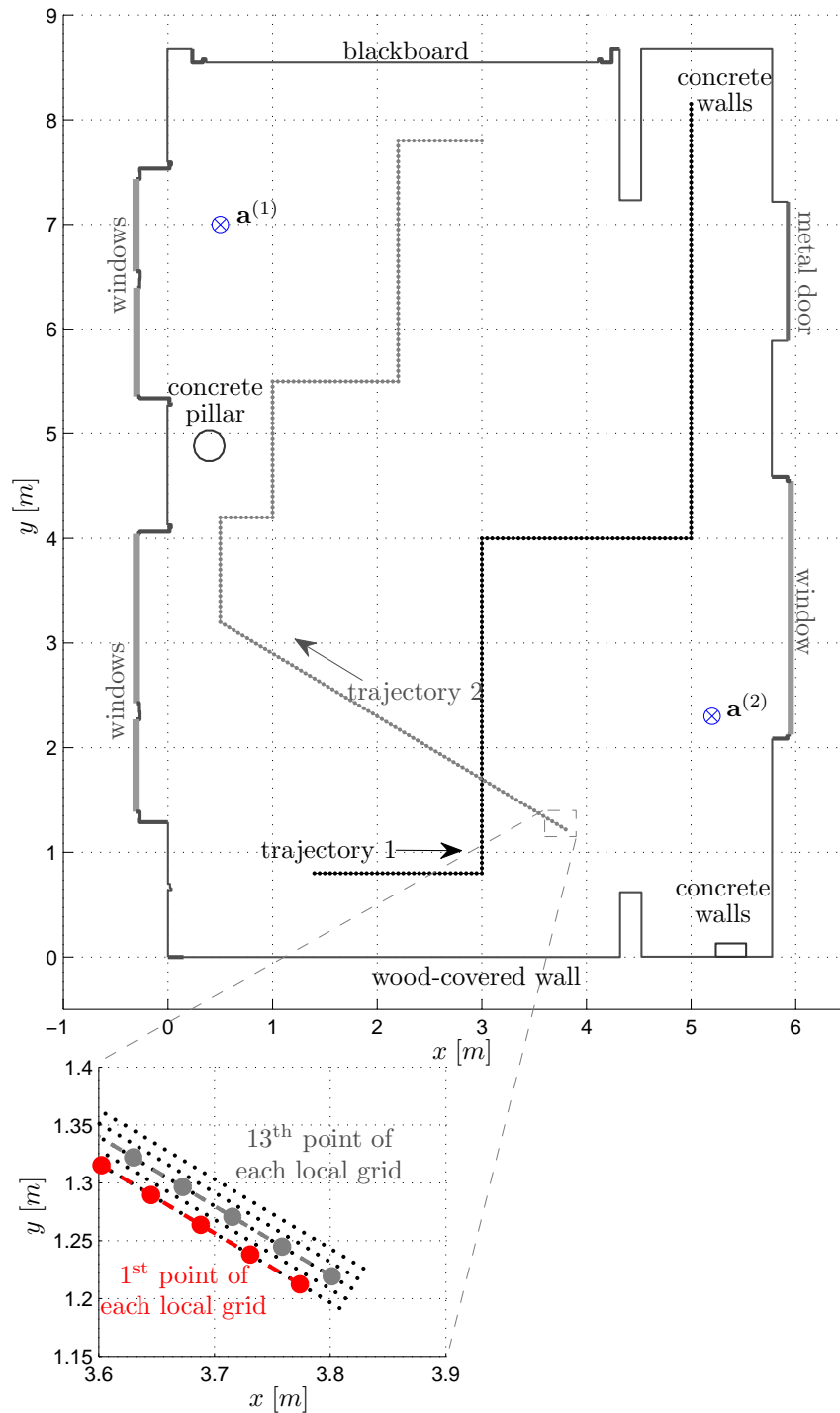


Figure A.6: Medium-scale measurement scenario in a seminar room of the laboratory. In this scenario, two anchors are available. Two different measurement setups are used: 1) Two trajectories with 220 points each, spaced by 5 cm, and 2) measurements within a local grids around each of the points of the two trajectories with 1 cm spacing. As the zoom plot on the bottom shows, this e.g. enables 25 parallel test trajectories or allows for spatial averaging for each trajectory point.

Local Grid Measurements – M-sequence Radar

To enable a detailed local channel analysis for the two trajectories, grid measurements have been performed around them. Due to the large number of points, these have been obtained with the M-sequence radar, since it allows for much faster measurement times. Around each of the trajectory points, 5×5 points have been used with a spacing of 1 cm, hence in total, 11000 points



(a) Seminarroom scenario

(b) Monostatic setup

Figure A.7: Photo of Seminarroom scenario, view from the lower-left corner in Fig. A.6.

are available. As can be seen in the lower plot of Fig. A.6, this allows for e.g. 25 parallel test trajectories for tracking algorithms or to have multiple measurements around one point. The 13-th point of each local grid, i.e. the center point, corresponds to the respective measurement point in the trajectory measurements.

A.5.2 Demonstration Room at Graz University of Technology

In this room of our university, shown in Fig. A.8, two trajectories have been measured with the M-sequence radar. Trajectory 1 consists of 101 points, trajectory 2 of 235 points, each of them is spaced by 5 cm. The coin antennas were used for all anchors and mobiles.

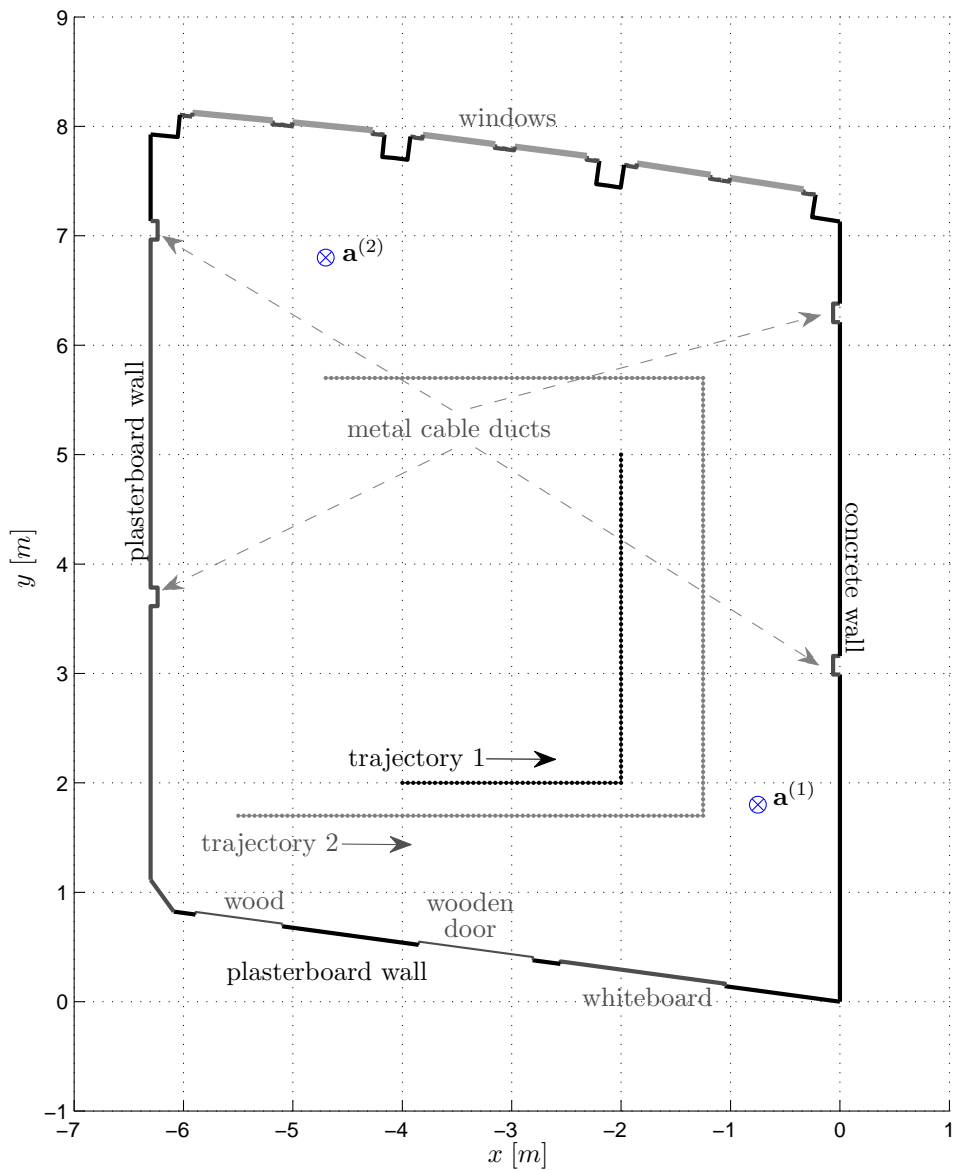


Figure A.8: Medium-scale measurement scenario in a room (called the demonstration room) of the laboratory. In this scenario, two anchors are available and two trajectories with 101 and 235 points, respectively, spaced by 5 cm.

A.5.3 Demonstration Room at Montbeliard, France

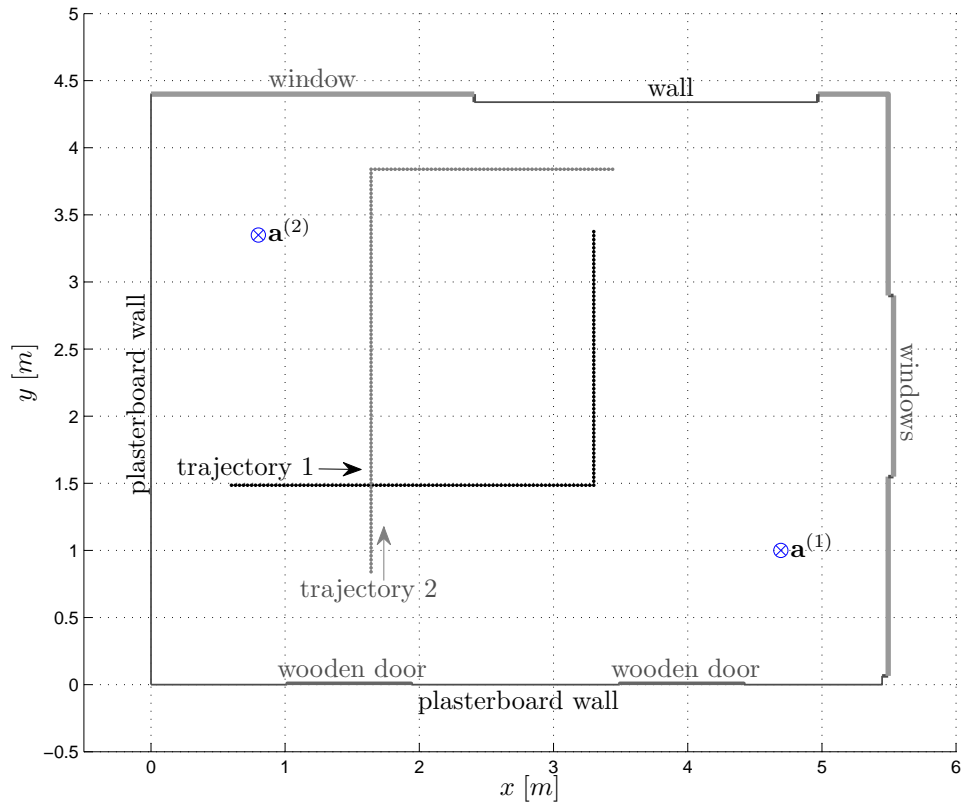


Figure A.9: Medium-scale measurement scenario in a room (called the IPIN room) of the university in Montbeliard, France. In this scenario, two anchors are available and two trajectories with 154 and 161 points, respectively, spaced by 3 cm.

In this room of the university in Montbeliard, France, shown in Fig. A.9, two trajectories have been measured with the M-sequence radar. Trajectory 1 consists of 154 points, trajectory 2 of 161 points, each of them is spaced by 3 cm. The coin antennas were used for all anchors and mobiles.

A.6 Small-Scale Environment – Laboratory Room

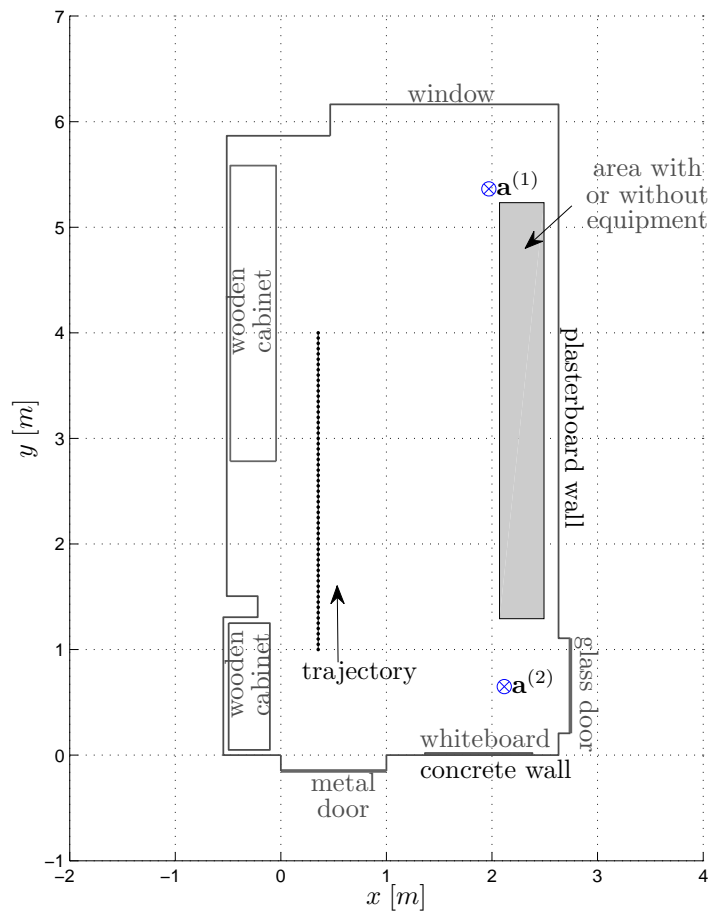


Figure A.10: Small-scale measurement scenario in a laboratory room. In this scenario, two anchors are available and one trajectory with 60 points, spaced by 5 cm. In this scenario, the measurements have been done with the laboratory room rather empty, and once with all the measurement equipment in the room (mostly on tables within the gray area).

In this laboratory room of our university, shown in Fig. A.10, test measurements were obtained with the VNA on a short trajectory of 60 points spaced by 5 cm. We have performed these measurements once with a rather empty room, and once with all the (mostly metallic) measurement equipment in it, see Fig. A.11. This is useful for the analysis of DM.



(a) Empty



(b) Full

Figure A.11: Photo of Laboratory room scenario, view from the metal door at the lower side in Fig. A.10.

B

Modeling of Floor Plan Uncertainties

The geometric prior information that is taken into account in this work contains the floor plan and the positions of the anchor nodes. Both are subject to measurement uncertainties. The floor plan consists of a list of end points of the wall segments. We take the simplifying assumption that these end points and the anchor positions are independent random variables

$$\mathbf{p}_i = \mathbf{p}_{i,\text{true}} + \boldsymbol{\eta}_i, \quad \boldsymbol{\eta}_i \sim \mathcal{N}(\boldsymbol{\eta}_i; \mathbf{0}, \sigma_{\text{FP}}^2 \mathbf{I}) \quad (\text{B.1})$$

$$\mathbf{a}_1^{(j)} = \mathbf{a}_{1,\text{true}}^{(j)} + \boldsymbol{\eta}_a, \quad \boldsymbol{\eta}_a \sim \mathcal{N}(\boldsymbol{\eta}_a; \mathbf{0}, \sigma_a^2 \mathbf{I}), \quad (\text{B.2})$$

where i is used as index for the wall end points. However, since we are interested in the uncertainties of the coordinates of some VA $\mathbf{a}_k^{(q,j)}$, a relationship to the uncertain floor plan entries is necessary. Any point \mathbf{p} on the i -th wall segment is defined by its end points \mathbf{p}_i and $\mathbf{p}_{i'}$ as

$$\mathbf{p} = \mathbf{p}_i + t(\mathbf{p}_{i'} - \mathbf{p}_i), \quad t \in [0, 1]. \quad (\text{B.3})$$

This also holds for the mirror point \mathbf{p}_m in (2.7), but without the restriction on t , since \mathbf{p}_m can lie outside of the wall segment (see Fig. 2.2). The specific mirror point \mathbf{p}_m for the j -th anchor w.r.t. the i -th wall in (2.7) can be found using

$$t_i^{(j)} = \left(\mathbf{a}_1^{(j)} - \mathbf{p}_i \right)^T (\mathbf{p}_{i'} - \mathbf{p}_i). \quad (\text{B.4})$$

Hence, the distribution of $t_i^{(j)}$ will be non-Gaussian and depends on all involved points. To obtain a tractable, Gaussian model for $\mathbf{a}_k^{(q,j)}$, we neglect this and treat $t_i^{(j)}$ as deterministic and constant. The covariance matrix of the coordinates of a first-order VA $\mathbf{a}_k^{(1,j)}$ can then be written using (2.7) as

$$\text{cov}\left\{ \mathbf{a}_k^{(1,j)} \right\} = \sigma_{\mathbf{a}_k}^2 \mathbf{I} = 4 \text{cov}\{\mathbf{p}_m\} + \text{cov}\left\{ \mathbf{a}_1^{(j)} \right\}. \quad (\text{B.5})$$

Using (B.1), (B.3) and (B.4), the covariance matrix of the mirror point \mathbf{p}_m is given as

$$\text{cov}\{\mathbf{p}_m\} = \text{cov}\left\{(t_i^{(j)} - 1)\mathbf{p}_i\right\} + \text{cov}\left\{t_i^{(j)}\mathbf{p}_i'\right\} \quad (\text{B.6})$$

$$= \sigma_{\text{FP}}^2 \mathbf{I}(2t_i^{(j)2} - 2t_i^{(j)} + 1) \quad (\text{B.7})$$

$$= \sigma_{\text{FP}}^2 \mathbf{I}\gamma_i^{(j)} \quad (\text{B.8})$$

where $\gamma_i^{(j)}$ is a mirroring coefficient describing the mirroring of the j -th (virtual) anchor with respect to the i -th wall. Fig. B.1 shows $\gamma_i^{(j)}$ as a function of $t_i^{(j)}$. Together with (B.8) it can be seen that if $t_i^{(j)} = 1$ or $t_i^{(j)} = 0$, the uncertainty reduces to the one of the respective wall segment point. For $|t_i^{(j)}| > 1$ it takes into account that the uncertainty of the mirror point can be much larger depending on the distance to the measured points.

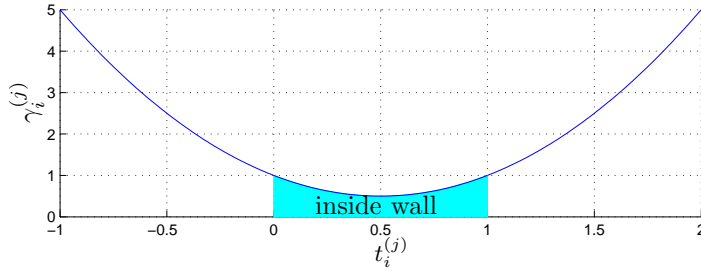


Figure B.1: Wall mirroring coefficient $\gamma_i^{(j)}$ in dependence of the parameter $t_i^{(j)}$ for mirroring anchor $\mathbf{a}_1^{(j)}$ w.r.t. the i -th wall. The region where the anchor is inside the wall segment is indicated.

Using (B.5), (B.8) and (2.7) to obtain higher-order VAs, the covariance matrix of the coordinates of a VA of arbitrary order q can be written as

$$\text{cov}\left\{\mathbf{a}_k^{(q,j)}\right\} = \mathbf{I} \left[4\sigma_{\text{FP}}^2 \sum_{i=1}^q \gamma_i^{(j)} + \sigma_a^2 \right]. \quad (\text{B.9})$$

To obtain a model for the corresponding uncertainty of the distance to the VA, we make the observation that under the assumption of a circular symmetric Gaussian distribution for the VA position, this distance follows a Ricean distribution. Under the additional assumption that this distance is significantly larger than the standard deviation of the VA position³⁹, the K-factor of this Rice distribution will be large. Hence, the distribution of the distance $d(\mathbf{a}_k^{(q,j)}, \mathbf{p}_\ell)$ can be approximated with a Gaussian distribution with a mean equal to the true distance and a variance according to (B.9).

Two examples for this model using Monte Carlo simulations with $N = 10^5$ samples are shown in Fig. B.2 for VAs up to order 3 with $\sigma_{\text{FP}} = 0.05$ m and $\sigma_a = 0.04$ m. Two horizontal walls a y -coordinates of 0 m and 2 m are used. Cyan point clouds indicate the Monte Carlo samples obtained using the models (B.1) and (B.2) and the mirroring operation. The three-standard-deviation circles of the model according to (B.9) are shown in black. For Fig. B.2a, the anchor at $\mathbf{a}_1^{(j)}$ is horizontally placed inside the wall segments, while for Fig. B.2b, it is horizontally placed outside of the lower wall and at the edge of the upper wall.

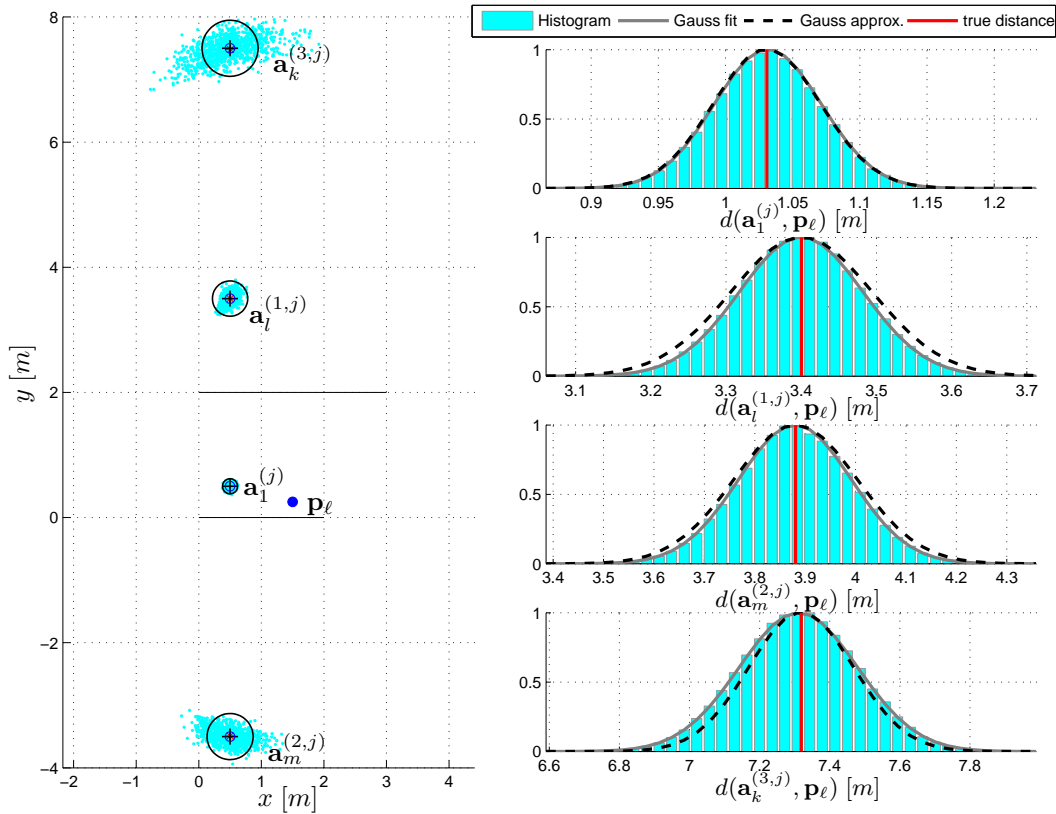
Although it is clearly visible that the distribution of the VA positions is not circular symmetric Gaussian, for low VA orders the approximation in (B.9) is suitable. The Gaussian approximation for the distance to the VAs, indicated on the right side by the black dashed curve, also seems reasonable compared to the cyan histograms.

For Fig. B.2a, the corresponding mirror coefficient is less than one. In this case, the models for

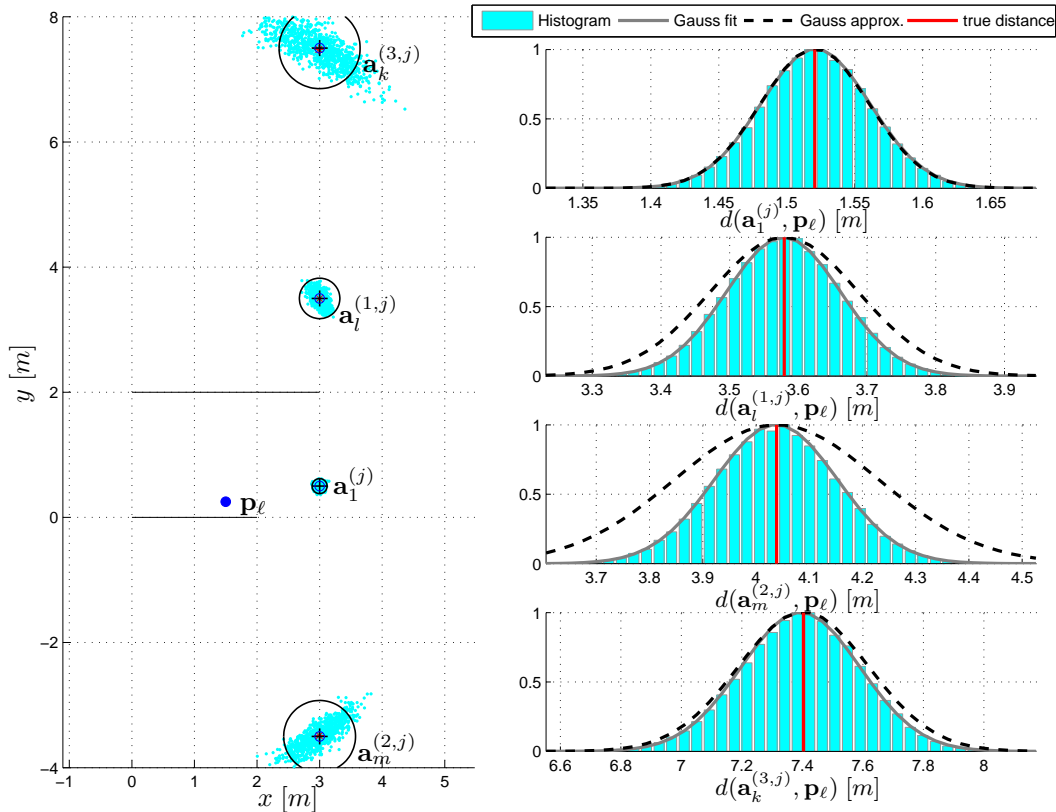
³⁹ This assumption is justified by the fact that most VAs are at least outside of the room.

position and distance are reasonable. In the second example shown in Fig. B.2b, the mirroring causes a more severe deviation from the circular symmetry. The Gaussian approximation of the corresponding distances is thus not accurate, especially for lower-order VAs. If the distance to the VA is large enough, such as for the third-order VA indicated, the large distance seems to outweigh this discrepancy and the model is reasonable again.

Despite its simplicity, this model gives an indication of the variance of VAs, caused by floor plan uncertainties and the mirroring. It can be used e.g. in tracking schemes that also incorporate the VAs as initialization.



(a) Anchor at $\mathbf{a}^{(j)}$ is inside of two horizontal walls, such that the corresponding $\gamma_i^{(j)} < 1$.



(b) Anchor at $\mathbf{a}^{(j)}$ is outside of one of two horizontal walls, such that the corresponding $\gamma_i^{(j)} > 1$.

Figure B.2: Monte Carlo simulation of VA uncertainty model. The anchor at $\mathbf{a}_1^{(j)}$ is between the inside parts of two horizontal walls, such that the corresponding $\gamma_i^{(j)} < 1$. Left plot shows the floor plan together with the samples for the VAs. The isotropic Gaussian model is illustrated with a circle indicating three standard deviations. Right plot shows histograms, Gaussian fit and Gaussian approximation for the corresponding distances.

Bibliography

- [1] Counting Crows, “August and Everything After,” 1993, copyright: Geffen Records.
- [2] Bob Dylan, “Bringing It All Back Home,” 1965, copyright: Columbia Records.
- [3] Pink Floyd, “Meddle,” 1971, copyright: Harvest, EMI.
- [4] B. Hoffman-Wellenhof, K. Legat, and M. Wieser, *Navigation – Principles of Positioning and Guidance*. Springer, 2003.
- [5] R. Mautz, “Overview of Current Indoor Positioning Systems,” *Geodesy and Cartography*, vol. 35, pp. 18–22, 2009.
- [6] —, “Indoor Positioning Technologies,” Habilitation Thesis, ETH Zurich, 2012.
- [7] D. Schneider, “New Indoor Navigation Technologies Work Where GPS Can’t,” *IEEE Spectrum*, 2013.
- [8] H. Liu, H. Darabi, P. Banerjee, and J. Liu, “Survey of wireless indoor positioning techniques and systems,” *IEEE Transactions on Systems, Man, and Cybernetics, Part C: Applications and Reviews*, vol. 37, no. 6, pp. 1067–1080, 2007.
- [9] Y. Gu, A. Lo, and I. Niemegeers, “A survey of indoor positioning systems for wireless personal networks,” *IEEE Communications Surveys Tutorials*, vol. 11, no. 1, pp. 13–32, 2009.
- [10] D. Dardari, E. Falletti, and M. Luise, *Satellite and Terrestrial Radio Positioning Techniques - A signal processing perspective*. Elsevier Academic Press, 2012.
- [11] C. Rüdiger, “The Impact of Clock Offset on Multipath-assisted Indoor Localization,” Master’s thesis, Graz University of Technology, 2014.
- [12] J. Andersen, J. Nielsen, G. Pedersen, G. Bauch, and M. Herdin, “Room electromagnetics,” *Antennas and Propagation Magazine, IEEE*, vol. 49, no. 2, pp. 27–33, apr. 2007.
- [13] R. Liepins, “Acoustic Source Localization with a Single Microphone using Reflected Signals,” Master’s thesis, Graz University of Technology, 2014.
- [14] D. Dardari, A. Conti, U. Ferner, A. Giorgetti, and M. Z. Win, “Ranging With Ultrawide Bandwidth Signals in Multipath Environments,” *Proceedings of the IEEE*, 2009.
- [15] D. Arnitz, “Tag Localization in Passive UHF RFID,” Ph.D. dissertation, Graz University of Technology, 2011.
- [16] S. Mazuelas, A. Bahillo, R. Lorenzo, P. Fernandez, F. Lago, E. Garcia, J. Blas, and E. Abril, “Robust Indoor Positioning Provided by Real-Time RSSI Values in Unmodified WLAN Networks,” *IEEE Journal of Selected Topics in Signal Processing*, vol. 3, no. 5, pp. 821–831, Oct 2009.
- [17] Z. Sahinoglu, S. Gezici, and I. Guvenc, *Ultra-wideband Positioning Systems – Theoretical Limits, Ranging Algorithms and Protocols*. Cambridge University Press, 2008.
- [18] S. Gezici and H. Poor, “Position estimation via ultra-wide-band signals,” *Proceedings of the IEEE*, vol. 97, no. 2, pp. 386–403, feb. 2009.
- [19] A. F. Molisch, “Ultra-Wide-Band Propagation Channels,” *Proceedings of the IEEE*, vol. 97, no. 2, pp. 353–371, Feb. 2009.
- [20] V. Renaudin, V. Demeule, and M. Ortiz, “Adaptative Pedestrian Displacement Estimation with a Smartphone for Free Inertial Navigation,” in *IEEE International Conference on Indoor Positioning and Indoor Navigation*, 2013.
- [21] J. Jahn, U. Batzer, J. Seitz, L. Patino-Studencka, and J. Gutierrez Boronat, “Comparison and evaluation of acceleration based step length estimators for handheld devices,” in *2010 International Conference on Indoor Positioning and Indoor Navigation (IPIN)*, 2010, pp. 1–6.
- [22] I. Skog, P. Handel, J.-O. Nilsson, and J. Rantakokko, “Zero-Velocity Detection - An Algorithm Evaluation,” *IEEE Transactions on Biomedical Engineering*, vol. 57, no. 11, pp. 2657–2666, Nov 2010.
- [23] F. Gustafsson and F. Gunnarsson, “Mobile positioning using wireless networks: possibilities and fundamental limitations based on available wireless network measurements,” *Signal Processing Magazine, IEEE*, vol. 22, no. 4, pp. 41–53, 2005.

- [24] K. Subbu, C. Zhang, J. Luo, and A. Vasilakos, "Analysis and status quo of smartphone-based indoor localization systems," *IEEE Wireless Communications*, vol. 21, no. 4, pp. 106–112, August 2014.
- [25] G. Kaupins and R. Minch, "Legal and Ethical Implications of Employee Location Monitoring," in *Proceedings of the 38th Annual Hawaii International Conference on System Sciences (HICSS)*, 2005.
- [26] J. Karedal, S. Wyne, P. Almers, F. Tufvesson, and A. Molisch, "A Measurement-Based Statistical Model for Industrial Ultra-Wideband Channels," *IEEE Transactions on Wireless Communications*, vol. 6, no. 8, pp. 3028–3037, 2007.
- [27] Y. Shen and M. Win, "On the Use of Multipath Geometry for Wideband Cooperative Localization," in *IEEE Global Telecommunications Conference (GLOBECOMM)*, 2009.
- [28] H. Lu, S. Mazuelas, and M. Win, "Ranging likelihood for wideband wireless localization," in *IEEE International Conference on Communications (ICC)*, 2013.
- [29] F. Montorsi, S. Mazuelas, G. Vitetta, and M. Z. Win, "On the Performance Limits of Map-Aware Localization," *IEEE Transactions on Information Theory*, no. 8, Aug 2013.
- [30] H. Wymeersch, J. Lien, and M. Z. Win, "Cooperative localization in wireless networks," *Proceedings of the IEEE*, vol. 97, no. 2, pp. 427–450, Feb. 2009.
- [31] C. Steiner and A. Wittneben, "Low Complexity Location Fingerprinting With Generalized UWB Energy Detection Receivers," *IEEE Transactions on Signal Processing*, 2010.
- [32] —, "Efficient Training Phase for Ultrawideband-Based Location Fingerprinting Systems," *IEEE Transactions on Signal Processing*, vol. 59, no. 12, pp. 6021–6032, 2011.
- [33] L. Zwirello, T. Schipper, M. Harter, and T. Zwick, "UWB Localization System for Indoor Applications: Concept, Realization and Analysis," *Journal of Electrical and Computer Engineering*, 2012.
- [34] S. Gezici, Z. Tian, G. B. Giannakis, H. Kobayashi, A. F. Molisch, H. V. Poor, and Z. Sahinoglu, "Localization via Ultra-Wideband Radios: A Look at Positioning Aspects for Future Sensor Networks," *IEEE Signal Processing Magazine*, vol. 22, no. 4, pp. 70–84, Jul. 2005.
- [35] T. Gigl, F. Troesch, J. Preishuber-Pfluegl, and K. Witrisal, "Maximal operating distance estimation for ranging in IEEE 802.15.4a Ultra Wideband," in *7th Workshop on Positioning, Navigation and Communication (WPNC)*, March 2010, pp. 10–18.
- [36] N. Decarli, D. Dardari, S. Gezici, and A. D'Amico, "LOS/NLOS detection for UWB signals: A comparative study using experimental data," in *5th IEEE International Symposium on Wireless Pervasive Computing (ISWPC)*, 2010, pp. 169–173.
- [37] I. Guvenc, C. Chia-Chin, F. Watanabe, and H. Inamura, "NLOS Identification and Weighted Least-Squares Localization for UWB Systems Using Multipath Channel Statistics," *EURASIP J. Adv. Signal Process.*, 2007.
- [38] H. Wymeersch, S. Marano, W. Gifford, and M. Win, "A Machine Learning Approach to Ranging Error Mitigation for UWB Localization," *IEEE Transactions on Communications*, vol. 60, pp. 1719–1728, 2012.
- [39] S. Marano and W. Gifford, H. Wymeersch, and M. Win, "NLOS identification and mitigation for localization based on UWB experimental data," *IEEE Journal on Selected Areas in Communications*, vol. 28, no. 7, pp. 1026–1035, 2010.
- [40] Y. Qi, H. Kobayashi, and H. Suda, "Analysis of wireless geolocation in a non-line-of-sight environment," *IEEE Transactions on Wireless Communications*, vol. 5, no. 3, pp. 672–681, 2006.
- [41] Y. Qi, "Wireless geolocation in a non-line-of-sight environment," Ph.D. dissertation, Princeton University, 2003.
- [42] Y. Shen and M. Z. Win, "Fundamental Limits of Wideband Localization - Part I: A General Framework," *IEEE Transactions on Information Theory*, 2010.
- [43] Y. Shen, H. Wymeersch, and M. Win, "Fundamental Limits of Wideband Localization - Part II: Cooperative Networks," *IEEE Transactions on Information Theory*, no. 10, 2010.
- [44] H. Godrich, A. Haimovich, and R. Blum, "Target Localization Accuracy Gain in MIMO Radar-Based Systems," *IEEE Transactions on Information Theory*, vol. 56, no. 6, pp. 2783–2803, June 2010.
- [45] N. Decarli, F. Guidi, and D. Dardari, "A Novel Joint RFID and Radar Sensor Network for Passive Localization: Design and Performance Bounds," *IEEE Journal of Selected Topics in Signal Processing*, 2014.
- [46] Y. Shen, S. Mazuelas, and M. Win, "Network Navigation: Theory and Interpretation," *IEEE Journal on Selected Areas in Communications*, 2012.
- [47] F. Ribeiro, D. Ba, C. Zhang, and D. Florencio, "Turning enemies into friends: Using reflections to improve sound source localization," in *IEEE International Conference on Multimedia and Expo (ICME)*, 2010, pp. 731–736.
- [48] Y. Kuang, K. Astrom, and F. Tufvesson, "Single antenna anchor-free UWB positioning based on multipath propagation," in *IEEE International Conference on Communications (ICC)*, 2013.

- [49] R. Parhizkar, I. Dokmanic, and M. Vetterli, "Single-Channel Indoor Microphone Localization," in *39th International Conference on Acoustics, Speech, and Signal Processing*, 2014.
- [50] O. Oecal, I. Dokmanic, and M. Vetterli, "Source Localization and Tracking in Non-Convex Rooms," in *39th International Conference on Acoustics, Speech, and Signal Processing*, 2014.
- [51] P. Svaizer, A. Brutti, and M. Omologo, "Use of reflected wavefronts for acoustic source localization with a line array," in *Joint Workshop on Hands-free Speech Communication and Microphone Arrays (HSCMA)*, 2011.
- [52] M. Leigsnering, M. Amin, F. Ahmad, and A. Zoubir, "Multipath Exploitation and Suppression for SAR Imaging of Building Interiors: An overview of recent advances," *IEEE Signal Processing Magazine*, vol. 31, no. 4, pp. 110–119, July 2014.
- [53] I. Dokmanic, R. Parhizkar, A. Walther, Y. M. Lu, and M. Vetterli, "Acoustic Echoes Reveal Room Shape," *Proceedings of the National Academy of Sciences*, 2013.
- [54] J. Kietlinski-Zaleski, "Ultra-Wideband Positioning using Reflections from Known Indoor Features," Ph.D. dissertation, Nagoya University, Japan, 2011.
- [55] J. Kietlinski-Zaleski, T. Yamazato, and M. Katayama, "Tdoa UWB positioning with three receivers using known indoor features," in *Ultra-Wideband (ICUWB), 2010 IEEE International Conference on*, vol. 2, 2010, pp. 1–4.
- [56] K. Papakonstantinou and D. Slock, "Direct Location Estimation using Single-Bounce NLOS Time-Varying Channel Models," in *Vehicular Technology Conference, 2008. VTC 2008-Fall. IEEE 68th*, 21-24 2008, pp. 1–5.
- [57] U. Hammes and A. Zoubir, "Robust Mobile Terminal Tracking in NLOS Environments Based on Data Association," *IEEE Transactions on Signal Processing*, vol. 58, no. 11, pp. 5872–5882, 2010.
- [58] V. La Tosa, B. Denis, and B. Uguen, "Maximum Averaged Likelihood Estimation Tree for Anchor-Less Localization Exploiting IR-UWB Multipaths," in *IEEE 71st Vehicular Technology Conference (VTC)*, 2010.
- [59] —, "Joint Anchor-less Tracking and Room Dimensions Estimation through IR-UWB Peer-to-peer Communications," in *IEEE International Conference on Ultra-Wideband (ICUWB)*, 2011.
- [60] M. des Noes and B. Denis, "Benefits from cooperation in simultaneous anchor-less tracking and room mapping based on Impulse Radio - Ultra Wideband devices," in *International Conference on Systems, Signals and Image Processing (IWSSIP)*, April 2012, pp. 17–21.
- [61] C. Gentner and T. Jost, "Indoor positioning using time difference of arrival between multipath components," in *International Conference on Indoor Positioning and Indoor Navigation (IPIN)*, Oct 2013, pp. 1–10.
- [62] C. Steiner, "Location fingerprinting for ultra-wideband systems," Ph.D. dissertation, ETH Zurich, 2010.
- [63] T. Deissler and J. Thielecke, "UWB SLAM with Rao-Blackwellized Monte Carlo data association," in *Indoor Positioning and Indoor Navigation (IPIN), 2010 International Conference on*, sept. 2010, pp. 1–5.
- [64] E. Leitinger, P. Meissner, C. Rüdissler, G. Dumphart, and K. Witrissal, "Evaluation of Position-related Information in Multipath Components for Indoor Positioning," *IEEE Journal on Selected Areas in Communications*, 2014, revised.
- [65] G. Dumphart, "Performance Bounds for Anchorless Cooperative Indoor Localization Exploiting Multipath," Master's thesis, Graz University of Technology, 2014.
- [66] M. Froehle, E. Leitinger, P. Meissner, and K. Witrissal, "Cooperative Multipath-Assisted Indoor Navigation and Tracking (Co-MINT) Using UWB Signals," in *IEEE ICC Workshop on Advances in Network Localization and Navigation (ANLN)*, Budapest, Hungary, 2013.
- [67] S. Van de Velde, H. Wymeersch, P. Meissner, K. Witrissal, and H. Steendam, "Cooperative Multipath-Aided Indoor Localization," in *2012 IEEE Wireless Communications and Networking Conference: Mobile and Wireless Networks (IEEE WCNC 2012)*, Paris, France, 2012.
- [68] A. Conti, D. Dardari, M. Guerra, L. Mucchi, and M. Win, "Experimental Characterization of Diversity Navigation," *IEEE Systems Journal*, 2014.
- [69] A. Conti, M. Guerra, D. Dardari, N. Decarli, and M. Win, "Network Experimentation for Cooperative Localization," *IEEE Journal on Selected Areas in Communications*, vol. 30, no. 2, pp. 467–475, 2012.
- [70] B. Denis, R. Raulefs, B. Fleury, B. Uguen, N. Amiot, L. de Celis, J. Dominguez, M. Koldsgaard, M. Laaraiedh, H. Nouredine, E. Staudinger, and G. Steinboeck, "Cooperative and heterogeneous indoor localization experiments," in *IEEE International Conference on Communications Workshops (ICC)*, 2013.
- [71] Microsoft Research, "Microsoft Indoor Localization Competition at IPSN 2014," ACM/IEEE International Conference on Information Processing in Sensor Networks, 2014, accessed at Sep. 1, 2014. [Online]. Available: <http://research.microsoft.com/en-us/events/ipsn2014indoorlocalizationcompetition/>

- [72] Evarilos, "Evaluation of RF-Based Indoor Localization Solution for the Future Internet," accessed at Sep. 1, 2014. [Online]. Available: <http://www.evarilos.eu/index.php>
- [73] A. Richter, "Estimation of Radio Channel Parameters: Models and Algorithms," Ph.D. dissertation, Technische Universitaet Illmenau, 2005.
- [74] A. Richter and R. Thoma, "Joint maximum likelihood estimation of specular paths and distributed diffuse scattering," in *Vehicular Technology Conference, VTC 2005-Spring*, vol. 1, May 2005, pp. 11–15 Vol. 1.
- [75] T. Santos, F. Tufvesson, and A. Molisch, "Modeling the Ultra-Wideband Outdoor Channel: Model Specification and Validation," *IEEE Transactions on Wireless Communications*, pp. 1987–1997, 2010.
- [76] N. Michelusi, U. Mitra, A. Molisch, and M. Zorzi, "Uwb Sparse/Diffuse Channels, Part I: Channel Models and Bayesian Estimators," *IEEE Transactions on Signal Processing*, vol. 60, no. 10, pp. 5307–5319, Oct 2012.
- [77] V. Degli-Esposti, F. Fuschini, E. M. Vitucci, and G. Falciasecca, "Measurement and Modelling of Scattering From Buildings," *Antennas and Propagation, IEEE Transactions on*, pp. 143–153, Jan. 2007.
- [78] P. Meissner, E. Leitinger, M. Lafer, and K. Witrissal, "MeasureMINT UWB database," www.spsc.tugraz.at/tools/UWBmeasurements, 2013, Publicly available database of UWB indoor channel measurements. [Online]. Available: www.spsc.tugraz.at/tools/UWBmeasurements
- [79] P. Meissner, C. Steiner, and K. Witrissal, "UWB Positioning with Virtual Anchors and Floor Plan Information," in *Proc. 7th Workshop on Positioning, Navigation and Communication, WPNC 2010*, Dresden, Germany, 2010.
- [80] M. Gan, P. Meissner, F. Mani, E. Leitinger, M. Froehle, C. Oestges, K. Witrissal, and T. Zemen, "Low-Complexity Sub-band Divided Ray Tracing for UWB Indoor Channels," in *IEEE Wireless Communications and Networking Conference (WCNC)*, Istanbul, Turkey, 2014.
- [81] P. Meissner, M. Lafer, E. Leitinger, and K. Witrissal, "Multipath-Assisted Indoor Navigation and Tracking," Live Demonstration at International Conference on Indoor Positioning and Indoor Navigation, IPIN, Montbéliard, France, 2013.
- [82] M. Froehle, P. Meissner, T. Gigl, and K. Witrissal, "Scatterer and Virtual Source Detection for Indoor UWB Channels," in *2011 IEEE International Conference on Ultra-Wideband (ICUWB 2011)*, Bologna, Italy, 2011.
- [83] T. Santos, J. Karedal, P. Almers, F. Tufvesson, and A. Molisch, "Scatterer detection by successive cancellation for uwb - method and experimental verification," in *Vehicular Technology Conference, 2008. VTC Spring 2008. IEEE*, may 2008, pp. 445–449.
- [84] —, "Modeling the ultra-wideband outdoor channel: Measurements and parameter extraction method," *IEEE Transactions on Wireless Communications*, vol. 9, no. 1, pp. 282–290, Jan. 2010.
- [85] M. Froehle, P. Meissner, and K. Witrissal, "Tracking of UWB Multipath Components Using Probability Hypothesis Density Filters," in *2012 IEEE International Conference on Ultra-Wideband (ICUWB 2012)*, Syracuse, USA, 2012.
- [86] B. Fleury, M. Tschudin, R. Heddergott, D. Dahlhaus, and K. Ingeman Pedersen, "Channel parameter estimation in mobile radio environments using the SAGE algorithm," *IEEE Journal on Selected Areas in Communications*, vol. 17, no. 3, pp. 434–450, 1999.
- [87] K. Hausmair, K. Witrissal, P. Meissner, C. Steiner, and G. Kail, "SAGE Algorithm for UWB Channel Parameter Estimation," in *COST 2100 Management Committee Meeting*, Athens, Greece, 2010.
- [88] M. Gan, P. Meissner, F. Mani, E. Leitinger, M. Froehle, C. Oestges, K. Witrissal, and T. Zemen, "Calibration of Indoor UWB Sub-band Divided Ray Tracing Using Multiobjective Simulated Annealing," in *IEEE International Conference on Communications (ICC)*, Sydney, Australia, 2014.
- [89] G. Steinböck, T. Pedersen, M. Gan, T. Zemen, P. Meissner, E. Leitinger, and K. Witrissal, "Preliminary Hybrid Model For Reverberant Indoor Radio Channels," in *10th MC Meeting of COST Action IC1004*, Aalborg, Denmark, 2014.
- [90] E. Leitinger, P. Meissner, M. Froehle, and K. Witrissal, "Performance Bounds for Multipath-assisted Indoor Localization on Backscatter Channels," in *IEEE Radar Conference*, 2014.
- [91] K. Witrissal, E. Leitinger, P. Meissner, and D. Arnitz, "Cognitive Radar for the Localization of RFID Transponders in Dense Multipath Environments," in *IEEE Radar Conference*, Ottawa, Canada, 2013.
- [92] E. Leitinger, M. Froehle, P. Meissner, and K. Witrissal, "Multipath-Assisted Maximum-Likelihood Indoor Positioning using UWB Signals," in *IEEE ICC Workshop on Advances in Network Localization and Navigation (ANLN)*, 2014.
- [93] T. Gigl, P. Meissner, J. Preishuber-Pfluegl, and K. Witrissal, "Ultra-Wideband System-Level Simulator for Positioning and Tracking (U-SPOT)," in *Proc. 2010 International Conference on Indoor Positioning and Indoor Navigation, IPIN, Zurich*, 2010.
- [94] M. Froehle, "Multi-target Tracking for UWB Channels Using PHD Filters," Master's thesis, Graz University of Technology, 2011.

- [95] M. Lafer, “Real-Time Multipath-Assisted Indoor Tracking and Feature Detection,” Master’s thesis, Graz University of Technology, 2014.
- [96] J. Kunisch and J. Pamp, “An ultra-wideband space-variant multipath indoor radio channel model,” in *IEEE Conference on Ultra Wideband Systems and Technologies*, 2003.
- [97] J. B. Allen and D. A. Berkley, “Image Method for efficiently simulating Small-Room Acoustics,” *J. Acoust. Soc. Am.*, 1979.
- [98] B. M. Gibbs and D. K. Jones, “A Simple Image Method for Calculating the Distribution of Sound Pressure Levels within an Enclosure,” *Acta Acustica united with Acustica*, vol. 26, no. 1, pp. 24–32, 1972.
- [99] J. Borish, “Extension of the image model to arbitrary polyhedra,” *The Journal of the Acoustical Society of America*, vol. 75, no. 6, pp. 1827–1836, 1984.
- [100] A. Molisch, *Wireless Communications*. John Wiley & Sons, 2005.
- [101] P. Bello, “Characterization of Randomly Time-Variant Linear Channels,” *IEEE Transactions on Communications Systems*, vol. 11, no. 4, pp. 360–393, 1963.
- [102] G. L. Turin, “Communication through noisy, random-multipath channels,” Ph.D. dissertation, Massachusetts Institute of Technology, 1956.
- [103] G. Turin, F. Clapp, T. Johnston, S. Fine, and D. Lavry, “A statistical model of urban multipath propagation,” *IEEE Transactions on Vehicular Technology*, vol. 21, no. 1, pp. 1–9, Feb 1972.
- [104] S. O. Rice, “Statistical Properties of a Sine Wave Plus Random Noise,” *Bell System Technical Journal*, vol. 27, pp. 109–157, 1948.
- [105] “Multipath Propagation and Parameterization of its Characteristics,” Recommendation ITU-R P.1407, 2009.
- [106] D. Arnitz, U. Muehlmann, and K. Witrisal, “Wideband Characterization and Modeling of UHF RFID Channels for Ranging and Localization,” *IEEE Transactions on Antennas and Propagation*, vol. 60, no. 5, pp. 2491–2501, May 2012.
- [107] N. Amiot, M. Laaraiedh, and B. Uguen, “Pylayers: An open source dynamic simulator for indoor propagation and localization,” in *2013 IEEE International Conference on Communications Workshops (ICC)*, June 2013, pp. 84–88.
- [108] S. Kay, *Fundamentals of Statistical Signal Processing: Estimation Theory*. Prentice Hall Signal Processing Series, 1993.
- [109] H. Van Trees, *Detection, Estimation, and Modulation Theory, Part I*. John Wiley & Sons, 2001.
- [110] H. V. Poor, *An Introduction to Signal Detection and Estimation*. Springer, 1994.
- [111] F. van Diggelen, “Gnss Accuracy - Lies, Damn Lies and Statistics,” *GPS World*, vol. 18, no. 1, 2007.
- [112] R. B. Langley, “Dilution of Precision,” *GPS World*, May 1999.
- [113] F. Athley, “Threshold region performance of maximum likelihood direction of arrival estimators,” *IEEE Transactions on Signal Processing*, vol. 53, no. 4, pp. 1359–1373, April 2005.
- [114] Y. Shen and M. Win, “Effect of Path-Overlap on Localization Accuracy in Dense Multipath Environments,” in *IEEE International Conference on Communications (ICC)*, may 2008, pp. 4197–4202.
- [115] M. Win and R. Scholtz, “Characterization of ultra-wide bandwidth wireless indoor channels: A communication-theoretic view,” *IEEE Journal on Selected Areas in Communications*, vol. 20, no. 9, pp. 1613–1627, Dec. 2002.
- [116] L. Greenstein, D. Michelson, and V. Erceg, “Moment-method estimation of the Ricean K-factor,” *IEEE Communications Letters*, vol. 3, no. 6, pp. 175–176, June 1999.
- [117] L. Greenstein, S. Ghassemzadeh, V. Erceg, and D. Michelson, “Ricean K -Factors in Narrow-Band Fixed Wireless Channels: Theory, Experiments, and Statistical Models,” *IEEE Transactions on Vehicular Technology*, vol. 58, no. 8, pp. 4000–4012, Oct 2009.
- [118] C. Tepedelenlioglu, A. Abdi, G. Giannakis, and M. Kaveh, “Performance analysis of moment-based estimators for the K parameter of the Rice fading distribution,” in *IEEE International Conference on Acoustics, Speech, and Signal Processing (ICASSP)*, vol. 4, 2001, pp. 2521–2524 vol.4.
- [119] C. Tepedelenlioglu, A. Abdi, and G. Giannakis, “The Ricean K factor: estimation and performance analysis,” *IEEE Transactions on Wireless Communications*, vol. 2, no. 4, pp. 799–810, 2003.
- [120] T. Marzetta, “EM algorithm for estimating the parameters of a multivariate complex Rician density for polarimetric SAR,” in *International Conference on Acoustics, Speech, and Signal Processing (ICASSP)*, vol. 5, May 1995, pp. 3651–3654.
- [121] D. Simon, *Optimal State Estimation*, 1st ed. Wiley, 2006.

- [122] O. Cappe, S. Godsill, and E. Moulines, “An Overview of Existing Methods and Recent Advances in Sequential Monte Carlo,” *Proceedings of the IEEE*, vol. 95, no. 5, pp. 899–924, may 2007.
- [123] M. Arulampalam, S. Maskell, N. Gordon, and T. Clapp, “A tutorial on particle filters for online nonlinear/non-Gaussian Bayesian tracking,” *IEEE Transactions on Signal Processing*, vol. 50, no. 2, pp. 174–188, feb 2002.
- [124] X. Rong Li and V. Jilkov, “Survey of maneuvering target tracking. Part I. Dynamic models,” *IEEE Transactions on Aerospace and Electronic Systems*, vol. 39, no. 4, pp. 1333–1364, 2003.
- [125] Y. Bar-Shalom and T. Fortmann, *Tracking and Data Association*. Academic Press, 1988.
- [126] T. Bailey and H. Durrant-Whyte, “Simultaneous localization and mapping (SLAM): part II,” *Robotics Automation Magazine, IEEE*, vol. 13, no. 3, pp. 108–117, sept. 2006.
- [127] J. Leonard, R. Rikoski, P. Newman, and M. Bosse, “Mapping partially observable features from multiple uncertain vantage points,” *Intern. J. Robotics Research*, 2002.
- [128] D. Alspach and H. Sorenson, “Nonlinear Bayesian estimation using Gaussian sum approximations,” *IEEE Transactions on Automatic Control*, vol. 17, no. 4, pp. 439–448, Aug. 1972.
- [129] P. Georgiou, P. Tsakalides, and C. Kyriakakis, “Alpha-stable modeling of noise and robust time-delay estimation in the presence of impulsive noise,” *IEEE Transactions on Multimedia*, vol. 1, no. 3, pp. 291–301, sep. 1999.
- [130] G. Tsihrintzis and C. Nikias, “Incoherent receivers in alpha-stable impulsive noise,” *IEEE Transactions on Signal Processing*, vol. 43, no. 9, pp. 2225–2229, sep 1995.
- [131] T. S. Ferguson, “A Representation of the Symmetric Bivariate Cauchy Distribution,” *The Annals of Mathematical Statistics*, vol. 33, no. 4, pp. 1256–1266, 1962.
- [132] D. Schuhmacher, B.-T. Vo, and B.-N. Vo, “A Consistent Metric for Performance Evaluation of Multi-Object Filters,” *IEEE Transactions on Signal Processing*, 2008.
- [133] J. Munkres, “Algorithms for the Assignment and Transportation Problems,” *Journal of the Society for Industrial and Applied Mathematics*, vol. 5, no. 1, pp. pp. 32–38, 1957.
- [134] S. Thrun, W. Burgard, and D. Fox, *Probabilistic Robotics*. MIT, 2006.
- [135] T. Bailey, B. Upcroft, and H. Durrant-Whyte, “Validation Gating for Non-Linear Non-Gaussian Target Tracking,” in *9th International Conference on Information Fusion*, 2006.
- [136] I. Güvenç, C.-C. Chong, F. Watanabe, and H. Inamura, “Nlos identification and weighted least-squares localization for ubw systems using multipath channel statistics,” *EURASIP J. Adv. Signal Process*, vol. 2008, January 2008.
- [137] R. Buehrer, W. Davis, A. Safaai-Jazi, and D. Sweeney, “Ultra Wideband Propagation Measurements and Modeling – Final Report to DARPA NETEX Program,” Virginia Tech, Tech. Rep., 2004.
- [138] R.-R. Lao, J.-H. Tarng, and C. Hsiao, “Transmission coefficients measurement of building materials for UWB systems in 3–10 GHz,” in *57th Vehicular Technology Conference (VTC), 2003*, vol. 1, 2003, pp. 11–14 vol.1.
- [139] T. Pedersen, G. Steinbock, and B. Fleury, “Modeling of reverberant radio channels using propagation graphs,” *IEEE Transactions on Antennas and Propagation Magazine, IEEE*, vol. 60, no. 12, pp. 5978–5988, Dec 2012.
- [140] F. Mani, F. Quitin, and C. Oestges, “Directional Spreads of Dense Multipath Components in Indoor Environments: Experimental Validation of a Ray-Tracing Approach,” *IEEE Transactions on Antennas and Propagation*, pp. 3389–3396, July 2012.
- [141] T. Gigl, G. Janssen, V. Dizdarevic, K. Witrisal, and Z. Irahhtauten, “Analysis of a UWB Indoor Positioning System Based on Received Signal Strength,” in *4th Workshop on Positioning, Navigation and Communication (WPNC)*, march 2007, pp. 97–101.
- [142] G. Steinböck, T. Pedersen, B. Fleury, W. Wang, and R. Raulefs, “Distance Dependent Model for the Delay Power Spectrum of In-room Radio Channels,” *IEEE Transactions on Antennas and Propagation*, vol. 61, no. 8, pp. 4327–4340, Aug 2013.
- [143] A. Meijerink and A. Molisch, “On the physical interpretation of the Saleh-Valenzuela model and the definition of its power delay profiles,” *IEEE Transactions on Antennas and Propagation*, vol. in press, 2014.
- [144] A. A. M. Saleh and R. Valenzuela, “A Statistical Model for Indoor Multipath Propagation,” *IEEE Journal on Selected Areas in Communications*, vol. 5, no. 2, pp. 128–137, February 1987.
- [145] L. Liu, C. Oestges, J. Poutanen, K. Haneda, P. Vainikainen, F. Quitin, F. Tufvesson, and P. Doncker, “The COST 2100 MIMO channel model,” *IEEE Wireless Communications*, vol. 19, no. 6, pp. 92–99, December 2012.

- [146] M. Jakobsen, T. Pedersen, and B. Fleury, "Analysis of Stochastic Radio Channels With Temporal Birth-Death Dynamics: A Marked Spatial Point Process Perspective," *IEEE Transactions on Antennas and Propagation*, vol. 62, no. 7, pp. 3761–3775, July 2014.
- [147] P. Meissner, D. Arnitz, T. Gigl, and K. Witrisal, "Indoor UWB Channel Analysis in an Atrium-Style Office Building for Multipath-Aided Localization," in *COST Action IC1004 Scientific Meeting*, Lund, Sweden, 2011.
- [148] C. Krall, "Signal processing for ultra wideband transceivers," PhD thesis, Graz Univ. of Techn. (Austria), 2008.
- [149] W. Wiesbeck, G. Adamiuk, and C. Sturm, "Basic Properties and Design Principles of UWB Antennas," *Proceedings of the IEEE*, vol. 97, no. 2, pp. 372–385, 2009.
- [150] J. Sachs, R. Herrmann, M. Kmec, M. Helbig, and K. Schilling, "Recent Advances and Applications of M-Sequence based Ultra-Wideband Sensors," in *IEEE International Conference on Ultra-Wideband, ICUWB 2007.*, 2007.
- [151] R. Cepeda, S. C. J. Parker, and M. Beach, "The Measurement of Frequency Dependent Path Loss in Residential LOS Environments using Time Domain UWB Channel Sounding," in *Ultra-Wideband, 2007. ICUWB 2007. IEEE International Conference on*, 2007.